ANISOTROPY AND MANTLE FLOW OF THE INDO-BURMA SUBDUCTION ZONE FROM SHEAR WAVE SPLITTING AND SHEAR WAVE SPLITTING TOMOGRAPHY

A Thesis

presented to

the Faculty of the Graduate School

at the University of Missouri-Columbia

In Partial Fulfillment

of the Requirements for the Degree

Master of Science

---

by

MD MOHIMANUL ISLAM

Dr. Eric Sandvol, Thesis Supervisor

DECEMBER 2020

The undersigned, appointed by the dean of the Graduate School, have examined the thesis entitled

Anisotropy and Mantle Flow of the Indo-Burma Subduction Zone from Shear Wave Splitting and Shear Wave Splitting Tomography

presented by Md Mohimanul Islam,

a candidate for the degree of Master of Science, and hereby certify that, in their opinion, it is worthy of acceptance.

_____

Dr. Eric Sandvol

_____

Dr. Francisco Gomez

_____

Dr. Brent L. Rosenblad

ACKNOWLEDGEMENTS

First of all, I would like to express my gratefulness to Almighty Allah for giving me the strength and patience for the successful completion of my Master's thesis research on "Anisotropy and Mantle Flow of the Indo-Burma Subduction Zone from Shear Wave Splitting and Shear Wave Splitting Tomography" at the Department of Geological Sciences, University of Missouri-Columbia.

I would like to express my utmost respect and gratitude to my supervisor Dr. Eric Sandvol, Professor, Department of Geological Sciences, the University of Missouri-Columbia for giving me the opportunity to pursue my MS thesis under his kind supervision. This work would not be possible without his proper guidance, valuable suggestions, and endless encouragement. It has been my great honor to work with him.

I would like to convey my deep sense of tribute to my committee members Dr. Francisco (Paco) Gomez, Associate Professor, Department of Geological Sciences, and Dr. Brent L. Rosenblad, Department of Civil and Environmental Engineering for their insightful suggestion, constructive criticism in completing the thesis work.

I would like to thank the Division of Earth and Atmospheric Science, National Science Foundation for providing funding to deploy the Bangladesh India Myanmar Array (BIMA) seismic network. Also, many thanks to Incorporated Research Institutions for Seismology (IRIS) providing the necessary instruments, training, and logistics to install and maintain the seismic network in Myanmar.

My thanks go out to Dr. Wei Shengji, Assistant Professor, Nanyang Technological University, Singapore to provide their Earth Observatory of Singapore (EOS) network data which helps to expand my research area.

My deep appreciation goes out to the teammates of the fieldwork in Myanmar especially Oo Than and Tun Lin Kyaw, scientist, Department of Meteorology and Hydrology (DMH), Myanmar. Without their constant support, it would be difficult to install and service the seismometers in remote and hilly terrain in Myanmar. I am also grateful to the seismology people at DMH and local people in Myanmar for their supporting role in the fieldwork.

I would also like to say a heartfelt thank you to my Mum, Dad, and my little brother for their endless love and encouragement. Last but not least, I would like to take the opportunity to convey my immense love and gratitude to my friends for their encouragement and inspiration.

TABLE OF CONTENTS

ACKNOWLEDGEMENTS ii

LIST OF FIGURES vi

Abstract 1

Chapter 1 2

Introduction 2

Regional Tectonic Settings 5

Indo-Burman Ranges 5

Burma Terrain (BT) 8

Volcanic Arc 10

Shan Plateau 11

Seismicity 11

Subduction Style 14

Crustal deformation and thickness 18

Chapter 2 23

Shear Wave Splitting 23

Anisotropy and Mantle Deformation Fabric 29

BIMA Seismic Network 34

Data Processing 39

Locating Deep Events 40

Triggering Algorithm 40

Windowing and Measurements 43

Quality Control 43

Model Space 48

Forward Modeling 49

Inversion 50

Resolution Test 51

Chapter 3: Results and Discussions 55

Teleseismic Splitting Results 55

Local S wave Splitting Results 60

Depth Dependency 64

Back-azimuth dependency 71
SWST Results 76
Tectonic Implications 84
Conclusion 93
References 95
Appendix 107
List of local splitting results 107
List of XKS splitting results 113
Station average XKS splitting results 117
List of XKS null results 118
BAZ variations of splitting parameters (local) 123
BAZ variations of splitting parameters (XKS) 132

LIST OF FIGURES

Figure 1: (a) Tectonic map showing the Alpine-Himalayan Orogenic Belt and location of Indo-Burma Ranges(IBR) [Modified from Furnes et al., 2020]; (b) Regional structural map of the Indo-Burma Range with major fault systems. 6

Figure 2: Simplified map showing the major tectonic units of the IBR and surroundings [form Najman et al., 2020] 7

Figure 3: Wuntho-Popa Arc system (blue polygon) and active volcanos (yellow triangle) in Myanmar; BT-Burman Terrane, SF- Sagaing Fault, IBR- Indo Burman Range, WPA - Wuntho-Popa Arc 9

Figure 4: Seismicity of the study area (inside the box) and surrounding regions (from Russo, 2012). 12

Figure 5: Active faults and major earthquakes in the study area (> M_w 7.0) 13

Figure 6: 3D Geometry of the subducting Indian Slab; blue triangles are the active Quaternary volcanos [modified from Hurukawa et at., 2012] 14

Figure 7: Plot of earthquake epicenters and focal mechanisms; earthquakes from ±50 km on either side of the profile are projected onto the profile to highlight the geometry of the down-going Indian plate.[from Kumar et at., 2015] 15

Figure 8: P wave tomographic image of subducting Indian Slab [from Wei et al., 2012] 17

Figure 9: Thickness of the crust from the base of the low velocity sedimentary layer to the Moho. (from Wang et al.,2019) 19

Figure 10: GPS vectors show velocities relative to the fixed Indian plate. [from Steckler et. al., 2016 and Gahalaut et al., 2013]. 20

Figure 11: Age of the Indian and surrounding oceanic lithosphere (from Müller et at., 2008) 21

Figure 12: Schematic diagram of shear wave splitting due to upper mantle anisotropy, [after Long and Becker, 2010] 23

Figure 13: Characteristics wave front of P and S wave travelling through an isotropic and an anisotropic medium 25

Figure 14: (a) Teleseismic core phase XKS splitting; (b) local direct S wave splitting on a subduction zone (from Savage, 1999) 27

Figure 15: Example of lattice preferred orientation and shape preferred orientation (SPO) [modified from Moore et al., 2004) 29

Figure 16: Schematic diagram of the relationship between horizontal mantle flow and the resulting azimuthal anisotropy for different olivine fabric types (from Long & Becker, 2010) 31

Figure 17: Teleseismic shear wave splitting of the Indo-Eurasian collisional belt showing strong correspondence with present day crustal deformation (from the global shear wave splitting database (Wüstefeld et. at., 2009; Liu et. al., 2014; Yang et. al., 2014; IRIS DMC, 2012). Black block shows the location of our study area. 33

Figure 18: BIMA seismic array; Blue and pink triangles are stations deployed in Myanmar and Bangladesh respectively 34

Figure 19: Servicing and station location of BIMA array; (a) servicing of station MS05; (b) Sensor box covered with Styrofoam casing; (c) Outside plastic box containing data logger, bailer and battery; (d) typical mountainous site (station MP02) of western part of the array. 35

Figure 20: All currently active networks in Myanmar; EHS – Eastern Himalayan Syntaxis; SF- Sagaing Fault 36

Figure 21: Location of seismic stations used for this study 38

Figure 22: Distribution of teleseismic events used in this study 39

Figure 23: Network arrays used in locating deep events 41

Figure 24: Distribution of relocated local events using Hypoinverse 42

Figure 25: Selection of the S wave window for local events; (a) event showing P and S wave arrivals; (b) zoomed- in view showing the visible S wave splitting (blue arrow); start and end are the beginning and end of the window respectively 44

Figure 26 : Quality control of splitting results for local S wave; (a) uncorrected and corrected waveform and ppm; (b) energy plot. 45

Figure 27: Quality control of splitting results for local SKS phase; (a) corrected and uncorrected waveform and ppm; (d) energy plot. 46

Figure 28: SWST model space and distribution of events and stations. Green circles are local spitting events, pink circles at base of 400 km is projected tele-seismic events; red and yellow triangles are stations and Quaternary volcanoes, respectively. 47

Figure 29: Resolution Test result using real event-station pairs 53

Figure 30: Weighted mean misfit of splitting parameters with iterations; (a) fast direction; (b) lag time .. 54

Figure 31: Station average teleseismic shear wave splitting measurements 56

Figure 32: Example of a well resolved teleseismic splitting result producing higher δt 57

Figure 33: Example of a well resolved teleseismic splitting result producing one of the lowest results (station MP21). 58

Figure 34: Stations across the Shan Plateau having smaller lag times and nulls with their azimuthal coverage. 59

Figure 35: Local S wave splitting results; splitting vectors are plotted at the midpoint of the event-station pair. 61

Figure 36: Ray path coverage of the local splitting results. Each black line connects an event-station pair. Splitting parameters are on the Fig-35, plotted at the midpoints. 62

Figure 37: Example of well resolved local splitting results; (a) very low lag time 0.2 s; (b) high lag time 0.9 s. 63

Figure 38: Local S wave splitting result of upper 50 km events. 65

Figure 39: Local splitting results of 50-100 km deep events. 66

Figure 40: Local splitting results of 100-150km deep events. 67

Figure 41: E-W local splitting measurements and their ray-path coverage 68

Figure 42: Local (red) and SKS (blue) splitting results on the western forearc and the eastern arc and the back arc; dotted lines are slab contours and yellow triangles are volcanoes. 69

Figure 43: SKS splitting results of the southern part of the study area..... 70

Figure 44: An example of a multiple anisotropic layer splitting (from Silver and Savage, 1994) 71

Figure 45: Division of the study area for investigating back-azimuth dependency of the splitting parameters. Red inverted triangles are the location of the stations and yellow triangles are the active volcanoes. SF-Sagaing Fault 72

Figure 46: Back-azimuth variations of splitting parameters on (a), (b) the northwest and (c), (d) northeast part. 73

Figure 47: Back-azimuth variations of splitting parameters on (a), (b) the southwest and the southeast part. 74

Figure 48: Back-azimuth variations of SKS splitting parameters at station MDY shows relatively constant (a) lag time and (b) fast direction. 74

Figure 49: Back-azimuth variations of local splitting parameters at station showing relatively constant δt and variable φ; (a)MS05; and (b) MP19. 75

Figure 50: Back azimuth variations of local splitting parameters. Station (a)MP06 shows 90° periodicity and (b) MP04 shows only E-W fast direction. 76

Figure 51: Model area (blue box) used in SWST inversion and the input model for the checkerboard test. SF-Sagaing Fault. 77

Figure 52: Checkerboard test results using real event station pairs; recovered results of depth (a) 0-100 km; (b) 100-200 km ; (c) 200-300 km; (d) 300-400 km, ray-paths that only sample the blocks are shown. 78

Figure 53: Final SWST results showing the orientation and strength of anisotropic fabric;(a) in map view; (b) 3D view 79

Figure 54: SWST results of the individual depth slices (a) 0-50 km; (b) 50-100 km. Red dotted circles are the region of high anisotropic strength; other legends are same as Fig-53. 81

Figure 55: SWST results of the individual depth slices (a) 50-100 km; (b) 150-200 km. Legends are same as Fig-53. 82

Figure 56: SWST results viewing (a) across longitude and (b) across latitude 83

Figure 57: Comparison of SKS splitting results between the EHS and its southern part (our study area); EHS SKS splitting data are taken from McNamara et at., 1994; Sol et al., 2007; Wang et al., 2008; León Soto et al., 2012; Chang et al., 2015. 84

Figure 59: SKS splitting of Indo-Eurasian collisional belt integrated with newer results; previous results are from SWS the database (from Wüstefeld et. at., 2009; Liu et. al., 2014; Yang et. al., 2014; IRIS DMC, 2012) 85

Figure 60: Relationship between the trench migration velocity and lag time of the subduction system (form Long & Silver, 2008) worldwide; red and blue lines are advancing and retreating trench respectively. This model assumes that the IBR trench migrates same rate as the average convergence velocity. 86

Figure 61: Histogram of average lag time from the global shear wave splitting database (Wüstefeld et. at., 2009; Liu et. al., 2014; Yang et. al., 2014; IRIS DMC, 2012); arrow shows the average lag time of sub-slab region of the Indo-Burman subduction system. 87

Figure 62: Comparison of δt between the central wedge and proximity of Sagaing fault (within 0.5° of the trace of Sagaing faults 89

Figure 63: Shear wave splitting observations and associated mantle flow domains 91

Figure 64: Schematic cross-section along the profile 'A-B ' [Fig-63] showing mantle flow models of the subducting Indian Slab. SF- Sagaing Fault 92

Abstract

The Indo-Burma subduction zone lies on the eastern boundary of the 1500 km long Alpine-Himalayan orogenic belt. Despite highly oblique plate motion with limited arc development, convergence is still ongoing with the potential to generate megathrust earthquakes that could affect more than 140 million people. This sub-aerial subduction system provides an excellent opportunity to study the nature of mantle deformational fabric resulting from the active convergence and collision with possible clockwise rotation of the Indian plate. Characterizing the mantle flow field helps us to better understanding the geodynamics and regional tectonics of this part of the plate boundary. Shear wave splitting is a simple yet powerful technique to investigate anisotropy and mantle strain fabric. I have used both teleseismic and local shear waves to create a detailed map of the upper mantle anisotropic fabrics using a recently deployed temporary and permanent seismic stations, across the northern and central parts of Myanmar. Along with the detailed analysis of splitting parameters, I have generated a tomographic model inverting local and teleseismic shear waves splitting results. The resulting 3D anisotropic model helps to image the prevailing mantle flow below the slab in the sub-slab region and above the slab in the mantle wedge. I found a trench parallel fast direction with high lag time (>2.0s) on the fore-arc that primarily accumulated in the sub-slab region. Such observed fabric results from the toroidal flow around the slab in response to the slab roll-back. The mantle wedge shows a complex deformational fabric with an average lag time of over 0.5s. Dextral motion along the Sagaing fault induces a dominant trench parallel fabric on the mantle wedge. Null results in the southern part of the Shan plateau suggest that back-arc upwelling may exist between the transition of the east-west fast direction on the southern Yunnan and the north-south fast direction of the western subduction margin. The nature of the transition of the mantle fabric and back-arc upwelling is not well understood due to the lack of seismic station coverage on the Shan plateau.

Chapter 1

Introduction

The Indo-Burman subduction, an eastward continuation of the Indo-Eurasia collision, forms an oblique subduction system where the Indian plate is subducting beneath the Burma microplate. It connects the main Himalayan collisional belt in the north and the Sumatra- Andaman subduction zone in the south through a sharp bend along the Eastern Himalayan Syntaxis. Unlike other subduction zones, it is characterized by limited arc magmatism and the development of a thick, sub-aerial accretionary wedge. This poses the question of whether the subduction is still active (Rao & Kumar, 1999; Guzmán-Speziale & Ni, 2000); however, recent studies show 12-24 mmy^{-1} of convergence along with the dextral motion, revealing its active nature (Steckler et al., 2016; Mollick et al., 2019).

Since the breakup of Gondwana, the Indian Plate has moved northward and collided with the Eurasian plate around 50 million years ago (Meng et al., 2012). The resulting collision created the largest deforming region on the planet (Molnar & Tapponnier., 1975). The continued northward convergence of the Indian plate created the Himalayas and the Tibetan plateau with the thickest crust, whereas the eastward oblique convergence leads to the formation of the Indo-Burman subduction zone. This oblique convergence also facilitates strain partitioning, much of which is accommodated by the arc-parallel dextral Sagaing Fault along the eastern boundary of the Burma microplate (Fitch., 1972; McCaffrey., 1992, Steckler et al., 2016; Khin et al., 2017). Structurally from west to east, this region consists of the Indo-Burman ranges, the Central Myanmar Basin (CMB), and the Shan Plateau. Major tectonic processes such as accretion, collision, and subduction events have been identified from the Early Cretaceous to the Quaternary (Mitchell., 1992; 1993;

Allen et al., 2008; Liu et al., 2016). The detailed tectonic framework and its evolution remain elusive; however, with the recent efforts of many researchers and renewed interest among the scientific community, the geodynamic model of this part of the plate boundary is constantly evolving and being refined. This complex tectonic system potentially provides an excellent opportunity to study the nature of mantle deformation in response to the collision and clockwise rotation around the Eastern Himalayan Syntaxis. While GPS velocity and geological observations allow us to infer the present-day crustal deformation, the study of shear wave splitting enables us to identify mantle deformation fabrics.

This research aims to delineate the mantle deformation fabric of this complex subduction system by detailed characterization of the splitting parameters. Despite recent advances in our understanding based on seismological observations, the nature of mantle deformation fabrics of this part of the plate boundary remains unknown. The dynamics of the slab-trench system controls the active mantle deformation of a subduction margin. Subduction of the Indian plate since the Paleogene (Mitchell, 1993; Curray, 2014; Najman et al., 2018, Zhang et al., 2017) would induce a distinct mantle strain fabric. The stagnant Indian slab model as proposed by some earlier researchers (Rao & Kumar, 1999; Guzmán-Speziale & Ni, 2000) would produce little or no sub-slab splitting (Long & Silver, 2008). On the other hand, a migratory slab-trench system would produce strong trench-parallel mantle deformation as observed in many subduction systems around the world (Russo & Silver, 1994; Long and Silver 2008, 2009). The indentation of the Indian plate along with a clockwise rotation (Curry, 2005; Acharya, 2006) and the westward migration of the Neogene fold and thrust belt (Karig et al., 1979; Hurukawa et al., 2010; Lohman., 1995) would favor the subduction with slab-retreat model. In contrast, a relatively stationary slab-trench system with respect to the upper mantle would also induce little deformation fabric around the slab

(Facenda et al., 2014; Long and Silver 2008, 2009). The Cenozoic stable subduction margin without clockwise rotation proposed by Westerwheel et al., (2019) would favor the idea of a stationary slab-trench system. Mapping upper mantle deformation fabrics using shear wave splitting can help to resolve the competing slab-trench evolution models. Combining local and teleseismic splitting measurements, the main objective is to generate a shear wave splitting tomographic (SWST) model. The resulting 3D anisotropic model helps to reveal the prevailing mantle flow within different domains of the Indo-Burma subduction system (i.e., sub-slab, mantle wedge, or slab itself) and its slab-trench dynamics. I have used 31 recently deployed seismic stations which are part of the Bangladesh India Myanmar Array (BIMA) network, 29 stations from the Earth Observatory of Singapore (EOS) network, and nine permanent stations from the Myanmar National Seismic Network (MM).

Regional Tectonic Settings

Indo-Burman Ranges

The Indo-Burman Ranges (IBR), also known as Indo-Myanmar Ranges, are primarily composed of a thick sequence of Mesozoic-Cenozoic flysch and molasse type of rock that stretches from western Myanmar to Bangladesh. To the north, it connects the Eastern Himalayan Syntaxis (EHS) as a southward continuation of the India-Eurasia collisional belt and a transition between the continent-continent collision to the oceanic subduction. Forming a 1400 km N-S to NNE-SSW long mountain range, it merges with the Sumatran subduction to the south. The eastern margin of the IBR gradually merges with the Ganges-Brahmaputra Delta (GBD) with a blind deformation front, whereas the western part is separated from the Burmese microplate by the Kaladan fault [Fig-1]. Tectonically, the IBR is an accretionary wedge formed by the subduction of thinned attenuated continental and oceanic crust of the Indian plate under the Western Burma Block since early Paleogene (Mitchell., 1993; Curray., 2014; Najman et al., 2018, Zhang et al., 2017). This westward younging of the mountain range is subdivided into the outer belt, the inner belt, and the metamorphic core from the west to east (Maurin and Rangin., 2009; Socquet et al., 2002) [Fig-1]. Fold and thrust systems of the outer belts are primarily developed in the Neogene period. The intensity of the deformation decreases westward and merges with the Bengal basin. Thick Eocene-Oligocene flysch and overlying Mio-Pliocene molasse rock type form the bulk of the stratigraphic units of the outer belt. Separated by the Kaladan fault (especially on the southern part), the inner

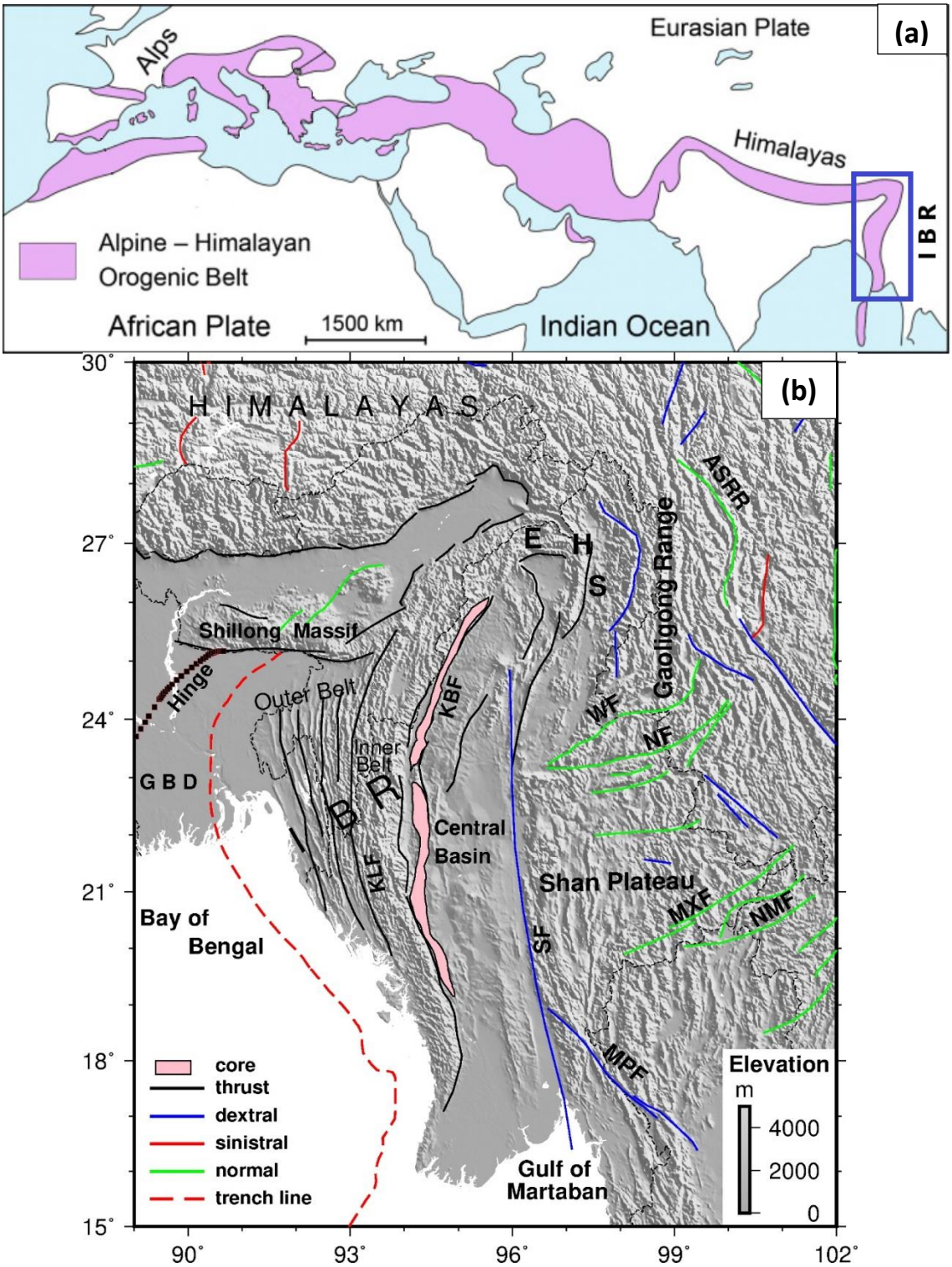

Figure 1: (a) Tectonic map showing the Alpine-Himalayan Orogenic Belt and location of Indo-Burma Ranges(IBR) [Modified from Furnes et al., 2020]; (b) Regional structural map of the Indo-Burma Range with major fault systems; GBD-Ganges Brahmaputra Delta, IBR-Indo-Burma Ranges, EHS- Easter Himalayan Syntaxis, KLF- Kaladan Fault, KBF-Kabaw Fault, SF-Sagaing Fault, MPF- Mae Ping Fault, MXF-Mengxing Fault, NMF-Nam Ma Fault, NF-Nanting Fault, WF-Wanding Fault, ASSR- Ailao Shan–Red River Shear Zone. Faults are from Taylor & Yin (2009) with minor additions and adjustments.

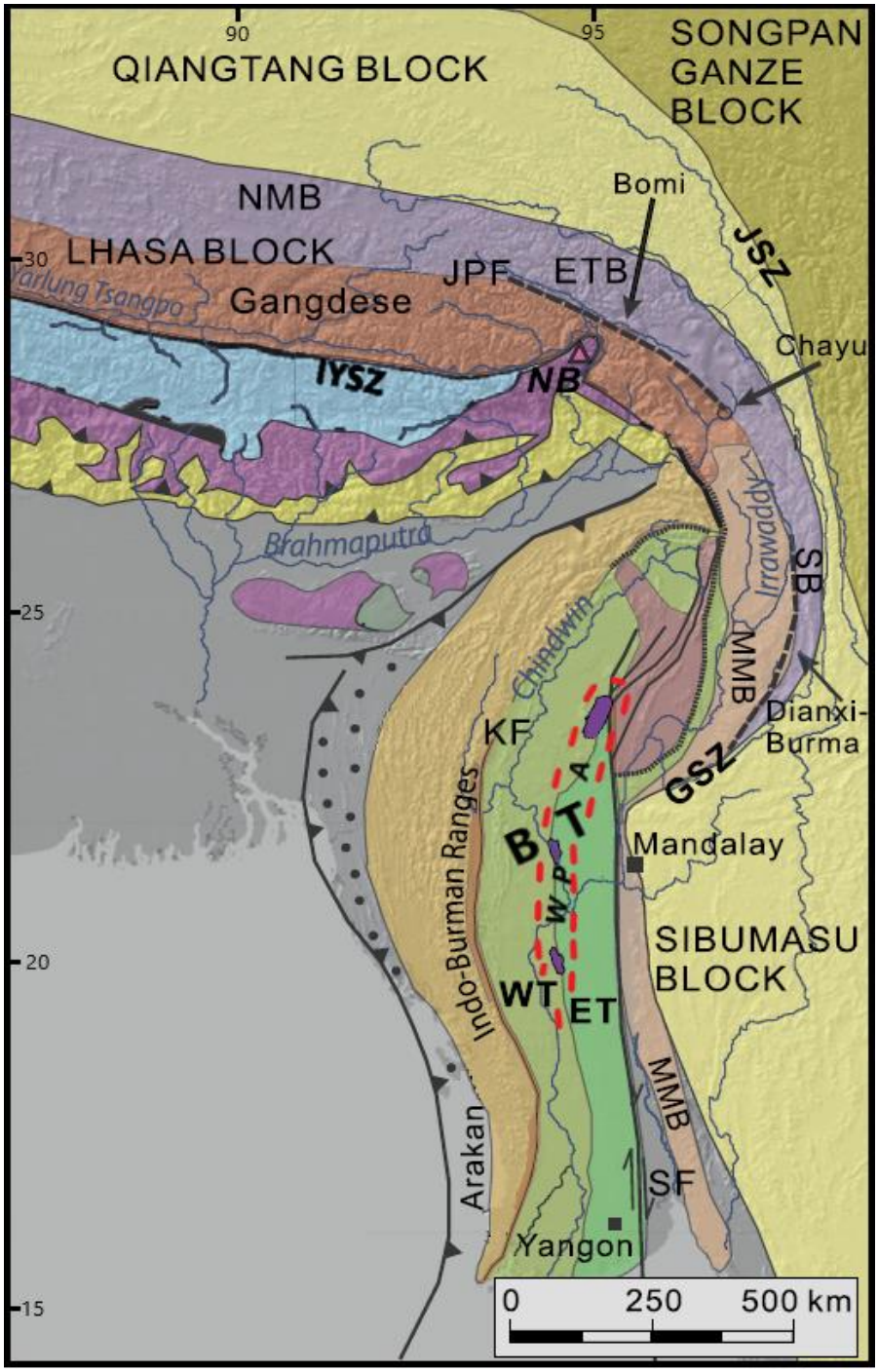

Figure 2: Simplified map showing the major tectonic units of the IBR and surroundings [form Najman et al., 2020]; KF-Kaladan Fault, BT- Burma Terrain, SF-Sagaing Fault, WPA- Wunthu-Popa Arc, MMB- Mogok-Mandalay-Mergui Belt, NB- Namcha Barwa, IYSZ- Yarlung-Tsangpo suture, MMB- Mogok-Mandalay-Mergui Belt, GSZ- Gaoligong Shear Zone, JSZ-Jinsha Suture zone, JPF- Jiali-Parlung Fault

belt represents the Late Cretaceous-Paleogene section of the highly folded thrust belt (Bekta et al., 2018; Najman et al., 2020) of the IBR. The easternmost core complex unit is composed of ophiolite sequences, Triassic flysch, and some metamorphic units. The Kalaymyo ophiolite is the southward continuation of the Yarlung-Tsangpo suture (IYTS) and represents the Neo-Tethys suture zone equivalent [Fig-2].

Burma Terrain (BT)

Also known as the Western Myanmar Block or the Burma Microplate, the N-S trending tectonic block acts as a forearc sliver bounded by the mobile IBR on the west and the stable Sibumasu Block on the east [Fig-2]. The western boundary is delineated by the Kabaw Faults and the Kaleymyo Ophiolite (Fitch 1972; Curray et al. 1979; Bertrand & Rangin 2003). This central part of Myanmar is topographically lower and also is known as the Central Myanmar Basin (CMB). It is covered by Paleogene marine to Oligo-Miocene continental fluvial sedimentary facies. The Wunthu-Popa Arc separates the CMB into the western fore-arc and the eastern back-arc basin [Fig-2 &3]. Several sub-basins (e.g. Chindwin Basin, Shwebo–Monywa Basin, Salin Basin, Pyay Basin, Ayeyarwady Embayment Basin) are identified within the CMB and are filled primarily with Cenozoic sediments.

The eastern margin of the BT is demarcated by the active dextral strike-slip Sagaing fault. It likely formed due to the oblique convergence of the Indian plate with respect to the Sunda plate by means of a strain partitioning (Fitch, 1972; McCaffrey, 1992). It has an estimated displacement of 400 to 1100 km since the Miocene (Mitchell 1993; Morely 2017; Morely & Arboit 2019). It extends over 1200 km, connecting the Eastern Himalayan Syntaxis to the north and the Andaman spreading center to the south. Traces of the fault zone become wider towards the north and it

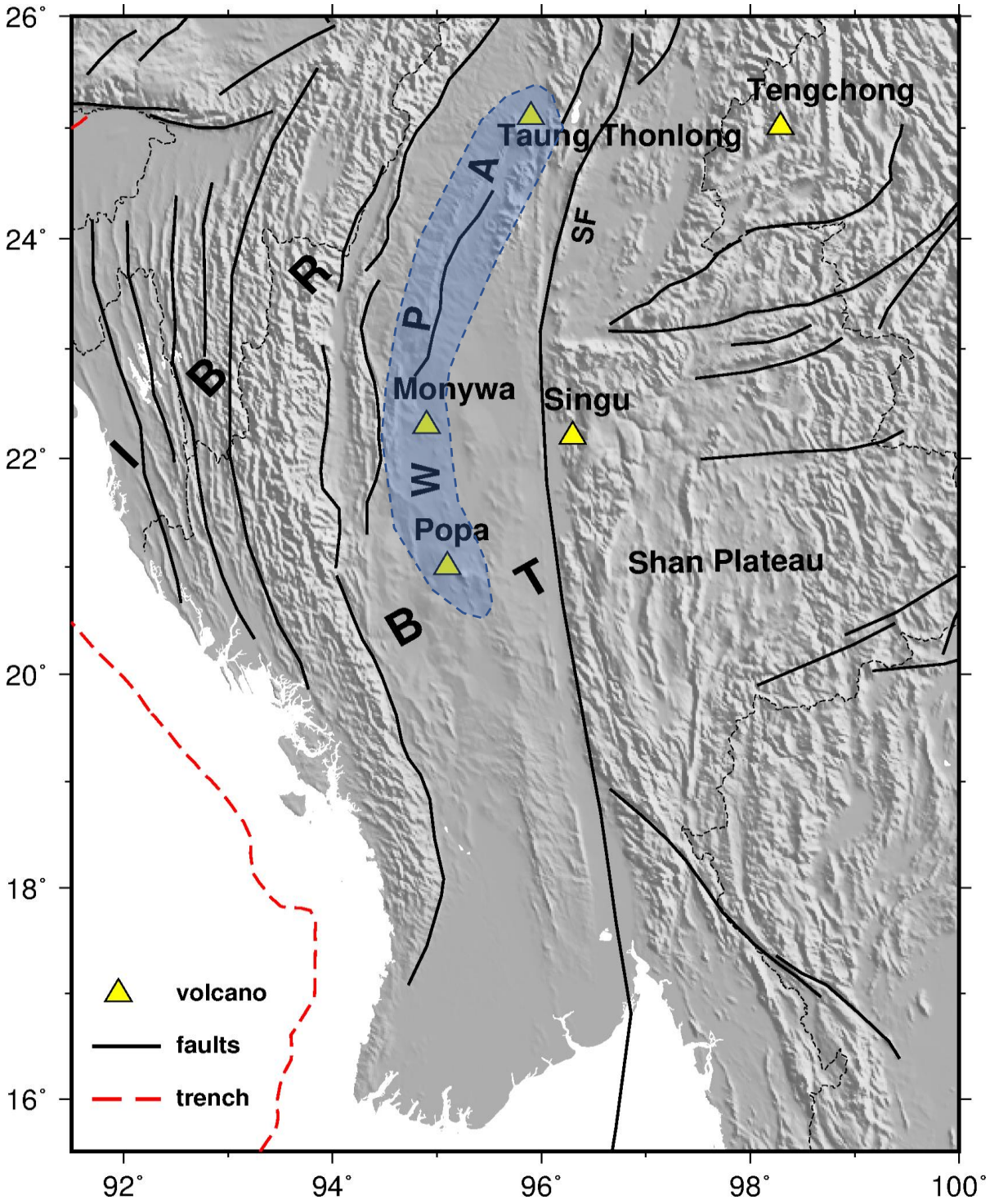

Figure 3: Wuntho-Popa Arc system (blue polygon) and active volcanos (yellow triangle) in Myanmar; BT- Burman Terrane, SF- Sagaing Fault, IBR- Indo Burman Range, WPA - Wuntho-Popa Arc

splits into three distinct branches around at ~24°N (Maurin et al., 2010). Dextral motions along this fault absorb ~21 mm/yr of the total ~46 mm/yr of Indian plate motion (Steckler et al., 2016; Mallick et al., 2019).

Immediately east of the Sagaing Fault, a metamorphic belt known as the Mogok-Mandalay-Mergui Belt (MMB) lies between the BT and the Shan Plateau [Fig-3]. This 700km long arcuate belt [Fig-2] consists of a medium pressure high-temperature regionally metamorphosed rock. This unit has been considered to be the extension of the Trans-Himalayan arc and the Lassa terrane. (Mitchell et a., 2007; Serale et al., 2007; Allen et al., 2008).

Volcanic Arc

Unlike other active subduction zones, magmatic activity is very limited here. Five active volcanos characterize the Late Cenozoic volcanism in Myanmar, three of which [Fig-3] were formed as the consequence of active subduction (Lee et al., 2015). However, a linear belt of Cretaceous to Paleogene volcanic rocks and granitoid batholiths signifies the pre-Cenozoic subduction-related arc magmatism (Mitchell et at., 2012). Known as the Wuntho-Popa arc, it divides the central basin into western terrain (WT) and eastern terrain (ET) [Fig-2 & 3]. A large gap in arc volcanism exists from the Mid-Miocene to Quaternary (Maury et al., 2004; Mitchell et at., 2012; Lee et al., 2015). The Mid-Miocene volcanic rocks are andesitic in composition, whereas the Quaternary volcanic rocks (e.g. Mt. Monywa) are heterogeneous in nature, ranging from basaltic to andesitic. Lee et al. (2015) suggest that the Quaternary volcanism results from the asthenospheric upwelling that leads to a small-degree of melting of the pre-Miocene subduction-enriched lithospheric mantle and the asthenosphere beneath the central Myanmar basin.

Shan Plateau

With an average elevation of over 1000m, the Shan Plateau lies in the eastern part of Myanmar. (Mitchell, 1989). It is considered the western edge of the rigid and stable Sundaland block (Sibumasu Block). The Shan plateau escarpment, characterized by a steep topographic gradient, lies between the BT and the Shan plateau. Evidence of remnant dextral deformation along the Shan Scarp is observed which suggests the presence of pre-Miocene oblique subduction. (Morley, 2017).

Seismicity

Situated at the eastern boundary of the Alpine Himalayan earthquake belt, Myanmar is one of the most earthquake-prone countries in the world. Two distinct active tectonics processes control the seismicity of this region. The first is the E-W convergence between the Indian and the Burma microplate. The focal depth of the earthquakes can be as deep as 200 km. The subducting slab is illuminated [Fig-4] by the Benioff zone earthquakes (Stork et al., 2008). The second is to the northward movement of the Burma microplate along the Sagaing and other dextral fault systems. These earthquakes are generally shallow focused and can cause severe damage to the infrastructure. Historical records indicate that several large earthquakes ($M_w > 7.0$) have occurred along the Sagaing Fault [Fig-5] that caused considerable structural damage and casualties (Hurukawa & Maung, 2011; Thant, 2012). A recent study suggests the presence of a locked megathrust plate boundary fault close to the deformation front that can produce an earthquake of M_w ~8.0 (Steckler et al., 2016).

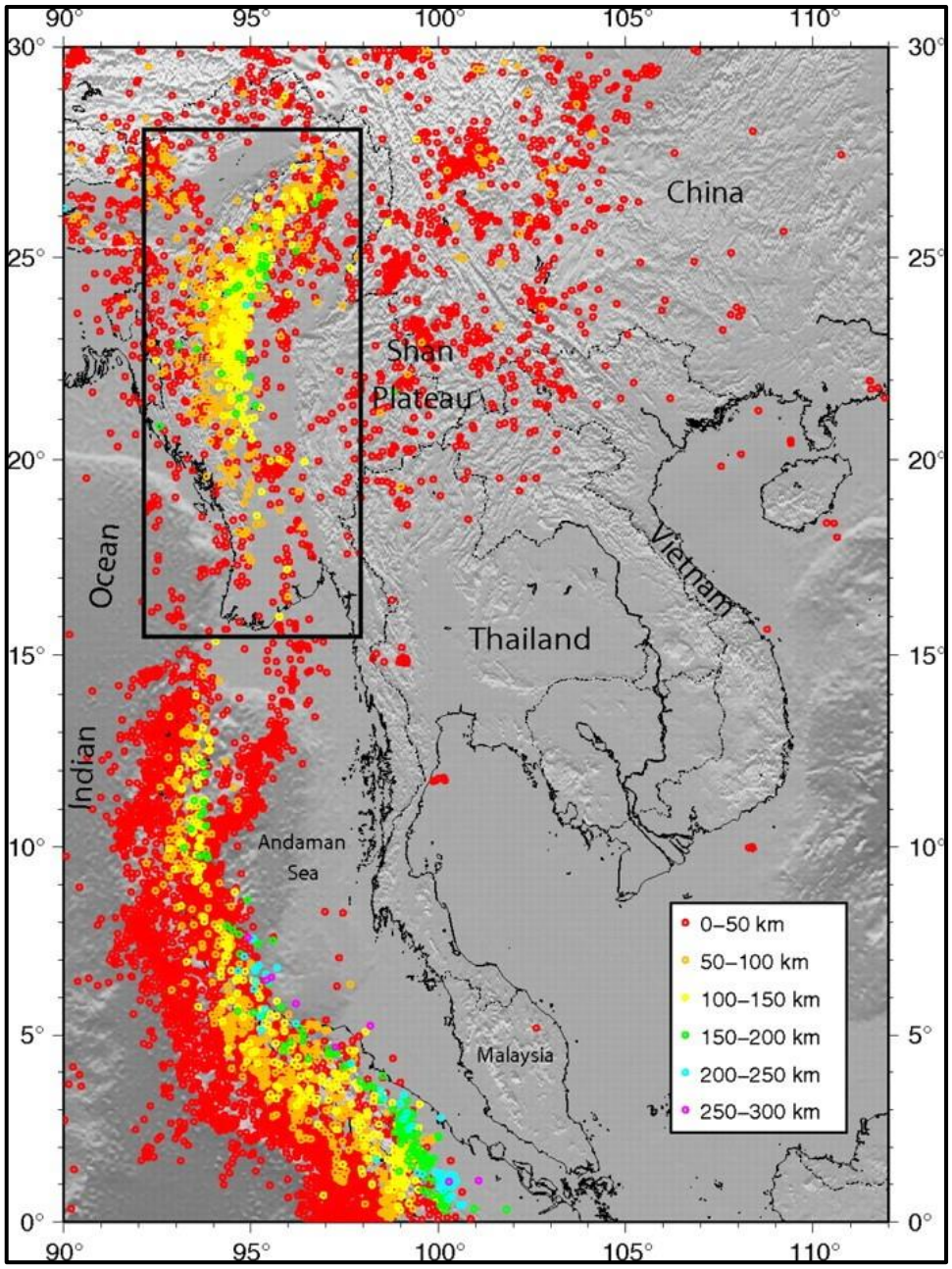

Figure 4: Seismicity of the study area (inside the box) and surrounding regions (from Russo, 2012).

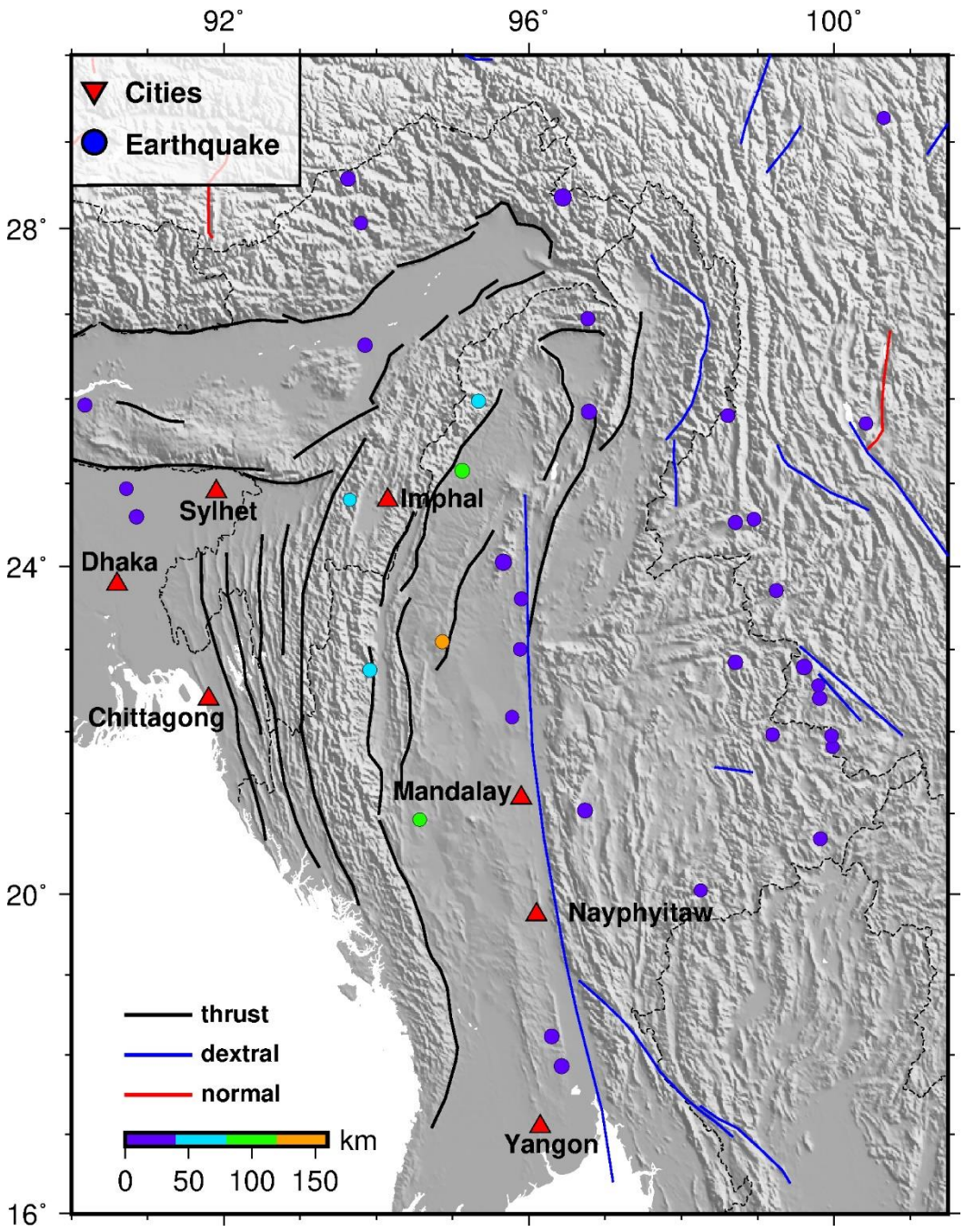

Figure 5: Active faults and major earthquakes in the study area (> M_w 7.0)

Subduction Style

The Wadati–Benioff zone earthquakes illuminate the geometry of the subduction system. Relocation of earthquakes up to 160 km depth reveals the rapid change in the slab dip from 25° at 40-48 km depth to 60° at 120-160 km depth (Ni et al., 1989; Stork et al., 2008). Hurukawa et al. (2012) produced a detailed geometry of the iso-depth contour of the slab using

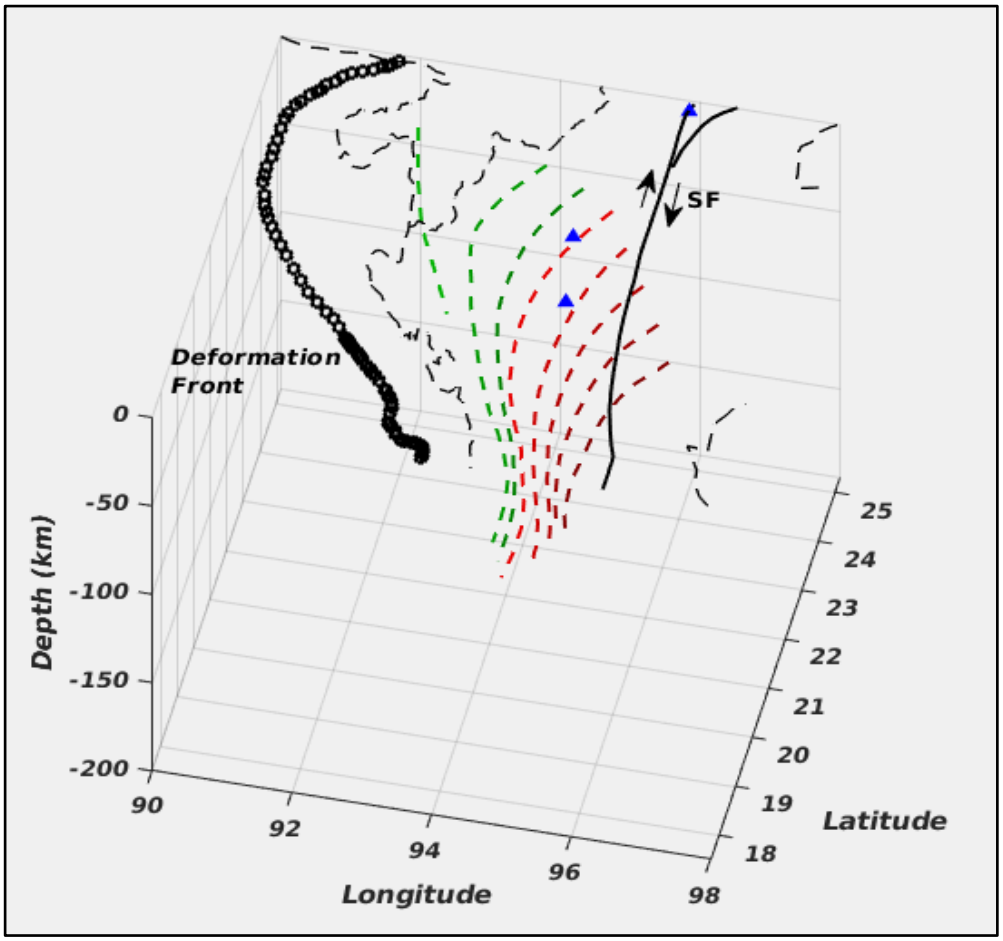

Figure 6: 3D Geometry of the subducting Indian Slab; blue triangles are the active Quaternary volcanos [modified from Hurukawa et at., 2012]

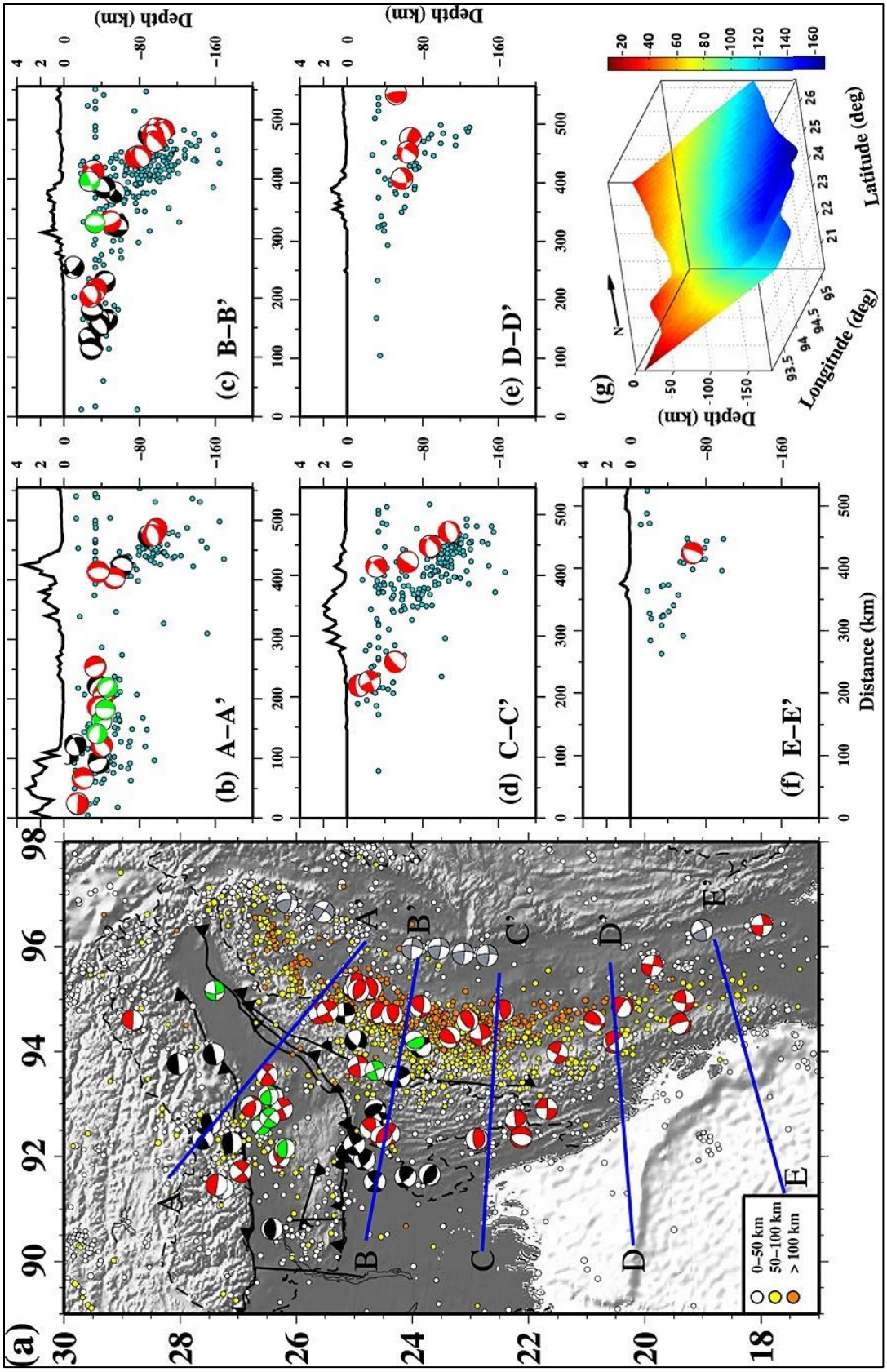

Figure 7: Plot of earthquake epicenters and focal mechanisms; earthquakes from ±50 km on either side of the profile are projected onto the profile to highlight the geometry of the down-going Indian plate.[from Kumar et at., 2015]

joint hypocenter relocation of the teleseismic P wave arrivals [Fig-6]. The strike of the slab is approximately N-S and shows an “S” shaped pattern following the trend of the IBR. The focal mechanism of the upper part of the slab shows NNE and ESE slip vectors, towards the direction of the ambient stress of the plate motion [Fig-7]. Conversely, the deeper part of the slab has a well-defined T axis in the down-dip direction (Ni et al., 1989; Rao & Kumar 1999; Rao & Kalpna 2005; Kumar et al., 2015). This downdip extension suggests that the deformation of the deeper part is governed entirely by the tensile force due to the gravitational loading on the subducted slab. Besides, the subducted Indian plate might be flexed at depth due to the intraplate stress that produced along-arc variation in the depth distribution of deep earthquakes and arc parallel orientation of the slip vectors (Kumar et al., 2015).

Global P wave travel time tomography by Bijwaard et al. (1998) shows evidence for a subducting Indian slab beneath the Burma microplate. This coarse resolution image could not resolve the detailed slab morphology. Later, Huang and Zhao (2006) found a high-velocity anomaly below the arc down to 400km and a low-velocity zone under the active Tenchong volcano with a deep root. They suggested the slab dehydration and the development of corner flow above the slab results the observed high velocity anomaly.

Wei et al. (2012) produced a higher resolution P-wave tomographic image using seismic networks of East Asia and Tibet. The tomographic image clearly shows the subducting Indian plate as a high-velocity anomaly [Fig-8], dipping eastward steeply in the upper mantle and gradually flattens in the Mantle Transition Zone (MTZ). Most of the subducted Tethyan lithosphere seems to have been detached as indicated by the scattered pieces of the slab down to the lower mantle.

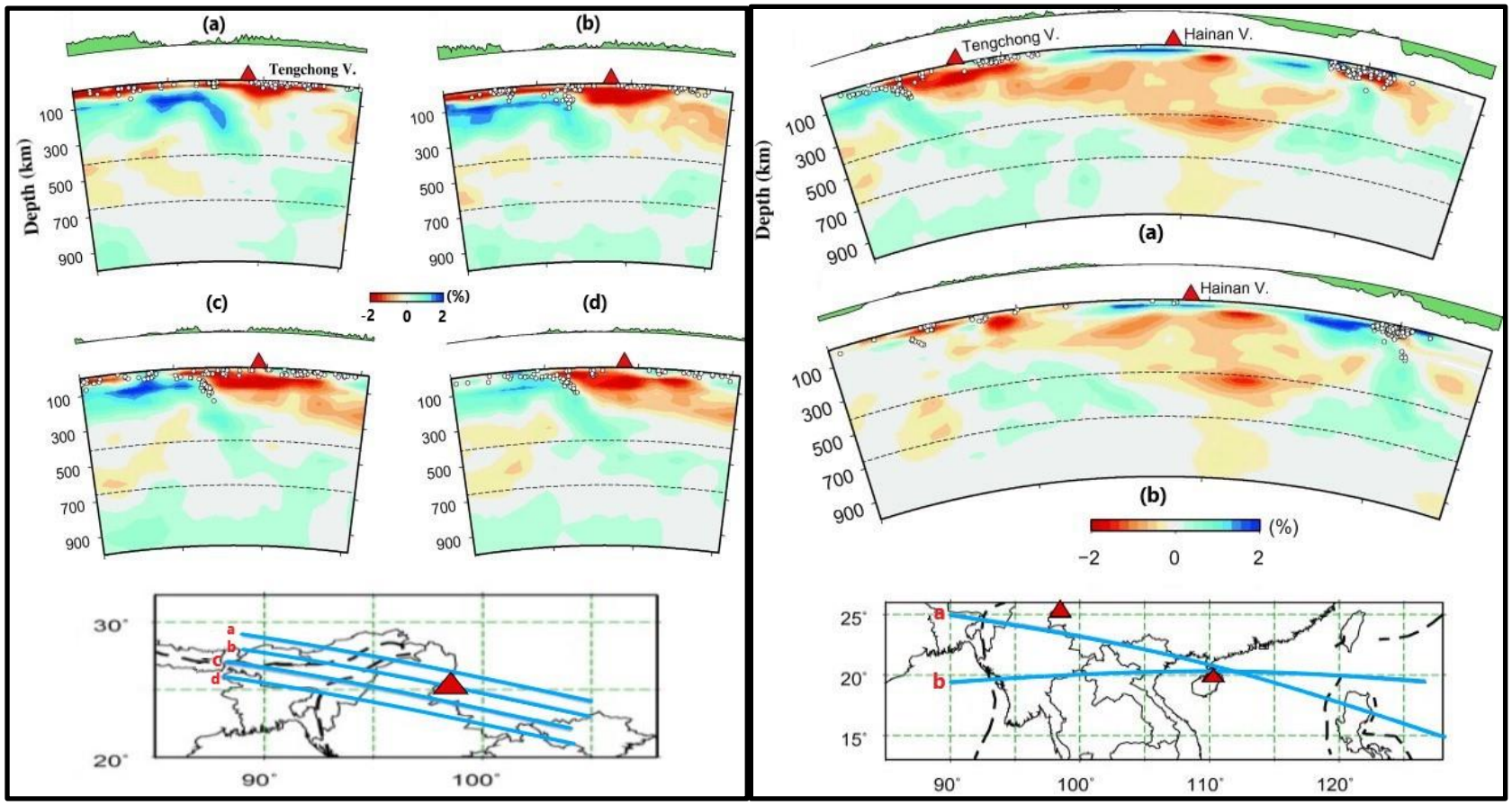

Figure 8: P wave tomographic image of subducting Indian Slab [from Wei et al., 2012]

The steeply descending slab suggests the rapid westward trench migration and slab-retreat from Early Oligocene to Present due to the slowing down of convergence and possible clockwise rotation of convergence (Klootwiik et at., 1979).

Crustal deformation and thickness

Active deformation due to the convergence and dextral motion is evident from the surface topography (Fielding et al., 1994), seismicity (Priestley et al., 2008), and geodetic strain rates (Kreemer et al., 2014). The present-day ~N20°E of motion of the Indian plate is accommodated by collision on the north and subduction on the east. The regional deformation and the major fault movements from the Global Positioning System (GPS) measurements divide the area into two major geodynamic regions (Maurin et al.,2010): first, the development of crustal shortening and thrust faulting primarily on the Neogene section of the outer fold belt and second, the development of a series of en-echelon pull-apart basins on the CMB and the dextral motions primarily along the Sagaing fault (Socquet et al., 2002). Steckler et al (2016) published GPS measurements of the recently deployed stations across Bangladesh and Myanmar [Fig-9]. They found 46 mmy^{-1} of net oblique motion between the India plate and the Shan Plateau with 21 $mmyr^{-1}$ of shear motion along the Sagaing Fault. The dextral motion is also accommodated by multiple strike-slip to oblique-slip faults in the east. The remaining 13–17 mmy^{-1} of motion can be attributed to the convergence and crustal shortening. Later, Mallick et al. (2019) found a convergence rate of 12–24 mmy^{-1} and a dextral shear rate of 25-32 mmy^{-1} using more GPS stations form the Myanmar-India-Bangladesh-Bhutan networks.

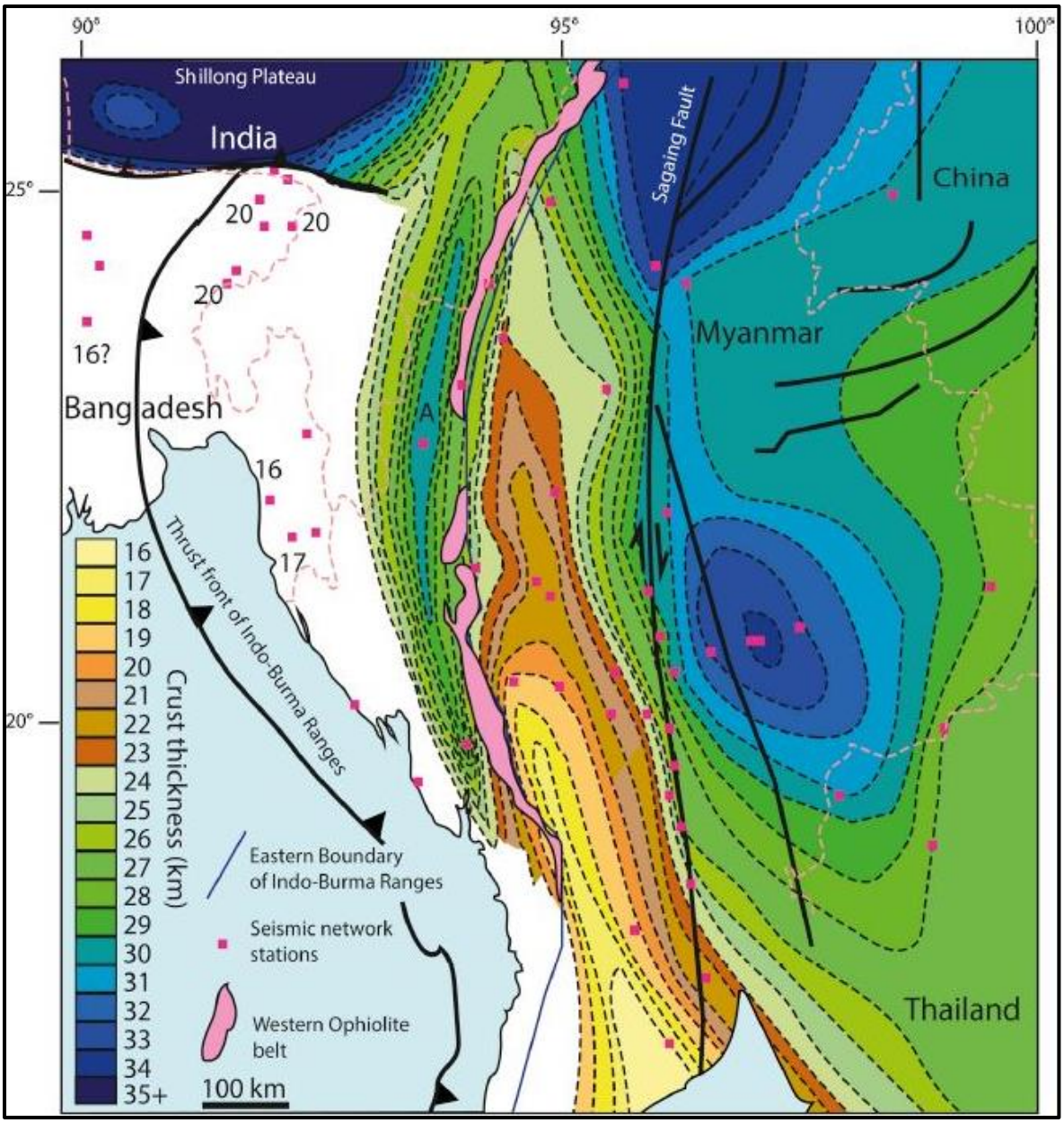

Figure 9: Thickness of the crust from the base of the low velocity sedimentary layer to the Moho. (from Wang et al.,2019)

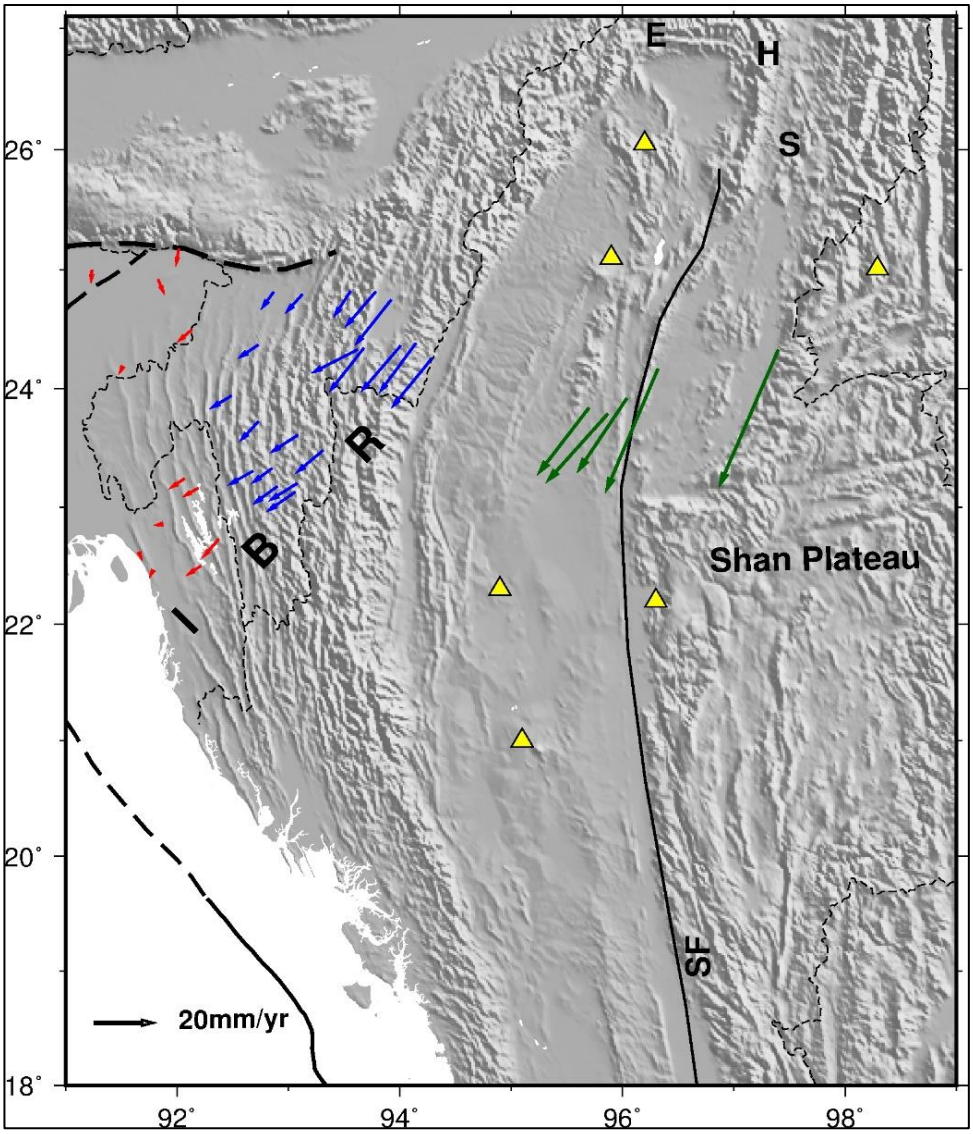

Figure 10: GPS vectors show velocities relative to the fixed Indian plate. Red,blue and green arrows are the stations form Bangladesh, India and Myanmar, respectively; [from Steckler et. al., 2016 and Gahalaut et al., 2013]; SF- Sagaing fault, IBR- Indo Burman Range, EHS- Eastern Himalayan Syntaxis.

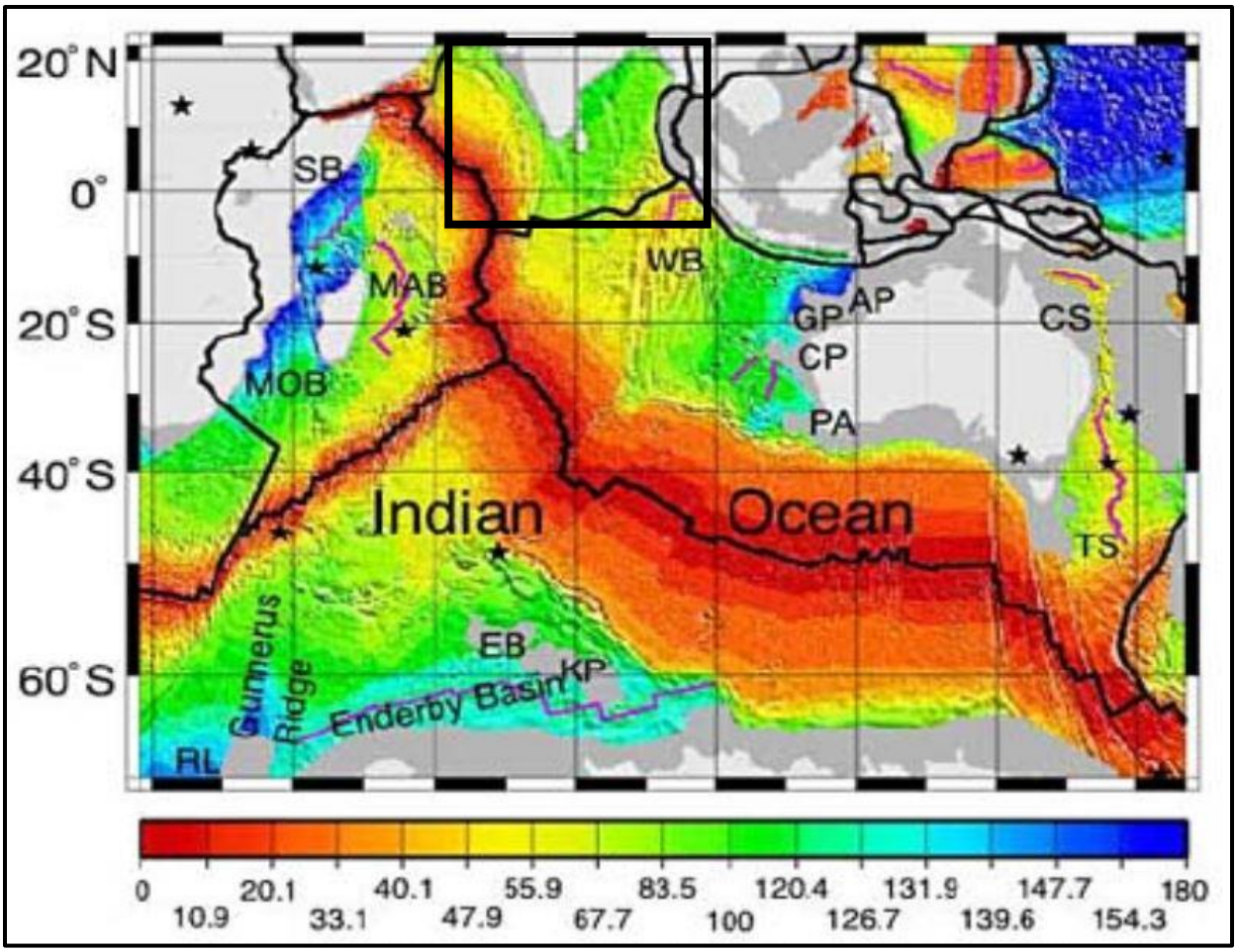

Figure 11: Age of the Indian and surrounding oceanic lithosphere (from Müller et at., 2008)

Wang et al. (2019) generated a 3D shear wave velocity structure as well as crustal thickness model combining receiver functions, H/V amplitude ratio of Rayleigh waves, and surface wave dispersion measurements. The Moho depth map shows [Fig-10] a typical crustal thickness (around 30-35km) in the Shan Plateau and the N-E part of Myanmar around the Shan-Scrap that gradually becomes thinner towards the Burma Terrane. The Sagaing fault marks the boundary between the thin crust of the Burma Terrane and the relatively thicker crust of the Shan Plateau. Crustal thickness of the IBR becomes higher towards the center due to the crustal thickening and the accretionary prism development.

Estimation of the crustal type and the thickness is particularly important for this research because the presence of crustal anisotropy could be problematic in interpreting the upper mantle deformational fabrics. The type of the subducting Indian crust remains unclear due to their being fewer seismological observations. From the receiver functions and the Raleigh wave dispersion analysis, Mirtra et al. (2008) identified a signature of a thin high-velocity region (~6 km) below the ~36 km thick upper crust. They proposed that the hinge zone, where the thickness of the overlying sediments sharply increases, separates the continental crust of the western stable Indian craton from the eastern oceanic crust. Later observation of the decrease of the Moho depth and the presence of gravity high along the hinge zone supports the idea of the continent to oceanic transition (Rajasekher & Mishra, 2008). The oceanic crust is overlain by thick wedge sediments that reached up to 22km at the depocenter (Brune et al., 1992).

From the global data set (Müller et al., 2008), the age of the Indian oceanic lithosphere ranges from 100-120Ma along the Andaman convergence zone and the Bay of Bengal [Fig-11]. Because all formed from the same spreading center, the assumption of a similar age range for the subducting Indian lithosphere would be a good approximation. The older oceanic lithosphere facilitates the demolition of the past frozen spreading fabrics and provides sufficient time to decouple and form subduction-induced sub-slab deformational fabric.

Chapter 2

Shear Wave Splitting

Shear wave splitting (SWS) is an unambiguous manifestation of seismic anisotropy in which seismic wave speed depends on the propagation and polarization directions of the waves. Like optical birefringence, the shear wave splits into two orthogonally polarized components and accumulates a delay time between the fast and the slow waves [Fig-12]. It has become the most

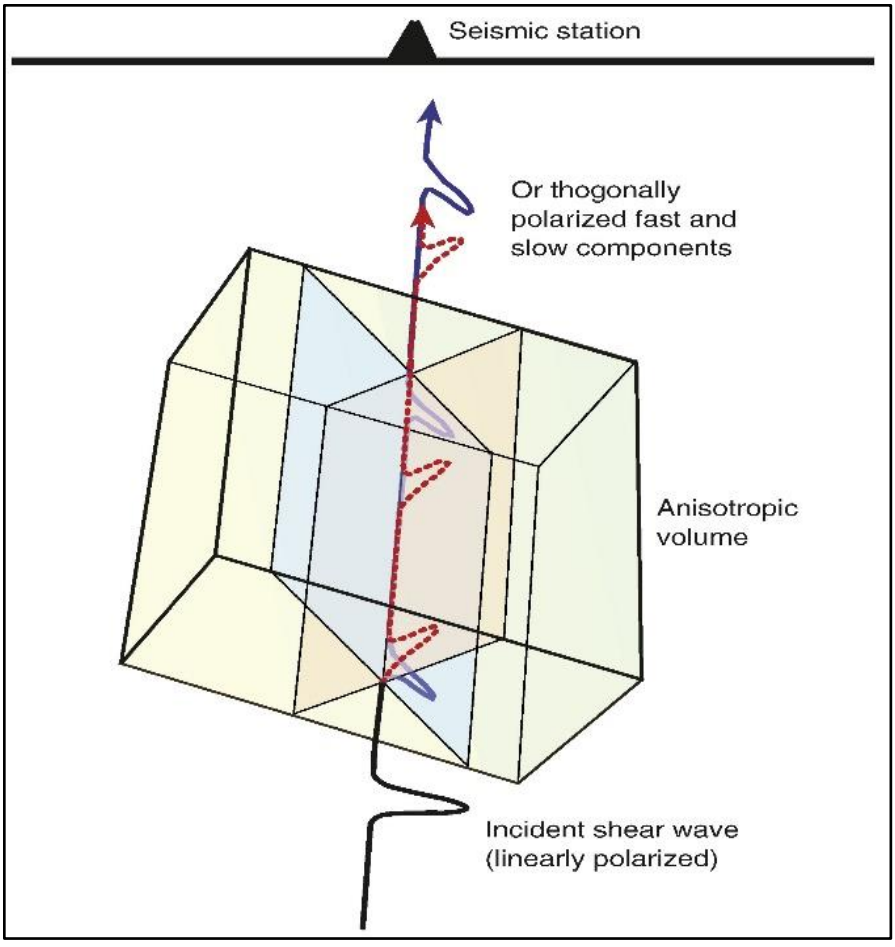

Figure 12: Schematic diagram of shear wave splitting due to upper mantle anisotropy, [after Long and Becker, 2010]

popular tool for characterizing anisotropy inside the earth in recent times (Keith and Crampin., 1977; Ando et al., 1983; Crampin et al., 1991; Long & Silver, 2009).

In an isotropic earth, body waves would travel at the same speed in every direction and produce spherical wavefronts [Fig-13]. Faster traveling P waves have radial particle motions, whereas the slower shear waves have S_H and S_V components that are both orthogonal to the P waves. Both S waves travel at the same speeds and produce two concentric spherical P and S wavefronts upon propagation [Fig-13]. When the waves encounter an anisotropic medium, they reorient parallel and perpendicular to the anisotropic plane. Since the wave travels faster in the direction parallel to the anisotropic plane, the two waves accumulate a delay time. The fast and slow S waves arrive at the station at different times depending upon the thickness and the strength of the anisotropic medium. From the measurement point of view, we generally introduce two parameters, (i) the polarization direction of the fast wave, known as fast direction (ϕ), and (ii) time difference between fast and slow waves, known as lag time (δt). If we assume fast and slow wave velocities are V_{s1} and V_{s2}, δt can be expressed by

$$\delta t \; = \; L(1/V_{s1} - 1/V_{s2})$$

where L defines the path length of the anisotropic medium.

For mathematical derivation of SWS, we need to recall the equation of motion in a Cartesian co-ordinate system which can be written as:

$$\frac{\partial}{\partial t}\left[C_{ijkl}\frac{\partial U_k}{\partial x_l}\right] = \rho\frac{\partial^2 U_j}{\partial t^2}$$

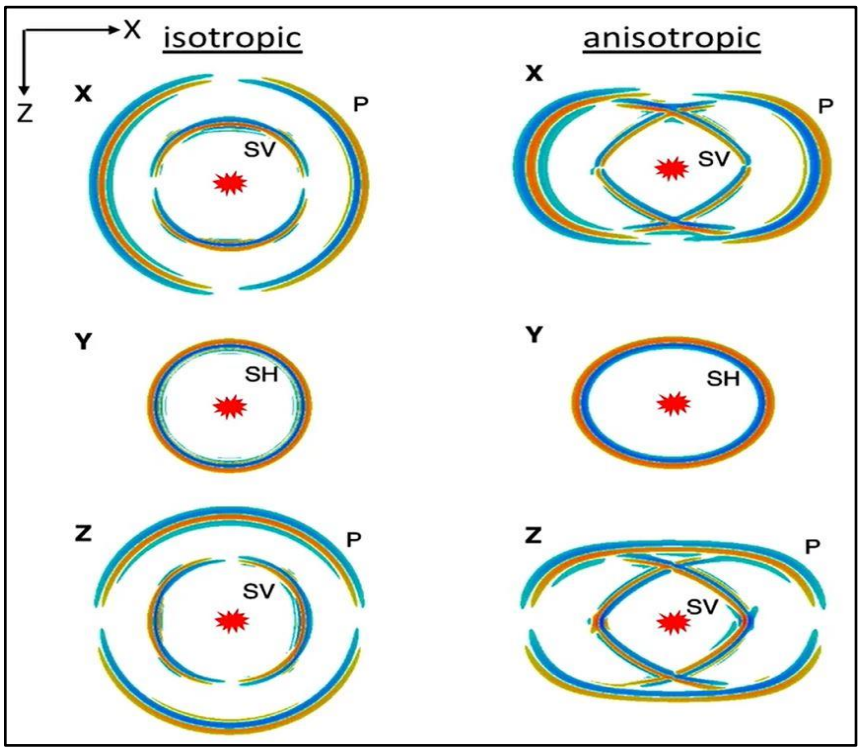

Figure 13: Characteristics wave front of P and S wave travelling through an isotropic and an anisotropic medium

Where, C_{ijkl} is the elastic stiffness tensor, displacement vector U and ρ is the density. If we assume the general expression of the wave front as, $t = \tau(x_i)$ and solve for the wave equation, we will find the solution as a ray series

$$\bigcup_k (x_i, t) = \sum_{n=0}^{\infty} U_k^{(n)}(x_i) f_n\big(t - \tau(x_i)\big)$$

Substituting the displacement into the wave equation, we find

$$L\big(U^{(n)}\big) - M(U^{n-1}) + N(U^{n-2}) = 0$$

Considering the 1st order $n = 0$, $U^{-1} = U^{-2} = 0$; subsequent vector operator M and N will be zero and the vector operator, L, can be written as:

$$L_j\big(U^{(n)}\big) = \Gamma_{jk} U_k^{(n)} - U_j^{(n)}$$

Where $\alpha_{ijkl} = C_{ijkl}, \Gamma_{jk} = \rho_i \rho_l \alpha_{ijkl}$ and $\rho_i = \frac{\partial \tau}{\partial x_i}$

Introducing Kronecker delta (δ_{jk}), the final solution becomes,

$$\left(\Gamma_{jk} - \delta_{jk}\right) U_k^{(o)} = 0$$

We can solve this equation and get three eigenvectors (λ_1, λ_2, λ_3) and eigenvalues (A_1, A_2, A_3) of the matrix Γ_{jk} . Here, A_1 relates to the P wave velocity (α), and both A_2 and A_3 relate to the S wave velocity (S_H and S_V,). For an isotropic medium, $A_2 = A_3$, meaning that both S_H and S_V travel at the same speeds, and we will observe no splitting. On the other hand, for an anisotropic medium, $A_2 \neq A_3$ and the two S waves travel at a different speed and accumulate a lag time.

Several different S wave phases can be used for SWS analysis; however, P to S converted phases at the core-mantle boundary (e.g. SKS, PKS, SKKS) are the most popular for characterizing seismic anisotropy. Core refracted phases have several advantages over direct phases. They effectively remove the source side anisotropy by S to P conversion at the outer core. Any observed splitting must be due to the anisotropic structure on the receiver side between the CMB and the surface. Also, core refracted phases generally have lower incidence angles that fall within the shear wave window (~ 35°). Direct S waves from local deep earthquakes can be used to characterize the deformation fabric underneath the station (Fig- 14). This is especially applicable in a subduction zone setting where numerous deep events are found with wide rages of depth and azimuth. In this study, I have used the combination of teleseismic core phases and local direct S phases to reveal mantle deformation fabrics of the Indo-Burma subduction system.

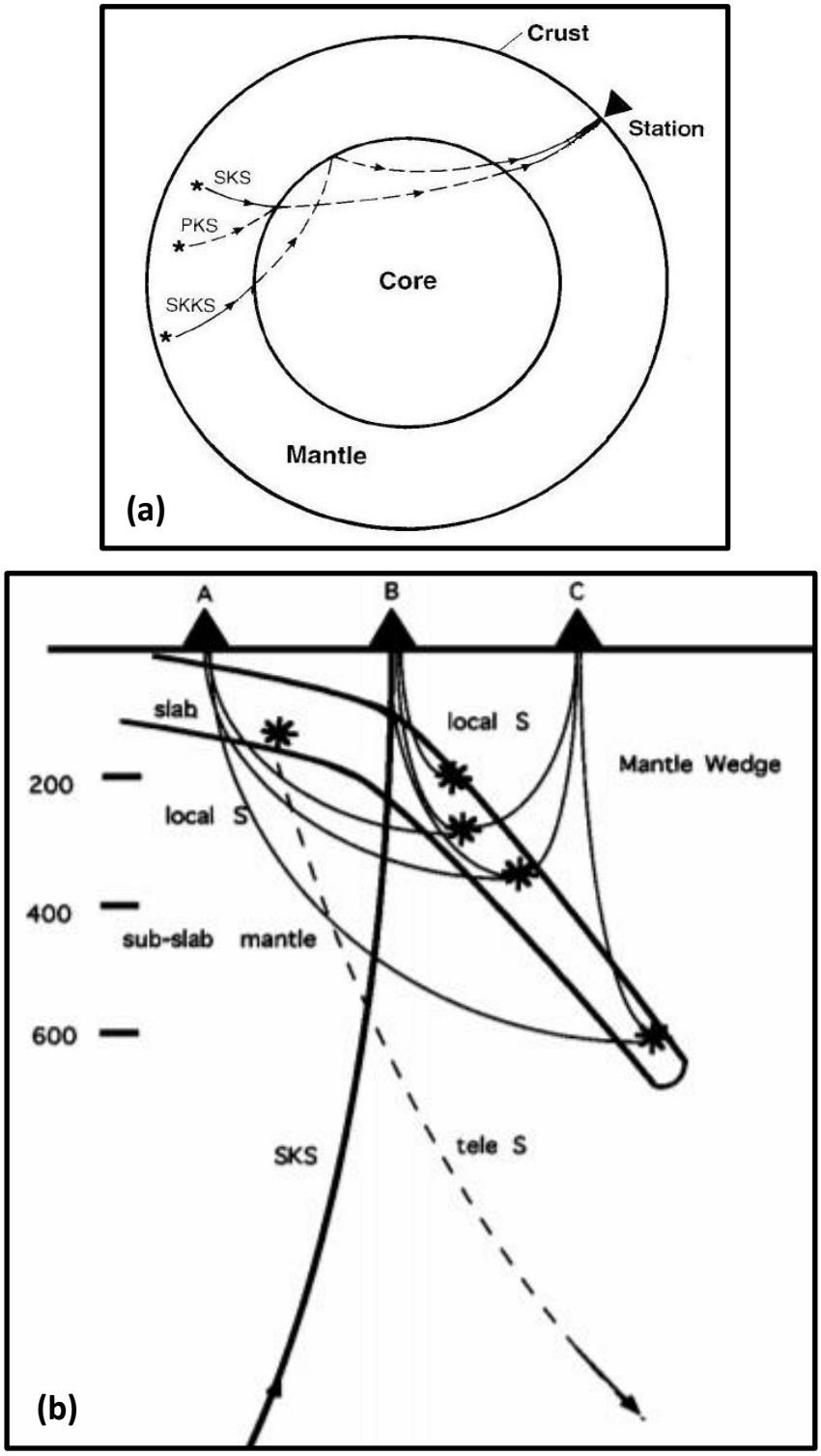

Figure 14: (a) Teleseismic core phase XKS splitting; (b) local direct S wave splitting on a subduction zone (from Savage, 1999)

Several methods are available for measuring SWS such as the Transverse Component Minimization [TCM] (Silver and Chan, 1991), the cross-correlation method (Bowman and Ando, 1987), the multichannel splitting intensity method (Chevrot, 2000), and the cross-convolution method (Menke & Levin, 2003). The TCM is the most popular method for measuring the splitting parameters. In the absence of anisotropy and without significant ray bending, an incident SKS waves will have no energy on the tangential component and produce a linear particle motion. The presence of anisotropy introduces significant energy on the tangential components. As a result, particle motion becomes elliptical, which is the diagnostic signature of splitting. I perform a grid search over all possible values of ϕ and δt, rotate and time shift the horizontal components accordingly, and measure the energy of the corrected tangential components. The best-fitting splitting parameters correspond to the minima on the energy contour plot of the tangential components from all possible pairs of splitting parameters. Errors on the measurements are estimated using F test formulation (Silver & Chan, 1991).

For the local S wave, I have used a slight variation of the TCM method that involves the minimization of the smaller eigenvalue of the corrected covariance matrix. Because identifying the singular time-domain covariance matrix is equivalent to identifying the most linear particle motion, this method is identical to the TCM method and does not require initial polarization direction (Long & Silver, 2009). However, the inversions are not well constrained like the TCM method and need quality control. For measuring the splitting parameter on a recorded seismogram, I globally search for a pair of splitting parameters (ϕ and δt) that completely removes the effects of anisotropy and returns the seismogram to its initial isotropic polarization. The covariance matrix (C_{ij}) of two orthogonal components can be represented by

$$C_{ij}(\varphi, \delta t) = \sum_{k=1}^{N} u_i(k) u_j(k - n\delta t)$$

Where subscripts $i \; and \; j$ are the radial and transverse components, respectively, N is the total number of data points, k is the time index, and n is the sampling rate.

Using a grid search approach by rotating from 0 -180° and time shifting from 0 – 3 s, the optimum value of splitting parameters can be estimated. After the calculation of the splitting parameter, I performed quality control to remove erroneous and noisy results.

Anisotropy and Mantle Deformation Fabric

Anisotropy is defined as the directional dependence property of a material. Seismic anisotropy is an intrinsic property of an elastic material that gives rise to the directional dependence of seismic wave speeds and polarization. After the first observation by Hess (1961), seismic anisotropy has been widely documented in many regions of the earth's interior including the crust, upper mantle,

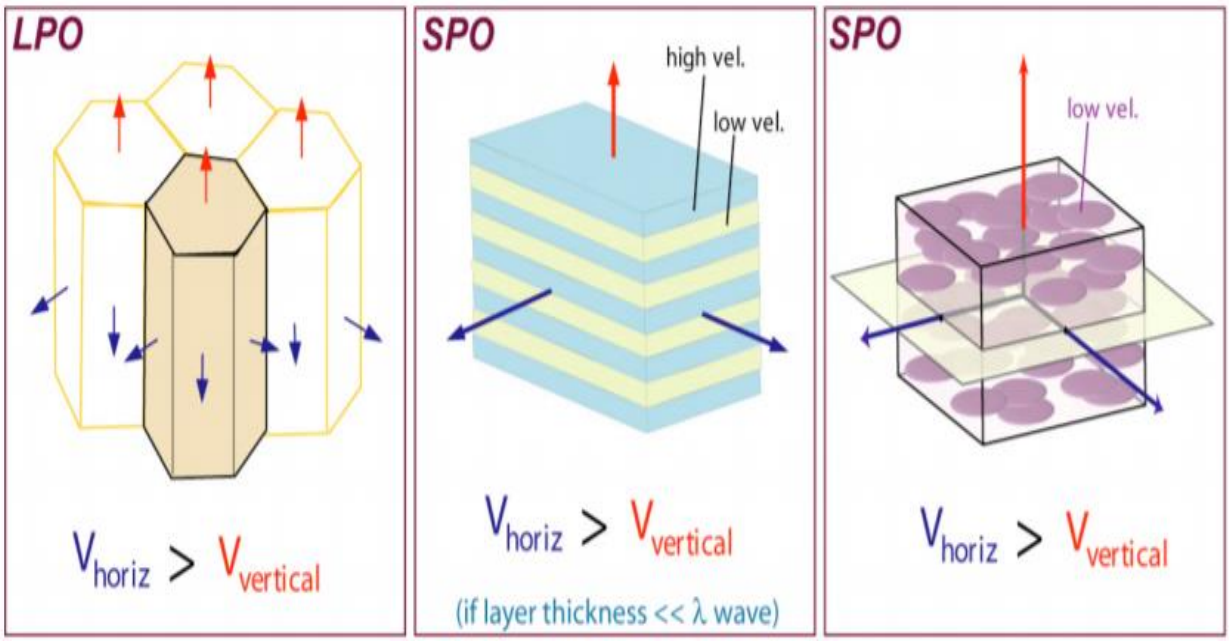

Figure 15: Example of lattice preferred orientation and shape preferred orientation (SPO) [modified from Moore et al., 2004)

mantle transition zone, “D" layer, and inner core (Mainprice et al., 2000; Karato et al., 2008; Romanowicz & Wenk, 2017). Since there is a link between the deformational process and the origin of anisotropy, the interpretation of anisotropy helps to understand the geodynamic processes. Although a range of seismological tools is available like the polarization analysis of long-period P waves, P wave travel time residuals, azimuthal anisotropy of surface waves, and anisotropic receiver function analysis, shear wave splitting is one of the most popular techniques to characterize anisotropy of mantle because it is not affected by the isotropic wave speed heterogeneity as are other methods.

In response to the deformation processes, seismic anisotropy originates either by the lattice preferred orientation (LPO) or the shape preferred orientation (SPO). SPO originates when isotropic materials are aligned in a preferred direction or plane [Fig-15]. This type of anisotropy is generally confined to the crustal depth where faults, cracks, sedimentary or metamorphic layers can be aligned in a preferred direction. Stress-induced fluid-filled cracks, microcracks, and preferentially oriented pore space in the curst are known as extensive-dilatancy anisotropy (EDA) (Crampin, 1978, 1991). However, the presence of SPO melt may contribute to the anisotropy in parts of the shallowest mantle (Gereve & Savage, 1991) or in the “D” region (Moore et al., 2004). Strain-induced lattice preferred orientation (LPO) of intrinsically isotropic minerals are the primary source of anisotropy in the upper mantle. Olivine, the primary constituent of mantle peridotite, has large single-crystal anisotropy. Maximum single crystal olivine anisotropy of propagating shear wave speed can be as high as ~18% under the ambient condition of the mantle olivine composition of Fo90 (Mainprice et al., 2000; Mainprice. 2010). However, due to the misalignment of crystals in a real mantle, peridotite aggregate of about 70 percent olivine can

generate LPO anisotropy of 3-6 percent (Christensen, 1984; Russo & Silver, 1994) that can be measured by shear wave splitting.

In the dislocation creep domain (upper ~400km), olivine is deformed by simple shear and developed LPO with the anisotropic strength increasing with strain until saturation. The relationship between the deformation and LPO fabric has been derived from the petrographic examination of the mantle peridotite and the laboratory experiments (Zhang & Karato, 1995; Ismail & Mainprice, 1998 Jung et al., 2009). A variety of olivine fabrics have been recognized including A, B, C, D, and E type. Under moderate stress, temperature and water-poor conditions, olive crystal shows A-type LPO fabric where [100] axis of olivine is subparallel to the shear direction and (010) plane subparallel to the shear plane (Jung et al., 2006; Mainprice et al., 2007; Karato et al., 2008). At high temperatures and low stresses, the dominant fabric type changes from A-type to E-type ([100] axis and (001) plane) with intermediate water content to C-type ([001]

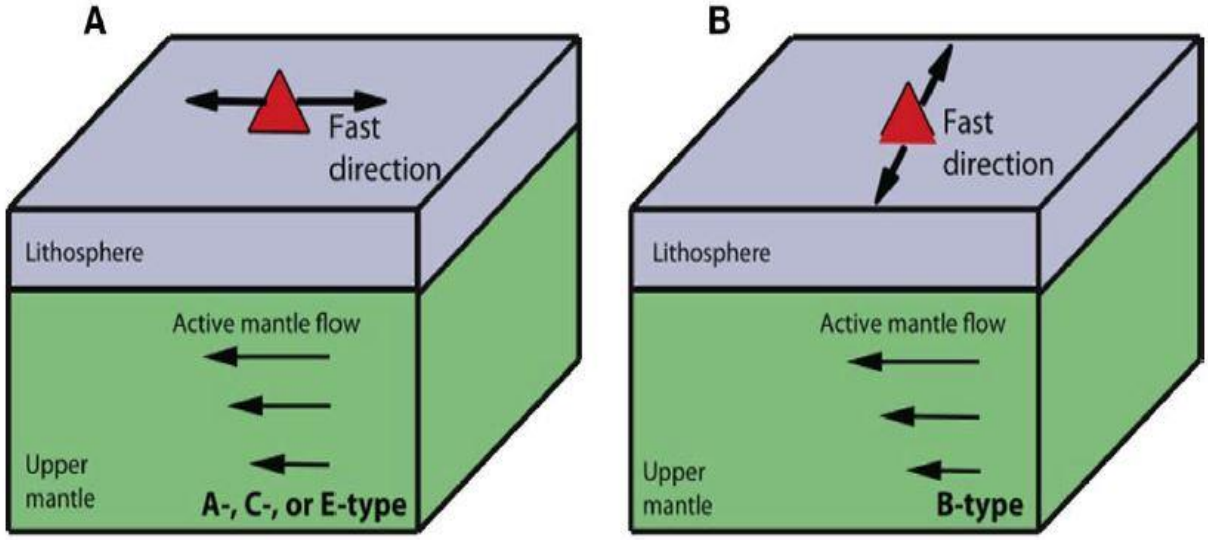

Figure 16: Schematic diagram of the relationship between horizontal mantle flow and the resulting azimuthal anisotropy for different olivine fabric types (from Long & Becker, 2010)

axis and (100) plane) with high water content. For all these LPO fabrics, the fast axes of olivine crystals align parallel to the horizontal mantle flow. As a result, the measured fast direction will

correspond to the horizontal mantle flow direction [Fig-16a]. On the other hand, at high stress and low temperature with the presence of water, olivine crystal shows B-type fabric with [001] axis subparallel to the shear direction and (010) plane subparallel to the shear plane that changes the relationship by 90° (Jung et al., 2006) [Fig-16b]. B-type fabric may be present in the cold corner of the mantle wedge above the subducting slab at higher stresses, lower temperatures, and the presence of water (Long & Becker, 2010). In D-type fabric, olivine [001] axis is subparallel to the shear direction, but its shear plane is not well defined. D-type olivine LPO fabric may develop at high stress and water-poor conditions. Based on the laboratory experiments and petrographic observation, upper mantle dislocation creep domains favor the development of A-type and E-type fabrics (Hansen et al., 2014). Thus, the shear wave splitting technique gives us a simple yet powerful method for mapping upper mantle deformational fabrics and geodynamic processes. However, care must be taken during interpretation because stress, temperatures, and water content can alter the olivine deformation fabrics (Jung & Karato, 2001; Jung et al., 2009; Ohuchi et al., 2011).

The main objective of this research is to delineate the mantle deformation fabrics of this subduction system by the detailed characterization of the splitting patterns. However, due to the lack of vertical resolution of SWS, contributions of anisotropy form various parts of the subduction system (sub-slab, slab, mantle wedge, and overriding plate) to the splitting parameter are difficult to quantify. Comparisons between local and teleseismic splitting parameters roughly isolate the main anisotropic zone; however, delineating individual flow domains is not possible. To overcome this, I have generated a shear wave splitting tomography (SWST) model combining local and teleseismic splitting measurements. The resulting 3D anisotropic model will help to understand the mantle flow domains and dynamics of this complex subduction system.

Mapping the mantle deformation fabric can also help to understand the geodynamics of this plate boundary on a regional scale. Study of crustal deformation from GPS and geological observations show the crustal deformation of the India-Eurasia continental collision zone primarily by shortening, lateral extrusion, and possible clockwise rotation (Liang et at.; 2013). Previous studies of core phase teleseismic S wave splitting analysis have revealed that the anisotropy in the upper mantle shows strong correspondence with the crustal deformation with an overall clockwise

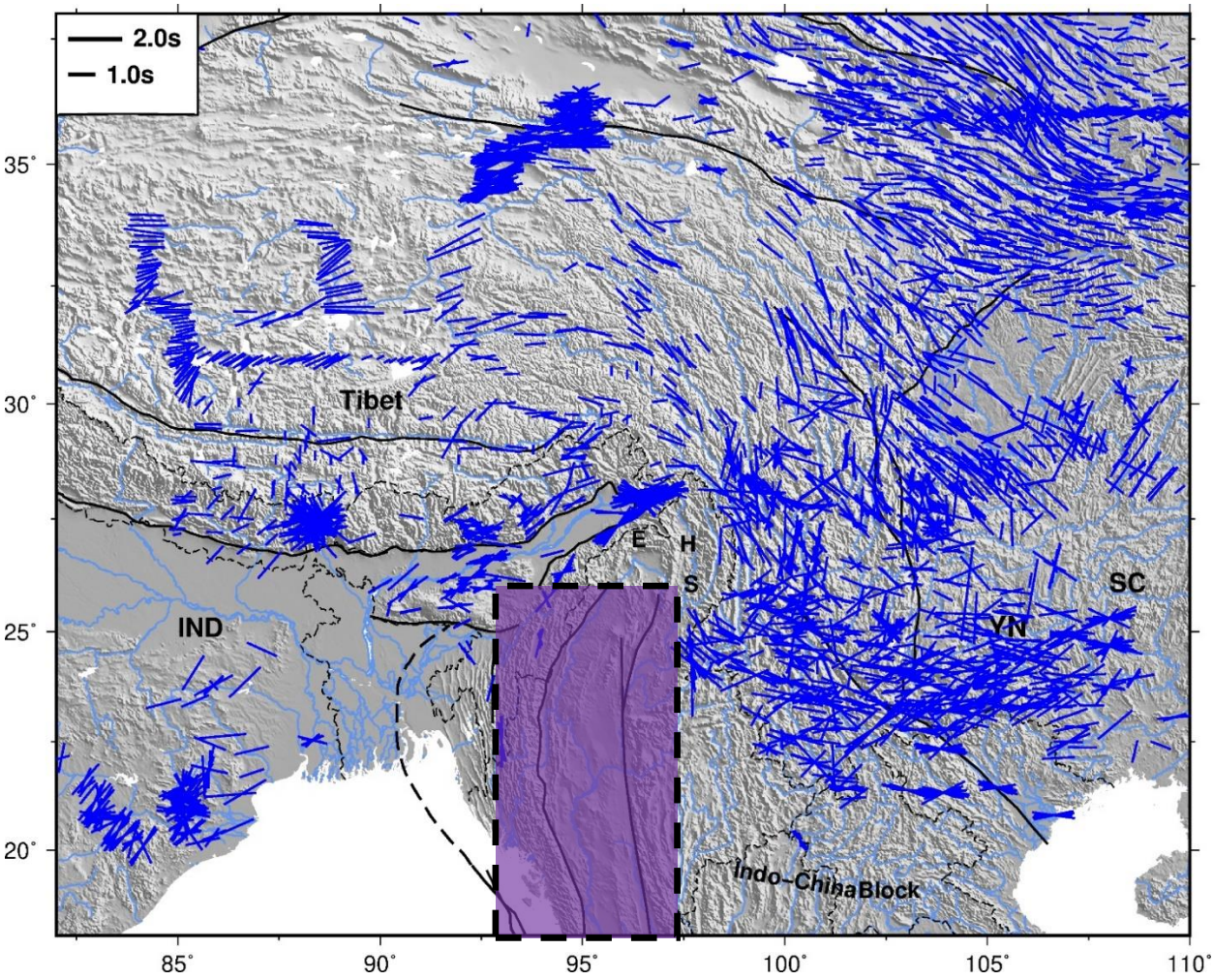

Figure 17: Teleseismic shear wave splitting of the Indo-Eurasian collisional belt showing strong correspondence with present day crustal deformation (from the global shear wave splitting database (Wüstefeld et. at., 2009; Liu et. al., 2014; Yang et. al., 2014; IRIS DMC, 2012). Black block shows the location of our study area.

rotation pattern of the fast directions around the EHS from E-W to N-S direction [Fig-17] (McNamara et at., 1994; Sol et at., 2007; Wang et at., 2008; León Soto et at., 2012; Chang et al., 2015). However, the SKS fast direction changes abruptly from N-S to E-W at ~26◦N in Yunnan and NE-SW further south (Huang et al., 2015), indicating a lack of vertical coherence between the mantle and crustal deformation. This research will help to fill the remaining gap on the S-W part [Fig-17] of the collisional belt and better elucidate the relationship between crust and mantle deformation.

BIMA Seismic Network

The Bangladesh India Myanmar Array (BIMA) is a seismic network deployed across the Indo-Burman subduction zone stretching from the blind deformation front in the west to the Sagaing fault in the east. Although the Bangladesh and Myanmar stations are in operation, the Indian

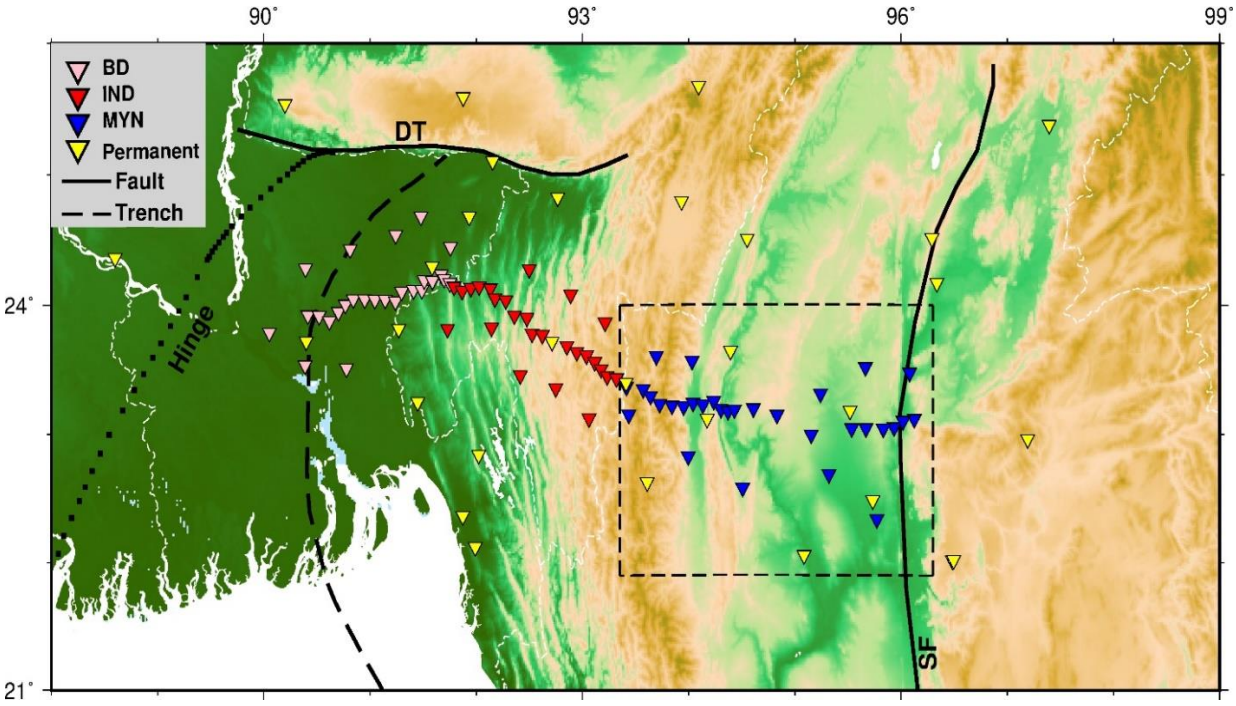

Figure 18: BIMA seismic array; Blue and pink triangles are stations deployed in Myanmar and Bangladesh respectively; red triangles are the proposed Indian stations; yellow triangles are permanent stations; DT- Dauki Thrust, SF- Sagaing Fault

stations have not been deployed yet. Incorporated Research Institute for Seismology (IRIS) provides the instruments and technical support. Installed portable broadband seismometers have flat response from 50 Hz to 120s with a sampling rate of 100 Hz. The high sensitivity of sensors having a wide frequency range can detect motions from local low magnitude high-frequency events to teleseismic events of long-period surface waves. The array is arranged in three lines where the middle profile stations are closely spaced (5 - 10 km). The flanking north and south swath profile stations are ~40 km apart [Fig-18].

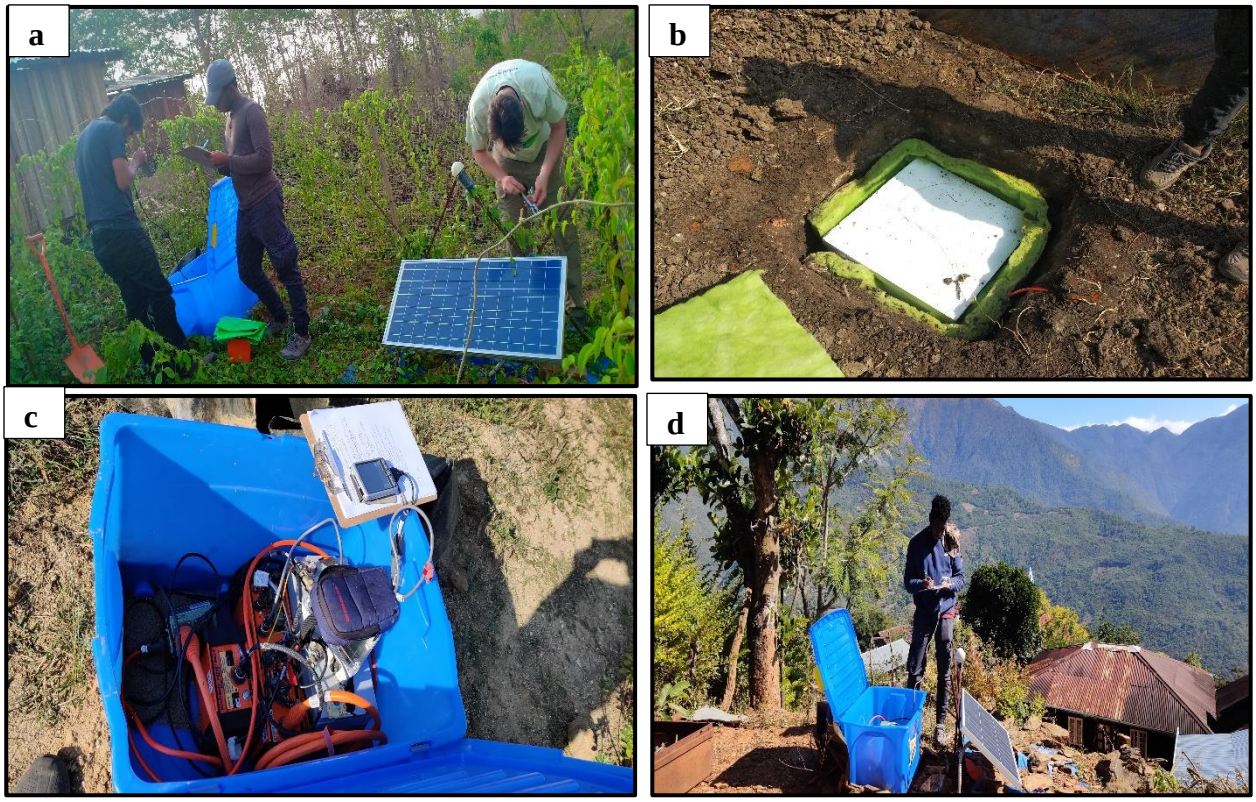

Figure 19: Servicing and station location of BIMA array; (a) servicing of station MS05; (b) Sensor box covered with Styrofoam casing; (c) Outside plastic box containing data logger, bailer and battery; (d) typical mountainous site (station MP02) of western part of the array.

Researchers of Columbia University and the University of Missouri-Columbia are responsible for the servicing and installation work in Bangladesh and Myanmar. All stations will stay in service for at least two years with a six-month servicing interval. Streckeisen STS-2, Guralp CMG-3T,

and

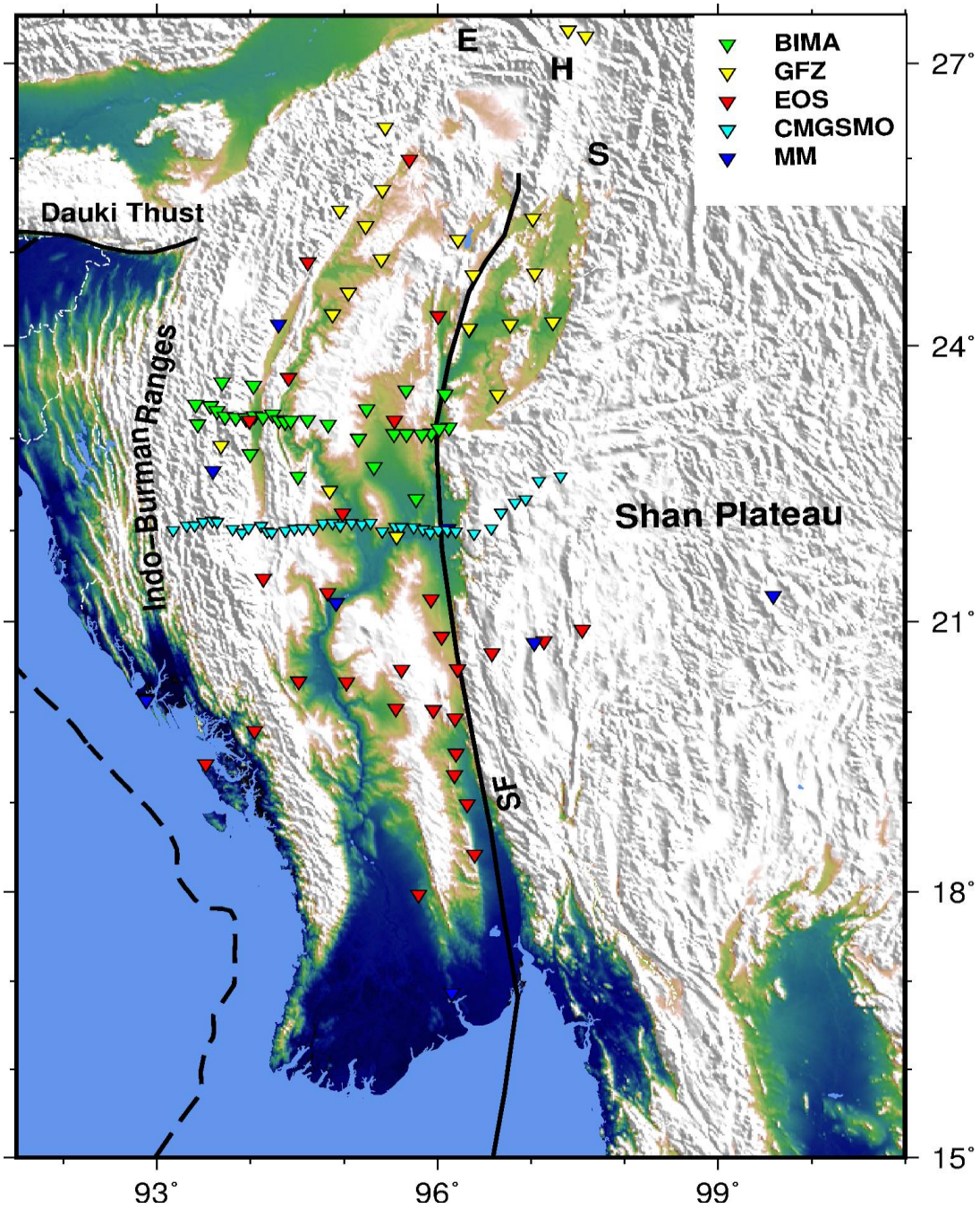

Figure 20: All currently active networks in Myanmar; EHS – Eastern Himalayan Syntaxis; SF- Sagaing Fault

Trillium Compact 120 Nanometrics three-component seismometers were installed. Continuous time-series data are recorded with Quanterra Q330 data logger at 100Hz. Each of the seismometers was placed inside a 1-1.5m deep hole on a concrete platform. They are also covered by a styrofoam

box with fiberglass to protect them from the burrowing animals [Fig-19]. The vault was then sealed by two metal sheets, a plaster trap, and dirt on the top. Together, it created a barometric and thermal seal to minimize external noise. The outside plastic box contains a data logger, a battery, and a bailer. The attached solar panel unit provides the main power for the seismometers during the day and recharges the battery. The seismometer is also connected to an external GPS unit that provides precise recording time within a few microseconds of accuracy. Most of the stations were in good condition during the first service run. Some western clay sites had an unstable mass position due to the clay contraction and cracking. We leveled and stabilized the hole with additional concrete during the servicing.

Several geophysical research projects are currently ongoing in this area. Deutsches GeoForschungs Zentrum GFZ (GFZ Potsdam) installed 30 broadband sensors in the N-E part of Myanmar. The primary goal is to understand the nature of the transition from continental collision to oceanic subduction and the partitioning of deformation along the accretionary prism as well as the strike-slip Sagaing fault system and to image the subducting Indian Plate beneath Myanmar and S-W China. Installed in operation from December 2018, this network will stay in service until 2021. The Earth Observatory of Singapore (EOS) has deployed a seismic network consisting of 30 broadband seismometers. Most of the stations from this array have been deployed across the southern part of the IBR and along the Sagaing fault [Fig-20]. Under the China–Myanmar Geophysical Survey in the Myanmar Orogen (CMGSMO) project, an E-W seismic array consisting of 38 stations has been deployed across north-central Myanmar [Fig-20]. This network has been is in operation since June 2016. The Myanmar National Seismic Network (MM) is a permanent seismic network in Myanmar, operated by the Department of Meteorology and

Hydrology (DMH). All 9 seismic stations have been in service since 2016. Currently, the number of total active stations has increased from under 10 to more than 100 within 3 years.

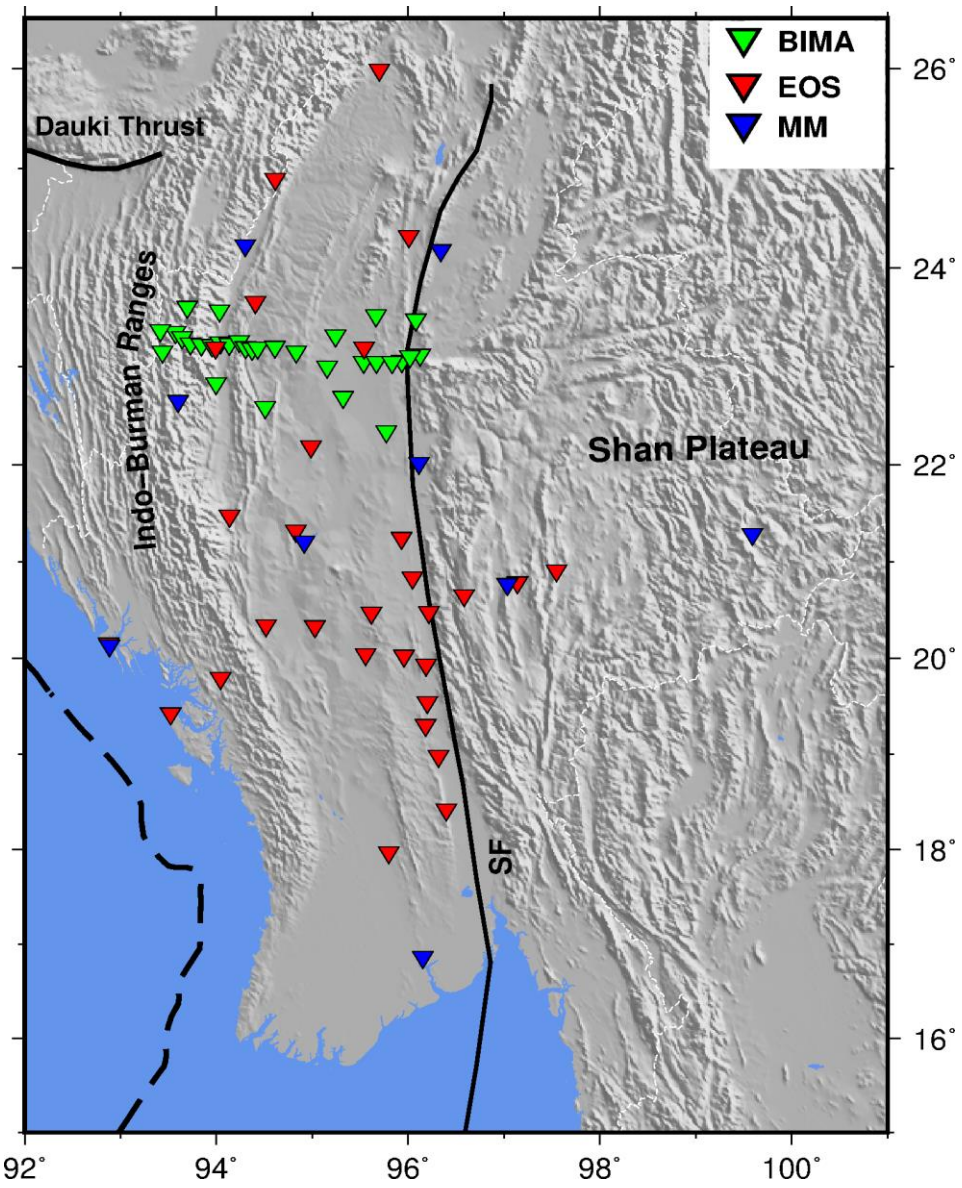

Figure 21: Location of seismic stations used for this study

In this research, I have used the BIMA network of first service run data (December 2018 to May 2019) [Fig-21]. I have also integrated data from the EOS (July 2017 to January 2019) and MM (July 2016 to January 2019) networks forming a large gird of 70 stations in total [Fig-21]. In

addition, I have also used three months of GFZ network data (January to March 2019) to locate local deep events.

Data Processing

Data processing begins with the sorting and uploading of data to the IRIS-DMC for archiving soon after coming back from a service run. Before uploading, all the datasets need to convert a day-long MiniSEED format and a station XML file containing station information and instrument response. For extracting data, I first made an event list file for both local and teleseismic events. Forteleseismic events, I have selected the events that are within the distance range of 85° to 180°

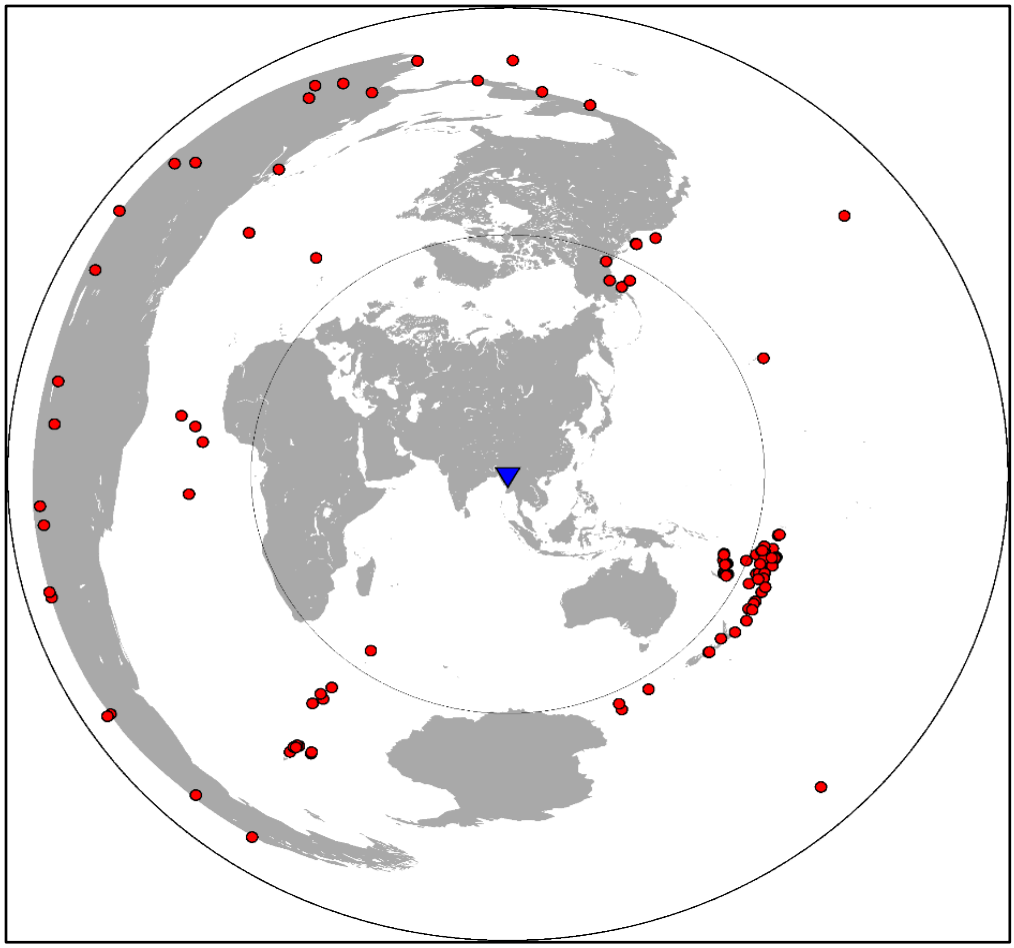

Figure 22: Distribution of teleseismic events used in this study

from the center of our array (94.5°E, 23.5°N) and have a body wave magnitude of 5.8 or greater. Local events deeper than 40 km have only been selected so that the waves can sample the mantle wedge. In addition, the local events must be within 2° away from the stations to make sure the incidence is < ~35°. This allows us to avoid the nonlinear particle motion due to free surface interactions and S-to P conversion (Kennett, 1991; Sandvol & Ni, 1997). I made a combined list of local events by integrating the USGS and ISC catalogs. Also, I have located the deep events using our BIMA and GFZ network. The addition of more local events helps to improve the SWST resolutions by introducing more crossing ray paths. Extracted time series data are in SAC format and 400s long for local and 3000s long for teleseismic events, respectively. After adding all the header information and marking the important phases, each SAC file is decimated to 2O Hz before windowing.

Locating Deep Events

Since ISC and USGS catalogs do not use local seismic stations in Myanmar, many deep low magnitude earthquakes are not possible to determine and relocate. This became obvious when we looked at raw data from our BIMA network. Mon et al. (2020) detected 854 events using the GMGSMO array for the investigation of focal mechanism and deep seismicity. As mentioned before, locating more local deep events is crucial to improve the resolution of SWST and interpretation. We have used a triggering algorithm to detect local events using stations of the BIMA and GFZ network [Fig-23].

Triggering Algorithm

I have used the ratio of short time average (STA) versus long time average (LTA) to detect local low magnitude events. It is a widely implemented simple algorithm to detect earthquakes

automatically. STA is sensitive to strong motions like earthquakes, whereas LTA provides information on the temporal noise level. This approach continuously calculates the ratio of STA and LTA of average values of the absolute amplitude in two consecutive moving time windows. A trigger is activated when it passed the given threshold ratio. I have used the STA/STA ratio of

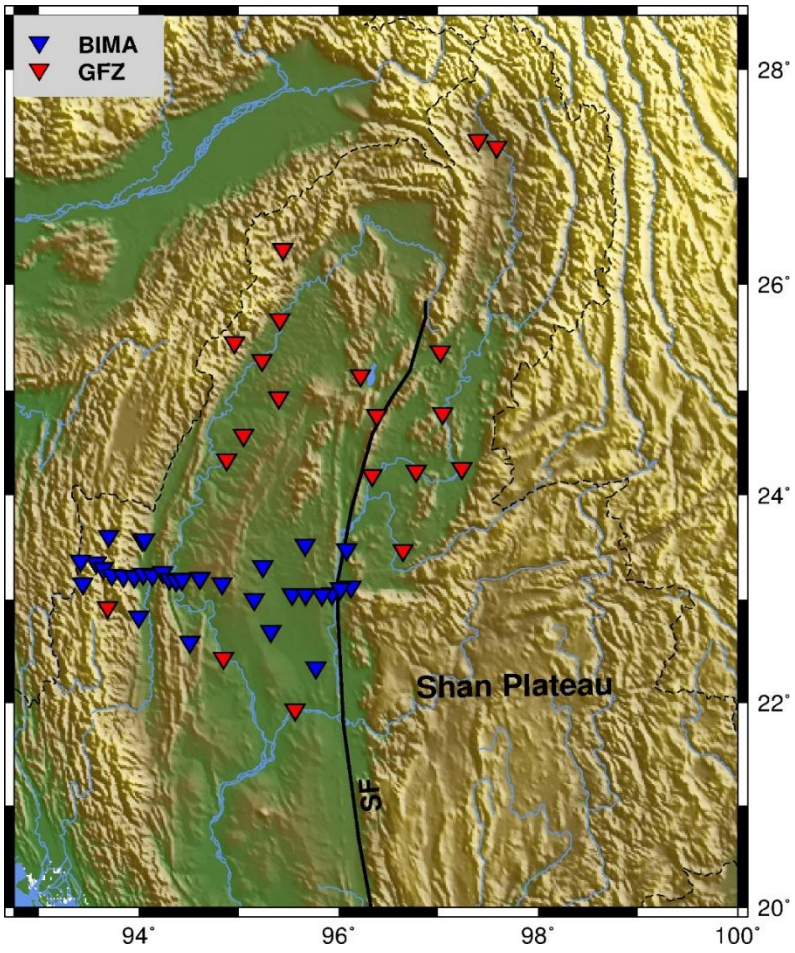

Figure 23: Network arrays used in locating deep events

1.5 to a day-long SAC file of every station for event detection. All data are filtered (0.4-3Hz) to get rid of noisy data and spikes before the computation of the moving average. Next, the trigger files of each station are matched for the final event detection. A network of a minimum of 5 stations and a time difference of 120s were used for the network trigger activation.

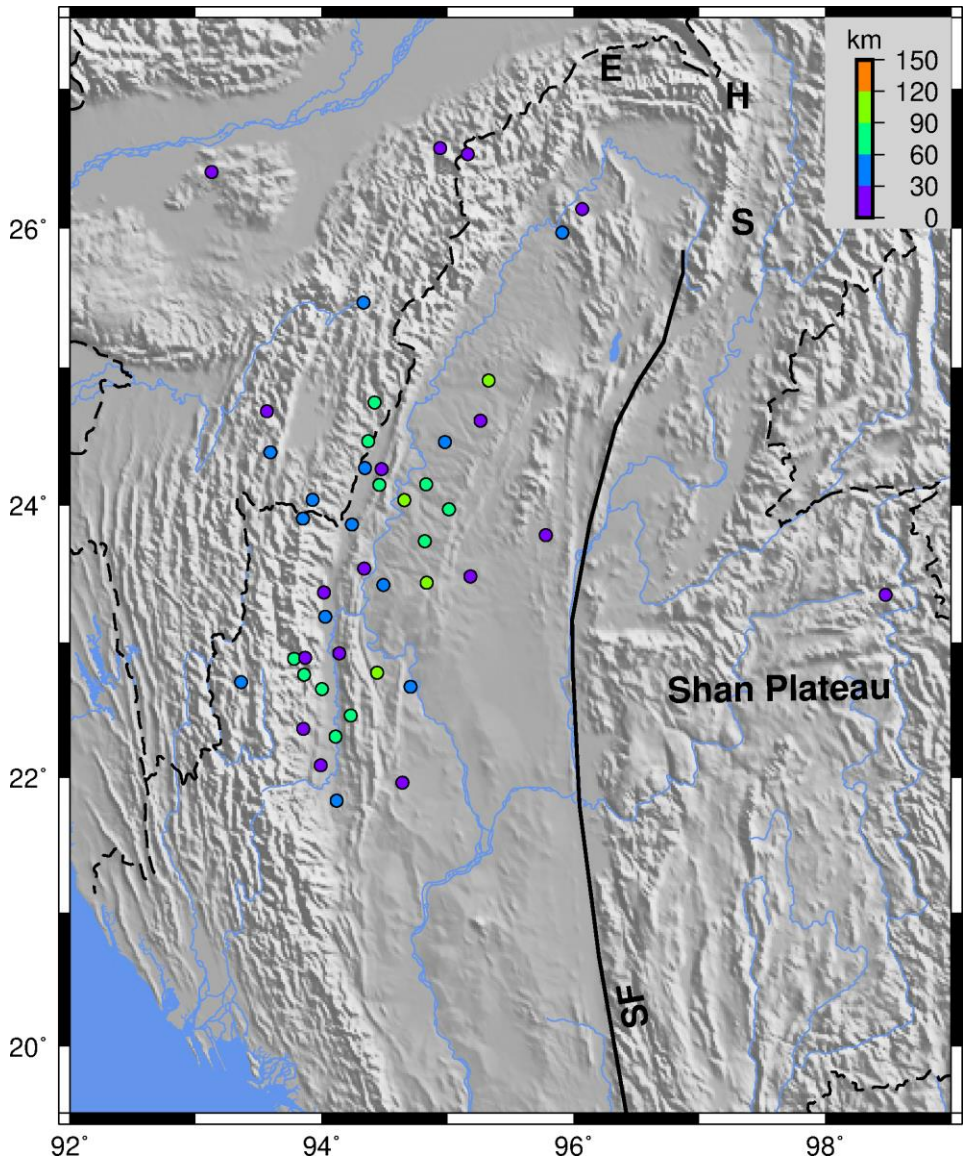

Figure 24: Distribution of relocated local events using Hypoinverse

In the next step, the triggered events were manually inspected for the phase picking. The resulting travel time arrival picks of P as well as S waves have been implemented to locate events using HYPOINVERSE 2000 (Klein et at 2003). It is an iterative inversion program that solves for location (latitude, longitude, and depth) and origin time parameter by minimizing the residuals between the theoretical and observed travel times (Klein et al., 1985, 2003). A recently published

1D velocity model (Shiddiqi et al., 2019) for the Myanmar region was used as an input crustal model. Finally, I have detected 65 local events from which 22 deep events were produced at least one good local splitting value.

Windowing and Measurements

Before the calculation of the splitting parameters, a shear-wave window needs to be selected manually. A bandpass filter is applied to remove noise and amplify signals. The cut-off frequency of the bandpass filter is 0.2 - 1 Hz for local and 0.03 - 1Hz for teleseismic events. S-wave phase for local events and SKS, SKKS, PKS core phases (collectively called XKS phases) for teleseismic events have been used. Windows were chosen very carefully because the splitting parameters are sensitive to the choice of shear-wave analysis window (Savage et al., 1989; Tenaby et al., 2004). Inaccurate window selection can lead to unwanted problems such as cycle skipping and over-, or underestimation in error analysis. To eliminate these problems, an optimum window length has been chosen that typically starts 10-15 s before the incoming S waves and has at least one complete cycle of clear S wave arrival [Fig-25]. After windowing, the gird search method was applied to calculate the splitting parameter. The minimum accepted signal to noise ratio (SNR) for local events has chosen as 4 and 3 for local and teleseismic events, respectively.

Quality Control

Individual splitting results have been passed through a strict quality control inspection procedure to get rid of spurious results. It involves the manual inspection of every waveform, particle motion, presence of residual tangential energy (for XKS phases), and minimum transverse energy. Good results have similar waveform after applying rotation and time shift, linear particle motions, little energy on the tangential components (for XKS phases), and localized minimum energy value on

the energy contour plots [Fig-26]. All the results are ranked into Q1 to Q4 (best, good, fair, poor) based on the waveform quality. A total of 274 local and 172 teleseismic splitting measurements passed through the quality control.

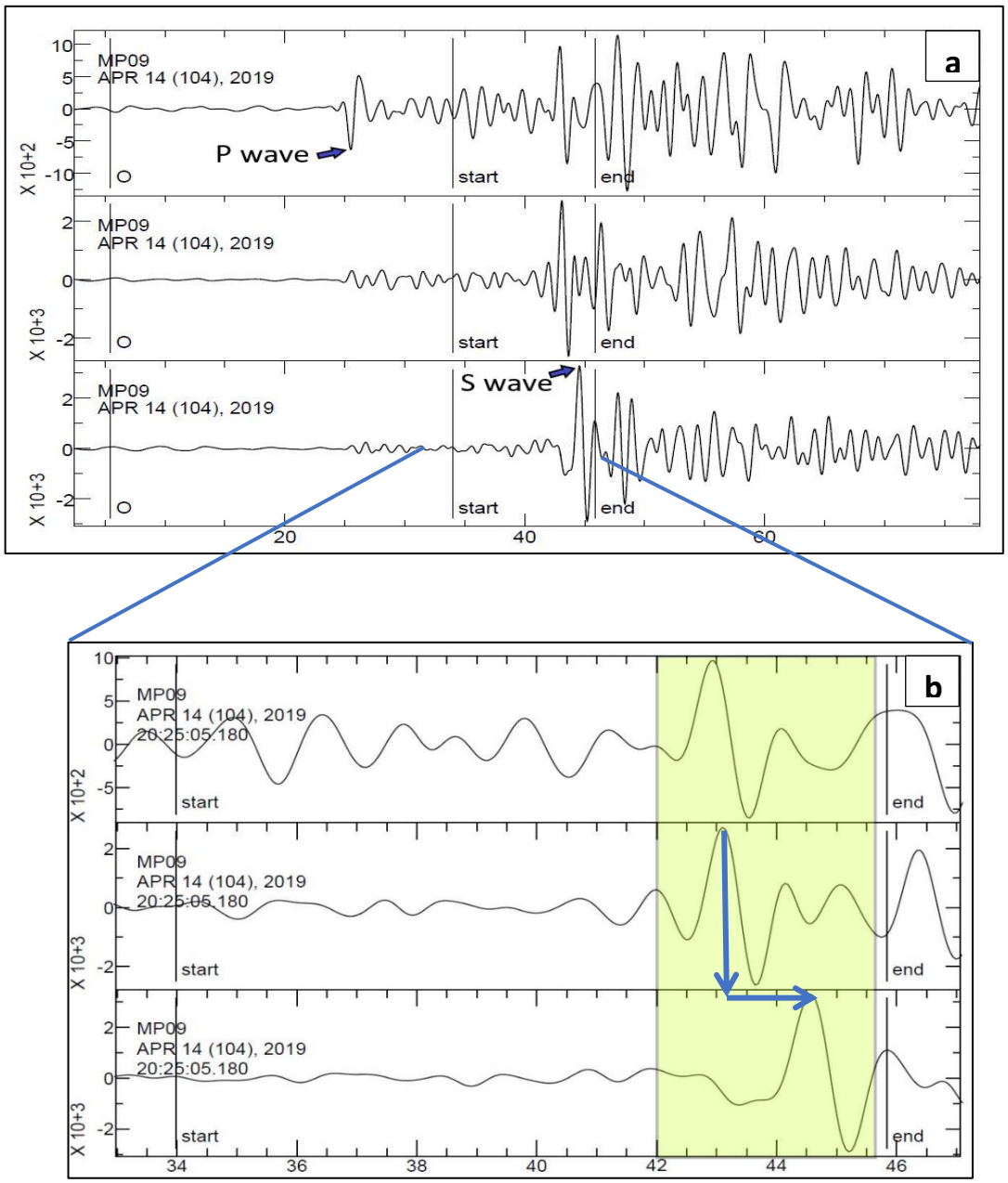

Figure 25: Selection of the S wave window for local events; (a) event showing P and S wave arrivals; (b) zoomed- in view showing the visible S wave splitting (blue arrow); start and end are the beginning and end of the window respectively

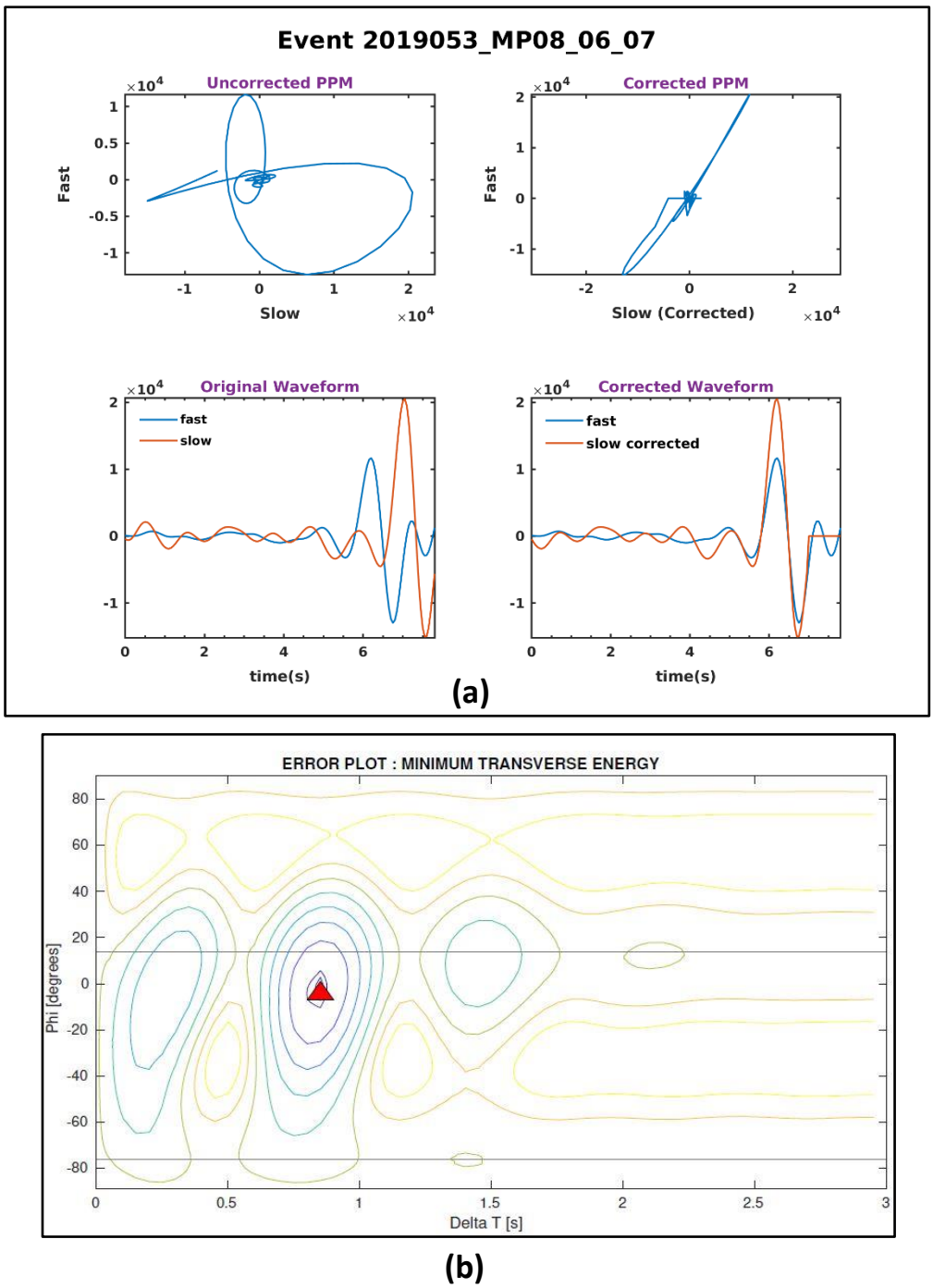

Figure 26 : Quality control of splitting results for local S wave; (a) uncorrected and corrected waveform and ppm; (b) energy plot.

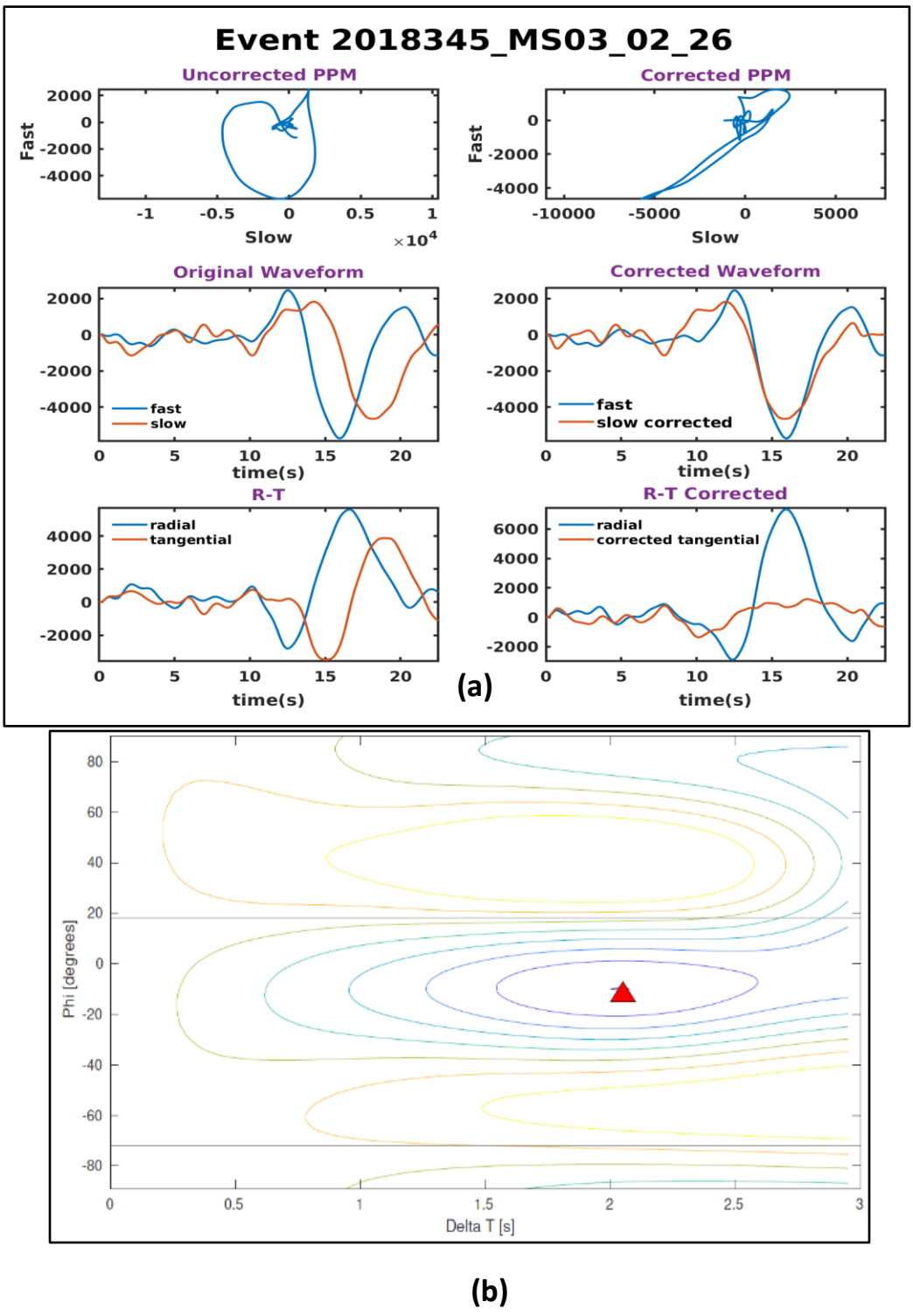

Figure 27: Quality control of splitting results for local SKS phase; (a) corrected and uncorrected waveform and ppm; (d) energy plot.

Shear Wave Splitting Tomography

As mentioned before, SWS is a path integrated results with no vertical resolution. An incoming SKS phase can encounter anisotropic structure anywhere above the upper mantle in the dislocation creep domain and split [Fig-14]. As a result, any investigation of mantle deformation fabric from

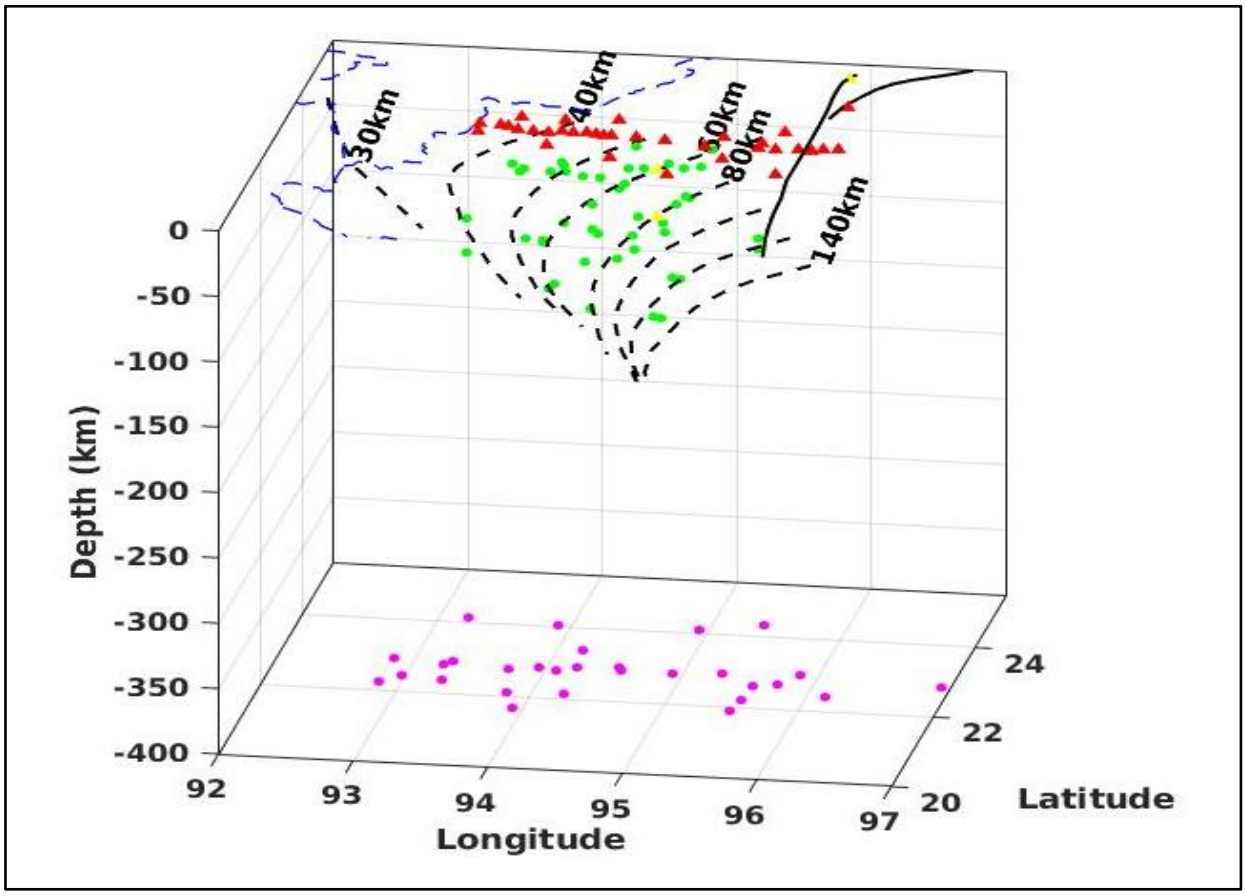

Figure 28: SWST model space and distribution of events and stations. Green circles are local spitting events, pink circles at base of 400 km is projected tele-seismic events; red and yellow triangles are stations and Quaternary volcanoes, respectively.

the SKS phase is problematic (Savage, 1999). It becomes more severe in a subduction setting where the SKS wave samples sub-slab, slab, and mantle wedge along the same path. Although comparing the local S and SKS splitting results provides some depth constraint, tomographic inversion can give more quantitative information. In this study, I have used Shear Wave Splitting

Tomography (SWST) developed by Abt and Fischer (2008) to resolve the 3D anisotropic fabric of this complex subduction system combining the local S and teleseismic SKS phases. Because the local S waves can have an incident angle up to ~35°, it can sample the mantle wedge with a wide variety of directions. These numerous crossing ray-paths produce an overdetermined inverse problem that can have a unique solution. Also, varying the hypo-central depth of local events provides additional depth constraint. In addition, I have integrated the SKS phases by projecting every ray-path at the base of the 410 discontinuity. It helps to resolve the anisotropic fabric within or below the slab on the sub-slab region.

Model Space

SWST starts by parameterizing the model space into 3-D cubic blocks having uniform crystallographic fabric and orientation. The Model extends to 300×400 km from the center of our array (94.5°N, 23.5°N) where the bulk of the event station pair exists. I have tested the inversion using a cubic block of 25km and 50km side length, respectively. Coarser block model inversion produced better results. Small block parameterization increased the underdetermined part of the model space due to the less dense ray-path coverage and hence became unstable. Each of these cubic blocks was assumed to be composed of mantle mineral composition having 70 percent olivine and 30 percent orthopyroxene from depth 0 to 400 km [Fig-27]. Since the crustal anisotropy is complex and varies on a smaller scale than our model block size, the of assumption mantle anisotropy at crustal depth is not likely to cause significant differences. Experimentally determined elastic constants and their temperature and pressure derivative of olivine and orthopyroxene have been used for the numerical calculation (Anderson & Isaak 1995; Abramson et al. 1997; Frisillo & Barsch 1972). Well constrained measurements that fall within the model space, 188 local and 29 teleseismic, have been used for the SWST inversion.

Both Olivine and Orthopyroxene resemble the orthorhombic system with unequal axis length (‘a’, ‘b’, and ‘c’). The crystallographic orientation is represented by the horizontal azimuth ‘θ’ and two plunges ‘ψ’ and ‘ϒ’. Several experimental and real-world observations of mantle peridotite show that ‘b’ and ‘c’ axes are randomly oriented (Bystricky et al., 2000; Mehl et al. 2003), simulating hexagonal symmetry. We can easily apply the hexagonal symmetry by orienting the ‘c’ axis parallel to the horizontal. The degree of anisotropy is defined as ‘α’, also called the strength parameter. It is the ratio between the predicted and parameterized single-crystal delay time. In general, due to the misalignment of crystal in the mantle, the observed delay time is always lower than the predicted delay time of the parametrized single crystal value. Hence, the strength will always be less than 1 and represented as 0 to 100 percent. Finally, the model vector is composed of three parameters: azimuth (θ), dip (ψ), and anisotropic strength (α). Parameterizing the model this way, the tomographic inversion enables us to investigate the 3-D orientation of anisotropic fabrics of the study area.

Forward Modeling

Tomographic inversion starts with the calculation of SWS parameter of each ray path. First, I have traced the ray-path from source to the receiver using the 1-D velocity/density model AK135 (Kennett et al. 1995) to obtain the path lengths and direction cosines. Then, the particle motion perturbation method (Fischer et at., 2000) has been used to calculate the 3D distribution of anisotropy for each block. The effects of anisotropy in each block encountered along a ray path are approximated by progressively rotating and time-shifting the horizontal components of a simple wavelet that has an initially linear horizontal particle motion. The initial polarization direction of local events has been calculated using a grid search algorithm that minimizes the energy in the radial component.

Inversion

SWST is a linearized, damped, least-squares inversion (Tarantola, 1987) method that iteratively solves the orientation and strength of anisotropy by minimizing the misfit between the predicted and observed splitting parameters.

$$M^{iter+1} = M^{iter} + C_{mm}G^T [GC_{mm}G^T + C_{dd}]^{-1}\delta D^{iter}$$

Where the new model M^{iter+1} is calculated by changing the model of the previous iteration M^{iter}. G is the numerically calculated matrix of partial derivatives that relates the change of model parameters in response to varying model parameters. δD^{iter} is the data misfit of the previous iteration. C_{dd} is the data covariance matrix having diagonal term containing the square sum of the 1σ error. C_{mm} is an priori model covariance matrix introducing damping relaxation and spatial smoothing.

The inversion has been initiated with a starting model from which iterative changes were made to improve the misfit between the observed and predicted splitting parameters. Average, random, and uniform starting models have been tested. Detail description of the individual starting models and assumptions has been discussed in Abt & Fischer (2009). The final inversion was performed using the average stating model as it produced the smallest average misfit as others have seen (Abt & Fischer., 2008; Calixto et at., 2014). The G matrix has been recalculated when the change of orientations (‘θ’ and ‘ψ’) and strength (α) became greater than 1° and 1%, respectively. A total of 50 iterations were done before reaching the final model. Relaxation of damping has been done after 20 iterations to ensure the global convergence towards the best fitting model.

Resolution Test

In a linear inverse problem, the resolution test of a tomographic inversion provides a direct way to quantify which parts the model space are well resolved (Menke, 1984; Tarantula, 1987; Yao et al.,1999). For our inverse problem setup, the Resolution matrix (R_M) of the model can be defined as:

$$R_M = C_{mm}G^T[GC_{mm}G^T + C_{dd}]^{-1}G$$

Here, the diagonal elements (R_M) of different model parameters [strength of anisotropy (α), azimuth (θ), and dip (ψ)] vary from 0 to 1, reflects how well the individual model parameters are resolved within the model space. Also, testing the model resolution using real event-station pairs helps to choose the optimum value of the different inversion parameters (e.g., initial model parameter variance, damping, starting model, spatial smoothing) before doing the actual inversion. It reduces the calculation time and enables us to test a wide range of model parameter values. Well resolved blocks [Fig 29] are concentrated in between the events and stations where the bulk of the ray paths crossed. Because we have fewer earthquakes deeper than 100 km, model resolution below 100 km depth tends to be worse, although we do have some well-resolved blocks below 150km close to the virtual hypocenter of teleseismic events. Overall, the resolving power of the azimuth of the fast direction is better than the dip. I have used the same optimal model parameters found on the resolution test to generate the final tomographic model. A total of 188 local and 29 XKS splitting measurements that fall within the model space have been used to get the final SWST model.

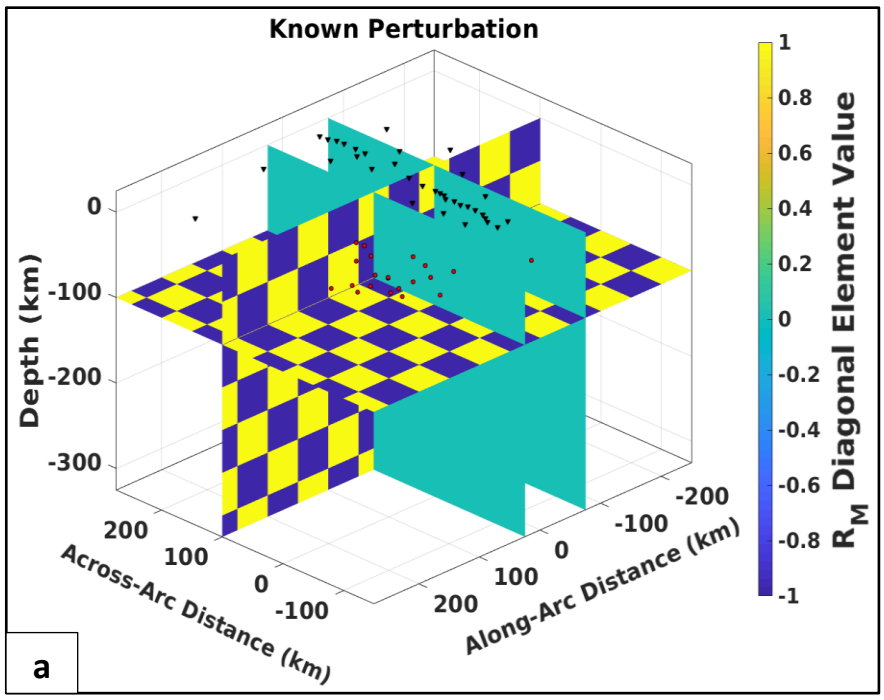
Known Perturbation
Depth (km)
0
-100
-200
-300
200
100
0
-100
Across-Arc Distance (km)
200
100
0
-100
-200
Along-Arc Distance (km)
1
0.8
0.6
0.4
0.2
0
-0.2
-0.4
-0.6
-0.8
-1
R_M Diagonal Element Value
a

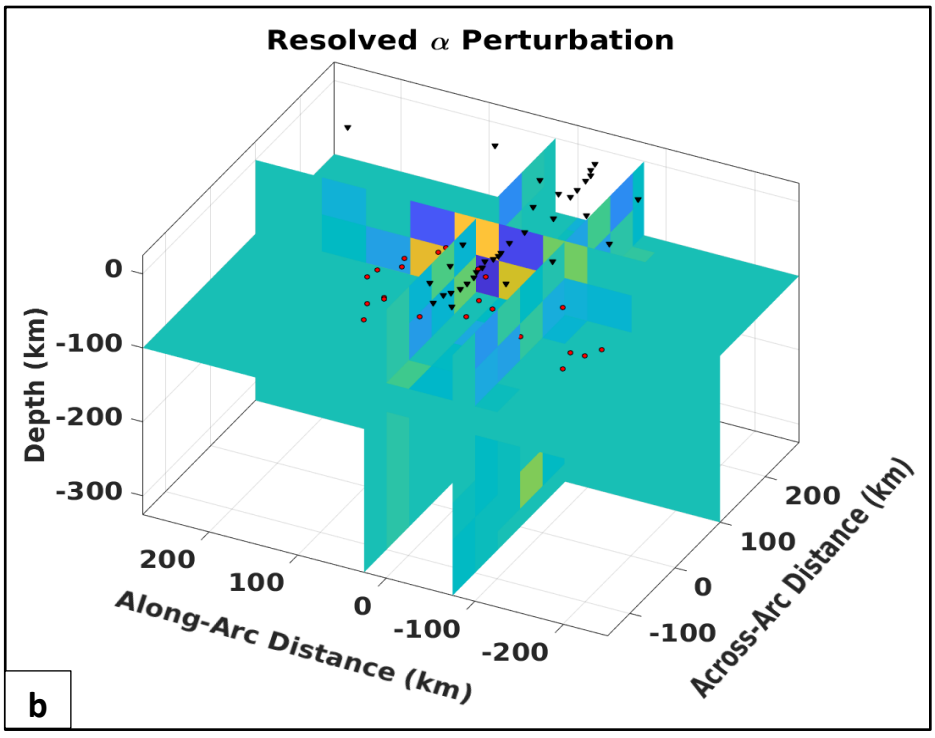
Resolved α Perturbation
Depth (km)
0
-100
-200
-300
200
100
0
-100
-200
Along-Arc Distance (km)
200
100
0
-100
Across-Arc Distance (km)
b

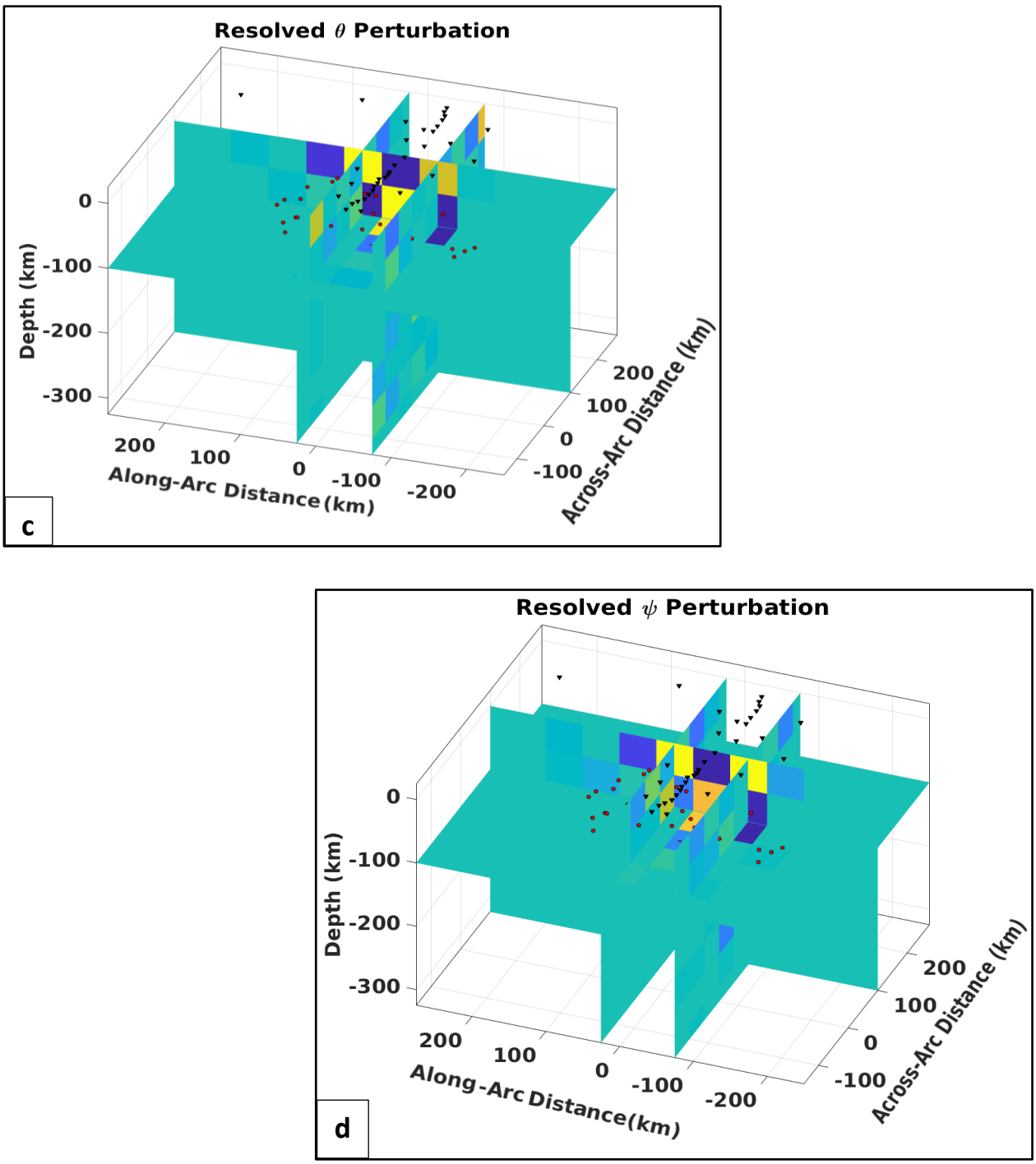

Figure 29: Resolution Test result using real event-station pairs. The diagonal elements of the resolution matrix (R_M) of different model parameter shows how well the input known models are recovered; (a) input known model; (b) resolved strength (α) perturbation; (c) resolved strength (θ) perturbation; (d) resolved strength (ψ) perturbation. Black inverted triangles and red circles are the location of the stations the events, respectively.

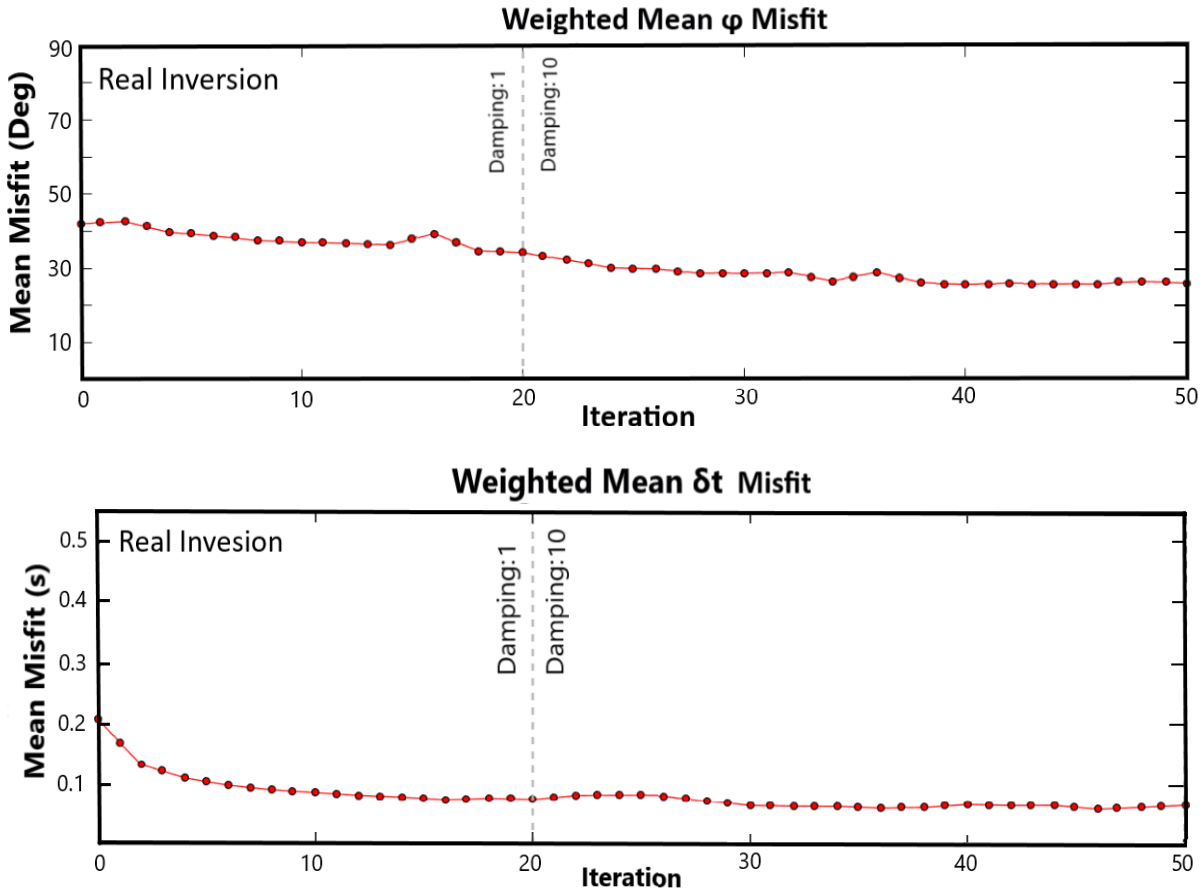

Figure 30: Weighted mean misfit of splitting parameters with iterations; (a) fast direction; (b) lag time

Chapter 3: Results and Discussions

To reveal the nature of the upper mantle deformation fabrics, I have analyzed 141 different teleseismic events of distance rages from 83° to 180° [Fig-22 & 31]. Following the steps of pre-processing, measurement, and quality controls, a total of 172 well-constrained split results have been found from the teleseismic SKS, SKKS, and PKS phases. In addition, many waveforms show null results where no splitting is detected. Similarly, we have analyzed 61 local deep events greater than 40 km to investigate the deformational fabric of the mantle wedge above the subducting slab. After quality control, I have extracted 274 local splitting results and 198 null results from all local events. I have used a maximum error margin for fast direction and lag time of 30° and 0.5 s, respectively.

Teleseismic Splitting Results

The station average teleseismic splitting result shows a consistent trench parallel N-S fast direction (φ) [Fig-32]. Fast directions also slightly bend from NN-E to NN-W direction as we move from north to south following the curvature of the trench line. We also observe some along-strike variations of lag time (δt). The average δt on the forearc region (west of 95°E) is about 2.0 s, higher than the global average XKS [Fig-57]. Although the analysis of 6 months of BIMA array data produces fewer good XKS splitting results per station, they all produce consistent N-S φ and over 2.0s of δt. Similar results have also been found at the nearby permanent station HKA (MM network) that produces 10 good results by analyzing ~2.5 years of data. The maximum observed lag time is 2.5s at MP01, one of the westernmost stations [Fig-32]. The lag time gradually reduces to ~1.0s when we move towards the back-arc, especially on the northern part above 22°N. In

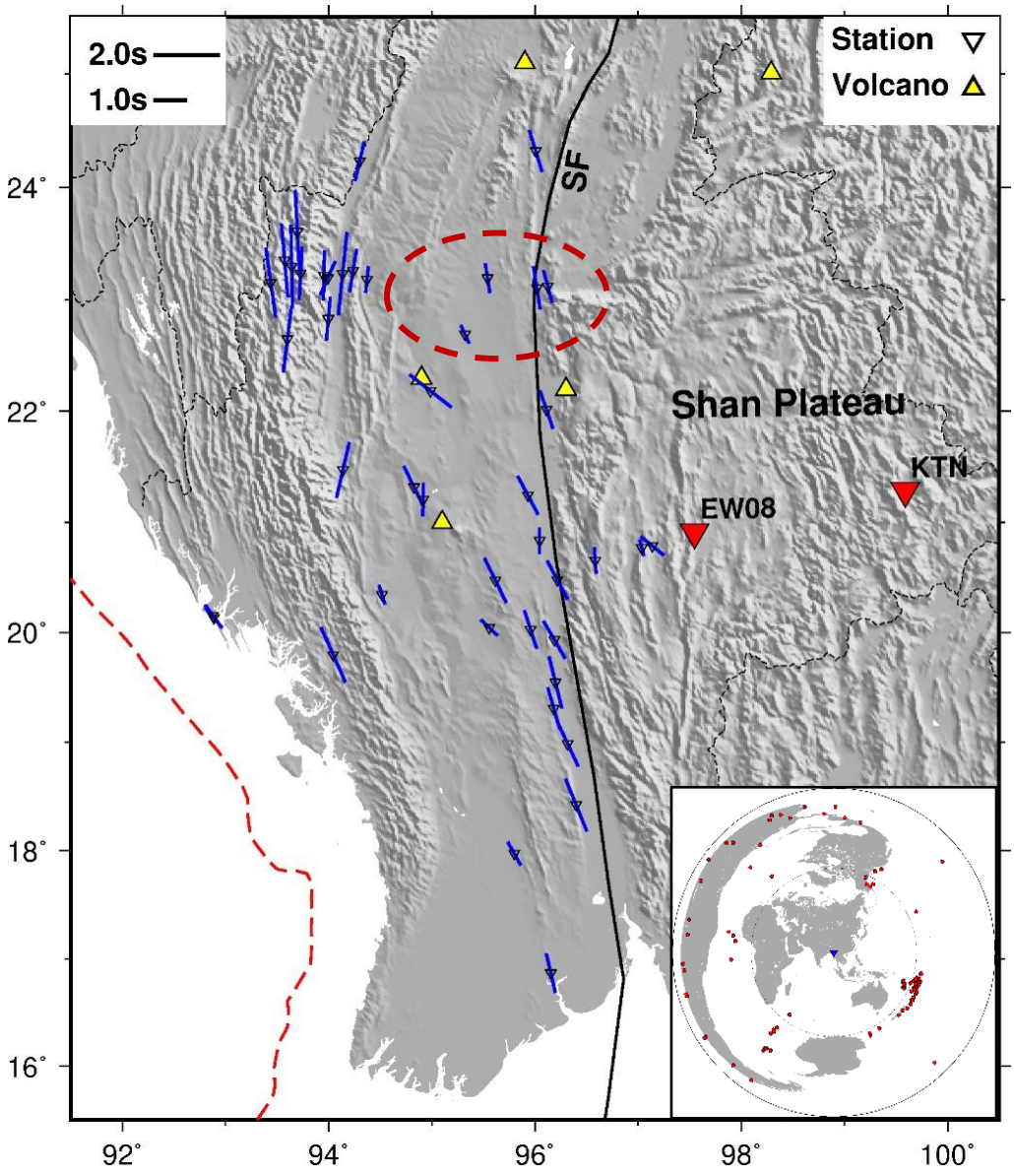

Figure 31: Station average teleseismic shear wave splitting measurements; red dotted line is the trench line, yellow triangles are active Quaternary Volcanoes, red inverted triangles are the null stations. Red dotted circles demarcate the low δt on the back-arc region.

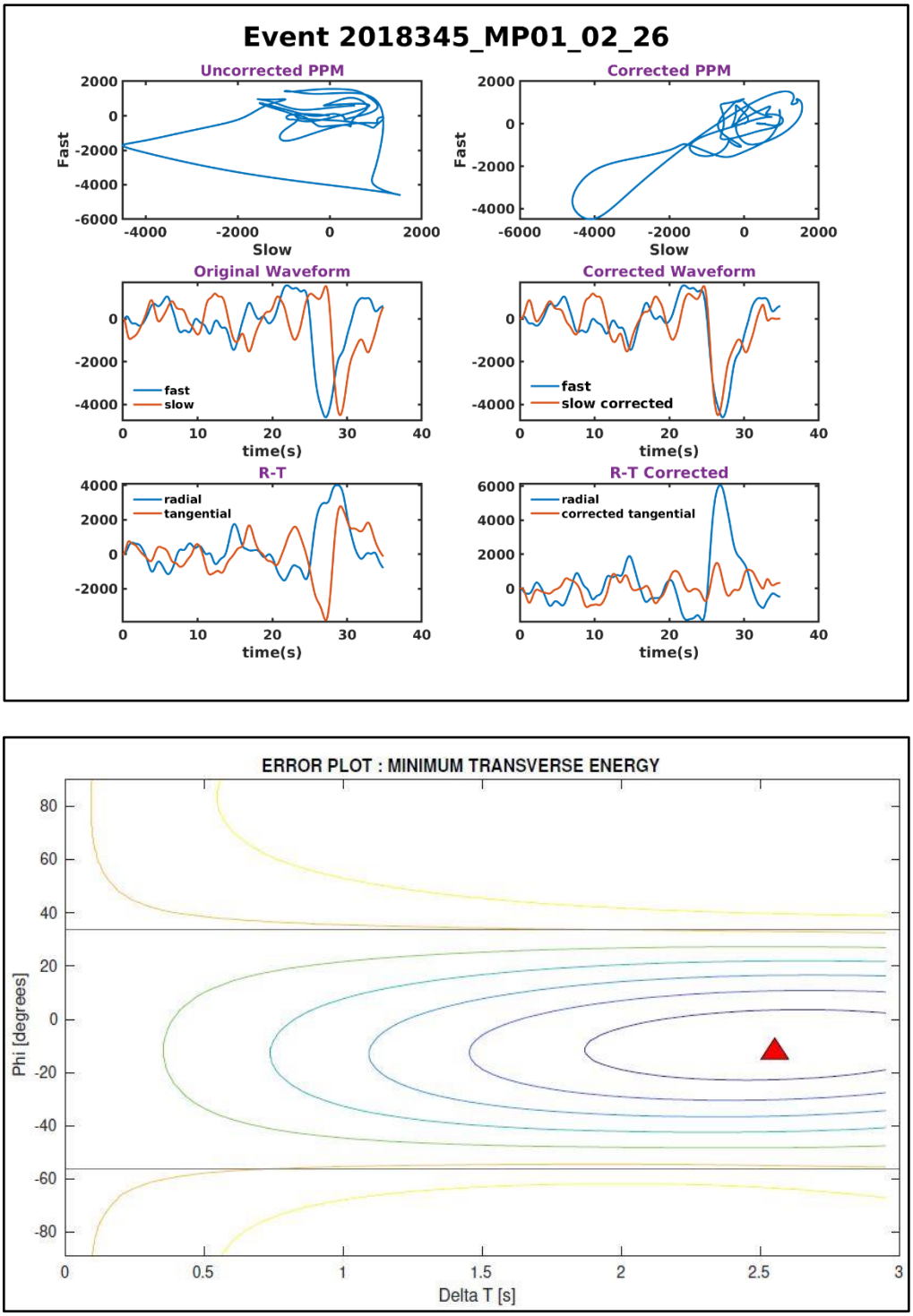

Figure 32: Example of a well resolved teleseismic splitting result producing higher δt.

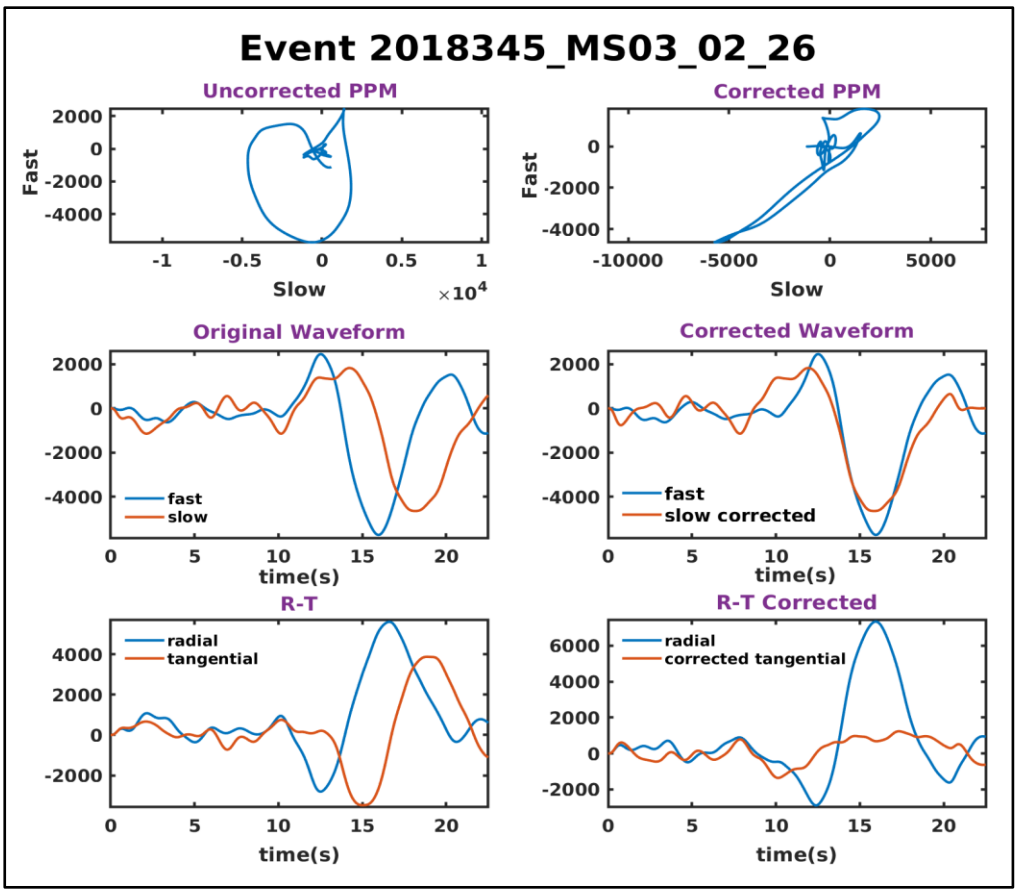

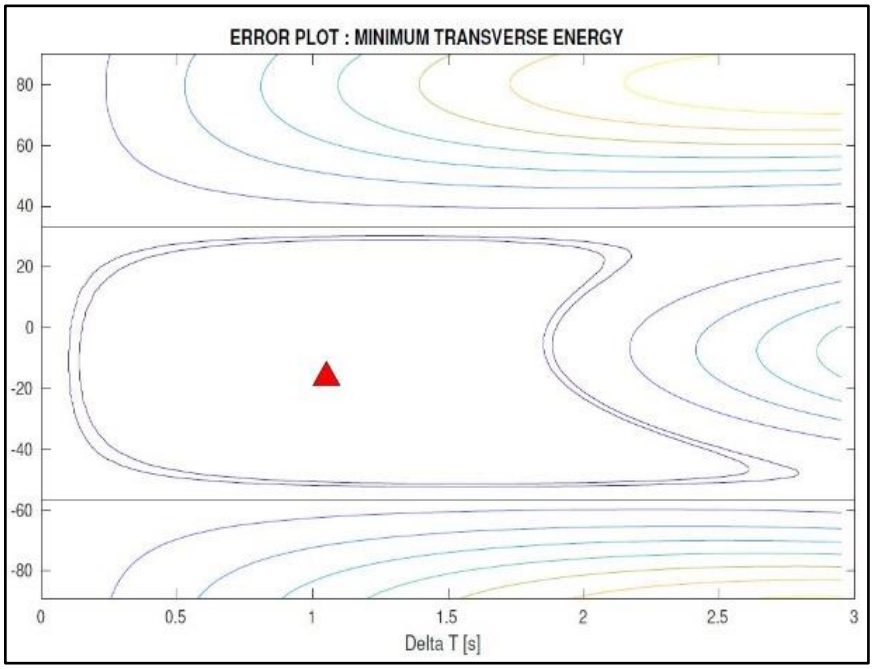

Figure 33: Example of a well resolved teleseismic splitting result producing one of the lowest results (station MP21).

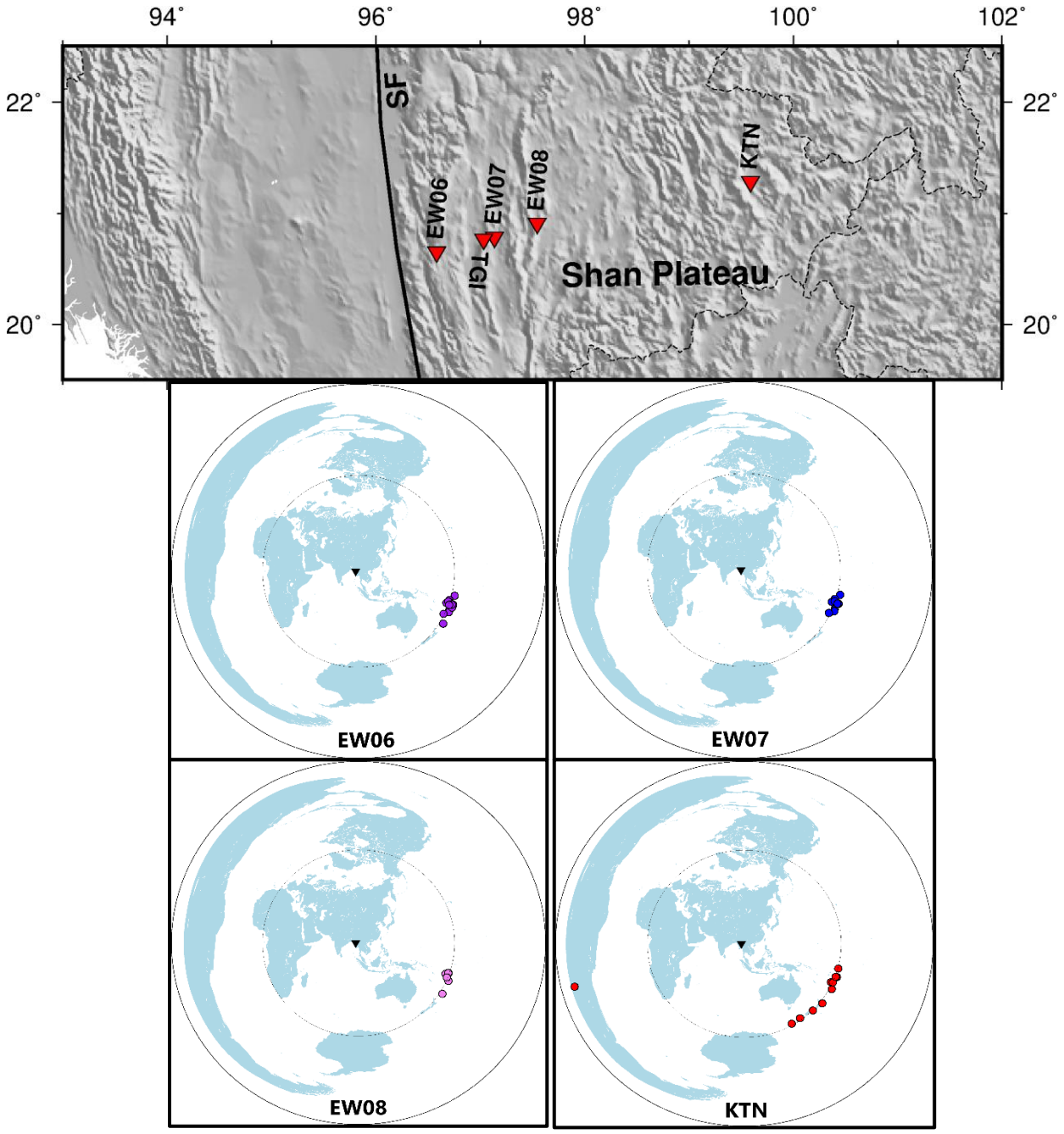

Figure 34: Stations across the Shan Plateau having smaller lag times and nulls with their azimuthal coverage.

the southern part, this transition is less pronounced. One station at the Central Basin(M023), close to an active Quaternary volcano (Mt. Monywa), produces a different NW (N52°W) fast direction. Lag times continues to shrink eastward, towards the Shan Plateau. Also, fewer events produce good splitting results for stations like EW06, EW07, and TGI with many nulls. Some easternmost

stations in our arrays (EW08 and KTN) have produced all null results [Fig-31 & 34]. Since we have no stations in the northern part of the Shan Plateau, the extent of the null measurements cannot be quantified.

Local S wave Splitting Results

Unlike the SKS splitting, individual local S wave splitting results show a complex pattern of fast direction. Even though the average φ tends to be N-S (average ~1.2°), we observed some interesting variation. The average δt is about ~0.5s and varies widely across the study area. We found a maximum δt of 1.2 s [Fig-37a] from deep events (133 km), where the wave samples the entire mantle wedge and perhaps part of the slab. Conversely, some shallow events produce smaller δt, which is typical for crustal splitting [Fig-37b]. Fig-35 shows all local results where each splitting vector is plotted between the event-station pair. The higher than global average δt for the mantle wedge indicates the presence of a highly anisotropic mantle wedge in this subduction setting (Long & Silver, 2008; Long, 2013. In general, due to the presence of strong corner flow, the anisotropic fabric of the mantle wedge tends to be trench normal (Long & Silver, 2008; Long, 2013). The dominance of the trench-parallel fast in axis both the fore and back-arc region implies a weaker corner flow and strong toroidal flow. Also, the observed spatial variation of the splitting parameters is indicative of complex deformational fabrics of the mantle wedge. In later sections, I will explore the wedge anisotropy in detail.

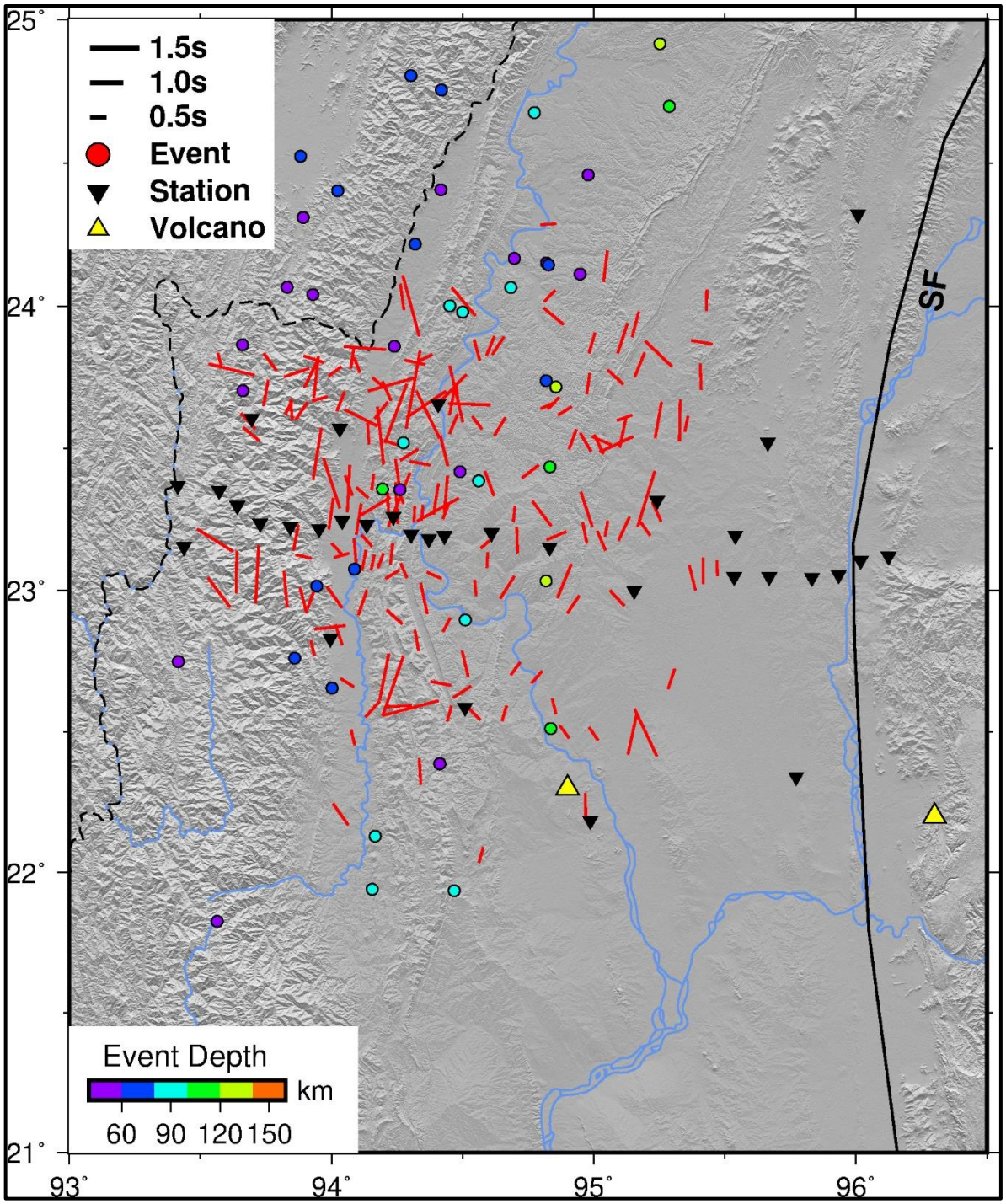

Figure 35: Local S wave splitting results; splitting vectors are plotted at the midpoint of the event-station pair.

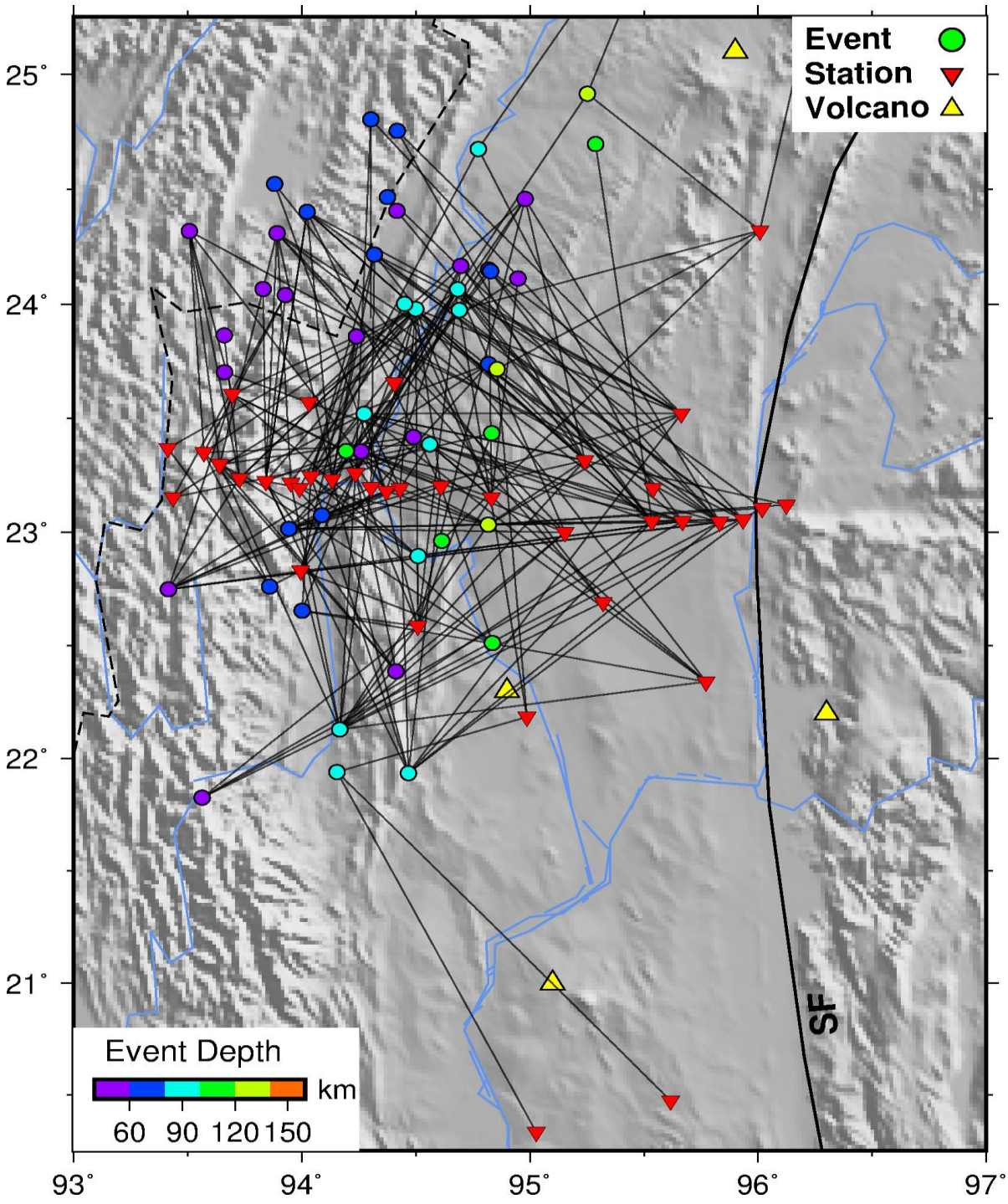

Figure 36: Ray path coverage of the local splitting results. Each black line connects an event-station pair. Splitting parameters are on the Fig-35, plotted at the midpoints.

a

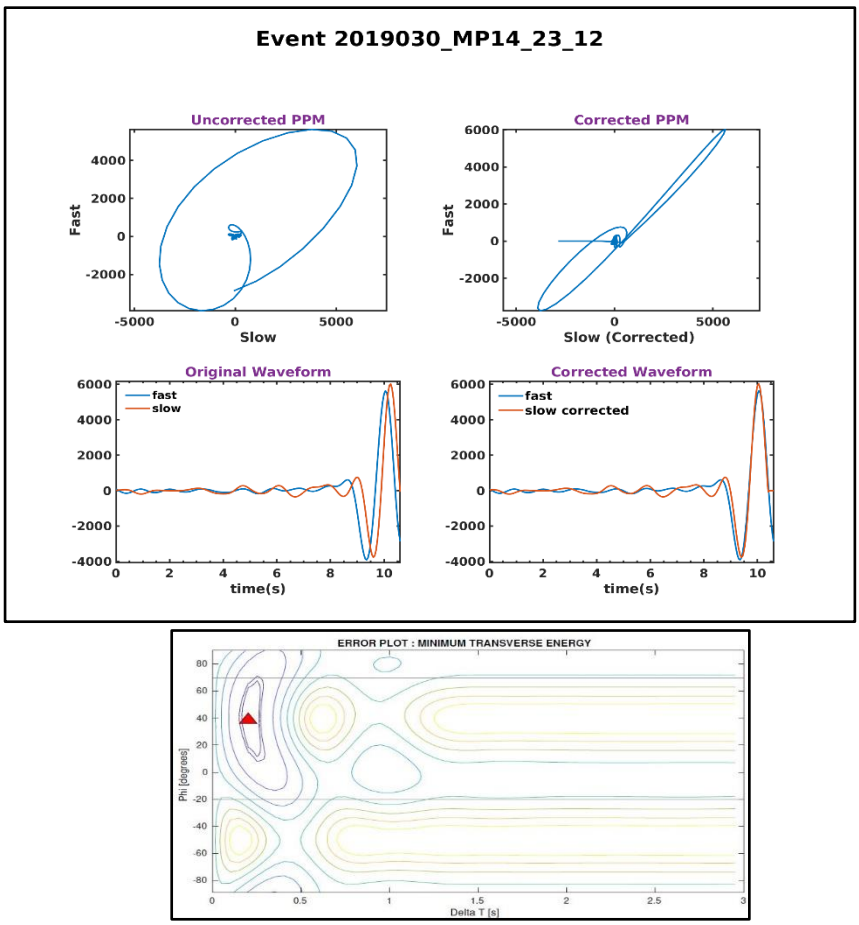

b

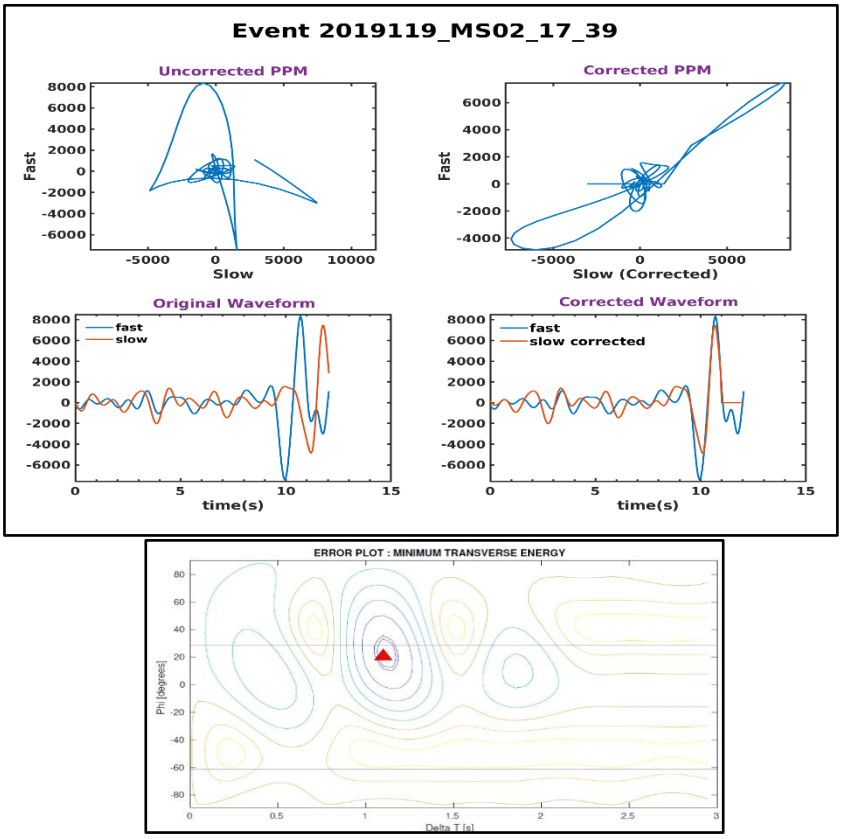

Figure 37: Example of well resolved local splitting results; (a) very low lag time 0.2 s; (b) high lag time 0.9 s.

Depth Dependency

Because shear wave splitting is a path-integrated result, it has no vertical resolution. In general, local deep events originate at the slab interface and travels upward through the mantle wedge. This allows us to constrain the depth of the anisotropy by comparing the local and teleseismic splitting. The variation of the depth distribution of local events also enables us to investigate the spatial variation of the anisotropic fabric of the mantle wedge. As mentioned before, because the local results have maximum event station spacing of 2°, the ray paths maximize the vertical path by minimizing the incidence angle. Analysis of the splitting parameters of less than 50 km deep events shows an average N-S fast direction (average ~4.0° with $1\sigma \approx 30°$). Closer event-station pairs of vertically traveling waves show a δt of ~0.3 - 0.4 s. These waves primarily sample the crust, hence showing the crustal anisotropy [Fig-38: green circle]. It results from the stress-induced alignment of microcracks, cracks, faults, or fracture zones (Crampin, 1987) and can be as high as to 0.5 s (Savage et al., 1990).Though, some distant events of greater incident angles accumulate higher lag time (~0.7 - 0.8 s) owing to its greater path length through the wedge. In addition, the fast direction aligns approximately N-S, which may result from the active northward dextral motion.

Results from 50-100km deep events [Fig-39] show a large variation of splitting parameters. Most of the events originate from the middle of the fore-arc region and sample the western forearc close to the trench, the eastern forearc, and the back-arc region. In general, the western fore-arc region (west of 94.5°) shows a higher lag time (>0.5 - 1.2 s) with an average N-S fast direction [Fig-39, white circle), whereas the eastern forearc regions show large spatial variation of both φ and δt (Fig-39, green circle).

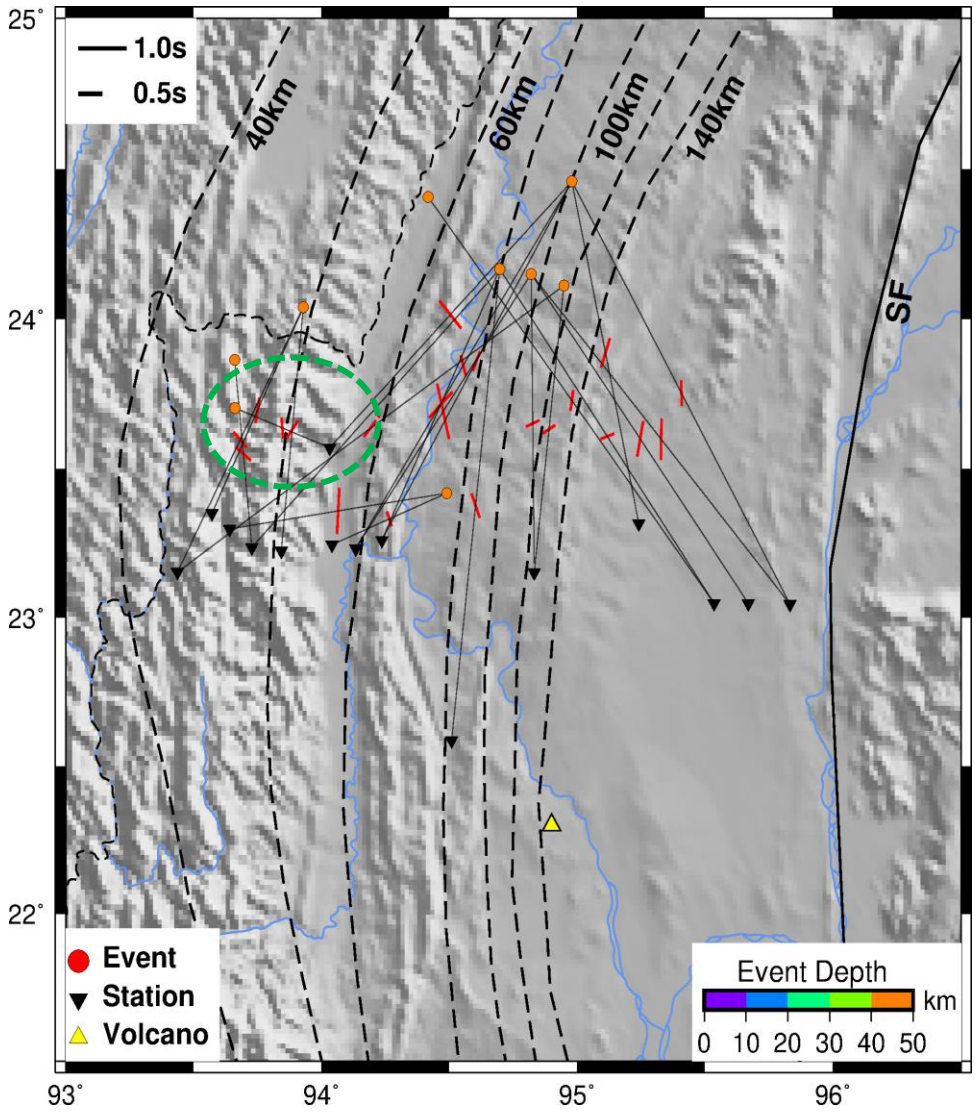

Figure 38: Local S wave splitting result of upper 50 km events. Black dotted lines are the slab contour; black solid lines are the event station pair lines. The green circle shows some of the crustal splitting.

Splitting results from the deeper events also show average N-S fast directions, although we have fewer deep events greater than 100 km with limited azimuthal coverage [Fig-40]. Some small δt (~0.2 - 0.4 s) close to the arc has also been observed [Fig-40, green circle]. The lag time becomes

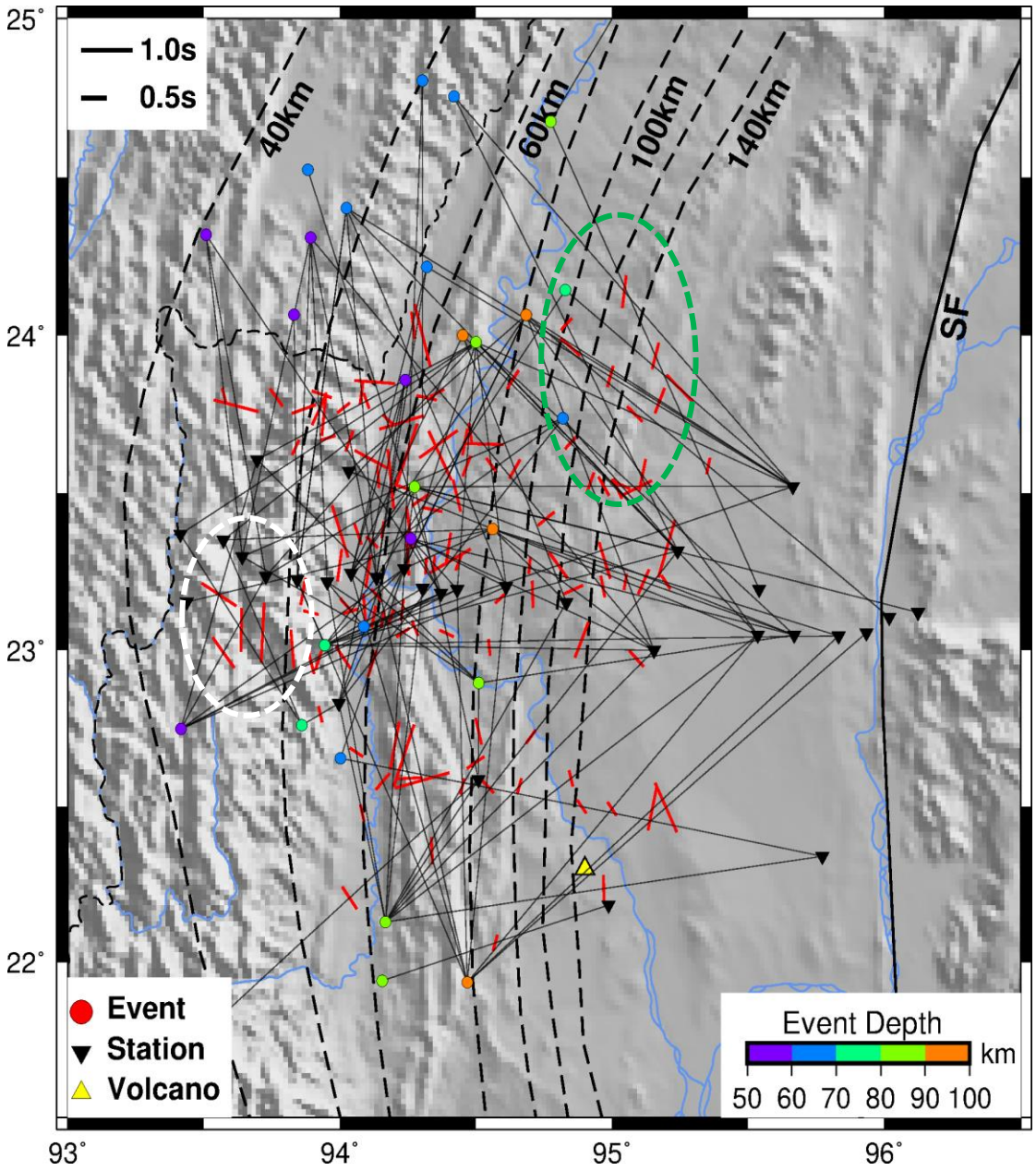

Figure 39: Local splitting results of 50-100 km deep events.

lower (~0.5 s) in the eastern back-arc region. Conversely, the western forearc region shows higher lag times (~1 s). This indicates the presence of spatially variable complex anisotropic mantle fabric on the wedge.

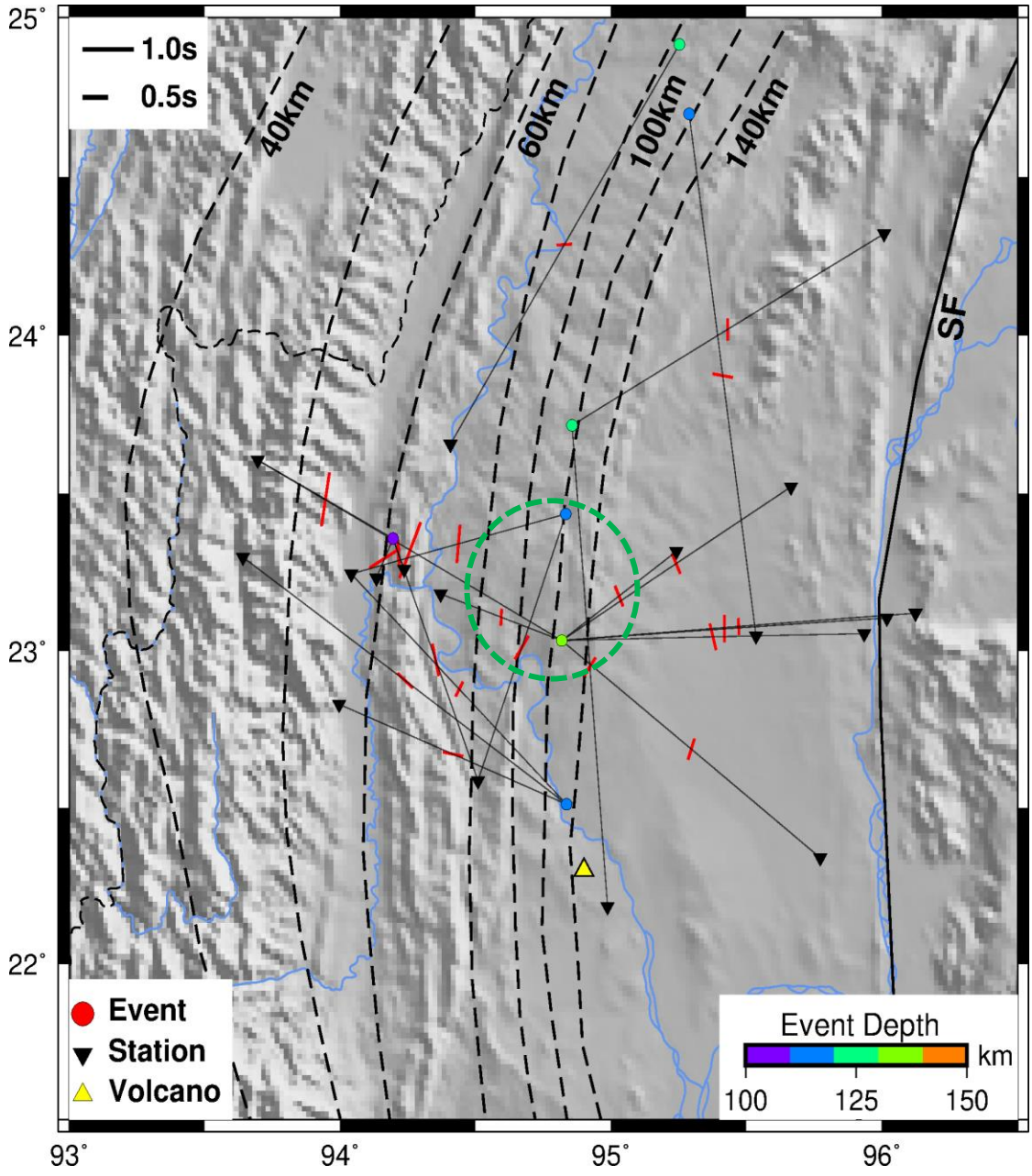

Figure 40: Local splitting results of 100-150km deep events.

We have also observed some E-W to ENE-WSW fast direction close to 23.5 - 24°N which indicates the presence of localized E-W deformational fabric [Fig-41]. Also, the splitting pattern is consistent with a 50 km to 120 km event depth, implying the deeper extent of the fabric. Active mantle flow through the slab tear as suggested by Russo., 2012 could produce such observed fabric.

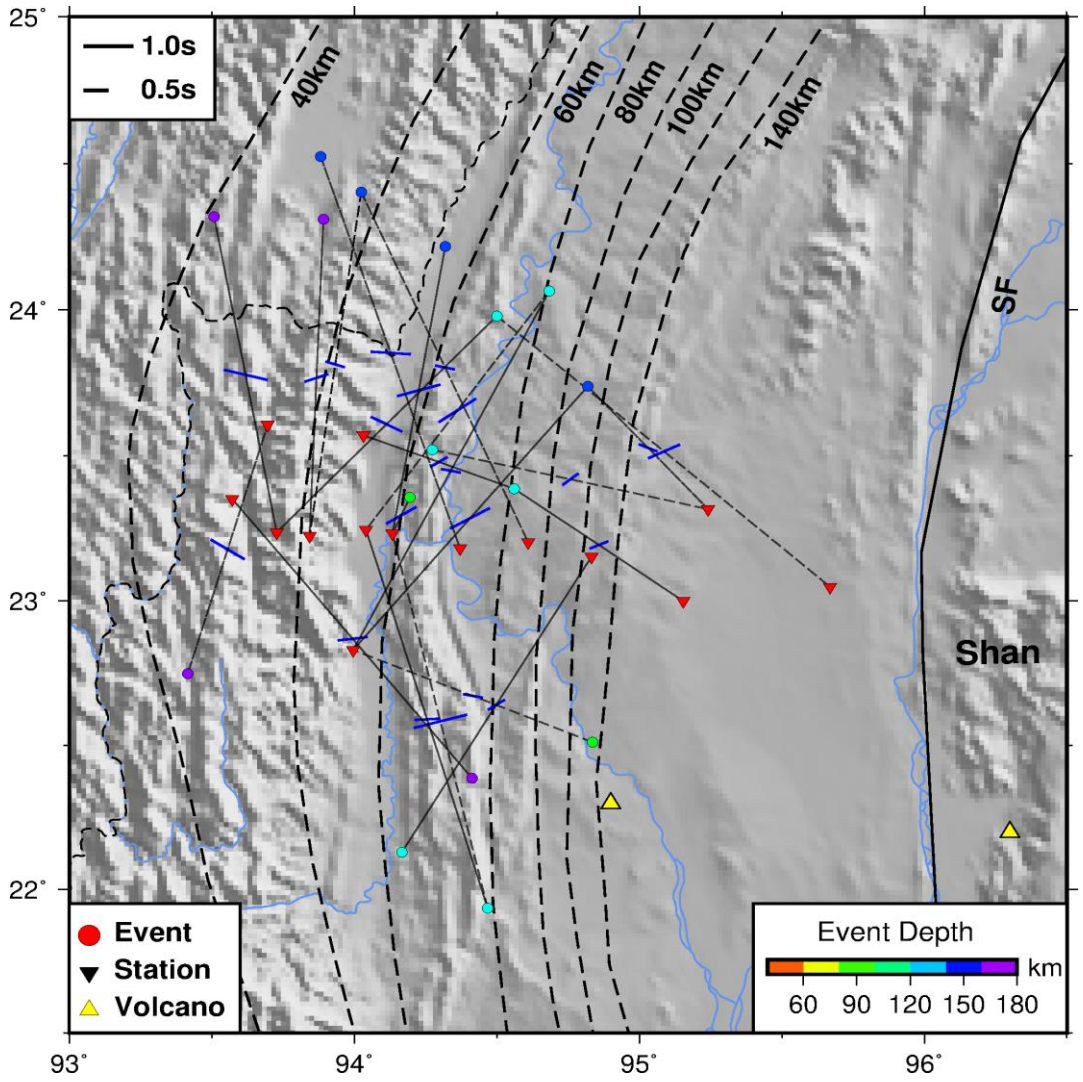

Figure 41: E-W local splitting measurements and their ray-path coverage

However, most of the events originate from either north or south, providing limited back- azimuth coverage. Comparing the local S and SKS also helps to isolate anisotropic zones. Whereas the teleseismic waves sample the entire sub-slab, slab, mantle wedge and crust, the local S wave can only travel through the mantle wedge. By comparing the SKS and local splitting results, a different pattern emerges on the western and eastern parts of the subduction system. The average SKS δt value on the western (west of 94.5°E) fore-arc is more than 2.0 s. The difference

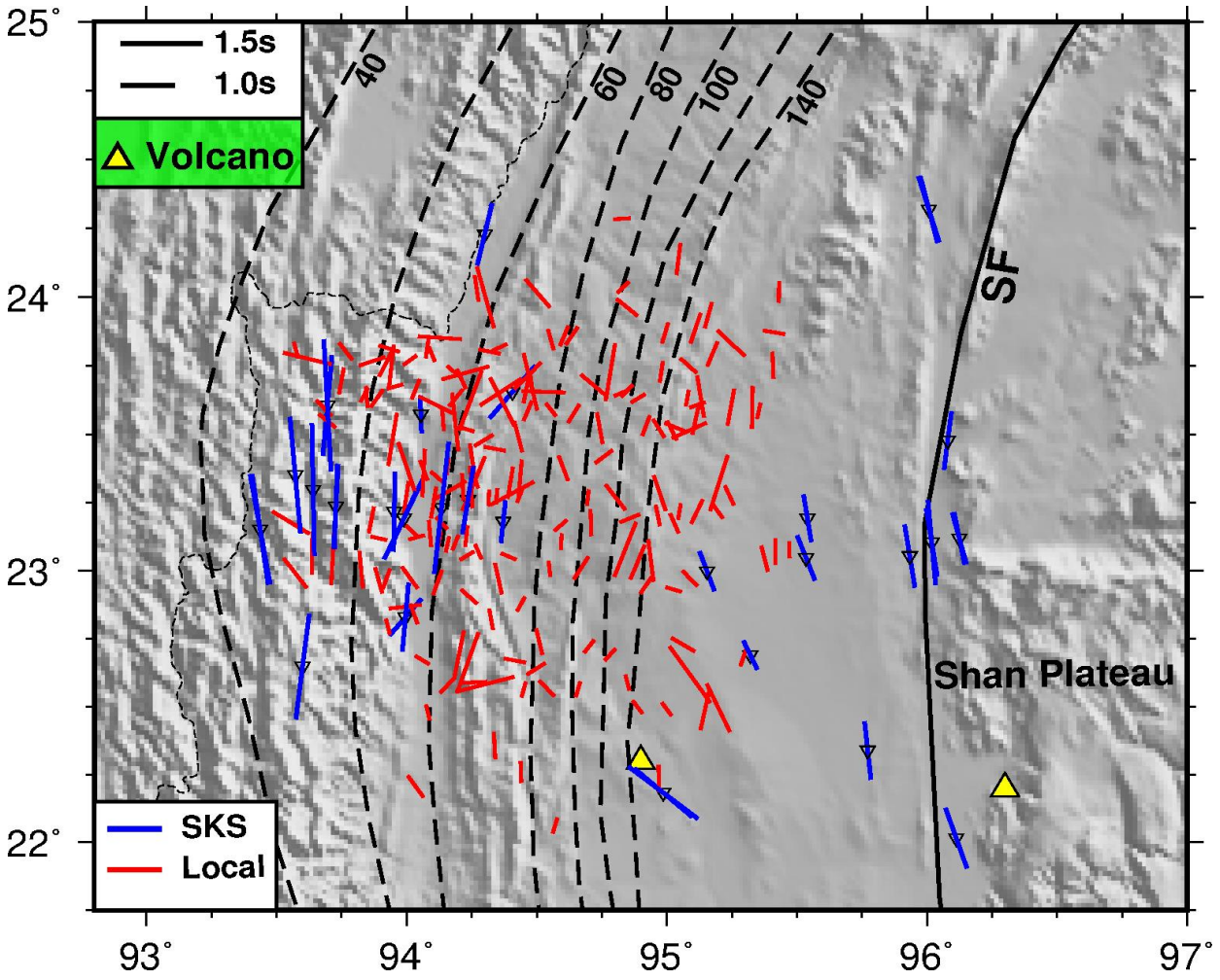

Figure 42: Local (red) and SKS (blue) splitting results on the western forearc and the eastern arc and the back arc; dotted lines are slab contours and yellow triangles are volcanoes.

in lag time between the SKS and local S splitting on the western part (west of 94.5°) is more than 1.0 s, although the average φ value remains the same [Fig 42]. This indicates that the incoming S wave primarily splits within and below the slab. Because the mantle wedge is thinner on the western part due to the gentle dip of the subducting Indian slab, the sub-slab region is the dominant source of anisotropy. Conversely, we see a very different splitting pattern on the eastern part (east to 94.5°E). Local deep events (up to 133 km) have an average lag time of ~0.5 - 0.8 s. Overall, the

difference between the SKS and local δt is lower (~0.3 s), suggesting that the bulk of anisotropy resides within the mantle wedge.

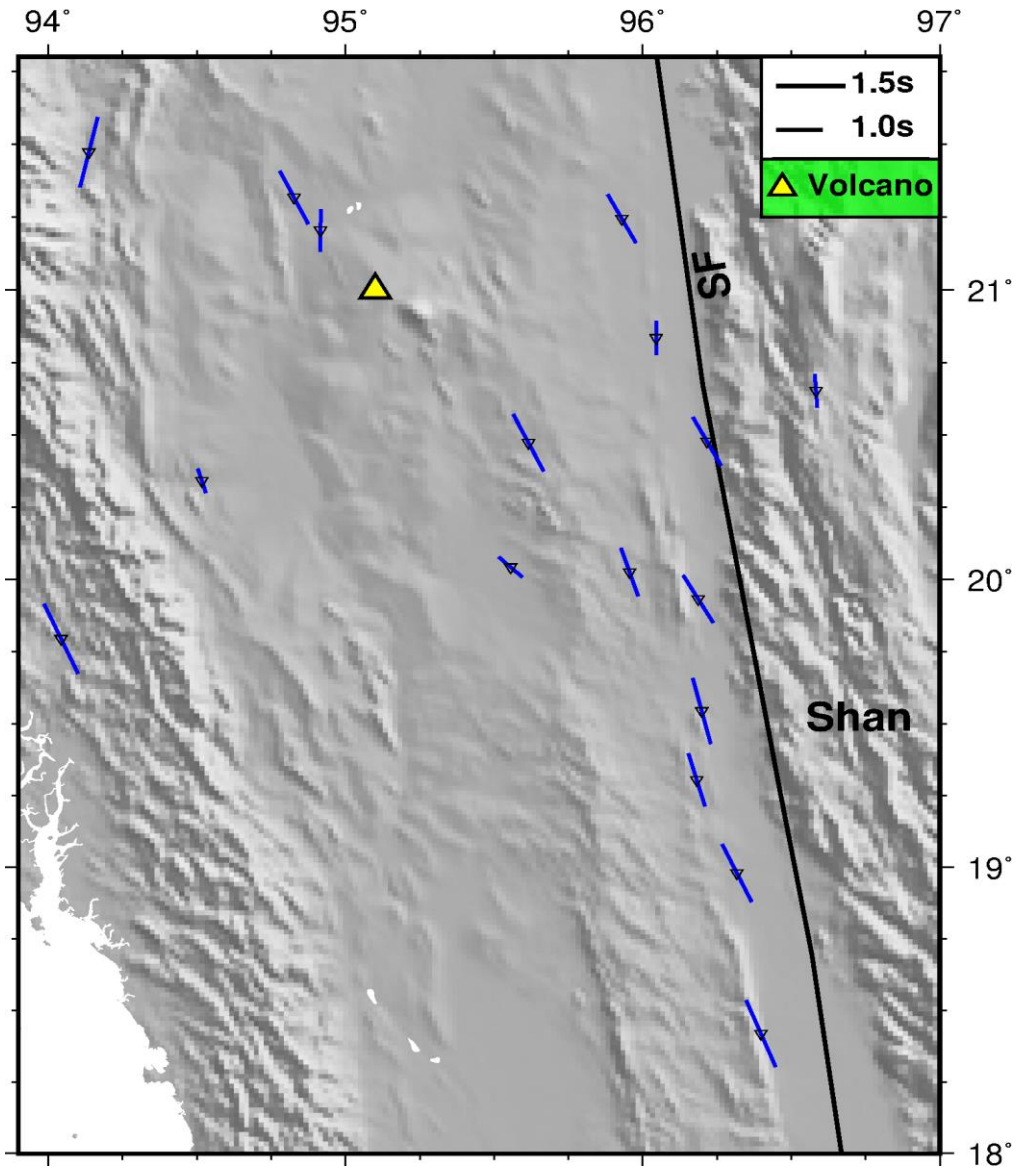

Figure 43: SKS splitting results of the southern part of the study area

Since we have no local deep events in the southern part <22°N, anisotropic zonation is not possible. From the available SKS results, we can see the δt becomes higher (~1.2 s - 1.6 s) than the northern wedge, especially closer to the Sagaing fault. This implies a different geodynamic process acted

on the southern part of the wedge that increased the anisotropic strength, thickness, or both. We can also see smaller lag times in some stations within the central basin (EW04 and M008).

Back-azimuth dependency

I have analyzed the back-azimuth dependency of the splitting parameters to investigate the presence of multiple anisotropic layers. An incoming S wave will split twice while propagating through the two-layer system and produces two pairs of split waves (Fig-44). However, since the separation between these waves is less than the full wavelength, we cannot see the four individual waves on the seismogram. Instead, we see the apparent splitting parameter varies with the back-azimuth, a distinctive signature of multiple anisotropic layers (Silver & Savage, 1994). The

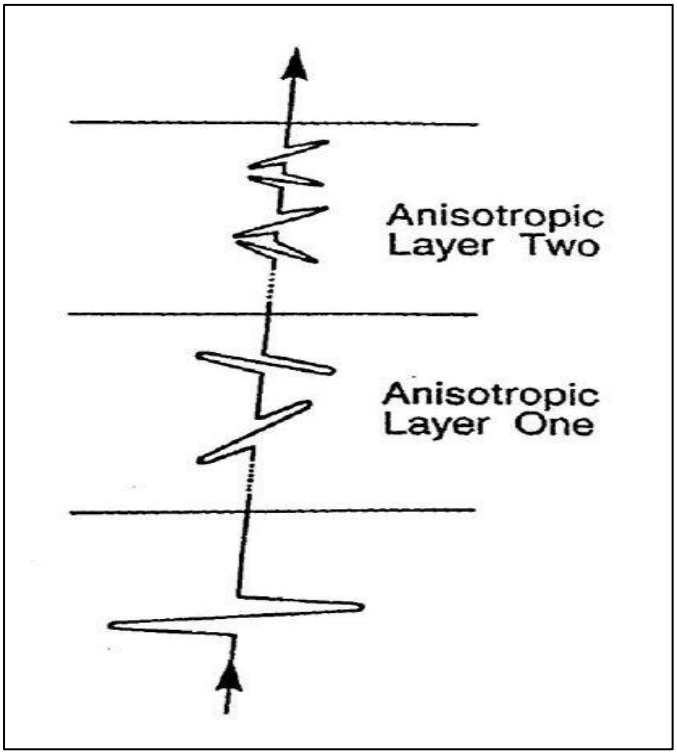

Figure 44: An example of a multiple anisotropic layer splitting (from Silver and Savage, 1994)

variation of splitting parameters with back-azimuth modulo-90 can be used to identify periodicity.

Because most of the stations within our array started operating quite recently, complete azimuthal coverage of the event distribution has not been achieved. Most of the teleseismic events are generally concentrated within a narrow back-azimuth (Fig-22) range, not ideal for this kind of analysis. Since the stations are relatively closer, plotting them as a group would have more azimuthal coverage. Keeping this mind, I have divided the study area into four quadrants (Fig-45) to analyze the back-azimuth variations.

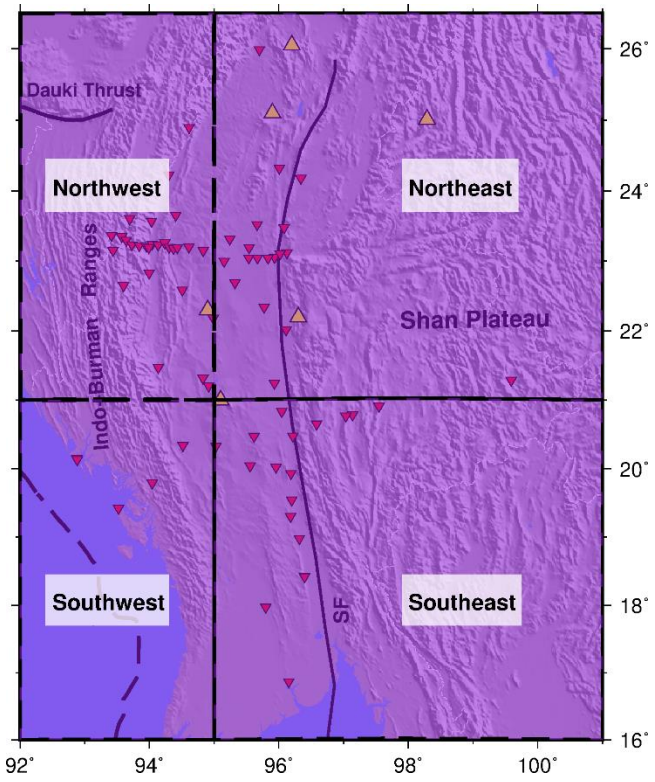

Figure 45: Division of the study area for investigating back-azimuth dependency of the splitting parameters. Red inverted triangles are the location of the stations and yellow triangles are the active volcanoes. SF- Sagaing Fault

SKS lag time on the N-W part varies from 2.5 s to 1.0 s without any systematic pattern [Fig-46a] with relatively constant fast polarization direction [Fig-46b]. Also, no periodic variation of either fast direction or lag time are visible on the N-E part [Fig-46cd]. A single anisotropic layer with a horizontal axis of symmetry is sufficient to explain such observed splitting properties. Similar

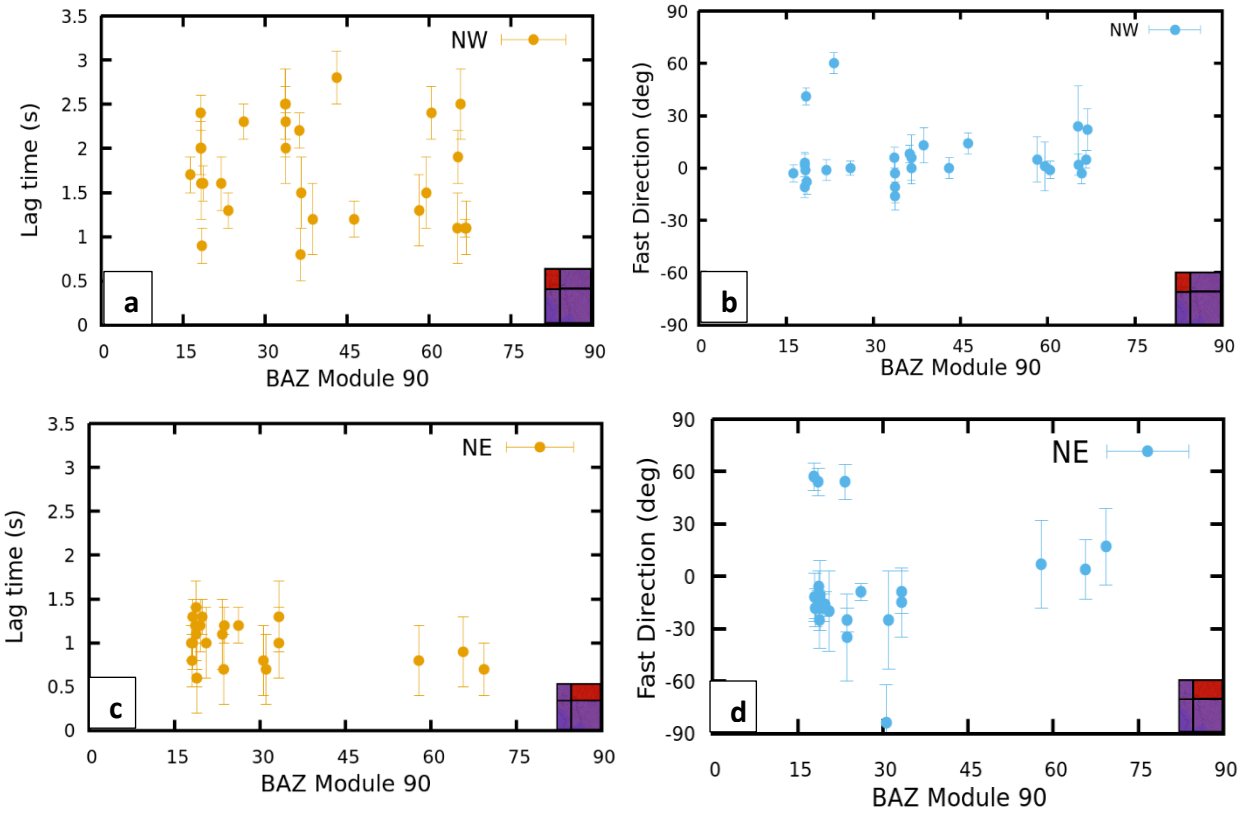

Figure 46: Back-azimuth variations of splitting parameters on (a), (b) the northwest and (c), (d) northeast part.

trends are visible on the S-W and S-E part [Fig-47] with limited azimuthal coverage. However, one of the southern stations (MDY) having wide azimuthal coverage shows no signs of periodicity [Fig-48], indicating the presence of a single anisotropic layer.

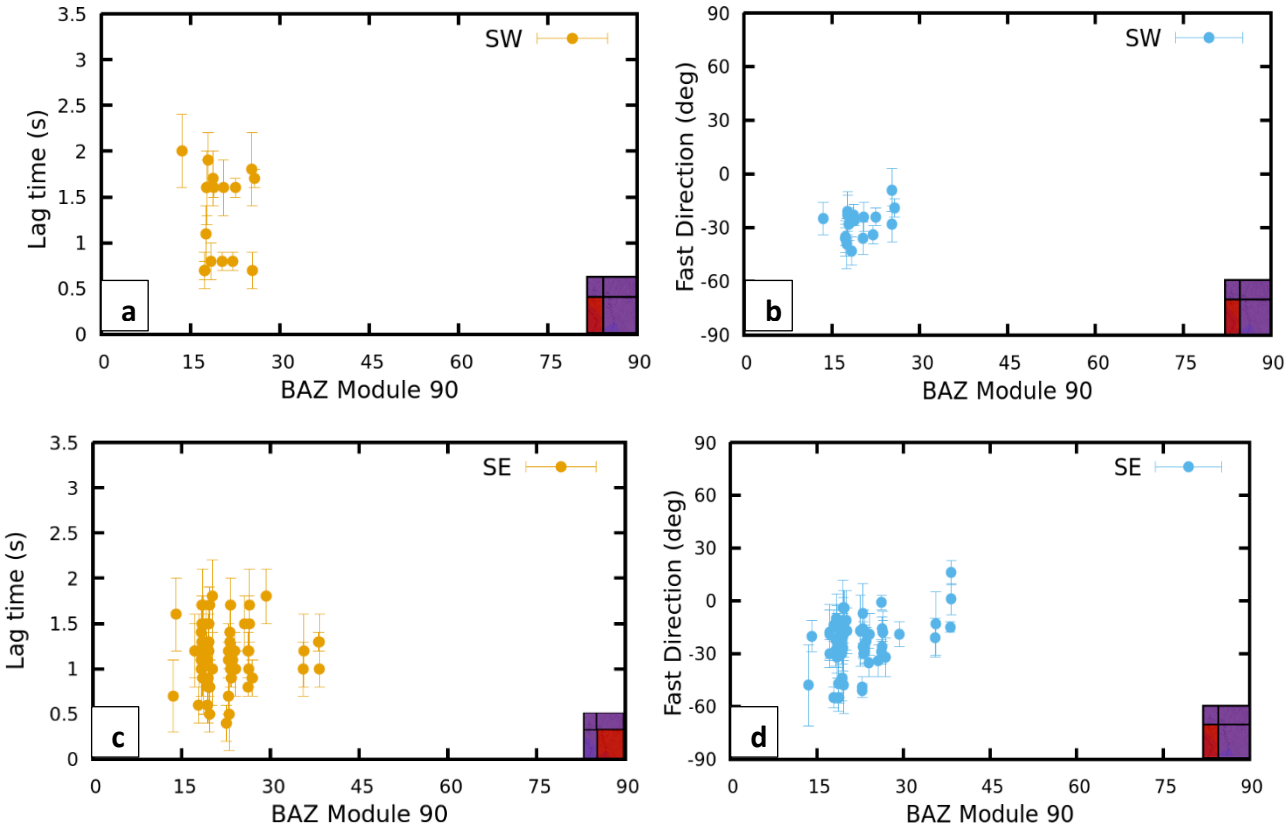

Figure 47: Back-azimuth variations of splitting parameters on (a), (b) the southwest and the southeast part.

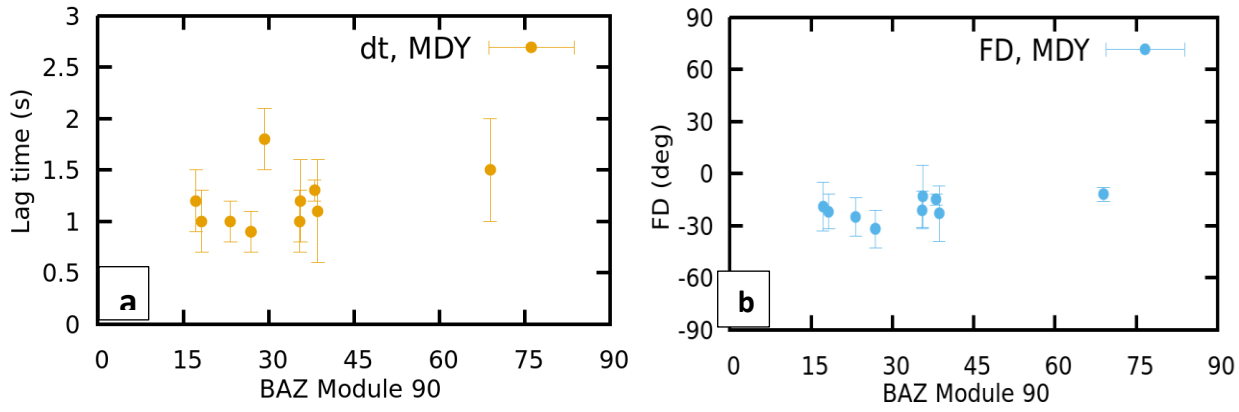

Figure 48: Back-azimuth variations of SKS splitting parameters at station MDY shows relatively constant (a) lag time and (b) fast direction.

Similarly, the back-azimuth variations of local splitting parameters help to identify the presence of multiple layers and complex deformations at shallow depths. Since the local results are inherently complex in nature and varied in smaller scales, an accurate estimation can be problematic. Most of the stations of the central basin show no systematic variation (e.g. MS05, MS10, MP16, and MP20; see Appendix). Some stations show relatively constant lag times with random variation of fast directions [Fig-49]. On the other hand, eastern stations show some evidence of 90° periodicity [Fig-50a]. Few stations also show stable lag time with only E-W fast directions [Fig-50b]. This intricate nature of back-azimuth dependency again indicates the presence of a complex deformational fabric within the mantle wedge.

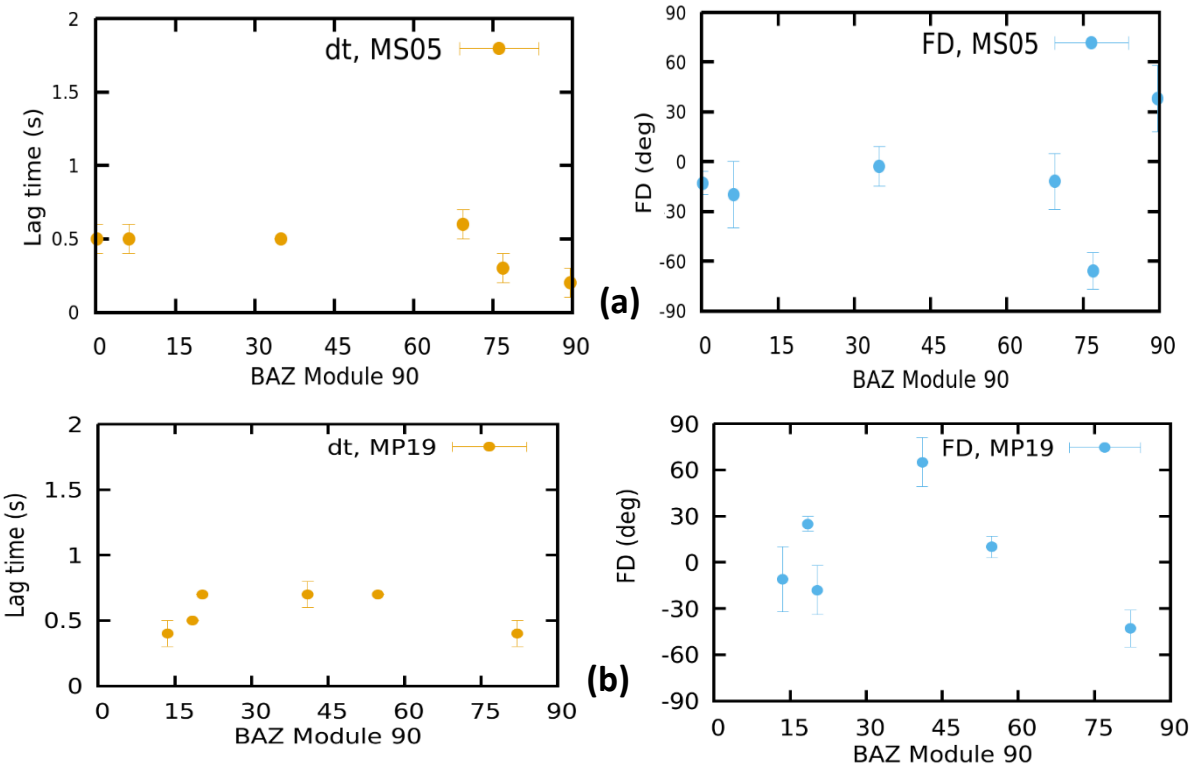

Figure 49: Back-azimuth variations of local splitting parameters at station showing relatively constant δt and variable φ; (a)MS05; and (b) MP19.

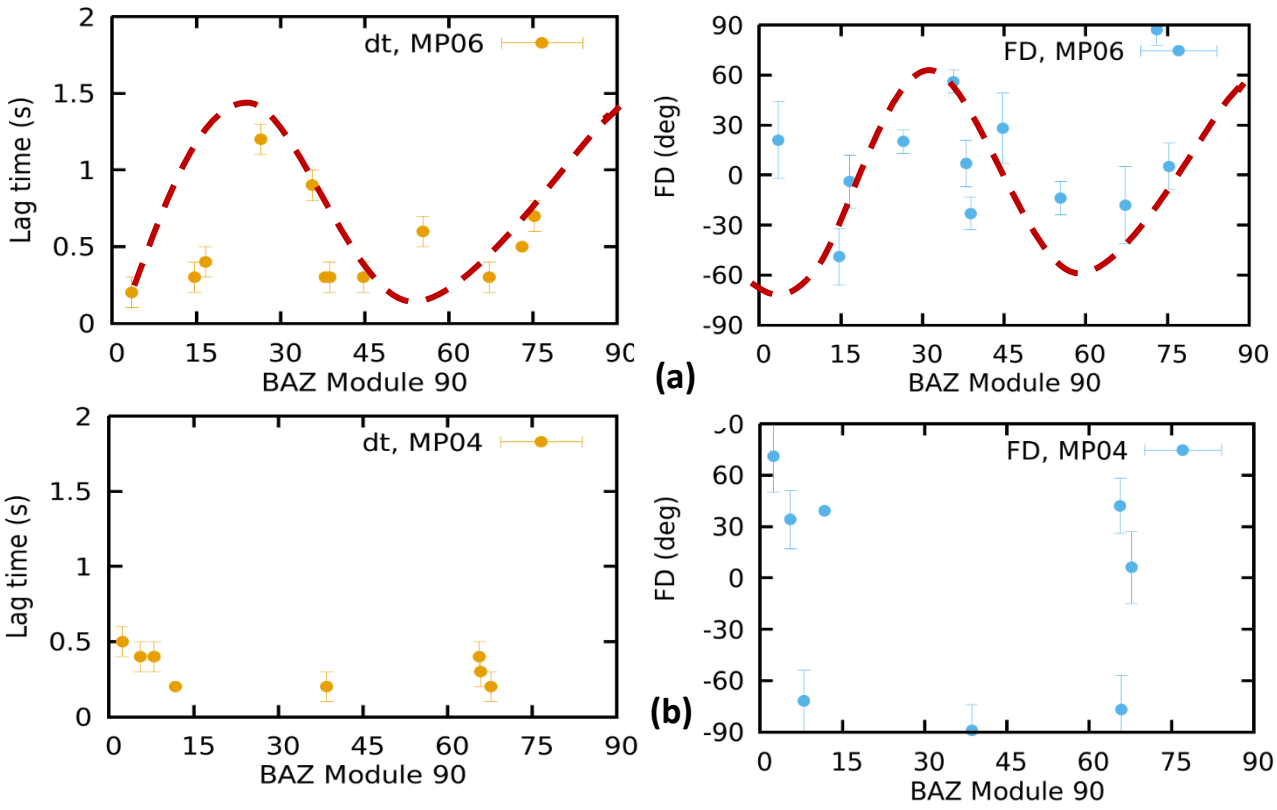

Figure 50: Back azimuth variations of local splitting parameters. Station (a)MP06 shows 90° periodicity and (b) MP04 shows only E-W fast direction.

SWST Results

Shear wave splitting tomography (SWST) helps to investigate the anisotropic fabric in detail. The final tomographic model consists of cubic blocks having a side length of 50 km, where the composition of each block is assumed to be 70% Olivine and 30% Orthopyroxene. Along with the experimental elastic constants and temperature-pressure derivatives, it represents the mantle mineralogy of the model space. In addition to the diagonal matrix [Fig-29], I have also tested the

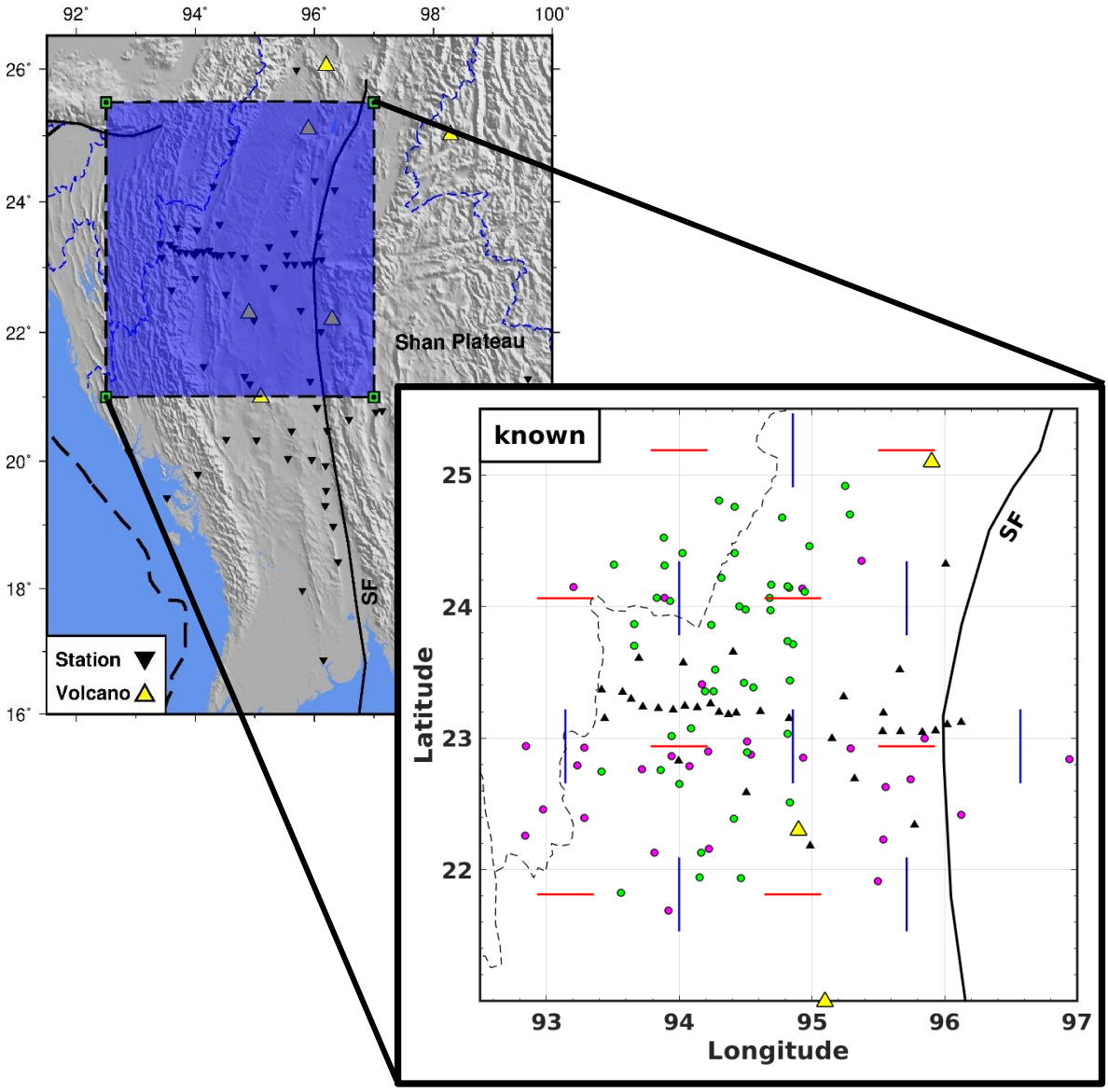

Figure 51: Model area (blue box) used in SWST inversion and the input model for the checkerboard test. SF-Sagaing Fault.

model resolution using a checkerboard test. The input synthetic model [Fig-51] is composed of alternating N-S (blue) and E-W (red) α-axis fabric. We see how well we can recover the input model after the inversion. Again, the average starting model has the best recovery after 50 iterations. The results are shown in Fig-52(b-e) from the depth of 0 to 400 km. Resolving power

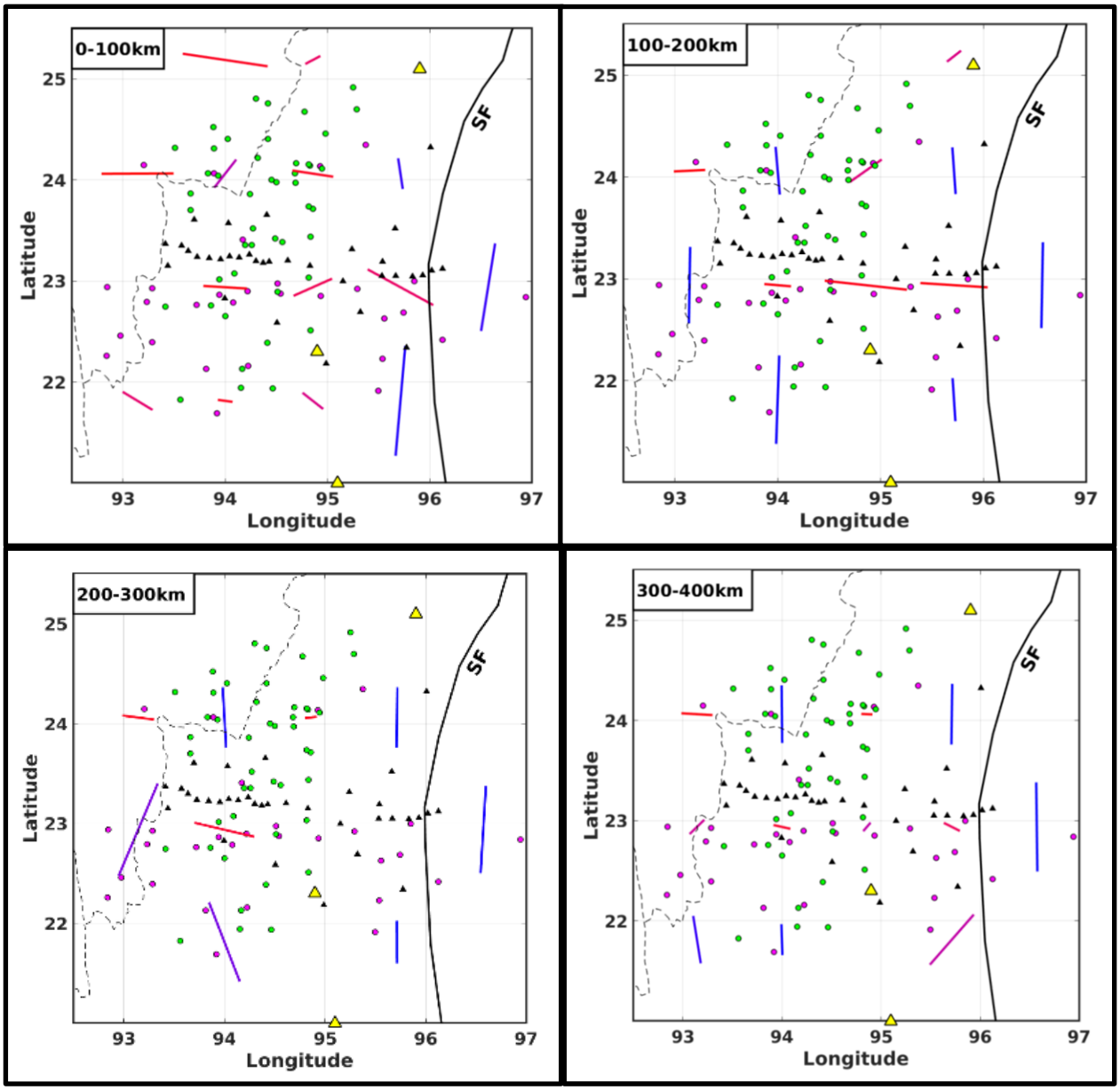

Figure 52: Checkerboard test results using real event station pairs; recovered results of depth (a) 0-100 km; (b) 100-200 km ; (c) 200-300 km; (d) 300-400 km, ray-paths that only sample the blocks are shown. Green and cyan circles are local and projected SKS hypocenter. Yellow triangles are the location of the Quaternary Volcanoes. SF-Sagaing Fault.

decreases gradually with depth and is concentrated close to the array. Within the 200 km depth range, the recovered model is good enough for meaningful interpretation. We have also recovered the synthetic model at deeper levels, especially for the N-S oriented α-axis [Fig-52cd]. Overall,

our model is less sensitive to the E-W α-axis fabric probably due to the geometry of our array and the splitting event distribution.

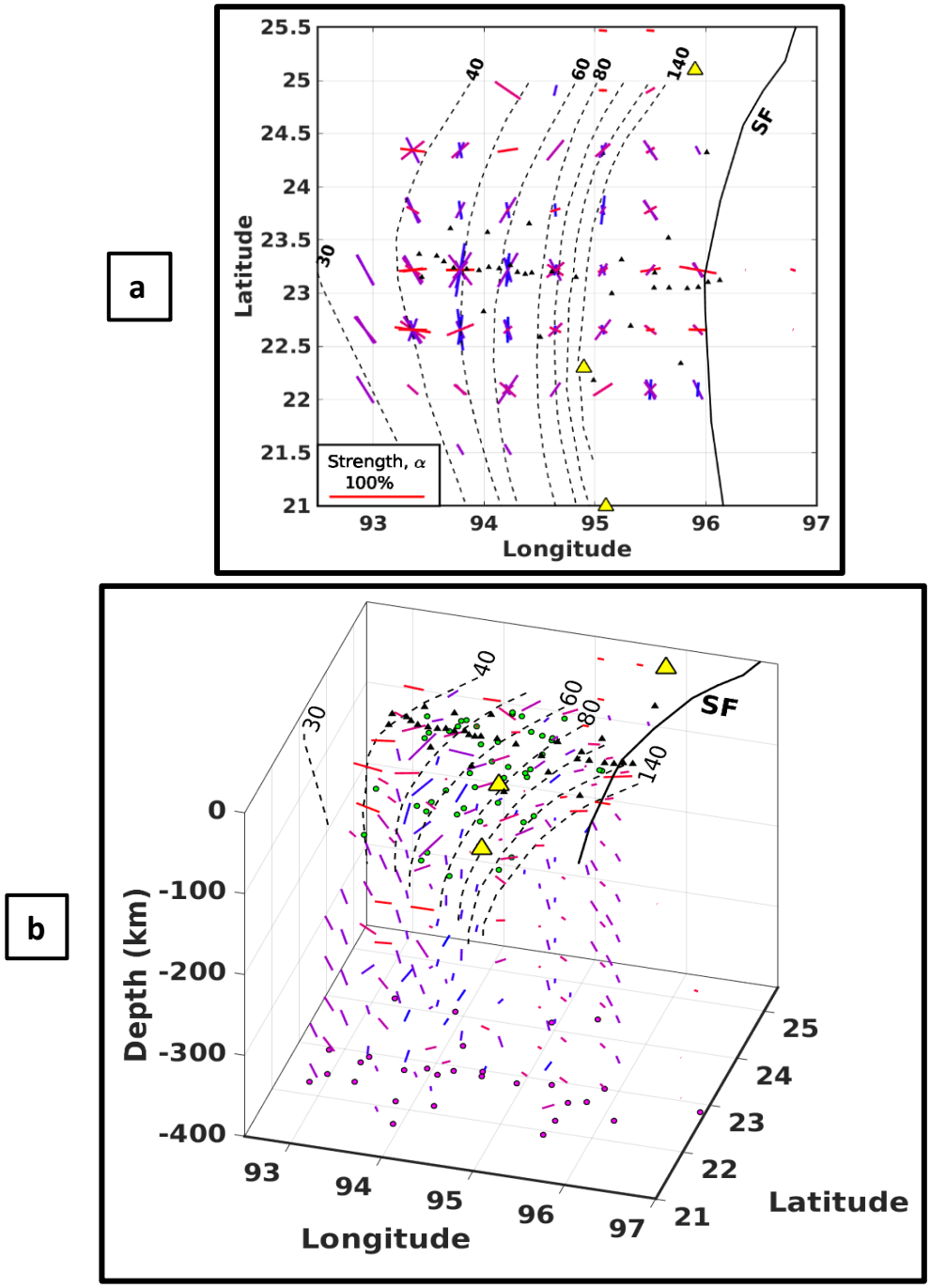

Figure 53: Final SWST results showing the orientation and strength of anisotropic fabric;(a) in map view; (b) 3D view; green and cyan circles are the local and projected SKS hypocenter; black and yellow triangles are location of stations and Quaternary volcanoes; black dotted lines are slab contour; SF-Sagging Fault.

Figure-53 shows the final inversion results combining 188 local and 29 SKS splitting measurements. The lack of local deep events on the southern part limits our model space to extend south of 21°N. The 3D vector represents the α-axis orientation (azimuth [θ] and dip [ψ]) and length represents the strength of anisotropy (α). The tomographic inversion shows the predominance of trench parallel α-axis fabric [Fig-53], especially in the western fore-arc region. Conversely, we can see a variable α-axis orientation and strength on the eastern part above the mantle wedge representing complex deformation fabrics. Figure 54-55 shows the individual depth slices up to 200 km, where our resolution is high enough for meaningful interpretation. Overall, the α-axis is oriented in the NNE direction on upper 50 km depth, parallel to the maximum principal stress directions revealed from the GPS (Steckler et al., 2016) observations. However, the assumption of mantle mineralogy on the crustal depth makes the 50km depth slice not well representative of the crustal anisotropy. 50-150 km depth slices [Fig 54b & 55a] show trench parallel α-axis orientation with higher anisotropic strength in the western part, where the slab surface reaches depths up to 60 km. This clearly indicates that the bulk of the anisotropy resides beneath the slab in the sub-slab region which produces >2.0s of lag time on SKS results. The entrained trench parallel mantle flow in the sub-slab region in response to slab rollback could produce such fabric (Long & Silver, 2008; Long 2013). This trench parallel α-axis strength decreases below the 150 km depth [Fig-55b]. This implies that the upper part of the sub-slab region is the primary source of anisotropy in the western fore-arc region.

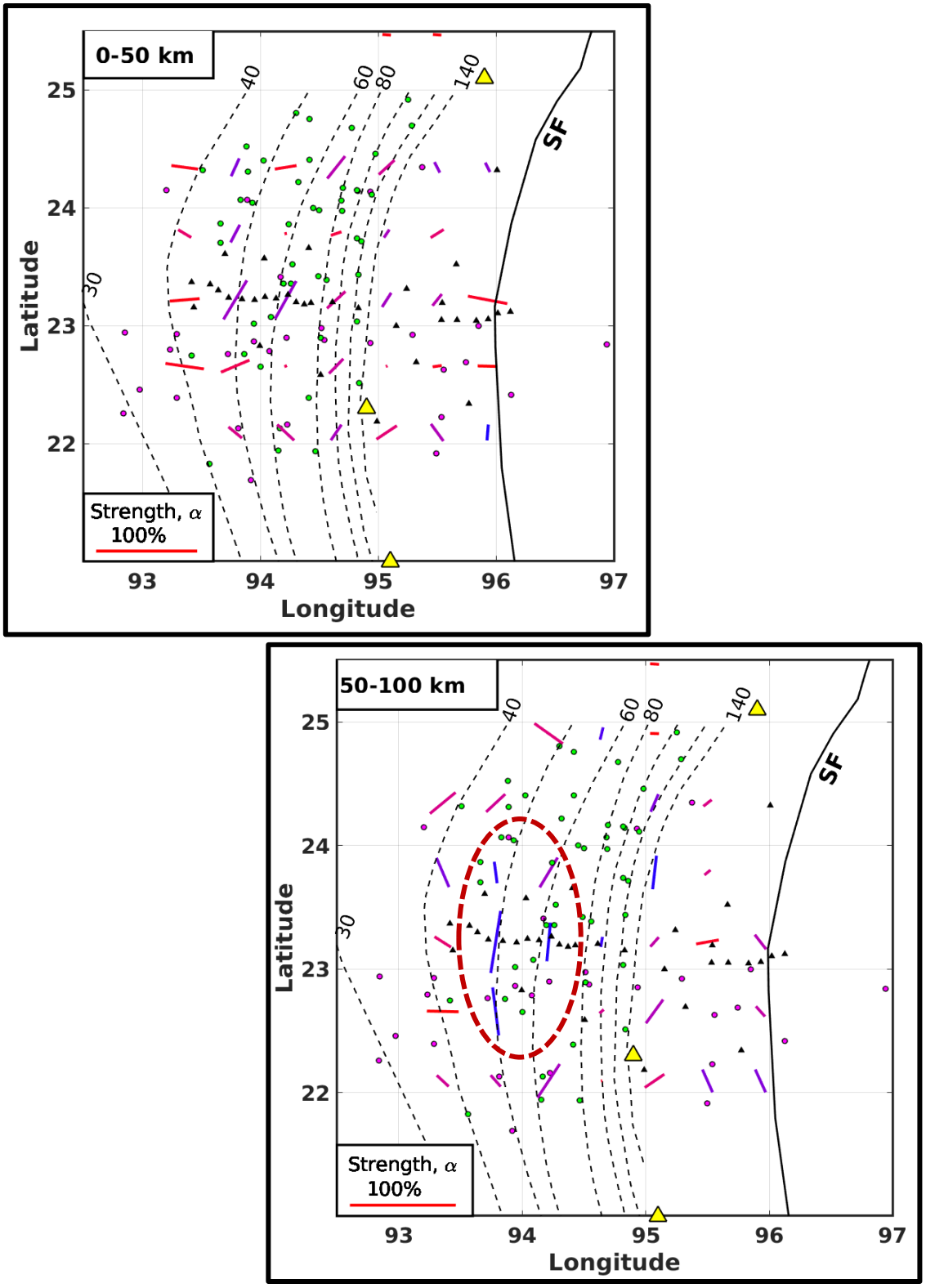

Figure 54: SWST results of the individual depth slices (a) 0-50 km; (b) 50-100 km. Red dotted circles are the region of high anisotropic strength; other legends are same as Fig-53.

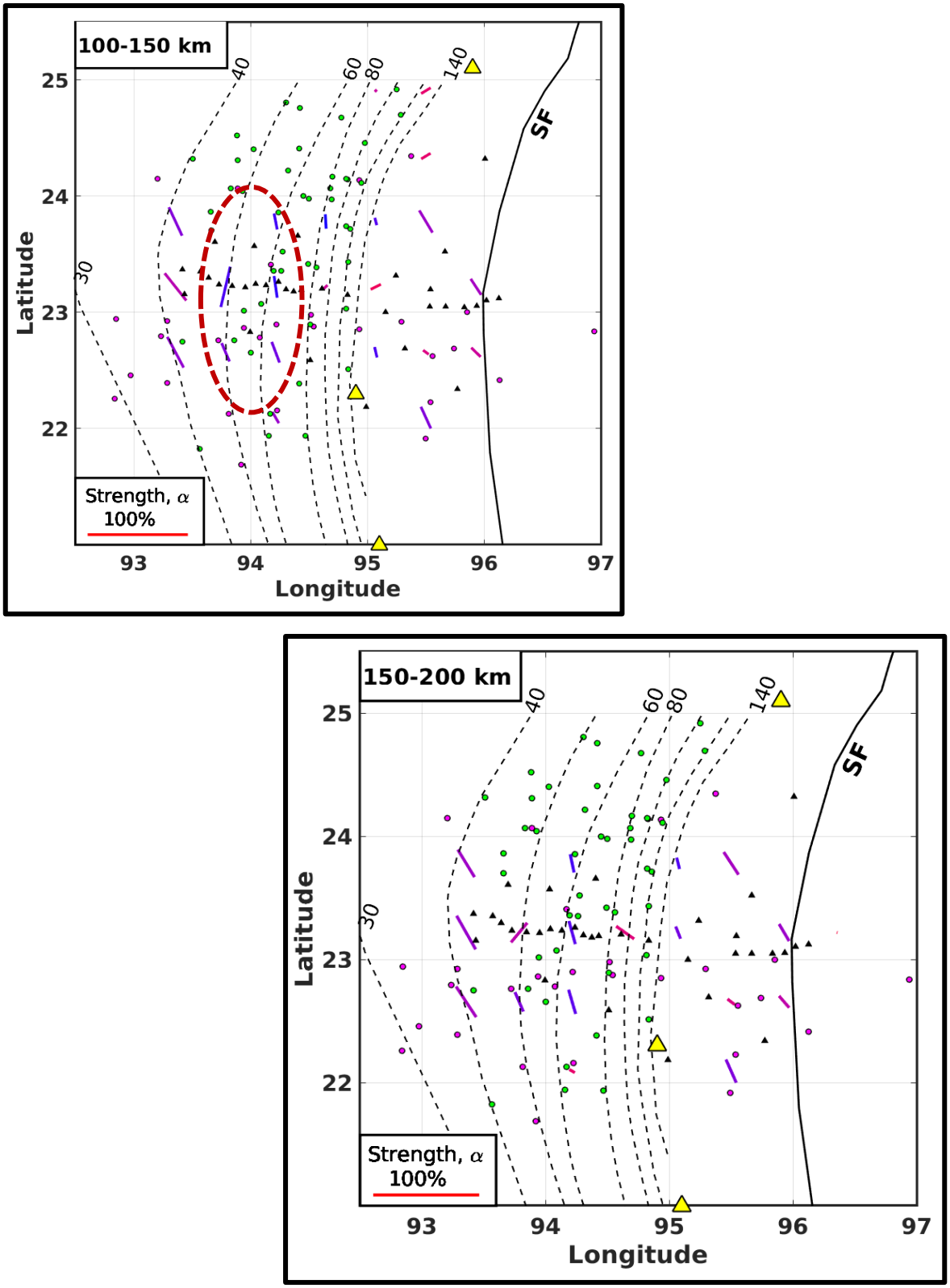

Figure 55: SWST results of the individual depth slices (a) 50-100 km; (b) 150-200 km. Red dotted circles are the region of high anisotropic strength; other legends are same as Fig-53.

On the other hand, we see a very different pattern on the eastern arc and back-arc region, where both the α-axis and strength are highly variable which cannot be explained by a simple wedge corner flow or poloidal flow above the slab (Long & Sliver, 2008; Long & Becker, 2010; Long 2013). There is clear evidence of changing the α-axis from N-S to NW-SE close to the back-arc

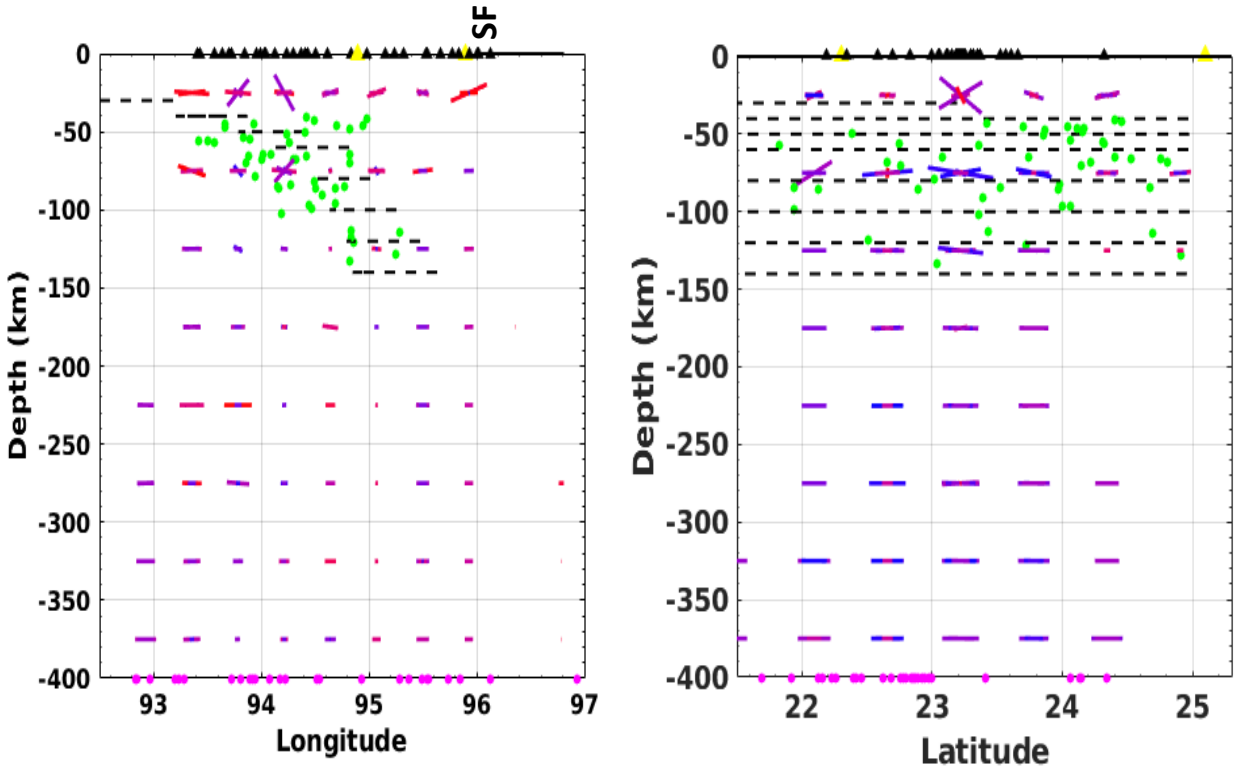

Figure 56: SWST results viewing (a) across longitude and (b) across latitude

region. We also see the decrease of anisotropic strength with depth [Fig-55ab], which indicates that the bulk of the anisotropy is in the upper part of the mantle wedge. We also found a similar result while analyzing the local splitting results of the deep events [Fig-39 & 40] and comparing them with the SKS results [Fig-41]. The E-W and N-S view [Fig-56] shows that both the sub-slab and wedge anisotropy have horizontal fabric.

Tectonic Implications

Filling the gap between the stable Indian Craton and South China Block, the SKS results enables us to infer the mantle deformation of the entire northern and eastern part of the Indian-Eurasian collision. After the clockwise rotation around the Eastern Himalayan Syntaxis (EHS) (Wang et al., 2008; León Soto et al., 2012; Chang et al., 2015), the fast polarization directions remains N-S throughout the entire length of the subduction zone [Fig-57 & 58], which seems to indicate the presence of vertical coherent deformation (VCD). However, the large differences of lag time

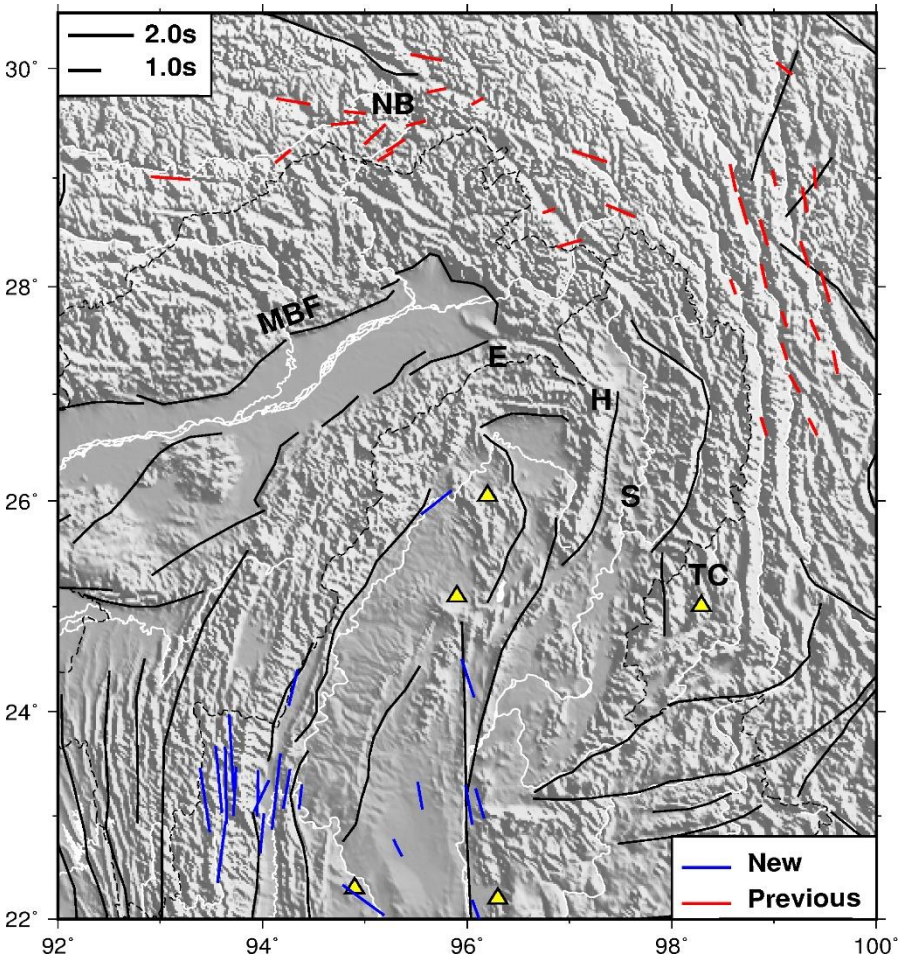

Figure 57: Comparison of SKS splitting results between the EHS and its southern part (our study area); EHS SKS splitting data are taken from McNamara et at., 1994; Sol et al., 2007; Wang et al., 2008; León Soto et al., 2012; Chang et al., 2015. MBF- Main Boundary Fault; TC- Tengchong volcanoes; NB- Namcha Barwa

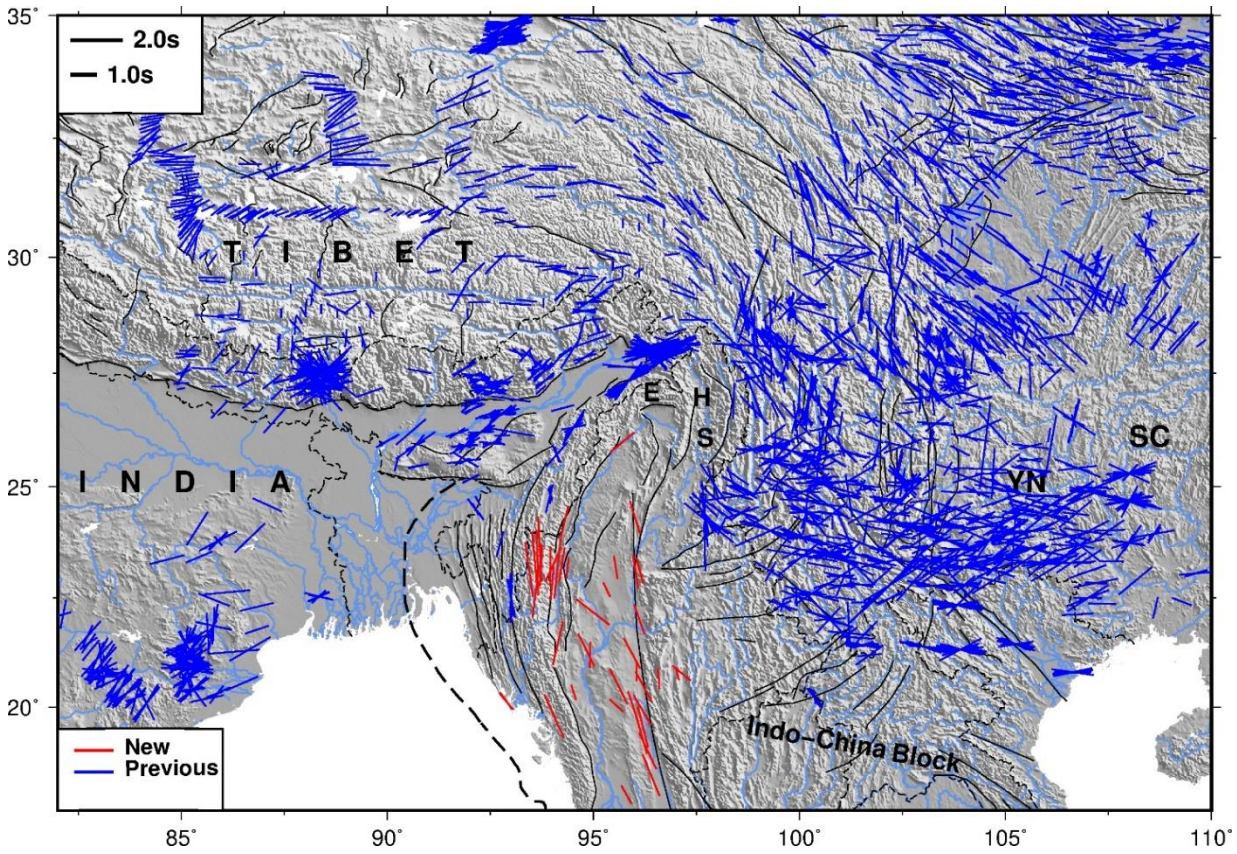

Figure 58: SKS splitting of Indo-Eurasian collisional belt integrated with newer results; previous results are from SWS the database (from Wüstefeld et. at., 2009; Liu et. al., 2014; Yang et. al., 2014; IRIS DMC, 2012*)*

(~>1.0 s) that exist between the EHS and IBR indicates the presence of additional subduction-related mechanism, inducing higher anisotropy on the southern part. Unlike the well-developed shear zones around the EHS (Ding et al., 2001, Zhang et al.,2004), thrusting and crustal shortening is the dominant mode of surface deformation, especially on the outer fold belt of IBR (Maurin & Rangin., 2009; Najman et al., 2020), implying that the coupling between the crust and mantle gradually reduces to the south. Since the fast direction remains N-S on the mantle wedge, some degree of coupling may exist on the mantle where the dextral component of the oblique convergence dominates.

From the observation of SKS splitting and SWST, we have seen evidence of trench parallel flow beneath the slab. Similar trench parallel flow in the sub-slab region has widely been observed in the other subduction zones worldwide (Russo & Silver., 1994; Long & Silver 2008., 2009) and predicted by numerical modeling (Faccenda & Capitanio., 2012, 2013; Schellart & Moresi., 2013; Becker & Faccenna., 2009). This leads to the sub-slab mantle flow model (Long & Becker, 2010), where the anisotropy is primarily controlled by the trench parallel 3D return flow induced by trench migration. Since the slab-trench system migrates relative to the upper mantle, sub-slab mantle is forced or "squeezed" around the slab edges and flows parallel to the trench.

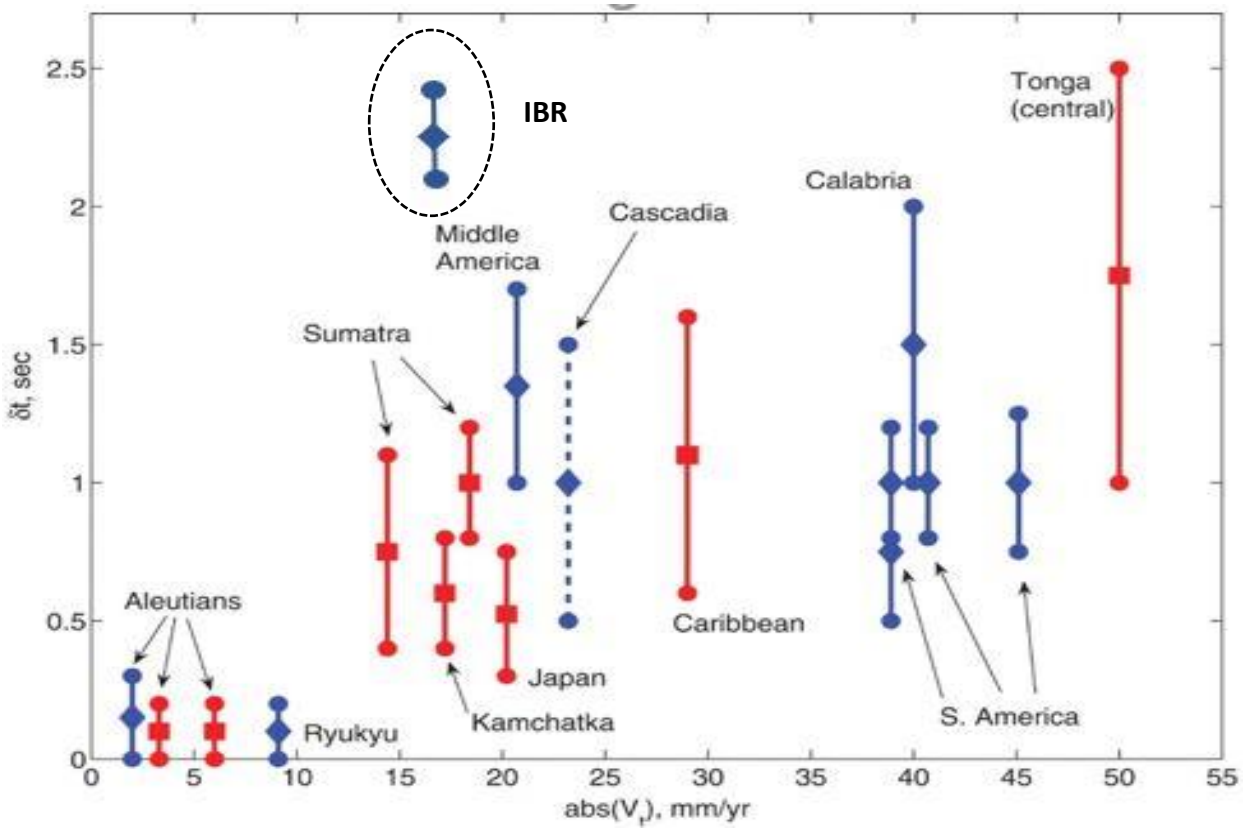

Figure 59: Relationship between the trench migration velocity and lag time of the subduction system (form Long & Silver, 2008) worldwide; red and blue lines are advancing and retreating trench respectively. This model assumes that the IBR trench migrates same rate as the average convergence velocity.

In addition, the existence of the flow barrier at the mantle transition zone (MTZ), the sub-slab mantle tends to flow parallel to the strike of the slab. Thus, the dominant trench parallel mantle fabric in the sub-slab region of the Indo-Burman subduction system arises due to the migration of

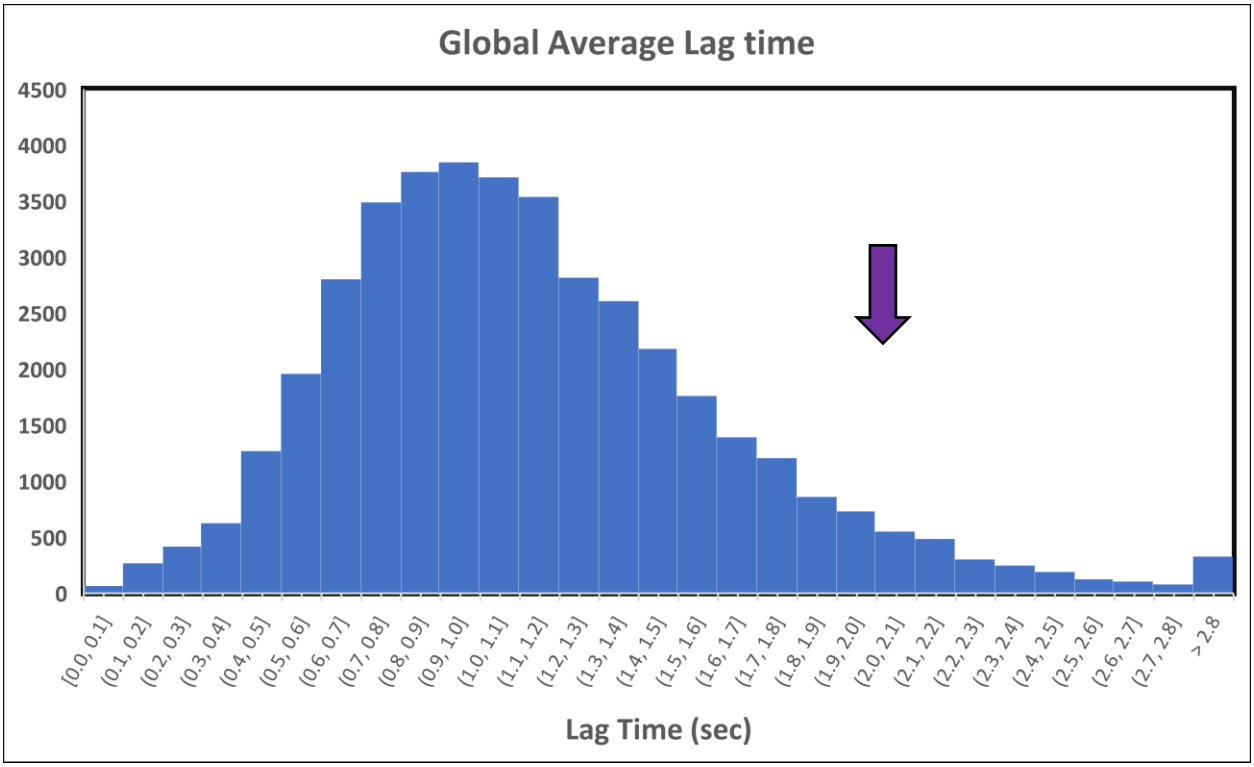

Figure 60: Histogram of average lag time from the global shear wave splitting database (Wüstefeld et. at., 2009; Liu et. al., 2014; Yang et. al., 2014; IRIS DMC, 2012); arrow shows the average lag time of sub-slab region of the Indo-Burman subduction system.

the slab-trench system. Lynner and Long (2014) also found a consistent relationship between the trench parallel fabric and older subducting oceanic slab (> 95Ma) due to the decoupling of the lithospheric mantle from the slab. The presence of older Indian oceanic [Fig-11, 95-120 Ma] (Müller et al., 2008) suggests that the lithospheric mantle has sufficient time to decouple and induce the trench parallel fabric.

Along with the trench parallel fast directions, Long and Silver found (2008) a positive correlation between the trench migration velocity and the lag time [Fig-60]. Both the advancing and retreating

trenches can produce a trench parallel flow around the slab. Several numerical models (Faccenda & Capitanio, 2012, 2013; Chen et al., 2016) shows that the development of toroidal flow is associated with a retreating slab. Westward migration of the trench is evident from the Neogene growth of the outer fold belt of the IBR (Karig et al., 1979; Hurukawa et al., 2010; Lohman., 1995). Indentation of Eurasia by the Indian plate and clockwise rotation (Curry, 2005; Acharya, 2006) would facilitate the rolling back process along with a rapid westward migration of the trench. Also, the arrival of the buoyant transitional or continental crust provides additional negative buoyancy for a rapidly sinking and rolling back slab. If 0.5 s of lag time can be attributed to the overlying thin mantle wedge and crust, we are still left with ~1.5s of lag time accumulated in the sub-slab region. Rolling back with the clockwise rotation could induce a strong toroidal flow around the slab, sufficient to produce the observed lag time.

Westerwheel et al. (2019) proposed a new finite plate motion model from the paleomagnetic data. According to this model, the significant clockwise rotation of Burma Terrane (BT) was initiated before the India-Eurasia collision (~80 and 50 Ma) where the subduction margin has not moved significantly relative to its present-day orientation. Later, the northward motion of BT was coupled with the Indian plate and formed the present configuration. According to this model, the slab retreat and subsequent westward migration of the trench initiated without rotation that induced the observed trench parallel fabric. However, this long northward motion would require a ~2000km long dextral movement along the east of the BT and the pathway of this paleo strike-slip system remains enigmatic. Also, the paleomagnetic data have errors (cone of confidence $\alpha 95$) that are more sensitive to the estimation of magnetic declinations and longitudes. The Quaternary arc volcanism and its compositional variations ranging from calc-alkaline to lherzolite along with the asthenospheric-derived melts (Lee et al., 2015) strongly suggest the rolling back of the Indian slab

from Miocene to present. The subducting Indian lithosphere could also accumulate N-S strain fabric due to the prolonged northward motion from late Cretaceous to Eocene.

On the mantle wedge, we see a complex deformational fabric with an average N-S fast axis. A simple 2D corner flow model (Long & Silver., 2008) in response to the subduction suction, would produce an E-W fabric close to the back-arc. The presence of higher anisotropic strength on the upper 100 km and similar δt value on both local and SKS splitting suggests the accumulation of wedge anisotropy. The difference of SKS lag time between the proximity of the Sagaing fault and the western wedge [Fig-62] indicates that oblique convergence with the dextral motions of BT could induce a significant anisotropy in the mantle wedge. Also, the presence of water and low-

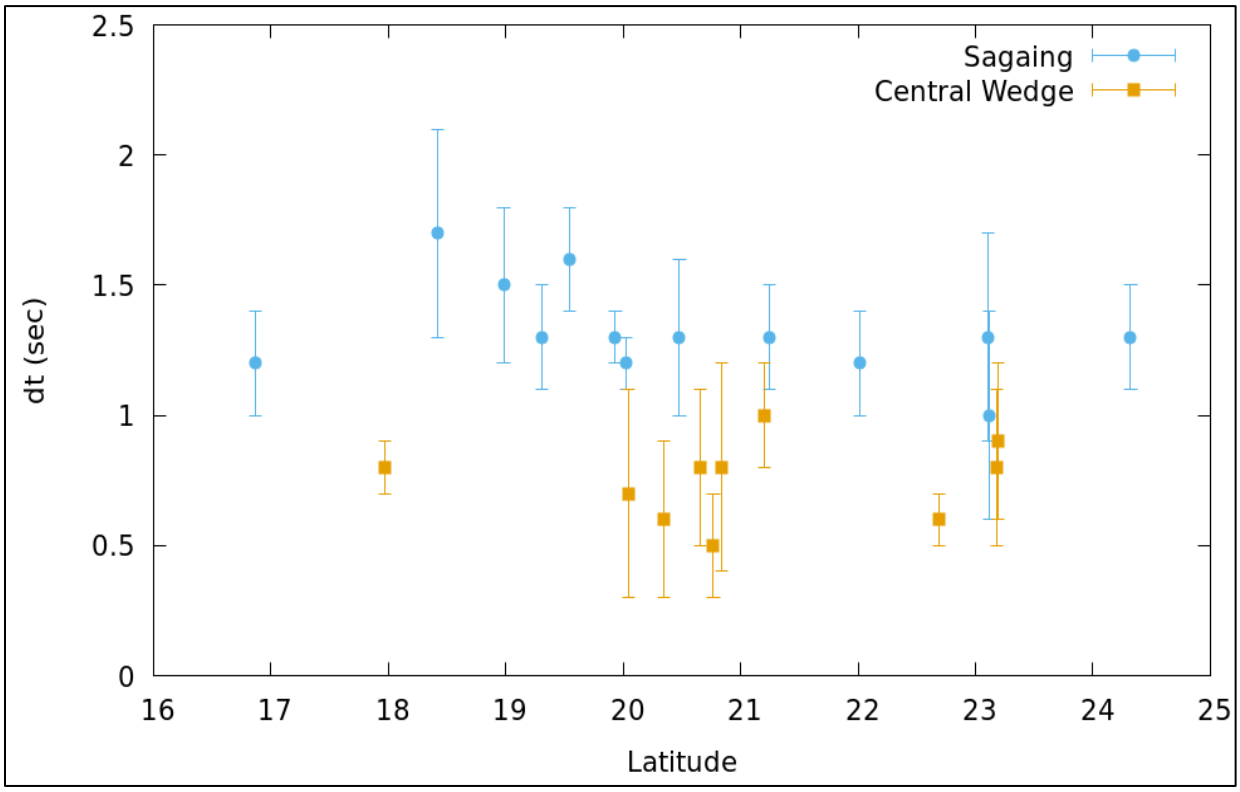

Figure 61: Comparison of δt between the central wedge and proximity of Sagaing fault (within 0.5° of the trace of Sagaing faults

temperature conditions (Kneller et al., 2005; Jung et al., 2006) of the fore-arc may favor the formation of B-type olivine fabrics that results in such complex splitting patterns. However, thick sediment input since the Oligocene would facilitate metamorphism and de-watering at the base of the overriding lithosphere (Curry et al., 2005; Steckel et al., 2016) and make the subduction zone unusually hot and dry.

We see the change of fast axis from N-S to NNW-SSW on the back-arc region that ultimately becomes E-W to NE-SW on the Yunnan province [Fig-59 & 63]. The null results in the southern part of the Shan plateau (EW08, KTN) suggests that a back-arc upwelling may exist in between this transition. Although the published tomographic models seem to demarcate the presence of hot mantle below the Shan Plateau (Huang et al., 2006; Wei et. al., 2012), without consistent geological evidence of back-arc extension and wider station coverage, it is difficult to constrain the presence and extent of such an upwelling. An alkaline mafic basaltic flow of Mio-Pliocene to Quaternary age has been recorded at the Singu volcanoes (Bender & Bannert, 1983; Maury et al., 2004) that could be related to this upwelling.

Further east in the Yunnan province, the fast directions become NE-SW (Huang et al., 2015) [Fig-63]. Although the NE-SW fast directions here are not quite aligned with the crustal deformation field inferred from the GPS and geological observations, the SKS splitting results are consistent with the maximum extension direction of the crust inverted from the GPS velocities, focal mechanisms, and geological observations (Wang et al., 2008; Zhao et al., 2013). The presence of thin lithosphere [< 80Km] (Pasyanos et al., 2014) does not explain the average high lag times (0.9-1.5 s) by mechanical coupling and asthenospheric flow extruded from the Tibet to eastern China (Wang et al., 2008; Cheng et al., 2015). Huang et al. (2015) proposed the existence of counter flow and slab retreat to explain the high lag time with NE-SW fast directions. My results are consistent

with the possible origin of smaller-scale counter flow with a back-arc upwelling in response to the subduction and subsequent slab retreat that produced the NE-SW fabrics.

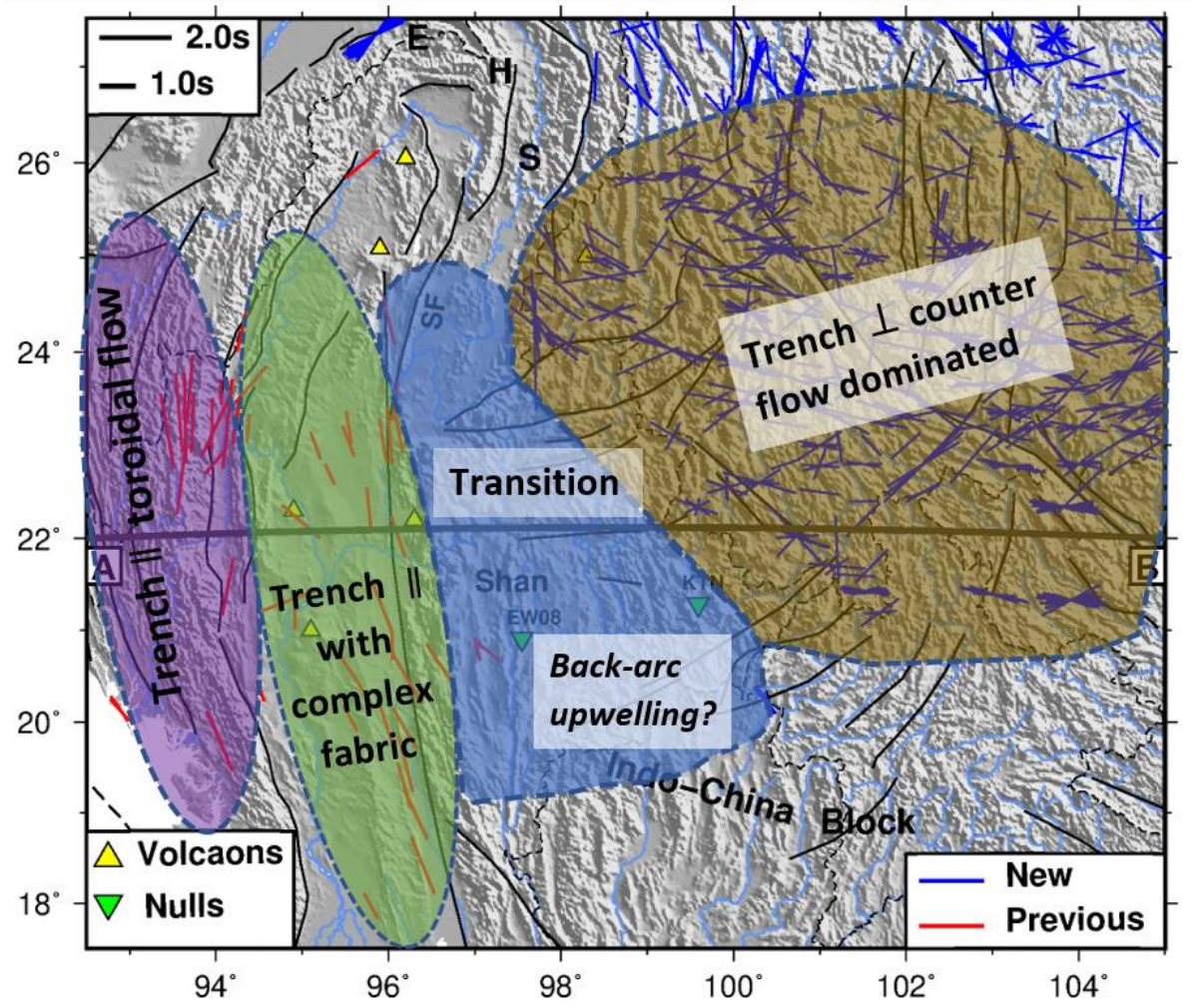

Figure 62: Shear wave splitting observations and associated mantle flow domains

The final SWS and SWST results along with the integration of the SKS splitting of the surrounding regions can reveal a complete picture of the mantle deformation fabric of the Indo-Burman subduction system and its geodynamic evolution. Rolling back of the subducting Indian slab produces the trench parallel toroidal flow. The dextral motion due to the oblique convergence induces the N-S anisotropic fabric on the wedge. The interaction between the classical 2D corner flow or weak poloidal flow with this N-S fabric results in the complex splitting pattern. The

transition between trench parallel to perpendicular fabrics lies to the east of the Sagaing fault where dextral motion diminishes. The nature of this transition and the presence of the back-arc upwelling remains enigmatic due to the lack of station coverage on the northern Shan Plateau. Finally, mantle convection due to the subduction and subsequent retreat induces trench perpendicular fabric that results the NE–SW fast direction in the mantle beneath the southern Yunnan.

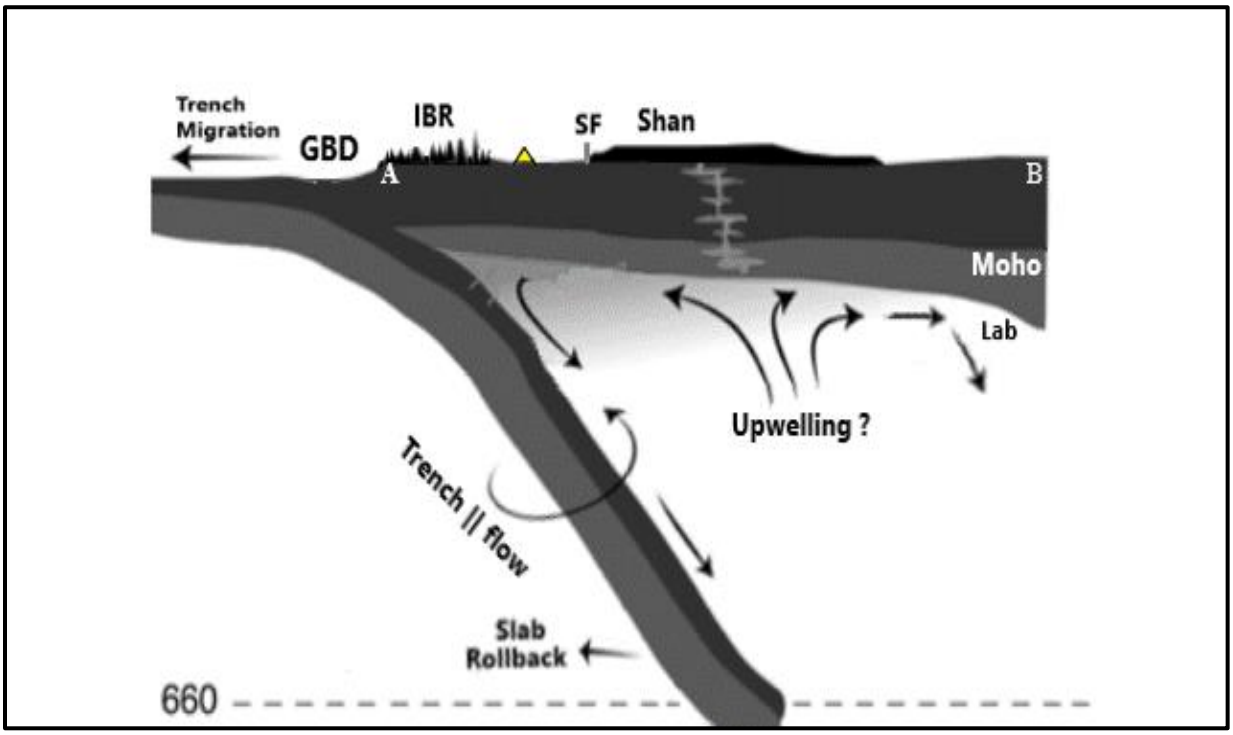

Figure 63: Schematic cross-section along the profile 'A-B ' [Fig-63] showing mantle flow models of the subducting Indian Slab. SF- Sagaing Fault

Conclusion

The study of the mantle deformational fabrics reveals the active nature of the oblique convergence between India and the Burma microplate. The presence of significant sub-slab splitting ruled out the stagnant slab with inactive subduction model (Rao & Kumar., 1999; Guzmán-Speziale & Ni., 2000). Similarly, over 2.0 s sub-slab splitting does not support the stationary slab-trench system (Westerwheel et al., 2019) with respect to the upper mantle as it will produce very little or no splitting. The slab retreat with trench migration can only be explained by the presence of toroidal trench-parallel flow around the slab that concentrates on the sub-slab region. However, the question still remains whether the suggested clockwise rotation around the EHS facilitated the slab retreat in the Late Cenozoic. More geological, geophysical, and paleomagnetic observation is necessary to better understand the rotation dynamics.

Integrating with the published SKS results, I found little evidence of VCD, especially on the IBR. The sub-slab mantle of the subducting older lithosphere may have decoupled from the overlying crust. The mantle wedge close to the EHS (~> 24°N) might suffer from some degree of coupling where the lag times are similar to the EHS. A future investigation, including the southern and southeastern part of EHS, may reveal the complete picture of the VCD.

The mantle wedge is highly anisotropic with an average lag time of ~0.5 s to 1 s and shows complex deformational fabrics which is difficult to explain with 2D corner flow. The dextral motion due to the oblique convergence produces a dominant N-S fabric. In addition, the weak poloidal flow and B-type olivine fabric might present and shape the deformation fabrics of the mantle wedge. Analysis of more local deep events with wider spatial coverage will produce a

robust tomographic model that will help to isolate the anisotropic zonation in the mantle wedge and the underlying mechanisms.

Finally, a small-scale counter flow could possibly be generated in response to the retreating of the subducting slab. This could induce back-arc upwelling as evidenced by the presence of nulls in Shan and E-W to NE-SW fast direction in southern Yunnan. The Mio-Pliocene to Quaternary alkaline volcanism and the presence of hot mantle could be related to such upwelling. Along with comprehensive seismological study, SWS observation with dense station coverage in the Shan Plateau could help to better understand the nature of the transition of mantle fabric and the back-arc upwelling model.

References

Abramson, E. H., Brown, J. M., Slutsky, L. J., & Zaug, J. (1997). The elastic constants of San Carlos olivine to 17 GPa. Journal of Geophysical Research: Solid Earth, 102(B6), 12253-12263.

Abt, D. L., & Fischer, K. M. (2008). Resolving three-dimensional anisotropic structure with shear wave splitting tomography. Geophysical Journal International, 173(3), 859-886.

Acharya, S. K. (2006), Collisional emplacement history of the Naga-Andaman ophiolites and the position of the eastern Indian suture, J. Asian Earth Sci., 29, 229–242, doi:10.1016/j.jseaes.2006.03.003

Acharyya, Subhrangsu. (2008). Tectonic evolution of Indo-Burma Range with special reference to Naga-Manipur Hills. Geol. Soc. India Memoir. 75.

Allen, R., Najman, Y., Carter, A., Barfod, D., Bickle, M. J., Chapman, H. J., ... & Parrish, R. R. (2008). Provenance of the Tertiary sedimentary rocks of the Indo-Burman Ranges, Burma (Myanmar): Burman arc or Himalayan-derived? Journal of the Geological Society, 165(6), 1045-1057.

Anderson, O. L., & Isaak, D. G. (1995). Elastic constants of mantle minerals at high temperature. Mineral Physics and crystallography: a handbook of physical constants, 2, 64-97.

Ando, M., Ishikawa, Y., & Yamazaki, F. (1983). Shear wave polarization anisotropy in the upper mantle beneath Honshu, Japan. Journal of Geophysical Research: Solid Earth, 88(B7), 5850-5864.

Becker, T.W., Faccenna, C. (2009). A review of the role of subduction dynamics for regional and global plate motions. In: Lallemand, S., Funiciello, F. (Eds.), Subduction Zone Geodynamics. Springer, pp. 3–34.

Bender, F., & Bannert, D. (1983). Geology of Burma.

Bertrand, G., & Rangin, C. (2003). Tectonics of the western margin of the Shan plateau (central Myanmar): implication for the India–Indochina oblique convergence since the Oligocene. Journal of Asian Earth Sciences, 21(10), 1139-1157.

Betka, P.M., Seeber, L., Thomson, S.N., Steckler, M.S., Sincavage, R., Zoramthara, C., 2018. Slip-partitioning above a shallow, weak decollement beneath the Indo-Burman accretionary prism. Earth Planet. Sci. Lett.503, 17–28.

Bijwaard, H., W. Spakman, and E. R. Engdahl (1998), Closing the gapbetween regional and global travel time tomography, J. Geophys. Res., 103, 30,055– 30,078.

Bowman JR, Ando M (1987) Shear-wave splitting in the upper-mantle wedge above the Tonga subduction zone. Geophys J Roy Astr Soc 88:25–41

Brune, J. N., Curray, J., Dorman, L., & Raitt, R. (1992). A proposed super-thick sedimentary basin, Bay of Bengal. *Geophysical Research Letters*, *19*(6), 565-568.

Bystricky, M., Kunze, K., Burlini, L., & Burg, J. P. (2000). High shear strain of olivine aggregates: Rheological and seismic consequences. Science, 290(5496), 1564-1567.

Crampin, S., & Lovell, J. H. (1991). A decade of shear-wave splitting in the Earth's crust: what does it mean? what use can we make of it? and what should we do next?. Geophysical Journal International, 107(3), 387-407.

Calixto, F. J., Robinson, D., Sandvol, E., Kay, S., Abt, D., Fischer, K., ... & Alvarado, P. (2014). Shear wave splitting and shear wave splitting tomography of the southern Puna plateau. Geophysical Journal International, 199(2), 688-699.

Chang, L., Flesch, L.M., Wang, C., Ding, Z., 2015. Vertical coherence of deformation in lithosphere in the eastern Himalayan syntaxis using GPS, Quaternary fault slip rates, and shear wave splitting data. Geophys. Res. Lett.42, 5813–5819.

Chen, Z., Schellart, W. P., Strak, V., & Duarte, J. C. (2016). Does subduction-induced mantle flow drive backarc extension?. Earth and Planetary Science Letters, 441, 200-210.

Chevrot, S. (2000). Multichannel analysis of shear wave splitting. Journal of Geophysical Research: Solid Earth, 105(B9), 21579-21590.

Christensen, N. I. (1984). The magnitude, symmetry and origin of upper mantle anisotropy based on fabric analyses of ultramafic tectonites. Geophysical Journal International, 76(1), 89-111.

Clark, M. K., and L. H. Royden (2000), Topographic ooze: Building the eastern margin of Tibet by lower crustal flow, Geology, 28, 703–706.

Curray, J. R., Moore, D. G., Lawver, L. A., Emmel, F. J., Raitt, R. W., Henry, M., & Kieckhefer, R. (1979). Tectonics of the Andaman Sea and Burma: convergent margins.

Curray, J. R. (2005), Tectonics and history of the Andaman Sea region, J. Asian Earth Sci., 25, 187–232, doi:10.1016/j.jseaes.2004.09.001.

Curray, J. R. (2014). The Bengal depositional system: from rift to orogeny. Marine Geology, 352, 59-69.

Crampin, S. (1987). Geological and industrial implications of extensive-dilatancy anisotropy. Nature, 328(6130), 491-496.

Crampin, S. (1991). Wave propagation through fluid-filled inclusions of various shapes: interpretation of extensive-dilatancy anisotropy. Geophysical Journal International, 104(3), 611-623.

Ding, L., Zhong, D., Yin, A., Kapp, P., & Harrison, T. M. (2001). Cenozoic structural and metamorphic evolution of the eastern Himalayan syntaxis (Namche Barwa). *Earth and Planetary Science Letters*, *192*(3), 423-438.

Faccenda, M., and Capitanio, F. A. (2012), Development of mantle seismic anisotropy during subduction-induced 3-D flow, Geophys. Res. Lett., 39, L11305, doi:10.1029/2012GL051988.

Faccenda, M., and Capitanio, F. A. (2013), Seismic anisotropy around subduction zones: Insights from three-dimensional modeling of upper mantle deformation and SKS splitting calculations, Geochem. Geophys. Geosyst., 14, 243– 262, doi:10.1002/ggge.20055.

Fielding, E., Isacks, B., Barazangi, M., & Duncan, C. (1994). How flat is Tibet?. Geology, 22(2), 163-167.

Fischer, K. M., Parmentier, E. M., Stine, A. R., & Wolf, E. R. (2000). Modeling anisotropy and plate-driven flow in the Tonga subduction zone back arc. Journal of Geophysical Research: Solid Earth, 105(B7), 16181-16191

Fitch, T. J. (1972). Plate convergence, transcurrent faults, and internal deformation adjacent to southeast Asia and the western Pacific. Journal of Geophysical research, 77(23), 4432-4460.

Flesch, L., Holt, W., Silver, P., Stephenson, M., Wang, C., Chan, W., 2005. Constraining the extent of crust–mantle coupling in central Asia using GPS, geologic, and shear wave splitting data. Earth Planet. Sci. Lett.238, 248–268

Frisillo, A. L., & Barsch, G. R. (1972). Measurement of single-crystal elastic constants of bronzite as a function of pressure and temperature. Journal of Geophysical Research, 77(32), 6360-6384.

Furnes, H., Dilek, Y., Zhao, G., Safonova, I., & Santosh, M. (2020). Geochemical characterization of ophiolites in the Alpine-Himalayan Orogenic Belt: Magmatically and tectonically diverse evolution of the Mesozoic Neotethyan oceanic crust. *Earth-Science Reviews*, 103258.

Gahalaut, V. K., Kundu, B., Laishram, S. S., Catherine, J., Kumar, A., Singh, M. D., ... & Mahesh, P. (2013). Aseismic plate boundary in the Indo-Burmese wedge, northwest Sunda Arc. *Geology*, *41*(2), 235-238.

Gan, W., Zhang, P., Shen, Z.-K., Niu, Z., Wang, M., Wan, Y., Zhou, D., Cheng, J., 2007. Present-day crustal motion within the Tibetan Plateau inferred from GPS measurements. J. Geophys. Res.112, B08416.

Greve, S. M., & Savage, M. K. (2009). Modelling seismic anisotropy variations across the Hikurangi subduction margin, New Zealand. Earth and Planetary Science Letters, 285(1-2), 16-26.

Guzmán-Speziale, M., & Ni, J. F. (2000). Comment on “Subduction in the Indo-Burma region: Is it still active?” Geophysical Research Letters, 27(7), 1065-1066.

Hansen, L. N., Zhao, Y. H., Zimmerman, M. E., & Kohlstedt, D. L. (2014). Protracted fabric evolution in olivine: Implications for the relationship among strain, crystallographic fabric, and seismic anisotropy. *Earth and Planetary Science Letters*, *387*, 157-168.

Hess, H. H. (1964). Seismic anisotropy of the uppermost mantle under oceans. Nature, 203(4945), 629-631.

Hu, X., Garzanti, E., Wang, J., Huang, W., An, W., & Webb, A. (2016). The timing of India-Asia collision onset—Facts, theories, controversies. Earth-Science Reviews, 160, 264–299.

Huang, J., & Zhao, D. (2006). High-resolution mantle tomography of China and surrounding regions. Journal of Geophysical Research: Solid Earth, 111(B9).

Huang, Z., Wang, L., Xu, M., Liu, J., Mi, N., Liu, S., 2007. Shear wave splitting across the Ailao Shan–Red River fault zone, SW China. Geophys. Res. Lett.34, L20301.

Huang, Z., Wang, L., Zhao, D., Mi, N., Xu, M., 2011. Seismic anisotropy and mantle dynamics beneath China. Earth Planet. Sci. Lett.306, 105–117.

Huang, Z., Wang, L., Xu, M., Ding, Z., Wu, Y., Wang, P., . . . Li, H. (2015). Teleseismic shear-wave splitting in SE tibet: Insight into complex crust and upper-mantle deformation. Earth and Planetary Science Letters, 432, 354-362. doi:10.1016/j.epsl.2015.10.027

Hurukawa, N., & Maung Maung, P. (2011). Two seismic gaps on the Sagaing Fault, Myanmar, derived from relocation of historical earthquakes since 1918. Geophysical Research Letters, 38(1).

Hurukawa, N., Tun, P. P., & Shibazaki, B. (2012). Detailed geometry of the subducting Indian Plate beneath the Burma Plate and subcrustal seismicity in the Burma Plate derived from joint hypocenter relocation. Earth, planets and space, 64(4), 333-343.

Ismaıl, W. B., & Mainprice, D. (1998). An olivine fabric database: an overview of upper mantle fabrics and seismic anisotropy. Tectonophysics, 296(1-2), 145-157.

IRIS DMC (2012), Data Services Products: SWS-DBs Shear-wave splitting databases, https://doi.org/10.17611/DP/SWS.1.

Jung, H., & Karato, S. I. (2001). Water-induced fabric transitions in olivine. Science, 293(5534), 1460-1463.

Jung, H., Katayama, I., Jiang, Z., Hiraga, T., & Karato, S. I. (2006). Effect of water and stress on the lattice-preferred orientation of olivine. Tectonophysics, 421(1-2), 1-22.

Jung, H., Mo, W., & Green, H. W. (2009). Upper mantle seismic anisotropy resulting from pressure-induced slip transition in olivine. Nature Geoscience, 2(1), 73-77.

Karato, S. I., Jung, H., Katayama, I., & Skemer, P. (2008). Geodynamic significance of seismic anisotropy of the upper mantle: new insights from laboratory studies. *Annu. Rev. Earth Planet. Sci.*, *36*, 59-95.

Keith, C. M., & Crampin, S. (1977). Seismic body waves in anisotropic media: synthetic seismograms. Geophysical Journal International, 49(1), 225-243.

Kennett, B. L. N. (1991). The removal of free surface interactions from three-component seismograms. Geophysical Journal International, 104(1), 153-163.

Kennett, B. L., Engdahl, E. R., & Buland, R. (1995). Constraints on seismic velocities in the Earth from traveltimes. Geophysical Journal International, 122(1), 108-124.

Khin, K., Zaw, K., & Aung, L. T. (2017). Geological and tectonic evolution of the Indo-Myanmar Ranges (IMR) in the Myanmar region. *Geological Society, London, Memoirs*, *48*(1), 65-79.

Klein, F. W. (1978). Hypocenter location program HYPOINVERSE. U.S. Geol. Surv. OpenFile Report. 78-694.

Klein, F. W. (1985). HYPOINVERSE, a program for VAX and professional 350 computers to solve the earthquake locations. U.S. Geological Survey Open-File Report 85-515, 53 pp.

Klein, F. W. (2003). The HYPOINVERSE2000 earthquake location program. In: Lee, W. H. K., Kanamori, H., Jennings, P. C., and Kisslinger, C. (Eds.) (2003), 1619-1620

Klootwijk, C., Sharma, M. L., Gergan, J., Tirkey, B., Shah, S. K., & Agarwal, V. (1979). The extent of Greater India, II. Palaeomagnetic data from the Ladakh intrusives at Kargil, northwestern Himalayas. Earth and Planetary Science Letters, 44(1), 47-64.

Kneller, E. A., Van Keken, P. E., Karato, S. I., & Park, J. (2005). B-type olivine fabric in the mantle wedge: Insights from high-resolution non-Newtonian subduction zone models. Earth and Planetary Science Letters, 237(3-4), 781-797.

Kumar, A., Mitra, S., & Suresh, G. (2015). Seismotectonics of the eastern Himalayan and Indo-Burman plate boundary systems. Tectonics, 34(11), 2279-2295.

Karig, D. E., Suparka, S., Moore, G. F., & Hehanussa, P. E. (1979). Structure and Cenozoic Evolution of the Sunda Arc in the Central Sumatra Region: Convergent Margins.

Kreemer, C., Blewitt, G., & Klein, E. C. (2014). A geodetic plate motion and Global Strain Rate Model. Geochemistry, Geophysics, Geosystems, 15, 3849–3889. https://doi.org/10.1002/2014GC005407

Lee, H. Y., Chung, S. L., & Yang, H. M. (2016). Late Cenozoic volcanism in central Myanmar: Geochemical characteristics and geodynamic significance. Lithos, 245, 174-190.

León Soto, G., Sandvol, E., Ni, J. F., Flesch, L., Hearn, T. M., Tilmann, F., ... & Brown, L. D. (2012). Significant and vertically coherent seismic anisotropy beneath eastern Tibet. Journal of Geophysical Research: Solid Earth, 117(B5).

Lev, E., Long, M.D., Vanderhilst, R., 2006. Seismic anisotropy in Eastern Tibet from shear wave splitting reveals changes in lithospheric deformation. Earth Planet. Sci. Lett.251, 293–304.

Liang, S., Gan, W., Shen, C., Xiao, G., Liu, J., Chen, W., Ding, X., and Zhou, D. (2013), Three-dimensional velocity field of present-day crustal motion of the Tibetan Plateau derived from GPS measurements, J. Geophys. Res. Solid Earth, 118, 5722– 5732, doi:10.1002/2013JB010503.

Liu, K.H., A. Elsheikh, A. Lemnifi, U. Purevsuren, M. Ray, H. Refayee, B. Yang, Y. Yu, and S.S. Gao (2014), A uniform database of teleseismic shear wave splitting measurements for the western and central United States, Geochemistry Geophysics Geosystems , https://doi.org/10.1002/2014GC005267

Liu, C. Z., Chung, S. L., Wu, F. Y., Zhang, C., Xu, Y., Wang, J. G., ... & Guo, S. (2016). Tethyan suturing in Southeast Asia: Zircon U-Pb and Hf-O isotopic constraints from Myanmar ophiolites. Geology, 44(4), 311-314.

Lohmann, H. H. (1995), On the tectonics of Bangladesh, Bull. Ver. Schweiz. Pet. Geol. Ing., 62(140), 29–48.

Long, M. D., & Silver, P. G. (2008). The subduction zone flow field from seismic anisotropy: A global view. science, 319(5861), 315-318.

Long, M. D., & Silver, P. G. (2009). Shear wave splitting and mantle anisotropy: Measurements, interpretations, and new directions. Surveys in Geophysics, 30(4), 407-461.

Long, M. D., and P. G. Silver (2009), Mantle flow in subduction systems: The sub-slab flow field and implications for mantle dynamics, J. Geophys. Res., 114, B10312, doi:10.1029/2008JB006200.

Long, M. D., & Becker, T. W. (2010). Mantle dynamics and seismic anisotropy. Earth and Planetary Science Letters, 297(3-4), 341-354.

Long, M. D. (2013). Constraints on subduction geodynamics from seismic anisotropy. Reviews of Geophysics, 51(1), 76-112.

Mainprice, D., Barruol, G., & Ismail, W. B. (2000). The seismic anisotropy of the Earth's mantle: from single crystal to polycrystal. Geophysical monograph-American Geophysical Union, 117, 237-264.

Mainprice, D. (2010). 2.16 Seismic anisotropy of the deep Earth from a mineral and rock physics perspective. Treatise on Geophysics, Volume 2: Mineral Physics, 437.

Mallick, R., Lindsey, E. O., Feng, L., Hubbard, J., Banerjee, P., & Hill, E. M. (2019). Active convergence of the india-burma-sunda plates revealed by a new continuous GPS network. Journal of Geophysical Research: Solid Earth, 124(3), 3155-3171. doi:10.1029/2018JB016480

Maury, R. C., Pubellier, M., Rangin, C., Wulput, L., Cotten, J., Socquet, A., ... & Htun, H. M. (2004). Quaternary calc-alkaline and alkaline volcanism in an hyper-oblique convergence setting, central Myanmar and western Yunnan. Bulletin de la Société Géologique de France, 175(5), 461-472.

Maurin, T., & Rangin, C. (2009). Structure and kinematics of the Indo-Burmese Wedge: Recent and fast growth of the outer wedge. Tectonics, 28(2).

Maurin, T., Masson, F., Rangin, C., Min, U. T., & Collard, P. (2010). First global positioning system results in northern Myanmar: Constant and localized slip rate along the Sagaing fault. Geology, 38(7), 591-594.

McCaffrey, R. (1992). Oblique plate convergence, slip vectors, and forearc deformation. Journal of Geophysical Research: Solid Earth, 97(B6), 8905-8915.

McNamara, D. E., T. J. Owens, P. G. Silver, and F. T. Wu (1994), Shear wave anisotropy beneath the Tibetan Plateau, J. Geophys. Res., 99, 13,655–13,665, doi:10.1029/93JB03406

Mehl, L., Hacker, B. R., Hirth, G., & Kelemen, P. B. (2003). Arc-parallel flow within the mantle wedge: Evidence from the accreted Talkeetna arc, south central Alaska. Journal of Geophysical Research: Solid Earth, 108(B8).

Meng, J., Wang, C., Zhao, X., Coe, R., Li, Y., & Finn, D. (2012). India-Asia collision was at 24 N and 50 Ma: palaeomagnetic proof from southernmost Asia. Scientific reports, 2, 925.

Menke, W., & Levin, V. (2003). The cross-convolution method for interpreting SKS splitting observations, with application to one and two-layer anisotropic earth models. Geophysical Journal International, 154(2), 379-392.

Mitchell, A. H. G. (1989). The Shan Plateau and western Burma: Mesozoic-Cenozoic plate boundaries and correlations with Tibet. In Tectonic Evolution of the Tethyan region (pp. 567-583). Springer, Dordrecht.

Mitchell, A. H. G. (1992). Late Permian-Mesozoic events and the Mergui group nappe in Myanmar and Thailand. Journal of Southeast Asian Earth Sciences, 7(2-3), 165-178.

Mitchell, A. H. G. (1993). Cretaceous–Cenozoic tectonic events in the western Myanmar (Burma)–Assam region. Journal of the Geological Society, 150(6), 1089-1102.

Mitchell, A.H.G., Htay, M.T., Htun, K.M., Win, M.N., Oo, T. & Hlaing, T. 2007. Rock relationships in the Mogok metamorphic belt, Tatkon to Mandalay, central Myanmar. Journal of Asian Earth Sciences, 29, 891–910.

Mitchell, A., Chung, S. L., Oo, T., Lin, T. H., & Hung, C. H. (2012). Zircon U–Pb ages in Myanmar: Magmatic–metamorphic events and the closure of a neo-Tethys ocean? Journal of Asian Earth Sciences, 56, 1-23.

Mitra, S., Bhattacharya, S. N., & Nath, S. K. (2008). Crustal structure of the Western Bengal Basin from joint analysis of teleseismic receiver functions and Rayleigh-wave dispersion. Bulletin of the Seismological Society of America, 98(6), 2715-2723.

Molnar, P., & Tapponnier, P. (1978). Active tectonics of Tibet. Journal of Geophysical Research, 83(B11), 5361–5375. https://doi.org/10.1029/JB083iB11p05361

Molnar, P., & Tapponnier, P. (1975). Cenozoic tectonics of Asia: effects of a continental collision. science, 189(4201), 419-426.

Mon, C. T., Gong, X., Wen, Y., Jiang, M., Chen, Q. F., Zhang, M., ... & He, Y. (2020). Insight into major active faults in Central Myanmar and the related geodynamic sources. Geophysical Research Letters, 47(8), e2019GL086236.

Moore, M. M., Garnero, E. J., Lay, T., & Williams, Q. (2004). Shear wave splitting and waveform complexity for lowermost mantle structures with low-velocity lamellae and transverse isotropy. Journal of Geophysical Research: Solid Earth, 109(B2).

Morley, C. K. (2017). Syn-kinematic sedimentation at a releasing splay in the northern Minwun Ranges, Sagaing Fault zone, Myanmar: significance for fault timing and displacement. Basin Research, 29, 684-700.

Morley, C. K., & Arboit, F. (2019). Dating the onset of motion on the Sagaing fault: Evidence from detrital zircon and titanite U-Pb geochronology from the North Minwun Basin, Myanmar. Geology, 47(6), 581-585.

Müller, R. D., Sdrolias, M., Gaina, C., & Roest, W. R. (2008). Age, spreading rates, and spreading asymmetry of the world's ocean crust. Geochemistry, Geophysics, Geosystems, 9(4).

Najman, Y., Sobel, E. R., Millar, I., Stockli, D. F., Govin, G., Lisker, F., ... & Zhang, P. (2020). The exhumation of the Indo-Burman Ranges, Myanmar. Earth and Planetary Science Letters, 530, 115948.

Ni, J.F., Guzman-Speziale, M., Bevis, M., Holt, W.E., Wallas, T.C., Seager, W.R., 1989. Accretionary tectonics of Burma and the three-dimensional geometry of the Burma subduction zone. Geology 17, 68-71.

Nicolas, A., & Christensen, N. I. (1987). Formation of anisotropy in upper mantle peridotites-A review. Composition, structure and dynamics of the lithosphere-asthenosphere system, 16, 111-123.

Ohuchi, T., Kawazoe, T., Nishihara, Y., Nishiyama, N., & Irifune, T. (2011). High pressure and temperature fabric transitions in olivine and variations in upper mantle seismic anisotropy. Earth and Planetary Science Letters, 304(1-2), 55-63.

Pasyanos, M. E., Masters, T. G., Laske, G., & Ma, Z. (2014). LITHO1.0: An updated crust and lithospheric model of the earth. Journal of Geophysical Research: Solid Earth, 119(3), 2153-2173. doi:10.1002/2013JB010626

Priestley, K., Jackson, J., & McKenzie, D. (2008). Lithospheric structure and deep earthquakes beneath India, the Himalaya and southern Tibet. Geophysical Journal International, 172(1), 345–362.

Rajkakati, M., Bhowmik, S. K., Ao, A., Ireland, T. R., Avila, J., Clarke, G. L., ... & Aitchison, J. C. (2019). Thermal history of Early Jurassic eclogite facies metamorphism in the Nagaland Ophiolite Complex, NE India: New insights into pre-Cretaceous subduction channel tectonics within the Neo-Tethys. Lithos, 346, 105166.

Rajasekhar, R. P., & Mishra, D. C. (2008). Crustal structure of Bengal basin and Shillong plateau: extension of Eastern Ghat and Satpura mobile belts to Himalayan fronts and seismotectonics. *Gondwana Research*, *14*(3), 523-534.

Rao, N. P., & Kumar, M. R. (1999). Evidences for cessation of Indian plate subduction in the Burmese arc region. Geophysical Research Letters, 26(20), 3149-3152.

Rao, N. P. (2005). Deformation of the subducted Indian lithospheric slab in the Burmese arc. Geophysical Research Letters, 32(5).

Ribe, N. M. (1992). On the relation between seismic anisotropy and finite strain. Journal of Geophysical Research: Solid Earth, 97(B6), 8737-8747

Romanowicz, B., & Wenk, H. R. (2017). Anisotropy in the deep Earth. *Physics of the Earth and Planetary Interiors*, *269*, 58-90.

Rümpker, G. and Silver, P. G., Apparent shear-wave splitting parameters in the presence of vertically varying anisotropy. Geo phys. J. Int., 1998, 135, 790-800.

Russo, R. M., & Silver, P. G. (1994). Trench-parallel flow beneath the Nazca plate from seismic anisotropy. Science, 263(5150), 1105-1111.

Russo, R. M., A. Gallego, D. Comte, V. I. Moncau, R. E. Murdie, and J. C. VanDecar (2010), Source-side shear wave splitting and upper mantle flow in the Chile Ridge subduction zone, Geology, 38, 707–710.

Russo, R. M. (2012). Source-side shear-wave splitting and upper-mantle flow beneath the Arakan slab, India-Asia-Sundalind triple junction. *Geosphere*, *8*(1), 158-178.

Sandvol, E., & Ni, J. (1997). Deep azimuthal seismic anisotropy in the southern Kurile and Japan subduction zones. Journal of Geophysical Research: Solid Earth, 102(B5), 9911-9922.

Savage, M. K., Shih, X. R., Meyer, R. P., & Aster, R. C. (1989). Shear-wave anisotropy of active tectonic regions via automated S-wave polarization analysis. Tectonophysics, 165(1-4), 279-292.

Savage, M. K., Silver, P. G., & Meyer, R. P. (1990). Observations of teleseismic shear-wave splitting in the Basin and Range from portable and permanent stations. Geophysical Research Letters, 17(1), 21-24.

Savage MK (1999) Seismic anisotropy and mantle deformation: what have we learned from shear wave splitting? Rev Geophys 37:65–106

Schellart, W. P., and Moresi, L. (2013), A new driving mechanism for backarc extension and backarc shortening through slab sinking induced toroidal and poloidal mantle flow: Results from dynamic subduction models with an overriding plate, J. Geophys. Res. Solid Earth, 118, 3221– 3248, doi:10.1002/jgrb.50173.

Searle, M.P., Noble, S.R., Cottle, J.M., Waters, D.J., Mitchell, A.H.G., Hiang, T. & Horstwood, M.S.A. 2007. Tectonic evolution of the Mogok Metamorphic Belt, Burma (Myanmar) constrained by U–Th–Pb dating of metamorphic and magmatic rocks. Tectonics, 26, article number TC3014.

Silver, P. G., & Chan, W. W. (1991). Shear wave splitting and subcontinental mantle deformation. Journal of Geophysical Research: Solid Earth, 96(B10), 16429-16454.

Silver, P. G., & Savage, M. K. (1994). The interpretation of shear-wave splitting parameters in the presence of two anisotropic layers. Geophysical Journal International, 119(3), 949-963.

Shiddiqi, H. A., Tun, P. P., & Ottemöller, L. (2019). Minimum 1D Velocity Model and Local Magnitude Scale for Myanmar. Seismological Research Letters, 90(5), 1923-1936.

Socquet, A., Goffé, B., Pubellier, M., & Rangin, C. (2002). Le métamorphisme Tardi-Crétacé à Éocène des zones internes de la chaîne Indo-Birmane (Myanmar occidental): implications géodynamiques. Comptes Rendus Geoscience, 334(8), 573-580.

Sol, S., Meltzer, A., Burgmann, R., Van der Hilst, R. D., King, R., Chen, Z., ... & Zhang, X. (2007). Geodynamics of the southeastern Tibetan Plateau from seismic anisotropy and geodesy. Geology, 35(6), 563-566.

Steckler, M. S., Mondal, D. R., Akhter, S. H., Seeber, L., Feng, L., Gale, J., ... & Howe, M. (2016). Locked and loading megathrust linked to active subduction beneath the Indo-Burman Ranges. Nature Geoscience, 9(8), 615-618.

Stork, A. L., Selby, N. D., Heyburn, R., & Searle, M. P. (2008). Accurate relative earthquake hypocenters reveal structure of the Burma subduction zone. Bulletin of the Seismological Society of America, 98(6), 2815-2827.

Tarantola, A. (1987). Inverse problem theory: Methods for data fitting and model parameter estimation. Elsevier, Netherlands, p. 386.

Taylor, M., & Yin, A. (2009). Active structures of the Himalayan-Tibetan orogen and their relationships to earthquake distribution, contemporary strain field, and Cenozoic volcanismActive structures on the Tibetan plateau and surrounding regions. *Geosphere*, *5*(3), 199-214.

Teanby, N. A., Kendall, J. M., & Van der Baan, M. (2004). Automation of shear-wave splitting measurements using cluster analysis. Bulletin of the Seismological Society of America, 94(2), 453-463.

Thant, M. (2012). Probabilistic Seismic hazard assessment for Yangon region, Myanmar. Journal of ASEAN Engineering Part C, 117.

Wang, C. Y., Flesch, L. M., Silver, P. G., Chang, L. J., & Chan, W. W. (2008). Evidence for mechanically coupled lithosphere in central Asia and resulting implications. Geology, 36(5), 363-366.

Wang, X., Wei, S., Wang, Y., Maung Maung, P., Hubbard, J., Banerjee, P., ... & Almeida, R. (2019). A 3-D shear wave velocity model for Myanmar region. Journal of Geophysical Research: Solid Earth, 124(1), 504-526.

Wei, W., Xu, J., Zhao, D., & Shi, Y. (2012). East Asia mantle tomography: New insight into plate subduction and intraplate volcanism. Journal of Asian Earth Sciences, 60, 88-103.

Wüstefeld, A., Bokelmann, G., Barruol, G., & Montagner, J. P. (2009). Identifying global seismic anisotropy patterns by correlating shear-wave splitting and surface-wave data. Physics of the Earth and Planetary Interiors, 176(3-4), 198-212

Yao, Z. S., Roberts, R. G., & Tryggvason, A. (1999). Calculating resolution and covariance matrices for seismic tomography with the LSQR method. Geophysical Journal International, 138(3), 886-894.

Zhang, S., & Karato, S. I. (1995). Lattice preferred orientation of olivine aggregates deformed in simple shear. Nature, 375(6534), 774-777

Zhao, L., Zheng, T., Lu, G., 2013. Distinct upper mantle deformation of cratons in response to subduction: constraints from SKS wave splitting measurements in eastern China. Gondwana Res.23, 39–53.

Zhang, J., Ji, J., Zhong, D., Ding, L., & He, S. (2004). Structural pattern of eastern Himalayan syntaxis in Namjagbarwa and its formation process. *Science in China Series D: Earth Sciences*, *47*(2), 138.

Zhang, J. E., Xiao, W., Windley, B. F., Cai, F., Sein, K., & Naing, S. (2017). Early Cretaceous wedge extrusion in the Indo-Burma Range accretionary complex: implications for the Mesozoic subduction of Neotethys in SE Asia. International Journal of Earth Sciences, 106(4), 1391-1408.

Appendix

List of local splitting results

Event ID	Station	φ(°)	**Δφ (°)**	dt(s)	Δdt(s)	BAZ **(°)**	Depth(km)	INPL	Quality
20183330357	MP03	-18	7	1	0	60.49	84	25	Q1
20183330357	MP06	7	14	0.3	0	37.98	84	54	Q2
20183330357	MP08	-8	7	0.8	0.1	7.68	84	153	Q3
20183330357	MP11	-43	18	0.2	0	336.12	84	342	Q3
20183330357	MP19	-18	16	0.7	0	290.39	84	219	Q2
20183330357	MP21	17	17	1.1	0.1	283.54	84	244	Q2
20183330357	MS04	-42	18	0.3	0.1	20.38	84	24	Q2
20183330357	MS05	-66	11	0.3	0.1	346.94	84	182	Q2
20183330357	MS06	-31	8	0.4	0	270.23	84	351	Q2
20183330357	MS07	-73	22	0.3	0	310.67	84	250	Q2
20183330357	MS10	52	10	0.4	0	283.07	84	277	Q1
20183610035	MP01	-20	10	0.4	0.1	87.61	91	48	Q1
20183610035	MP08	9	7	0.6	0.1	67.16	91	163	Q2
20183610035	MP11	-54	6	0.2	0.1	31.86	91	-40	Q3
20183610035	MP14	6	13	0.3	0.1	313.12	91	347	Q3
20183610035	MP16	67	4	0.4	0	305.34	91	218	Q1
20183610035	MP18	10	3	0.3	0	290.77	91	257	Q1
20183610035	MP19	25	5	0.5	0	288.48	91	275	Q3
20183610035	MP22	-35	13	0.3	0.1	286.44	91	298	Q2
20183610035	MS01	58	25	0.4	0.1	110.56	91	190	Q2
20183610035	MS03	8	15	0.6	0.1	77.13	91	63	Q1
20183610035	MS07	41	8	0.2	0	313.22	91	276	Q1
20183651333	MP19	2	17	0.4	0.1	238.42	57	250	Q3
20183651332	MP22	22	6	0.6	0.1	240.4	57	275	Q3
20183651333	MS05	-35	26	0.5	0.1	229.36	57	275	Q3
20183651332	MS06	-25	14	0.9	0.1	229.39	57	306	Q1
20183651333	MS08	-2	7	0.4	0.1	242.46	57	158	Q2
20190251706	MP02	-37	20	0.4	0.1	12.8	55	123	Q3
20190251706	MP04	71	21	0.5	0.1	2.37	55	128	Q1
20190251706	MP05	26	25	0.6	0.1	357.07	55	357	Q3
20190251707	MP07	53	17	0.3	0.1	348.37	55	300	Q2
20190251707	MP16	-88	15	0.8	0.1	318.69	55	118	Q2
20190251706	MP18	-49	12	0.6	0.1	310.15	55	247	Q3
20190251706	MP22	4	11	0.3	0.1	305.68	55	202	Q3
20190251707	MS08	-70	22	0.5	0.1	321.13	55	174	Q3
20190272345	MP04	-72	18	0.4	0.1	8	65	171	Q1
20190270449	MP08	-8	17	0.5	0.1	2.27	68	120	Q2

20190270449	MP09	-15	16	1.2	0.1	359.97	68	225	Q1
20190270449	MP20	7	11	0.5	0	319.74	68	238	Q2
20190272345	MP04	-72	18	0.4	0.1	8	65	171	Q2
20190272345	MP07	8	9	0.4	0	355.08	65	223	Q1
20190272345	MP13	-78	14	0.4	0	335.94	65	229	Q1
20190272345	MP18	9	18	1.1	0.1	314.55	65	329	Q2
20190272345	MP20	14	17	1	0.1	307.85	65	332	Q2
20190272345	MS06	-50	22	0.5	0.1	300.67	65	279	Q1
20190272345	MS07	50	15	0.4	0.1	322.31	65	262	Q2
20190272345	MS10	33	18	0.4	0.1	314.41	65	374	Q3
20190302312	MP01	21	19	0.4	0.1	53.51	82	136	Q3
20190302312	MP03	-63	17	0.7	0.1	43.6	82	172	Q1
20190302312	MP04	-89	15	0.2	0.1	38.6	82	143	Q2
20190302312	MP05	82	25	0.2	0.1	33.38	82	137	Q2
20190302312	MP08	-26	11	1	0.1	18.64	82	121	Q1
20190302312	MP09	-16	17	0.2	0.1	12.97	82	106	Q1
20190302312	MP11	22	10	0.4	0.1	4.61	82	131	Q3
20190302312	MP13	-37	4	0.3	0	352.59	82	260	Q1
20190302312	MP14	40	21	0.2	0.1	339.76	82	265	Q1
20190302312	MP18	-25	7	0.4	0	314.49	82	272	Q1
20190302312	MP19	65	16	0.7	0.1	311.05	82	213	Q1
20190302312	MP25	74	18	0.3	0.1	58.41	82	141	Q2
20190302312	MS02	-21	16	0.3	0.1	63.08	82	12	Q1
20190302312	MS05	38	20	0.2	0.1	359.66	82	187	Q1
20190302312	MS06	-47	11	0.4	0.1	293.38	82	289	Q1
20190341720	MP10	-86	14	0.8	0.1	341.58	66	298	Q3
20190341720	MS08	-87	20	0.3	0.1	324.4	66	168	Q3
20190721343	MP04	-77	20	0.3	0.1	155.9	79	150	Q1
20190721343	MP07	74	18	0.3	0.1	219.04	79	141	Q2
20190721344	MP08	-5	20	0.5	0.1	227.84	79	216	Q1
20190721344	MP09	11	11	0.4	0	241.41	79	243	Q1
20190721343	MP10	12	12	0.3	0	247.29	79	229	Q1
20190721343	MP11	21	7	0.3	0.1	248.53	79	222	Q2
20190721343	MP16	-6	10	0.3	0	271.05	79	236	Q1
20190721343	MP20	-7	8	0.8	0	269.14	79	235	Q2
20190721343	MP22	22	10	0.7	0.1	269.38	79	260	Q1
20190721344	MS06	-37	5	0.6	0	252.68	79	203	Q2
20190721344	MS10	48	25	0.3	0.1	256.16	79	261	Q2
20190751923	MP06	56	7	0.9	0.1	35.71	96	130	Q3
20190751923	MP07	12	0	0.2	0	31.2	96	154	Q1
20190751923	MP08	11	12	0.5	0.1	27.05	96	161	Q2
20190751923	MP16	20	9	0.4	0.1	337.97	96	263	Q2
20190751923	MP18	12	11	0.6	0	322.52	96	249	Q2
20190751923	MP23	12	6	0.3	0	308.25	96	331	Q2

20190751923	MS01	64	24	0.3	0.1	50.34	96	171	Q2
20190751923	MS04	-79	20	0.4	0.1	27.07	96	78	Q3
20190751923	MS06	22	5	0.5	0.1	301.3	96	269	Q2
20190751923	MS10	40	0	0.2	0	325.71	96	253	Q2
20190771654	MP04	42	16	0.4	0.1	155.64	99	197	Q2
20190771654	MP06	87	9	0.5	0	163.08	99	212	Q2
20190771654	MP07	75	10	1.1	0.1	166.49	99	184	Q3
20190771654	MP11	15	14	0.3	0.1	178.43	99	215	Q2
20190771654	MP13	-44	19	0.4	0.1	185.97	99	188	Q2
20190771654	MP18	-35	8	0.3	0	221.9	99	167	Q2
20190771654	MP20	-25	13	1	0.1	230.85	99	186	Q1
20190771654	MP22	12	11	0.8	0.1	229.05	99	249	Q2
20190771654	MS06	-59	23	0.5	0.2	215.21	99	153	Q2
20190840456	MP02	81	22	0.2	0.1	157.24	86	199	Q2
20190840456	MP05	-58	16	0.3	0.1	169.61	86	233	Q3
20190840456	MP08	11	19	0.9	0.1	183.25	86	233	Q3
20190840456	MP09	19	14	1.2	0.1	186.82	86	160	Q2
20190840456	MP14	57	26	0.4	0.1	211.23	86	200	Q2
20190840456	MP16	16	15	0.3	0	226.69	86	144	Q2
20190840456	MP18	-14	14	0.3	0.1	234.38	86	317	Q2
20190840456	MP23	-35	16	1.3	0.1	240.76	86	277	Q1
20190840456	MS04	-13	20	0.3	0.1	167.19	86	204	Q1
20190840456	MS05	-3	12	0.5	0	214.91	86	236	Q1
20190840456	MS07	-1	16	0.5	0.1	262.26	86	334	Q1
20190840456	MS10	37	16	0.3	0.1	220.22	86	164	Q1
20190841241	MP01	-58	18	0.2	0.1	356.53	56	344	Q2
20190841241	MP02	-15	15	0.3	0.1	353.19	56	188	Q2
20190841241	MP03	-76	8	0.9	0.1	349.46	56	213	Q3
20190841241	MP10	6	19	0.8	0.2	325.26	56	211	Q3
20190841241	MP22	-15	20	0.4	0.1	301.22	56	282	Q1
20190841241	MS02	-13	13	0.2	0.1	346.42	56	191	Q2
20190841241	MS07	40	17	0.4	0.1	313.87	56	277	Q2
20191050139	MP03	-37	0.1	0.7	0.1	210.68	56	144	Q3
20191050139	MP08	-5	11	0.7	0.1	236.16	56	299	Q2
20191050139	MP10	-15	29	0.5	0	244.1	56	298	Q1
20191050139	MP11	19	12	0.4	0	244.86	56	326	Q1
20191050139	MP13	-35	9	0.5	0.1	247.91	56	162	Q3
20191050139	MP19	-28	34	0.3	0.1	262.26	56	216	Q1
20191050139	MP20	52	0	0.4	0	262.99	56	290	Q2
20191050139	MP22	87	27	0.3	0.1	262.91	56	324	Q2
20191050139	MS02	-58	22	0.8	0.1	196.84	56	182	Q2
20191191739	MP04	39	0	0.2	0	101.77	133	57	Q3
20191191739	MP10	3	15	0.3	0.1	109.61	133	164	Q2
20191191739	MP11	22	0	0.1	0	114.01	133	175	Q2

20191191739	MP20	-14	8	0.5	0.1	269	133	238	Q3
20191191739	MP21	-2	11	0.3	0.1	266.14	133	232	Q1
20191191739	MP23	0	18	0.5	0	266.52	133	230	Q1
20191191739	MS02	22	13	1.1	0.1	118.72	133	60	Q1
20191191739	MS05	-12	31	0.2	0.1	32.59	133	10	Q2
20191191739	MS06	-24	7	0.4	0	238.19	133	212	Q1
20191191739	MS07	18	9	0.4	0.1	308.24	133	309	Q2
20191191739	MS10	-23	12	0.4	0	234.19	133	214	Q1
20190460350	MP05	58	25	0.3	0.1	121.88	86	104	Q3
20190460350	MP06	-23	10	0.3	0.1	128.8	86	50	Q3
20190460349	MP19	-43	12	0.4	0.1	262.11	86	345	Q2
20190460349	MS02	9	25	0.6	0.1	133.23	86	57	Q2
20190460349	MS05	-13	7	0.5	0.1	0.17	86	2	Q3
20190461619	MP03	-24	22	0.4	0.1	43.59	46	122	Q2
20190461618	MP08	44	14	0.7	0.1	24.99	46	106	Q1
20190461619	MP10	35	14	0.2	0.1	16.87	46	51	Q3
20190461619	MP18	70	28	0.3	0.2	325.56	46	398	Q3
20190461619	MS05	-20	20	0.5	0.1	6.23	46	32	Q1
20190471206	MP14	58	12	0.3	0	6.33	46	106	Q3
20190471206	MS03	38	22	0.4	0.1	55.14	46	98	Q3
20190491543	MP01	83	26	0.6	0.1	140.91	50	211	Q3
20190491543	MP02	-19	14	0.4	0.1	141.73	50	120	Q2
20190491543	MP04	12	35	0.6	0.1	147.65	50	138	Q3
20190491543	MP08	-10	29	0.4	0.2	169.33	50	195	Q3
20190491543	MP16	41	17	0.3	0.1	228.42	50	193	Q2
20190521537	MP03	-50	16	0.4	0.1	354.4	47	252	Q1
20190530607	MP08	-3	9	0.8	0	13.66	57	53	Q1
20190530607	MP10	3	10	0.3	0.1	329.73	57	293	Q2
20190530607	MP11	5	5	0.3	0.1	315.92	57	292	Q3
20190530607	MP13	21	26	0.3	0.1	295.46	57	253	Q1
20190530607	MP14	23	28	0.2	0.1	291.16	57	321	Q3
20190530607	MP16	-2	16	0.5	0.1	293.5	57	297	Q1
20190530607	MP19	-11	21	0.4	0.1	283.55	57	282	Q3
20190540608	MP07	-13	18	1.1	0.2	34.37	48	13	Q3
20190540608	MP14	66	11	0.3	0.1	359.37	48	346	Q3
20190540608	MP19	10	7	0.7	0	324.82	48	322	Q3
20190540608	MP22	1	14	0.8	0.1	320.06	48	314	Q1
20190602100	MP06	-4	16	0.4	0.1	16.6	51	117	Q2
20190602059	MP07	-6	21	1.1	0.1	8.84	51	121	Q2
20190602059	MS04	-48	16	0.3	0.1	12.3	51	-25	Q3
20190630656	MS01	-5	10	0.4	0.1	291.39	45	201	Q2
20190741959	MP06	21	23	0.2	0.1	183.5	68	146	Q2
20190741959	MP08	19	18	0.5	0.1	199.72	68	171	Q2
20190741959	MS05	-22	29	0.2	0.1	278.32	68	284	Q2

20190741959	MS07	-36	21	0.3	0.1	281.14	68	190	Q3
20190751936	MP07	-8	22	0.4	0.1	34.88	70	143	Q1
20190751937	MS06	-46	23	0.7	0.1	309.18	70	351	Q1
20190752327	MP07	-15	17	0.4	0.1	32.18	42	132	Q1
20190752327	MP08	22	10	0.4	0.1	29.53	42	177	Q1
20190752327	MP22	-2	12	0.5	0.1	331.13	42	234	Q2
20190752327	MS01	-40	15	0.7	0.2	44.19	42	115	Q3
20190752327	MS05	-10	17	0.6	0.1	12.94	42	28	Q2
20190752327	MS10	18	16	0.6	0.1	348.15	42	224	Q3
20190770006	MP01	3	13	1.1	0.1	155.67	70	209	Q3
20190770007	MP25	1	16	0.8	0.1	145.79	70	157	Q3
20190770007	MS04	-13	14	0.3	0.1	240.99	70	284	Q2
20190800818	MP18	-80	22	0.4	0.1	352.21	114	322	Q3
20190890433	MP22	1	30	0.9	0.2	316.99	75	225	Q1
20190892134	MP02	-48	22	0.4	0.1	125.18	118	102	Q3
20190892134	MP06	28	21	0.3	0.1	134.74	118	168	Q2
20190892134	MP13	27	26	0.2	0.1	163.09	118	232	Q3
20190892134	MS04	-79	23	0.4	0.1	112.09	118	68	Q3
20190970445	MP06	20	7	1.2	0.1	26.47	97	135	Q3
20190970445	MP14	31	10	0.4	0.1	337.6	97	282	Q3
20190970445	MS10	44	21	0.3	0.2	313.43	97	278	Q2
20191042025	MP06	-49	17	0.3	0.1	14.7	68	92	Q1
20191042025	MP07	74	14	0.9	0.1	9.77	68	23	Q1
20191042025	MP09	10	13	1.5	0.1	0.77	68	62	Q1
20191042025	MP20	-9	8	0.8	0.1	308.31	68	211	Q2
20191042024	MP22	10	10	0.3	0	310.36	68	239	Q3
20191042025	MS06	16	6	0.4	0	299.64	68	228	Q1
20191042025	MS07	57	12	0.2	0.1	324.71	68	205	Q2
20191051717	MP02	11	18	0.5	0	118.27	65	39	Q3
20191051718	MP03	21	0	0	0	115.74	65	33	Q2
20191051717	MP05	-44	17	0.3	0.1	138.65	65	100	Q3
20191051718	MP10	6	15	0.4	0.1	248.01	65	327	Q2
20191051718	MS04	-51	11	0.2	0	19.16	65	173	Q2
20191061741	MS06	7	7	0.6	0.1	317.46	66	245	Q1
20191061741	MS10	44	21	0.3	0.1	332.48	66	270	Q1
20191070138	MP01	10	14	0.5	0.1	25.44	45	46	Q3
20191070138	MP04	34	17	0.4	0.1	5.53	45	65	Q2
20191070138	MP20	-6	18	0.8	0	298.45	45	214	Q2
20191070138	MS03	-42	24	0.4	0.1	26.98	45	169	Q2
20191091117	MP06	5	14	0.7	0.1	75.28	113	56	Q1
20191091117	MS05	32	25	0.5	0.1	19.39	113	84	Q2
20191102204	MP02	3	13	0.9	0.1	81.13	43	29	Q2
20191102204	MP06	-18	23	0.3	0.1	67.26	43	37	Q2
20191110656	MP04	6	21	0.2	0.1	67.68	102	40	Q2

20191110656	MP07	59	13	0.7	0.1	24.25	102	129	Q3
20191110656	MP08	-3	12	0.5	0.1	338.68	102	197	Q3
20191110656	MP09	-1	16	0.1	0	327.84	102	229	Q2
20191110655	MP13	-49	22	0.1	0	292.09	102	181	Q2
20191110655	MS02	9	22	1	0.1	118.31	102	40	Q3
20191110656	MS05	-12	17	0.6	0.1	339.4	102	319	Q3
20191110836	MP02	-73	19	0.3	0.1	67.72	65	55	Q3
20191110836	MP06	-14	10	0.6	0.1	55.36	65	98	Q3
20191110836	MS04	61	12	0.9	0.1	39.78	65	83	Q3
20191110836	MS10	-67	18	0.4	0.1	317.41	65	257	Q2
20191181514	MP18	8	14	0.4	0.1	323.08	41	215	Q2
20191221327	MP04	26	25	0.3	0.1	359.25	54	226	Q3
20180120728	EW02	-44	11	0.6	0.2	12.16	128	143	Q2
20180201005	EW02	55	23	0.6	0.3	8.11	86	161	Q3
20181140407	EW03	56	0	0.3	0.2	15.95	106	60	Q2
20171940502	EW04	28	0	0.1	0.3	0.65	89	99	Q3
20181701105	EW04	56	0	0.2	0.2	348.04	85	49	Q2
20171820700	EW05	16	0	0.3	0.2	355.25	89	307	Q1
20181140407	EW05	16	0.1	0.1	0.1	351.7	106	377	Q2
20181701105	EW05	30	17	0.2	0.2	333.15	85	371	Q3
20171940502	EW06	-77	0	0.4	0.3	327.11	89	305	Q2
20180180202	EW06	14	0	0.3	0.1	342.87	83	345	Q3
20181140407	EW07	14	17	0.3	0.1	313.18	106	252	Q1
20181701105	EW07	28	0	0.5	0.2	292.96	85	332	Q2
20181140407	EW08	39	18	0.6	0.3	307.39	106	195	Q3
20181751106	M001	-52	0	0.1	0.2	338.2	121	239	Q2
20181140407	M002	-22	6	0.5	0.1	328.13	106	229	Q3
20181701105	M003	55	0	0.2	0.3	325.81	85	410	Q3
20181701105	M004	-78	90	0.2	0.1	324.43	85	225	Q2
20171820700	M005	21	20	1.1	0.1	343.3	89	348	Q1
20181701105	M006	49	40	0.3	0.1	321.59	85	343	Q3
20181140407	M007	-57	0	0	0	339.55	106	268	Q3
20181701105	M007	4	28	0.3	0	317.2	85	236	Q2
20171940502	M008	-51	40	0.6	0.1	345.21	89	278	Q2
20180180202	M010	59	0	0.5	0.3	347.22	83	248	Q3
20181751106	M010	35	0	0.4	0.2	338.86	121	388	Q2
20180120728	M021	39	52	0.2	0.1	16.45	128	158	Q2
20171820700	M022	54	37	0.3	0.2	357.58	89	300	Q1
20171940502	M022	61	0	0.3	0.1	353.58	89	324	Q3
20181701105	M022	47	0	0.4	0.1	314.8	85	263	Q3
20180201005	M023	21	7	1.1	0.1	351.37	86	313	Q2
20181701105	M023	16	14	0.3	0.1	252.67	85	264	Q2
20181751106	M023	34	16	0.4	0.1	355.51	121	327	Q2
20171940502	M024	82	0	0.6	0.3	56.9	89	148	Q3

20180201005	M024	-34	0	0.5	0.1	39.46	86	169	Q2
20182301202	M024	-38	29	0.2	0.1	25.75	85	82	Q3
20180201005	M025	39	0	0.2	0.1	315.1	86	268	Q1
20181751106	M025	52	19	0.2	0	309.76	121	205	Q2
20182301202	M025	15	19	0.5	0.2	334.75	85	307	Q2
20180120728	M026	86	13	0.3	0.1	31.4	128	194	Q3
20180120728	M027	21	0	0	0	86.28	128	90	Q3
20180120728	M028	-19	32	0.5	0.1	310.89	128	220	Q1
20180201005	M028	-62	33	0.2	0	254.25	86	246	Q3
20181140407	M028	-62	0.1	0.2	0.1	223.66	106	299	Q2
20181631307	M028	-37	31	0.3	0	11.74	116	102	Q2
20181751106	M028	1	14	0.4	0.1	240.48	121	241	Q2
20180120728	M029	43	21	0.2	0.1	200.89	12	281	Q1
20180180202	M029	-1	0	0.4	0.2	218.76	83	247	Q3
20181140407	M029	-39	0	0.3	0.1	198.41	106	138	Q2
20181631307	M029	-20	13	0.2	0.1	63.67	116	146	Q3
20182301202	M029	-52	25	0.3	0.1	212.89	85	245	Q2

List of XKS splitting results

Event ID	Station	φ(°)	Δ φ(°)	δt(s)	Δδt(s)	BAZ	Depth	Phase	Quality
20172699042	EW01	-34	5	0.8	0.1	112.08	96	SKS	Q2
20172699042	EW02	-24	5	1.6	0.1	112.46	96	SKS	Q2
20172699042	EW04	-17	20	0.4	0.2	112.55	96	SKS	Q2
20172699042	M001	-26	6	1.1	0.2	112.9	96	SKS	Q2
20172699042	M002	-7	17	0.5	0.4	112.97	96	SKS	Q2
20172699042	M004	-17	12	1.4	0.3	113.14	96	SKS	Q2
20172699042	M005	-16	4	1.1	0.1	113.01	96	SKS	Q2
20172699042	M007	-51	4	1.2	0.3	112.87	96	SKS	Q2
20172699042	M008	-49	6	0.7	0.2	112.89	96	SKS	Q2
20172699042	M009	-30	3	1.3	0.1	113.09	96	SKS	Q2
20172699042	M011	-27	8	1.7	0.3	113.27	96	SKS	Q2
20172699042	M029	57	18	1.2	0.5	112.29	96	SKS	Q1
20182311001	EW01	-36	10	0.7	0.2	107.3	600	SKS	Q2
20182311001	EW02	-23	11	1.6	0.4	107.7	600	SKS	Q2
20182311001	EW07	-47	16	0.9	0.4	108.67	600	SKS	Q3
20182311001	M001	-28	9	1.4	0.3	108.24	600	SKKS	Q2
20182311001	M004	-12	9	1.3	0.4	108.4	600	SKKS	Q2
20182311001	M005	-15	5	1.1	0.1	108.3	600	SKKS	Q2
20182311001	M006	-10	3	1.7	0.1	108.4	600	SKKS	Q2
20182311001	M023	-55	6	1.2	0.4	107.86	600	SKS	Q2
20182311001	M025	-12	14	0.8	0.3	108	600	SKS	Q2
20182311001	M028	-18	11	1	0.3	108.11	600	SKS	Q2

20182311001	M029	57	8	1	0.2	107.87	600	SKS	Q2
20182599211	EW01	-28	10	0.7	0.2	115.31	576	SKS	Q2
20182599211	EW02	-19	5	1.7	0.1	115.7	576	SKS	Q2
20182599211	M001	-26	10	1.2	0.3	116.25	576	SKS	Q2
20182599211	M003	-18	7	1.7	0.4	116.44	576	SKS	Q2
20182599211	M005	-16	7	1	0.2	116.3	576	SKS	Q2
20182599211	M006	-18	12	1.5	0.3	116.39	576	SKS	Q2
20182599211	M028	-9	5	1.2	0.2	116.14	576	SKS	Q2
20182733105	EW01	-39	14	1.1	0.3	107.5	550	SKS	Q2
20182733105	EW02	-28	9	1.9	0.3	107.9	550	SKS	Q2
20182733105	M001	-28	11	1.8	0.5	108.44	550	SKS	Q2
20182733105	M005	-27	17	1.1	0.4	108.5	550	SKS	Q2
20182733105	M007	-34	16	1.6	0.5	108.37	550	SKS	Q3
20182733105	M010	-24	10	1.5	0.3	108.57	550	SKS	Q2
20183222202	EW01	-35	5	0.7	0.1	107.32	540	SKS	Q2
20183222202	EW02	-21	11	1.6	0.3	107.72	540	SKS	Q2
20183222202	EW04	-14	9	0.6	0.2	107.84	540	SKS	Q2
20183222202	M003	-27	11	1.7	0.4	108.47	540	SKS	Q2
20183222202	M005	-14	5	1.2	0.2	108.33	540	SKS	Q2
20183222202	M006	-13	11	1.5	0.3	108.42	540	SKS	Q2
20183222202	M010	-11	15	1	0.4	108.41	540	SKS	Q3
20183222202	M028	-18	6	1.3	0.2	108.19	540	SKS	Q2
20183577230	EW01	-43	8	0.8	0.2	108.41	113	SKS	Q2
20183577230	EW02	-26	3	1.6	0.1	108.81	113	SKS	Q2
20183577230	EW07	-48	16	0.8	0.3	109.67	113	SKS	Q3
20183577230	M001	-30	6	1.2	0.2	109.23	113	SKS	Q2
20183577230	M003	-20	8	1.2	0.2	109.56	113	SKS	Q2
20183577230	M004	-27	13	0.9	0.2	109.49	113	SKS	Q2
20183577230	M005	-21	7	1.1	0.1	109.36	113	SKS	Q2
20183577230	M010	-45	7	1.8	0.5	109.4	113	SKS	Q3
20183577230	M011	-18	6	1.7	0.2	109.63	113	SKS	Q2
20183577230	M023	-55	3	1.3	0.2	108.81	113	SKS	Q3
20183577230	M025	-11	20	0.6	0.4	108.88	113	SKS	Q3
20183577230	M026	41	5	0.9	0.2	108.42	113	SKS	Q1
20183577230	M028	-9	11	1.5	0.6	108.92	113	SKS	Q2
20183577230	M029	54	8	1.2	0.2	108.59	113	SKS	Q1
20190266195	EW01	-36	9	0.8	0.1	110.32	588	SKS	Q2
20190266195	M001	-24	13	1.6	0.5	111.24	588	SKS	Q2
20190266195	M007	-37	24	0.9	0.6	111.17	588	SKS	Q2
20190266195	M028	-16	11	1.5	0.5	111.09	588	SKS	Q2
20172911120	EW02	-23	6	1.7	0.3	108.73	10	SKS	Q2
20172911120	M001	-20	7	1.5	0.2	109.11	10	SKS	Q2
20172911120	M004	-26	10	1.3	0.3	109.41	10	SKS	Q2
20172911120	M005	-18	8	1.2	0.2	109.26	10	SKS	Q2

20172911120	M007	-53	7	1.7	0.5	109.11	10	SKS	Q2
20172911120	M025	-6	9	1.1	0.3	108.72	10	SKS	Q2
20172911120	M029	46	10	1.4	0.5	108.37	10	SKS	Q2
20173088090	EW02	-25	9	2	0.4	103.5	10	SKS	Q2
20173088090	M005	-20	9	1.6	0.4	104.07	10	SKS	Q2
20173088090	M023	-48	23	0.7	0.4	103.51	10	SKS	Q3
20182533193	EW02	-9	12	1.8	0.4	115.28	12	SKS	Q2
20182533193	M021	2	12	1.3	0.5	115.43	12	SKS	Q2
20182533193	M028	-6	14	1.6	0.5	116.41	12	SKS	Q2
20182533193	M029	58	9	2.1	0.5	116.38	12	SKS	Q2
20183100161	EW02	-24	8	1.6	0.3	110.46	10	SKS	Q2
20183100161	M026	39	15	0.9	0.5	110.01	10	SKS	Q2
20183100161	M028	-20	23	1	0.4	110.48	10	SKS	Q3
20182499154	EW06	-4	10	0.8	0.3	109.69	670	SKS	Q2
20182499154	M002	-4	16	0.8	0.4	109.5	670	SKKS	Q3
20182499154	M004	-11	13	1.3	0.3	109.55	670	SKS	Q2
20182499154	M006	-13	6	1.5	0.2	109.55	670	SKKS	Q3
20182499154	M008	-44	13	0.6	0.2	109.34	670	SKKS	Q2
20182499154	M028	-18	8	1.2	0.3	109.42	670	SKS	Q3
20180922055	M001	-35	8	1.2	0.2	113.98	92	SKS	Q2
20180922055	M005	-19	12	1	0.3	114.1	92	SKS	Q2
20180922055	M025	-35	25	0.7	0.4	113.64	92	SKS	Q2
20180922055	M026	60	6	1.3	0.2	113.19	92	SKS	Q1
20180922055	M028	-25	7	1.2	0.2	113.67	92	SKS	Q2
20180922055	M029	54	10	1.1	0.4	113.35	92	SKS	Q1
20182311042	M001	-30	8	1.2	0.3	107.15	415	SKS	Q2
20182311042	M005	-18	16	1.2	0.4	107.2	415	SKS	Q2
20182311042	M025	-12	34	0.9	0.7	106.91	415	SKS	Q3
20180233093	M025	-1	22	1.5	1.1	30.75	10	SKS	Q1
20190277101	M006	-17	13	1.8	0.4	110.16	562	SKS	Q2
20190277101	M010	-11	17	1	0.4	110.11	562	SKS	Q2
20190277101	M028	-16	7	1.3	0.2	109.79	562	SKS	Q2
20190277101	M029	46	22	1.1	0.5	109.53	562	SKS	Q1
20190100170	M007	-34	9	1.5	0.3	115.63	10	SKS	Q2
20183344172	M012	-29	7	0.8	0.1	26.18	54	SKS	Q1
20180288160	M022	16	7	1.3	0.3	218.28	10	SKS	Q1
20180588172	M024	24	23	1.1	0.4	155.23	10	SKS	Q2
20180588172	M025	-1	25	1	0.7	155.73	10	SKS	Q2
20180588172	M029	4	17	0.9	0.4	155.67	10	SKS	Q2
20182533041	M025	-25	28	0.7	0.4	121.02	115	SKS	Q2
20182533041	M027	-84	22	0.8	0.4	120.58	115	SKS	Q2
20183144083	M028	-17	9	1.4	0.3	108.68	35	SKS	Q2
20183400232	M028	-18	23	1	0.5	116.96	9	SKS	Q2
20181944094	M029	50	18	1.6	0.8	114.24	167	SKS	Q2

20183450226	MP01	-16	8	2	0.4	213.77	133	SKS	Q1
20183450226	MP01	-11	9	2.5	0.4	213.77	133	SKKS	Q1
20183450226	MP03	-32	12	2.7	0.8	213.7	133	SKKS	Q3
20183450226	MP07	6	6	2.5	0.4	213.64	133	SKS	Q2
20183450226	MP21	-15	20	1	0.4	213.27	133	SKKS	Q2
20183450226	MP22	-24	20	1	0.6	213.29	133	SKS	Q2
20183450226	MP23	-9	12	1.3	0.4	213.29	133	SKKS	Q2
20183450226	MS03	-3	9	2.3	0.4	213.72	133	SKKS	Q1
20183450226	MS05	9	14	1	0.8	213.33	133	SKS	Q3
20183450226	MS07	5	17	1.5	1	213.03	133	SKS	Q3
20190200132	MP01	-1	5	2.4	0.3	240.43	63	SKKS	Q1
20190200132	MP05	1	14	1.5	0.4	239.48	63	SKKS	Q2
20190200132	MP20	-1	15	1.2	0.5	235.81	63	SKS	Q1
20190200132	MS04	5	13	1.3	0.4	238.18	63	SKKS	Q1
20190200132	MS10	7	25	0.8	0.4	237.89	63	SKS	Q2
20190531017	MP01	2	6	1.9	0.3	335.29	145	SKS	Q1
20190531017	MP08	22	12	1.1	0.3	336.79	145	SKS	Q1
20190531017	MS01	5	5	1.1	0.1	336.59	145	SKKS	Q2
20190531017	MS02	-3	6	2.5	0.4	335.83	145	SKS	Q2
20190531017	MS10	17	22	0.7	0.3	339.31	145	SKKS	Q3
20183572308	MP02	2	7	2.4	0.2	108.2	113	SKS	Q3
20183572308	MP03	3	5	1.6	0.4	108.24	113	SKS	Q1
20183572308	MS03	-11	6	2	0.3	108.15	113	SKS	Q2
20183572308	MS08	-25	16	0.6	0.1	108.86	113	SKS	Q1
20190651546	MP08	-21	17	1	0.5	120.38	29	SKS	Q3
20190951614	MP08	0	9	1.5	0.4	216.58	58	SKS	Q1
20190951614	MP10	6	13	0.8	0.3	216.52	58	SKS	Q1
20161955121	HKA	0	4	2.3	0.2	116.03	12	SKS	Q2
20161955121	MDY	-32	11	0.9	0.2	116.9	12	SKKS	Q2
20161955121	MDY	-32	11	0.9	0.2	116.9	12	SKS	Q2
20162455163	HKA	8	5	2.2	0.2	126.22	19	SKS	Q3
20162455163	MDY	-29	22	1.1	0.7	127.03	19	SKS	Q3
20162688210	HKA	-3	5	1.7	0.2	106.27	202	SKS	Q3
20162688210	MDY	-19	14	1.2	0.3	107.21	202	SKS	Q2
20163188110	HKA	0	6	2.8	0.3	133.05	15	SKS	Q3
20172699042	HKA	-1	6	1.6	0.3	111.97	96	SKS	Q2
20172699042	YGN	-29	7	0.9	0.1	113.31	96	SKS	Q2
20182499154	HKA	-8	7	1.6	0.2	108.57	670	SKS	Q3
20182733105	HKA	-1	6	2.1	0.5	107.53	550	SKS	Q2
20183577230	HKA	-1	6	2	0.4	108.28	113	SKS	Q2
20183577230	SIM	-46	13	1.1	0.5	108.42	113	SKS	Q2
20183577230	TGI	-14	20	0.5	0.2	109.63	113	SKS	Q2
20162077172	TMU	13	9	1.2	0.5	259.11	76	SKKS	Q1
20162077172	MDY	-12	4	1.5	0.5	248.95	76	SKS	Q3

20163099162	TMU	14	6	1.2	0.2	226.29	95	SKKS	Q1
20163099162	MDY	-15	3	1.3	0.1	218.1	95	SKKS	Q1
20180288160	TMU	13	10	1.2	0.4	218.66	10	SKS	Q1
20180288160	MDY	-23	16	1.1	0.5	218.62	10	SKS	Q1
20180288160	NGU	1	9	1	0.2	218.28	10	SKKS	Q1
20183199200	TMU	-4	20	1.4	0.6	216.37	15	SKS	Q1
20162344034	MDY	-13	18	1.2	0.4	215.59	12	SKS	Q1
20163133045	MDY	-19	7	1.8	0.3	209.29	170	SKKS	Q1
20170555172	MDY	-25	11	1	0.2	113.25	414	SKS	Q2
20170555172	YGN	-23	8	1.1	0.2	113.53	414	SKS	Q2
20170555234	MDY	-22	10	1	0.3	108.24	581	SKS	Q2
20171211141	MDY	-42	12	1.6	0.8	23.78	7	SKS	Q2
20171300232	MDY	-21	11	1	0.3	215.49	15	SKS	Q1
20182311001	YGN	-32	9	0.9	0.2	108.45	600	SKKS	Q2
20182599211	YGN	-31	14	1	0.5	116.41	576	SKS	Q2
20183344172	YGN	-1	4	1.2	0.2	26.23	54	SKS	Q1
20180233093	NGU	-8	31	2.3	0.8	30.47	10	SKS	Q3
20183222202	SIM	-36	8	0.7	0.2	107.33	540	SKS	Q2

Station average XKS splitting results

Station	Lat	Lon	φ(°)	Δφ(°)	δt(s)	Δδt(s)	No of good results
EW01	92.877	20.152	-36	8	0.8	0.2	7
EW02	94.043	19.795	-24	7	1.8	0.1	12
EW04	94.517	20.342	163	12	0.6	0.3	3
EW06	96.583	20.653	-4	10	0.8	0.3	1
EW07	97.138	20.786	-51	12	0.9	0.3	3
M001	95.93	21.245	-28	8	1.3	0.2	8
M002	96.045	20.835	0	12	0.8	0.4	3
M003	96.317	18.981	-25	9	1.5	0.3	5
M004	96.182	19.305	-16	11	1.3	0.2	6
M005	95.956	20.026	162	8	1.2	0.1	11
M006	96.199	19.544	166	9	1.6	0.2	6
M007	95.616	20.473	-26	8	1.5	0.2	8
M008	95.556	20.043	133	9	0.7	0.4	2
M009	96.187	19.933	-30	3	1.3	0.1	1
M010	96.216	20.478	152	12	1.3	0.3	4
M011	96.398	18.42	158	7	1.7	0.4	2
M012	95.798	17.971	151	7	0.8	0.1	1
M021	94.137	21.473	13	2	1.7	0.4	1
M022	94.827	21.318	-26	6	1.4	0.4	2
M023	94.986	22.184	-52	5	1.6	0.3	5

M024	93.99	23.193	24	23	1.1	0.4	1
M025	95.54	23.193	-9	14	0.9	0.3	3
M028	96.007	24.32	163	8	1.3	0.2	8
M029	95.699	25.987	50	10	1.2	0.3	5
MP01	93.572	23.351	-5	7	2.2	0.3	4
MP02	93.641	23.298	-1	8	2.5	0.4	2
MP03	93.728	23.236	3	5	1.6	0.4	1
MP05	93.953	23.217	1	14	1.5	0.4	1
MP07	94.134	23.232	6	6	2.5	0.4	1
MP08	94.236	23.26	9	10	1.3	0.4	2
MP10	94.371	23.181	6	13	0.8	0.3	1
MP21	96.124	23.12	-15	20	1	0.4	1
MP23	96.018	23.105	-9	12	1.3	0.4	1
MS02	93.696	23.606	-3	6	2.5	0.4	1
MS03	93.437	23.153	-8	7	2.1	0.4	2
MS04	93.996	22.83	5	13	1.3	0.4	1
MS08	95.321	22.691	-25	16	0.6	0.1	1
HKA	93.6	22.649	7	7	2	0.2	10
TMU	94.3	24.23	13	8	1.2	0.3	3
MDY	96.112	22.016	-19	10	1.2	0.2	10
YGN	96.153	16.865	-13	7	1.2	0.2	6
NGU	94.916	21.205	1	9	1	0.2	1
SIM	92.885	20.133	-40	10	0.8	0.4	2
TGI	97.034	20.768	-14	20	0.5	0.2	1

List of XKS null results

Event ID	Station	φ(°)	BAZ	Distance (°)	Phase
20190651546	MP01	5	120.16	100.84	SKS
20190690812	MP02	-20	107.25	94.92	SKS
20191131420	MP03	15	113.65	97.28	SKS
20183572308	MP04	65	108.28	98.71	SKS
20190321614	MP04	12	9.96	141.92	SKS
20190531017	MP04	-8	335.81	157.3	SKS
20183222025	MP05	26	107.47	94.33	SKS
20183450226	MP05	-67	213.66	125.27	SKS
20183572308	MP05	16	108.32	98.62	SKS
20190051925	MP05	3	314.9	159.57	SKKS
20190321614	MP05	-47	10.13	141.91	SKS
20183572308	MP06	17	108.35	98.55	SKS
20191131420	MP06	8	113.75	97.02	SKS
20190200132	MP08	71	239.23	165.48	SKS

20191131420	MP08	32	113.82	96.86	SKS
20183450226	MP09	-51	213.6	125.43	SKS
20183572308	MP09	17	108.45	98.3	SKS
20190321614	MP09	-82	10.68	141.87	SKKS
20183450226	MP10	-9	213.59	125.45	SKKS
20183450226	MP10	39	213.59	125.45	SKS
20190690812	MP10	-37	107.53	94.25	SKS
20190261956	MP11	-59	110.58	95.11	SKS
20190690812	MP11	-32	107.55	94.2	SKS
20183450226	MP13	-62	213.56	125.59	SKS
20183572308	MP13	-83	108.55	98.04	SKS
20190321614	MP14	74	11.5	141.82	SKS
20190531017	MP14	-2	338.15	157.72	SKS
20183572308	MP16	-20	108.77	97.5	SKS
20191131420	MP18	-38	114.29	95.68	SKS
20183572308	MP19	-53	108.94	97.07	SKS
20190261956	MP19	28	111.04	93.99	SKS
20190261956	MP20	34	111.14	93.76	SKS
20190651546	MP20	-49	120.94	98.82	SKS
20183450226	MP21	-35	213.27	126.29	SKS
20183572308	MP21	-42	109.1	96.69	SKS
20183572308	MP23	-19	109.06	96.78	SKS
20190261956	MP23	-11	111.17	93.71	SKS
20183572308	MP25	7	108.11	99.13	SKS
20191131420	MP25	14	113.52	97.6	SKS
20183450226	MS02	9	213.85	125.46	SKS
20183450226	MS03	-1	213.72	124.95	SKS
20191131420	MS03	51	113.56	97.49	SKS
20183572308	MS04	23	108.39	98.46	SKS
20191131420	MS04	78	113.78	96.89	SKS
20190200132	MS05	17	236.63	165.34	SKKS
20183450226	MS06	-19	213.51	126.39	SKSS
20183572308	MS06	-60	108.89	97.22	SKS
20190200132	MS06	-36	237.92	166.74	SKKS
20190321614	MS06	-58	12.67	141.3	SKKS
20191131420	MS06	23	114.3	95.77	SKS
20183572308	MS07	5	109.06	96.75	SKS
20190261956	MS07	-2	111.13	93.65	SKS
20183572308	MS10	-33	108.76	97.52	SKS
20190321614	MS10	23	12.09	141.58	SKS
20190690812	MS10	24	107.84	93.53	SKS
20180230931	EW01	5	29.81	88.05	SKS
20182530419	EW01	-2	120.6	98.5	SKS
20180230931	EW02	-38	30.17	87.81	SKS

20182310023	EW02	-1	107.85	94.57	SKS
20180230931	EW03	-49	30	88.37	SKS
20180281603	EW04	-47	218.08	102.98	SKS
20183101611	EW04	-69	110.53	98.29	SKS
20183572308	EW04	22	108.88	97.21	SKS
20190271016	EW04	-22	109.57	94.71	SKS
20172690420	EW05	24	112.7	96.28	SKS
20172911200	EW05	-61	108.94	97.97	SKS
20182530419	EW05	-46	121.17	96.86	SKS
20172310200	EW06	0	108.58	91.33	SKS
20172690420	EW06	24	113.16	95.06	SKS
20172911200	EW06	19	109.38	96.7	SKS
20173080900	EW06	-13	104.21	95.51	SKS
20182310019	EW06	0	108.49	91.99	SKS
20182310428	EW06	-86	107.39	91.7	SKS
20182530419	EW06	18	121.6	95.78	SKS
20182592111	EW06	18	116.49	91.5	SKS
20182731052	EW06	-82	108.69	92.16	SKS
20183101611	EW06	-77	111.12	96.59	SKS
20183572308	EW06	7	109.5	95.48	SKS
20172310200	EW07	-47	108.77	90.88	SKS
20173080900	EW07	-21	104.39	95.04	SKS
20180920557	EW07	26	114.41	94.99	SKS
20182310428	EW07	-42	107.58	91.24	SKS
20182731052	EW08	2	109.01	91.39	SKS
20180230931	M001	-42	30.78	85.67	SKS
20182530419	M002	20	121.42	96.31	SKS
20182592111	M002	22	116.31	92.03	SKS
20183572308	M002	21	109.31	96.01	SKS
20172690420	M003	33	113.21	94.64	SKS
20182310023	M003	-54	108.6	92.27	SKS
20182530419	M004	-30	121.6	95.4	SKS
20183222025	M004	37	108.42	91.15	SKS
20190271016	M004	33	110.16	92.89	SKS
20172310200	M006	-6	108.48	91.32	SKS
20181242232	M006	-84	65.25	100.18	SKS
20172310200	M007	22	108.26	92.13	SKS
20180581729	M007	-22	155.82	91.96	SKS
20172911200	M008	9	109.14	97.41	SKS
20180281603	M008	23	218.22	103.34	SKS
20183572308	M008	-47	109.24	96.19	SKS
20190271016	M008	14	109.92	93.69	SKS
20171971706	M010	34	108.98	97.2	SKS
20172310200	M010	-7	108.46	91.6	SKS

20172690420	M010	-7	113.06	95.31	SKS
20172911200	M010	-9	109.29	96.97	SKS
20180230931	M010	-49	30.84	86.18	SKS
20180581729	M010	-60	156.01	91.74	SKS
20182310023	M010	-53	108.51	92.84	SKS
20182592111	M010	-48	116.38	91.73	SKS
20172431746	M012	-34	29.61	85.1	SKS
20172690420	M012	-49	113.13	94.69	SKS
20182310428	M012	-55	107.21	91.61	SKS
20182592111	M012	23	116.3	90.98	SKS
20183222025	M012	-45	108.33	91.08	SKS
20183572308	M012	25	109.5	95.29	SKS
20172690420	M021	-17	112.3	97.48	SKS
20182530419	M021	25	120.79	98.16	SKS
20182592111	M021	-27	115.63	93.91	SKS
20183222025	M021	16	107.65	93.65	SKS
20183402326	M021	-56	115.97	85.51	SKS
20190271016	M021	15	109.35	95.42	SKS
20182310428	M022	-86	106.76	93.46	SKS
20182592111	M022	16	115.87	93.26	SKS
20183572308	M022	16	108.86	97.25	SKS
20180281603	M023	5	218.45	104.69	SKS
20180581729	M023	31	155.58	93.76	SKS
20180920557	M023	-53	113.57	97.39	SKS
20182310023	M023	-47	107.98	94.46	SKS
20182310428	M023	-57	106.77	93.57	SKS
20182531931	M023	-45	115.82	85.39	SKS
20183222025	M023	16	107.91	93.11	SKS
20183402326	M023	-53	116.36	85.11	SKS
20190271016	M023	23	109.58	94.92	SKS
20172310200	M024	25	107.54	94.4	SKS
20172690420	M024	24	112.03	98.26	SKS
20172911200	M024	11	108.19	99.79	SKS
20180230931	M024	10	30.26	84.91	SKS
20181940946	M024	48	113.21	84.36	SKS
20182531931	M024	27	115.48	86.65	SKS
20182592111	M024	24	115.47	94.77	SKS
20182890028	M024	65	115.7	86.07	SKS
20183572308	M024	60	108.34	98.58	SKS
20190261956	M024	26	110.42	95.49	SKS
20172690420	M025	26	112.57	96.94	SKS
20172812048	M025	-1	155.73	96.85	SKS
20180281603	M025	-16	218.72	105.79	SKS
20181242232	M025	58	64.4	99.19	SKS

20182310023	M025	14	108.11	94.28	SKS
20182531931	M025	10	116.13	85.37	SKS
20182592111	M025	32	116.03	93.49	SKS
20183101611	M025	-7	110.46	98.39	SKS
20183222025	M025	-14	108.07	92.94	SKS
20190101700	M025	16	115.23	99.25	SKS
20190261956	M025	-41	110.99	94.15	SKS
20172690420	M026	29	112.11	98.07	SKS
20181940946	M026	55	113.44	84.19	SKS
20182531931	M026	48	115.68	86.51	SKS
20182890028	M026	64	115.9	85.92	SKS
20183140833	M026	48	108.2	99.35	SKS
20173080900	M027	-34	103.13	98.01	SKS
20182310428	M027	23	106.56	94.41	SKS
20182592111	M027	27	115.68	94.74	SKS
20183101611	M027	14	109.99	99.52	SKS
20183140833	M027	7	108.19	99.29	SKS
20183222025	M027	-88	107.73	94	SKS
20172690420	M028	25	112.61	96.97	SKS
20172911200	M028	0	108.73	98.4	SKS
20182731052	M028	3	108.3	93.83	SKS
20190101700	M028	11	115.22	99.34	SKS
20172632009	M029	62	114.1	84.02	SKS
20183222025	M029	58	107.98	93.66	SKS
20190261956	M029	20	110.84	95.01	SKS
20162071726	HKA	3	253.45	165.14	SKS
20162522146	HKA	4	148.02	94.89	SKS
20172831853	HKA	-14	217.28	105.23	SKKS
20161580235	TMU	29	118.35	100	SKS
20161951211	TMU	39	115.99	100.38	SKKS
20161951211	TMU	-50	115.99	100.38	SKS
20162682107	TMU	-64	106.31	97.89	SKS
20162921636	TMU	20	112.86	95.74	SKS
20163130455	TMU	16	217.35	163.9	SKKS
20163190034	TMU	-19	132.88	98.41	SKS
20172911200	TMU	35	108.13	99.85	SKS
20182310019	TMU	32	107.45	95.1	SKKS
20182491549	TMU	25	108.75	93.08	SKS
20182731052	TMU	42	107.64	95.28	SKS
20182890028	TMU	34	115.89	86.26	SKS
20183390414	TMU	59	116.04	86.19	SKS
20183450226	TMU	8	214.02	126.29	SKS
20183572308	TMU	16	108.3	98.63	SKS
20162522146	KTN	75	150.05	90.87	SKS

20163181102	KTN	54	135.01	92.8	SKS
20170551728	KTN	27	114.5	90.95	SKKS
20170551728	KTN	67	114.5	90.95	SKS
20172911200	KTN	-86	110.31	94.27	SKS
20183030213	KTN	80	131.06	92.47	SKS
20170491210	MDY	-42	259.78	164.56	SKKS
20171081749	MDY	38	335.32	159.08	SKKS
20163181102	YGN	-31	134.12	92.03	SKS
20172690420	NGU	-51	112.58	96.71	SKKS
20172911200	NGU	-53	108.79	98.35	SKKS
20172690420	TGI	-50	113.29	94.72	SKS
20172911200	TGI	-25	109.51	96.34	SKS

BAZ variations of splitting parameters (local)

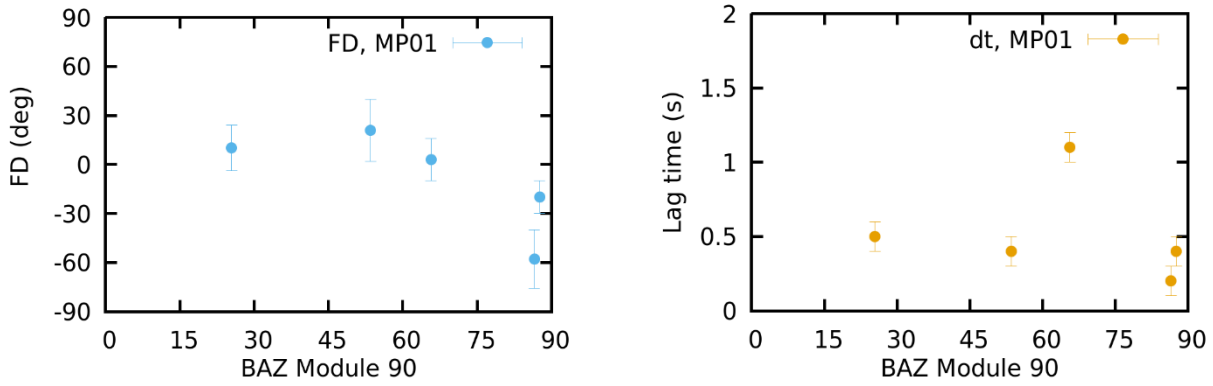

MP01

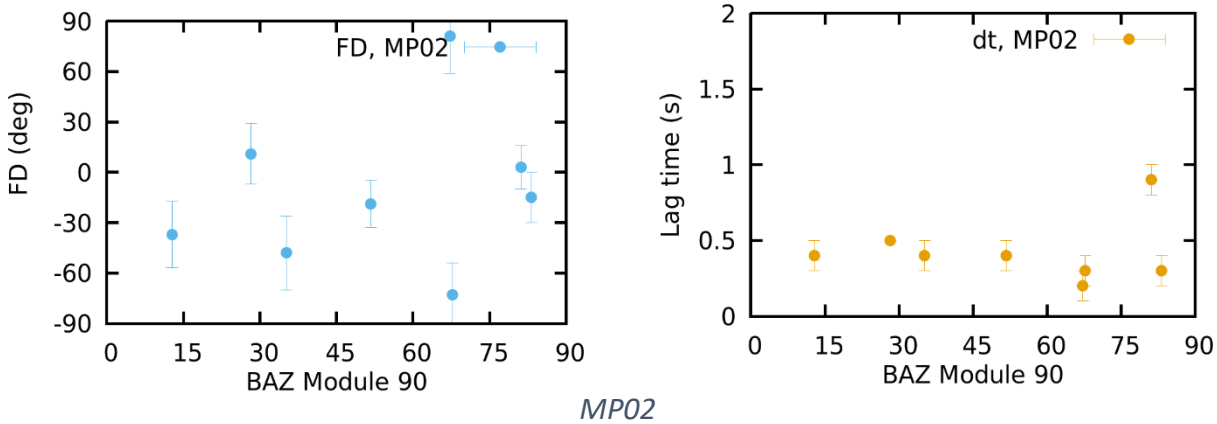

MP02

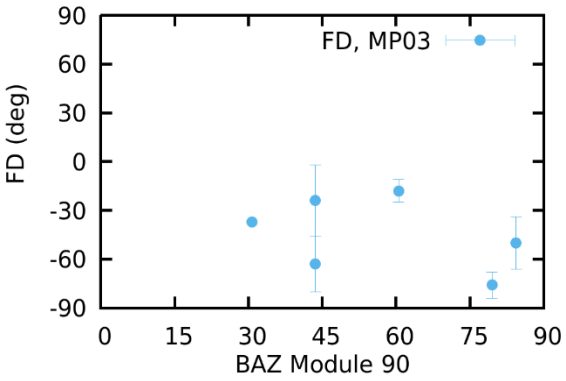

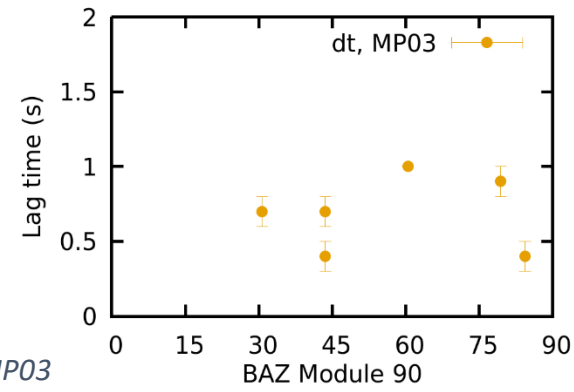

MP03

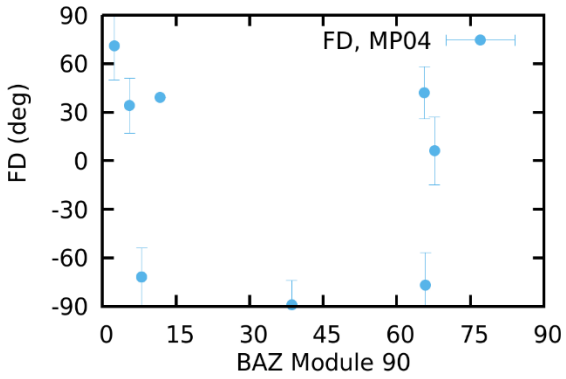

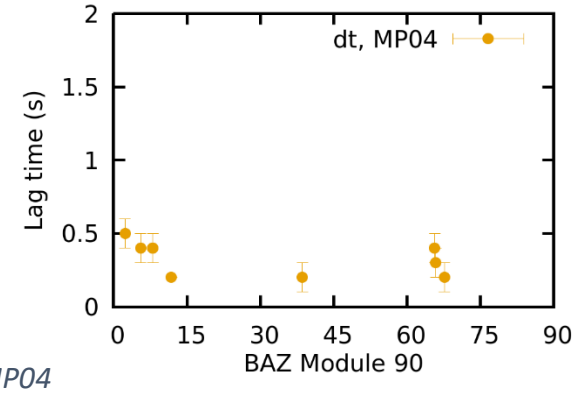

MP04

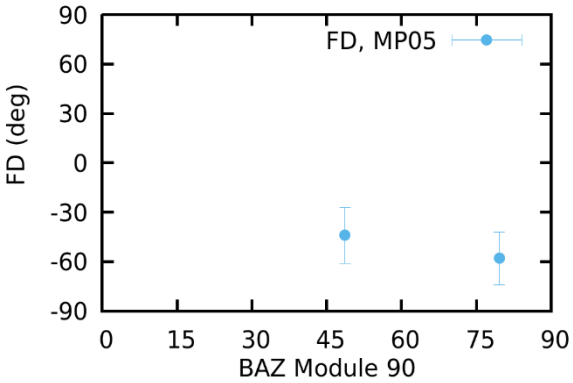

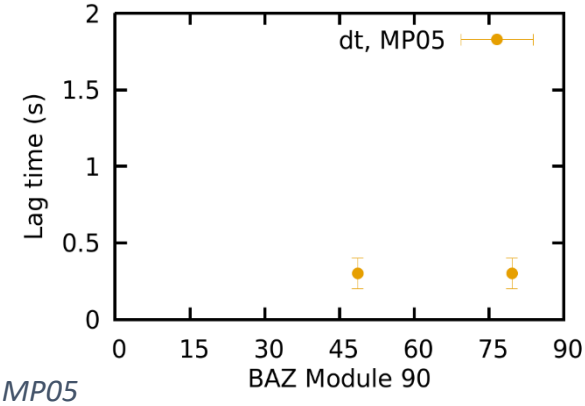

MP05

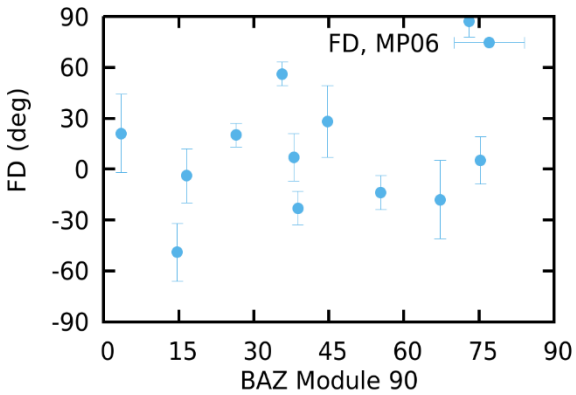

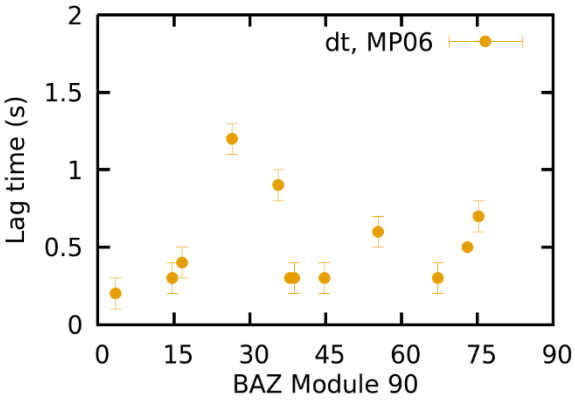

MP06

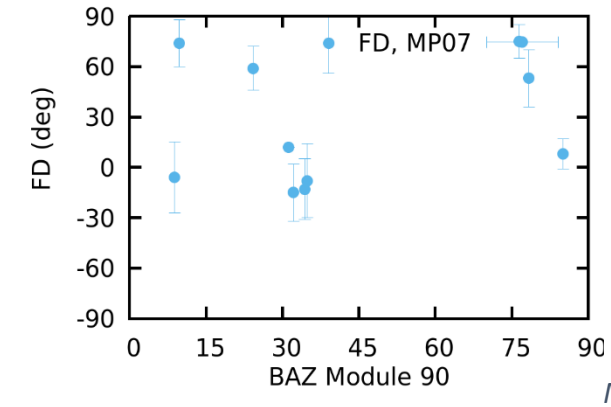

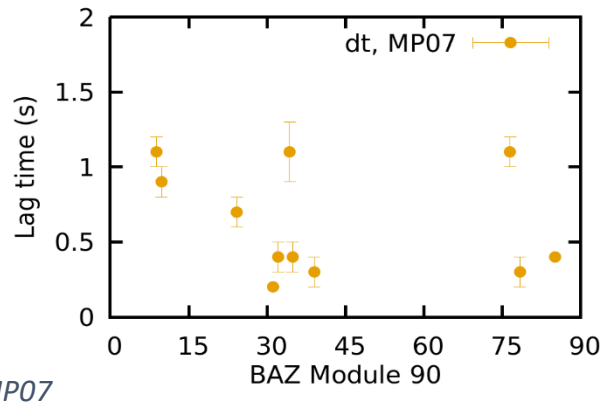

MP07

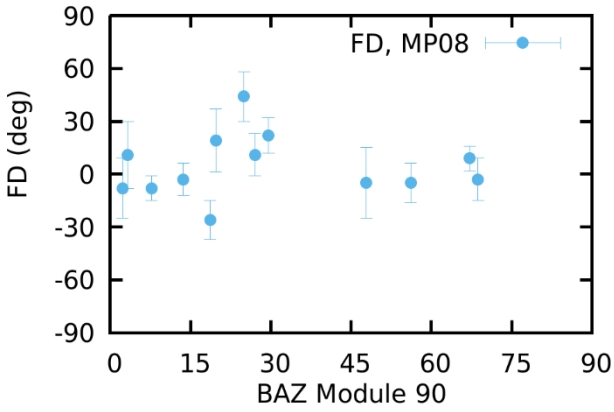

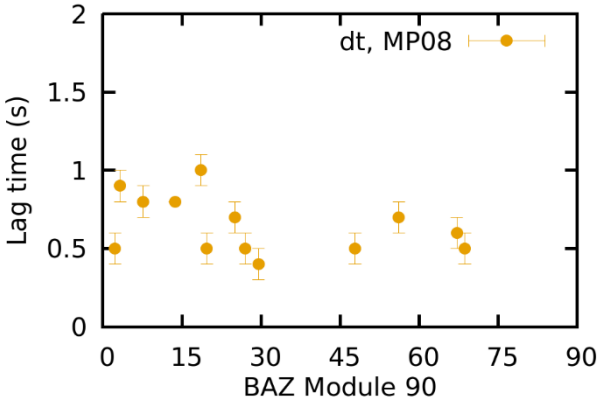

MP08

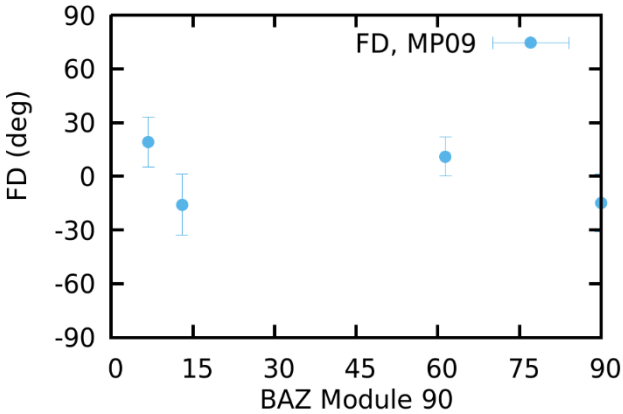

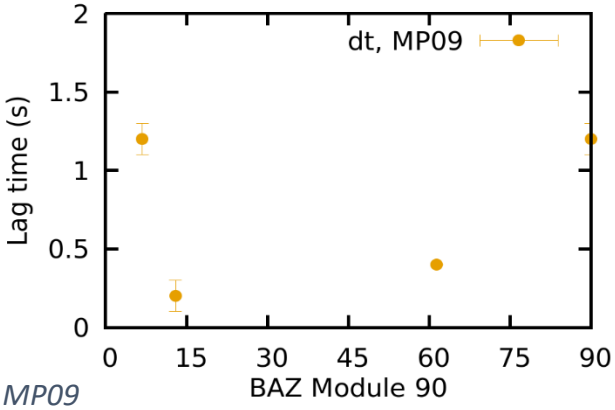

MP09

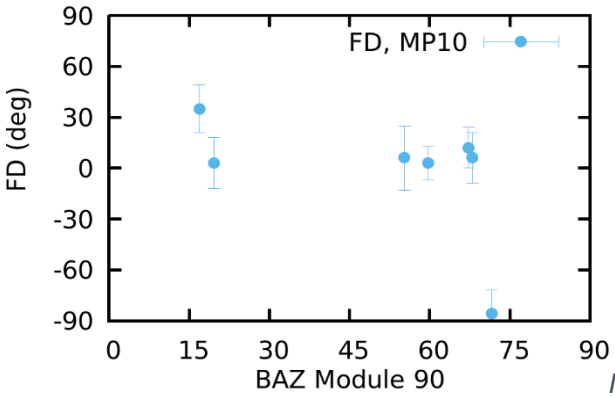

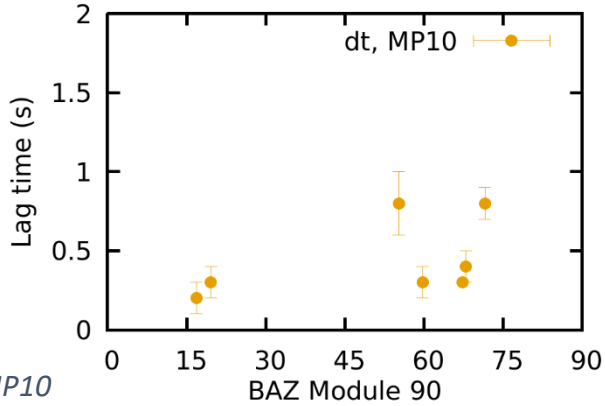

MP10

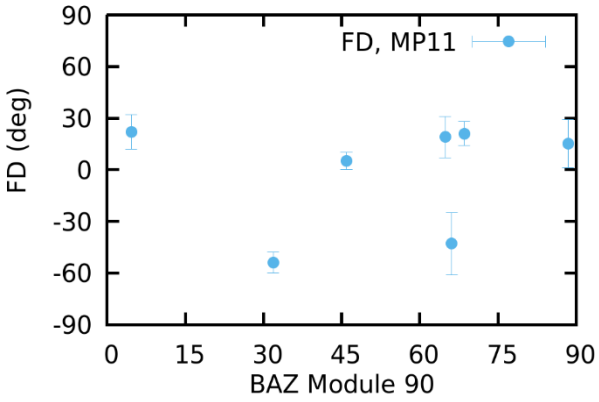

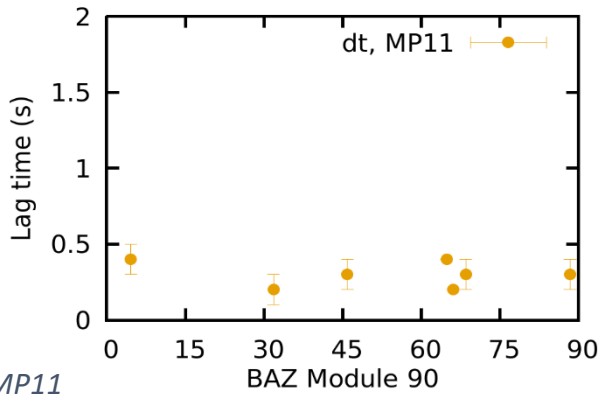

MP11

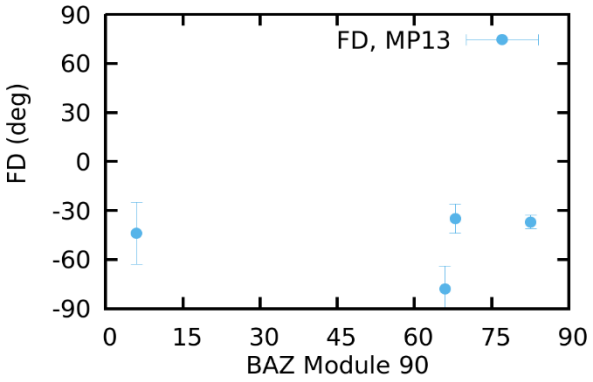

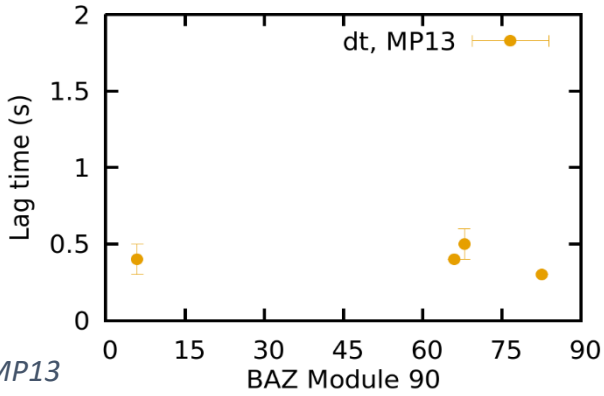

MP13

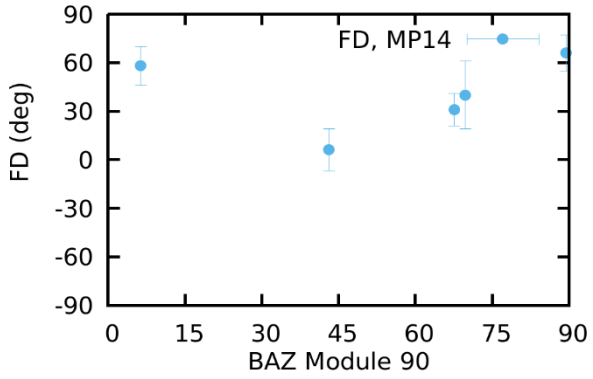

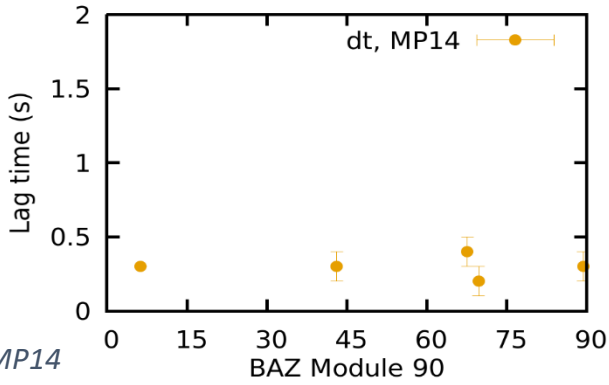

MP14

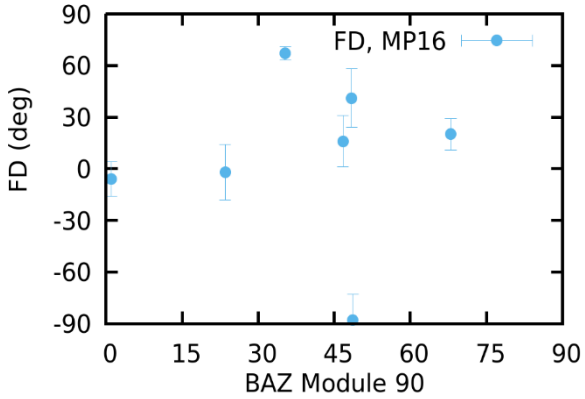

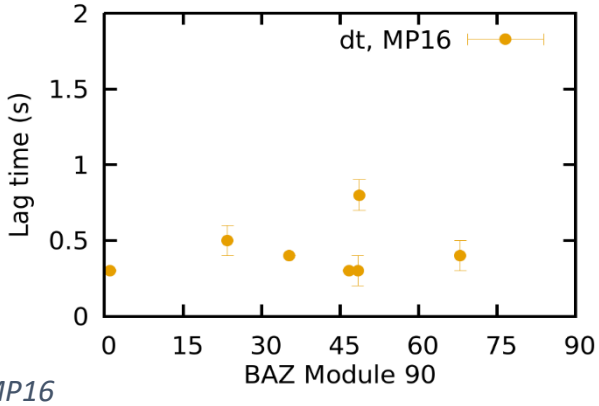

MP16

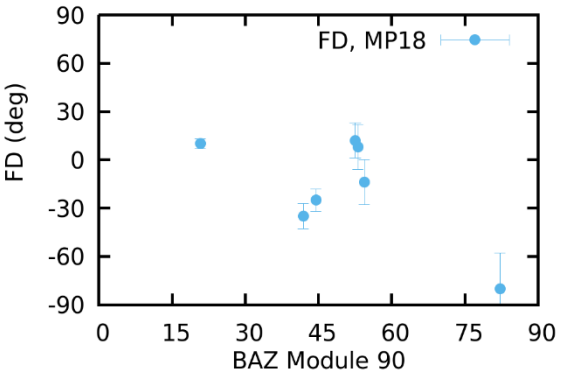

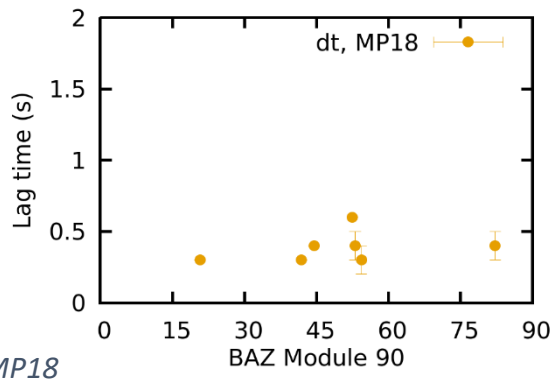

MP18

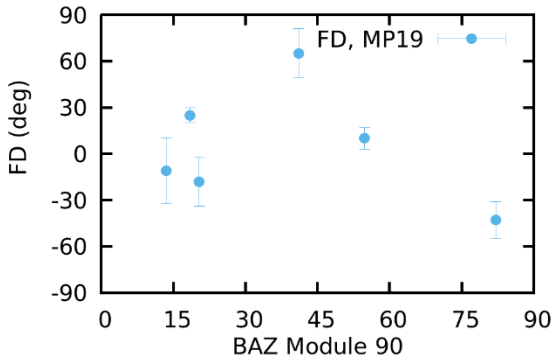

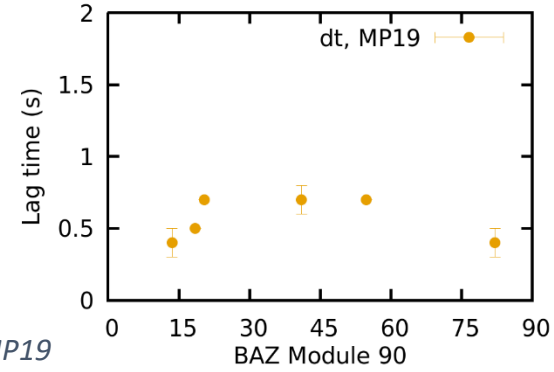

MP19

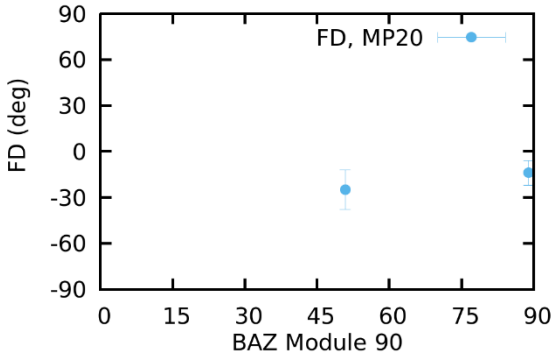

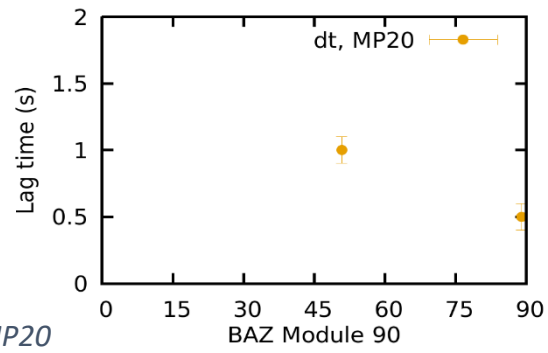

MP20

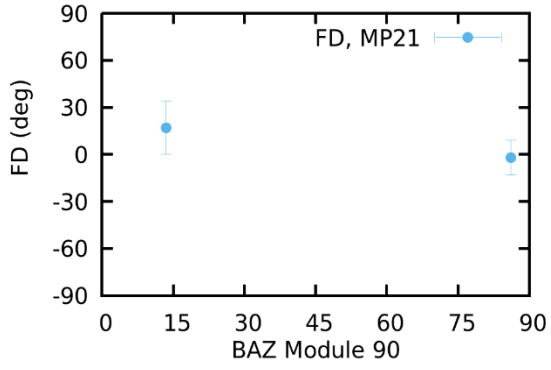

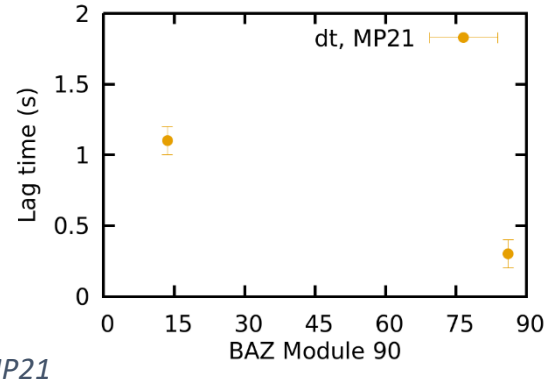

MP21

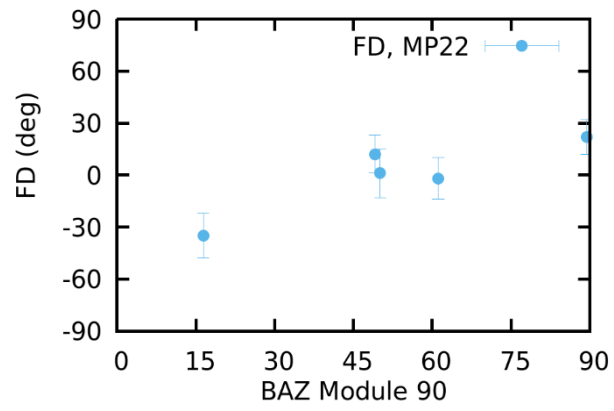

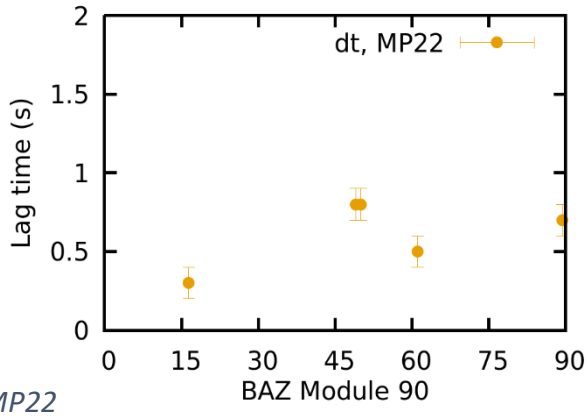

MP22

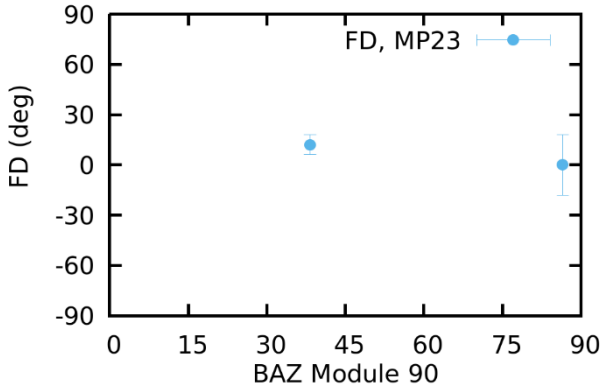

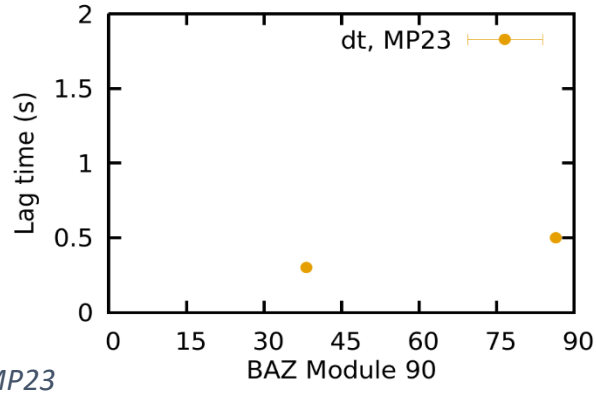

MP23

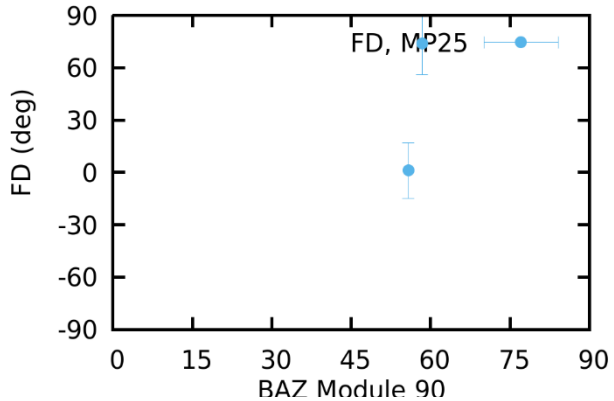

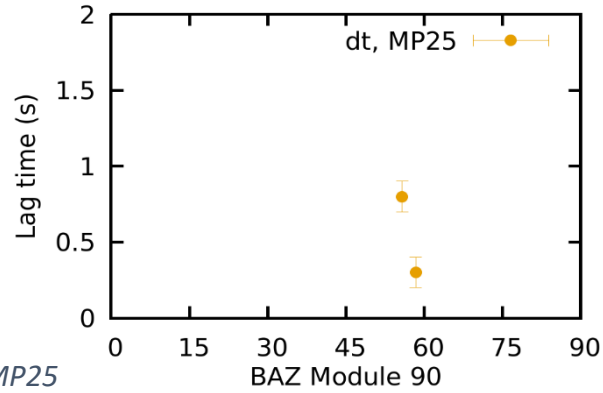

MP25

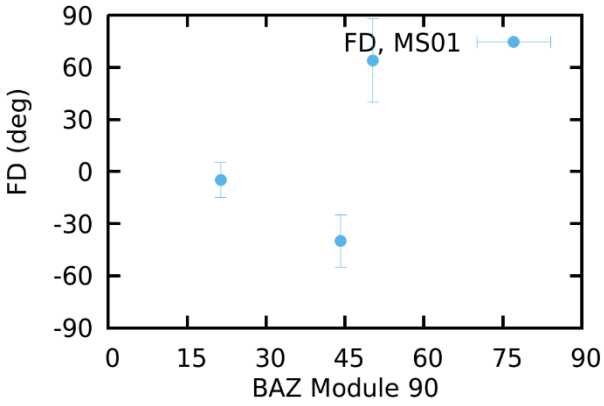

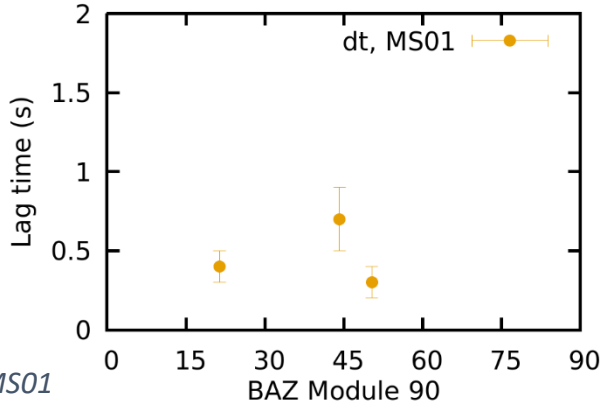

MS01

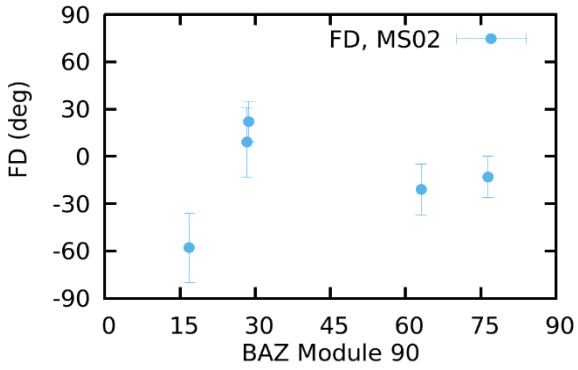

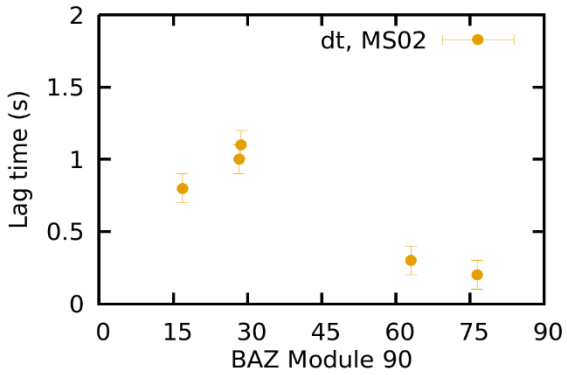

MS02

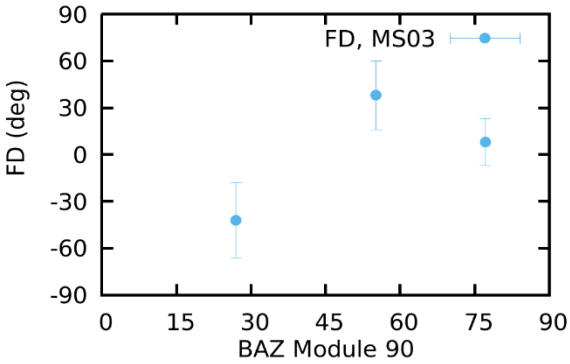

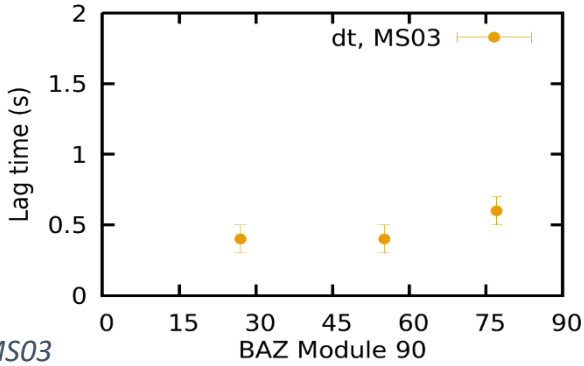

MS03

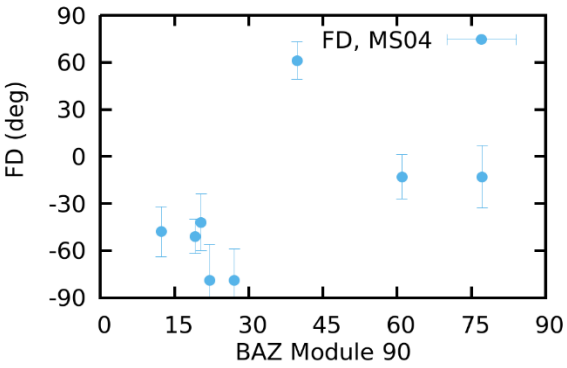

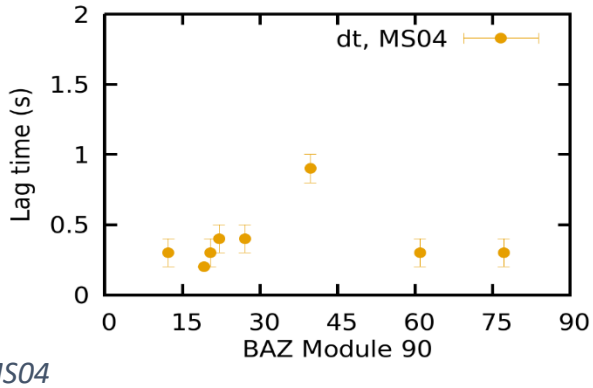

MS04

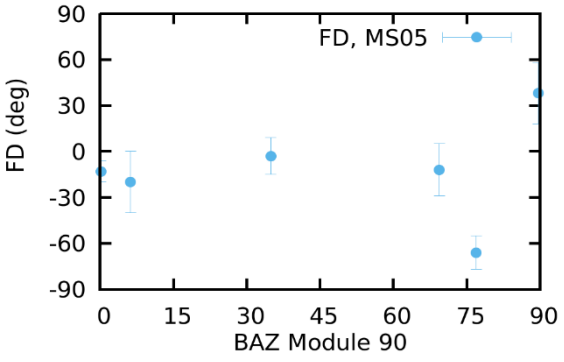

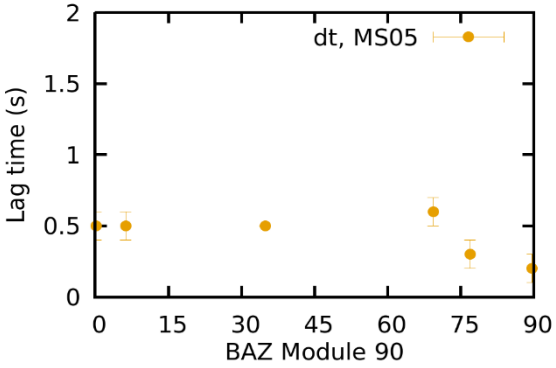

MS05

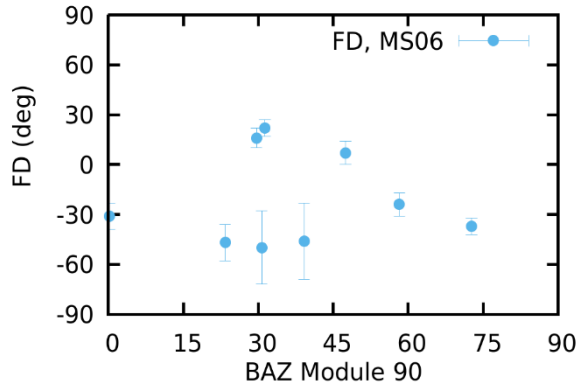

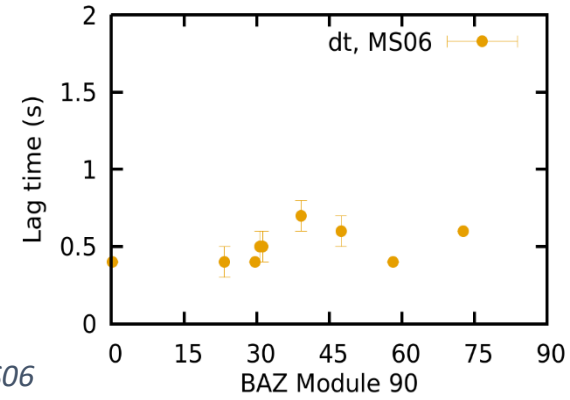

MS06

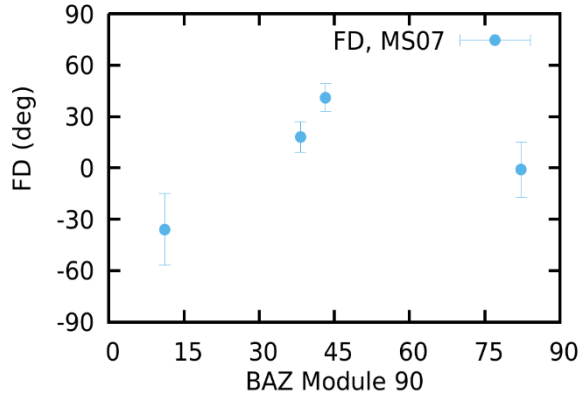

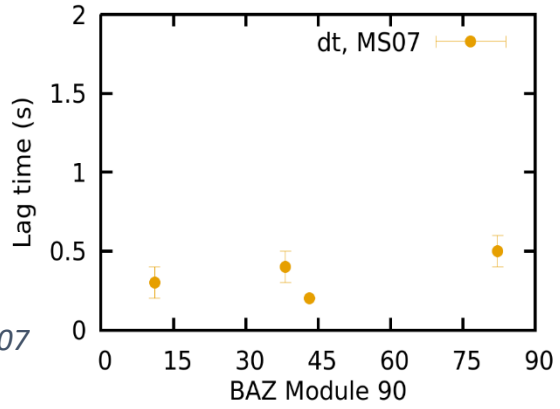

MS07

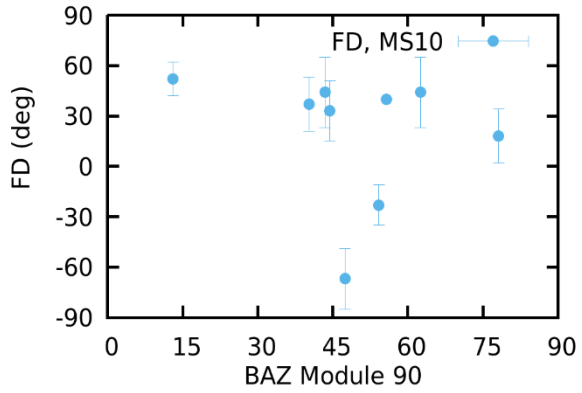

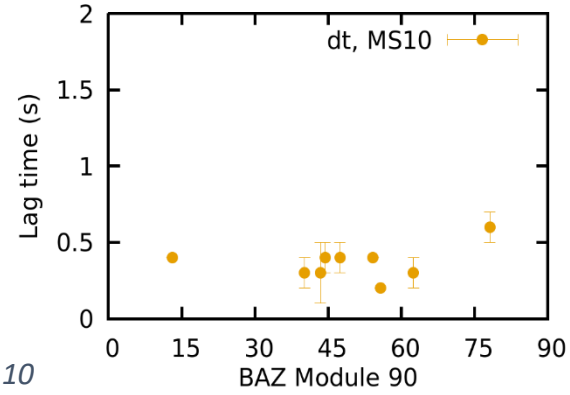

MS 10

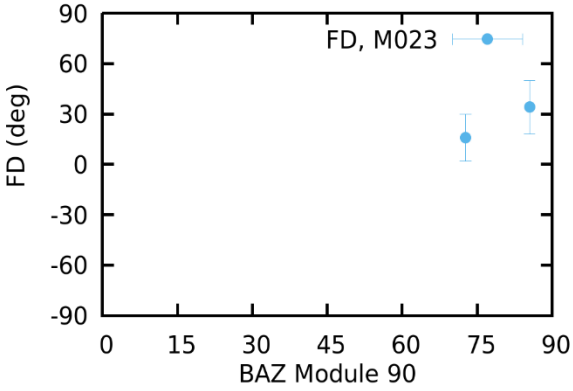

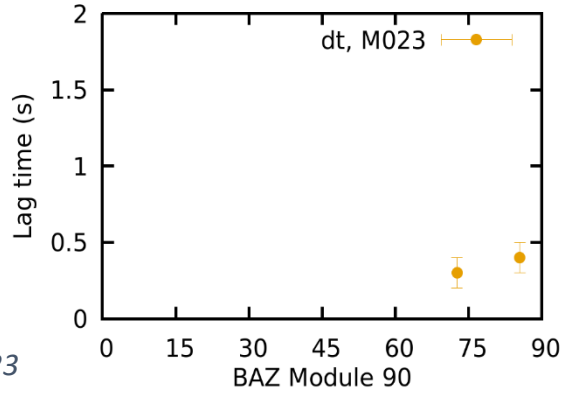

M023

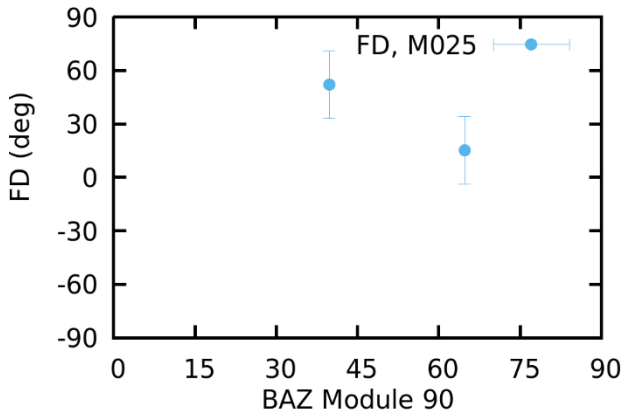
FD, M025
FD (deg)
BAZ Module 90
90
60
30
0
-30
-60
-90
0
15
30
45
60
75
90

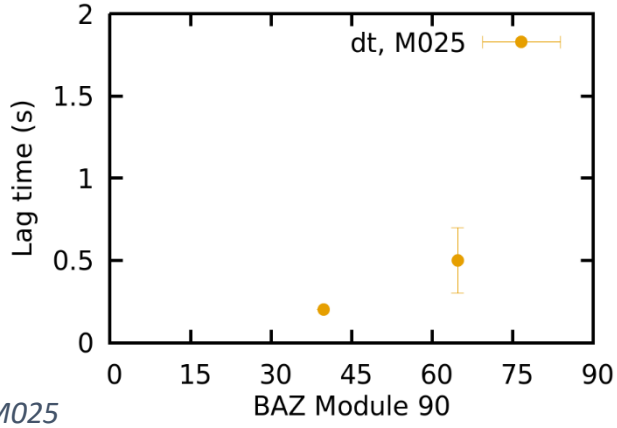
dt, M025
Lag time (s)
BAZ Module 90
2
1.5
1
0.5
0
0
15
30
45
60
75
90

M025

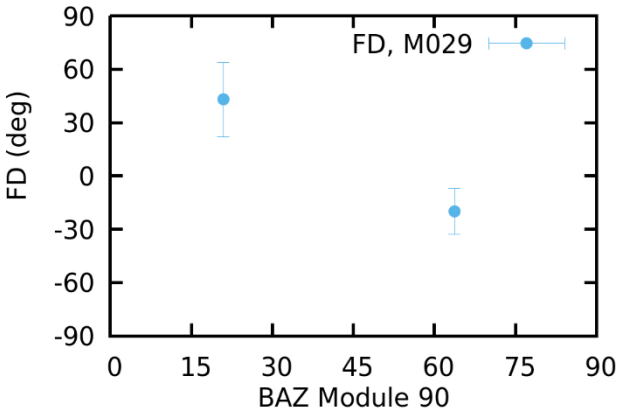
FD, M029
FD (deg)
BAZ Module 90
90
60
30
0
-30
-60
-90
0
15
30
45
60
75
90

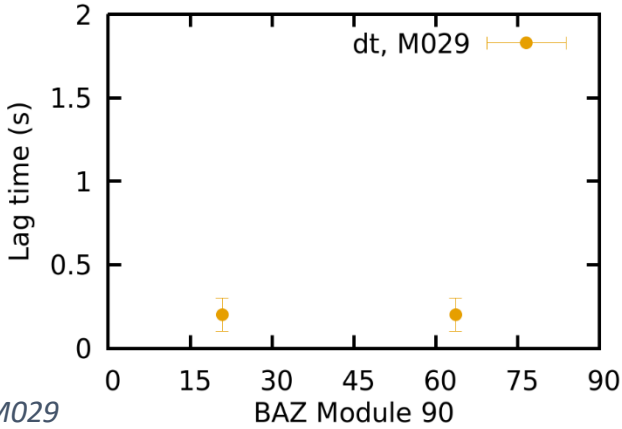
dt, M029
Lag time (s)
BAZ Module 90
2
1.5
1
0.5
0
0
15
30
45
60
75
90

M029

BAZ variations of splitting parameters (XKS)

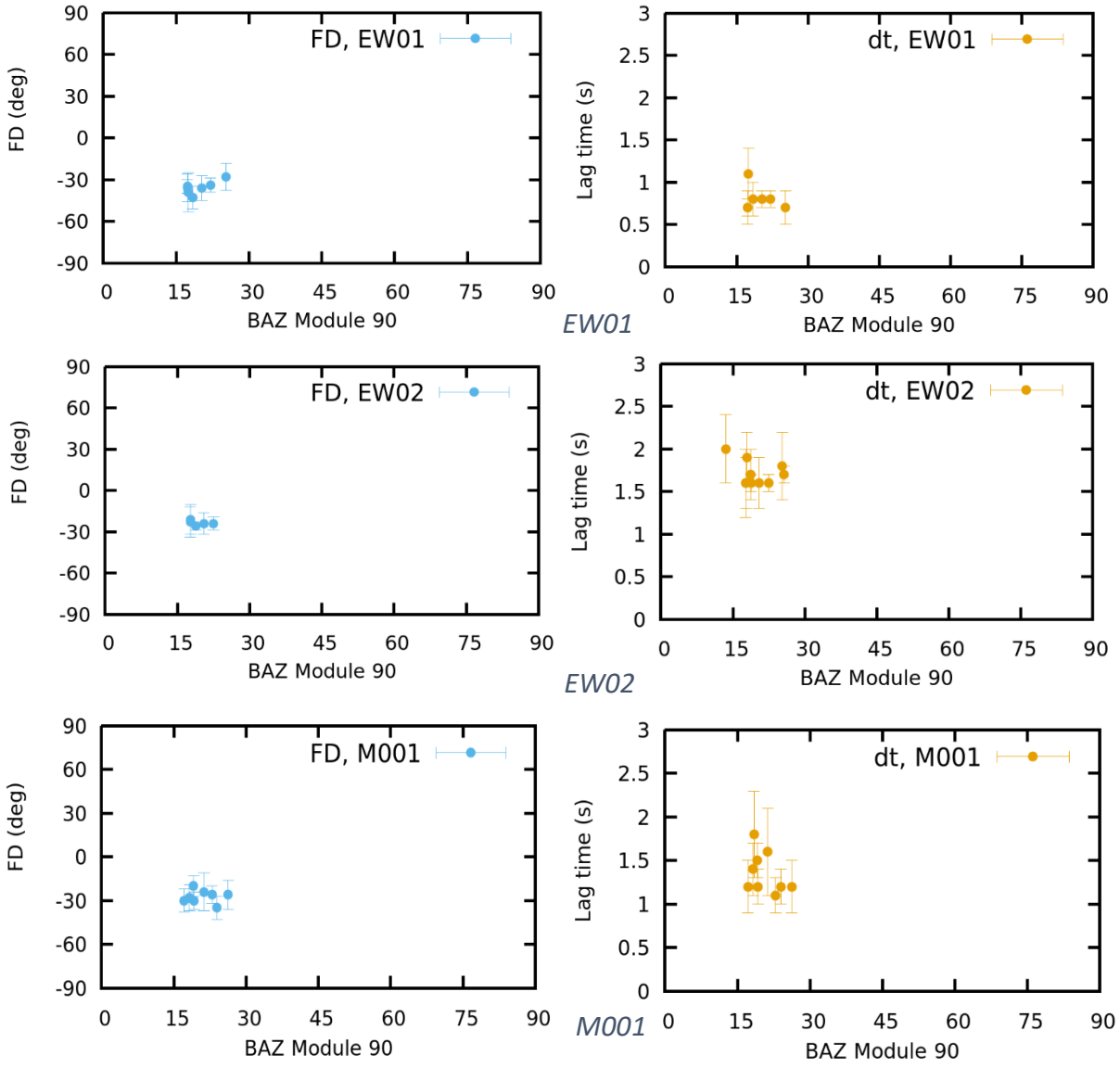

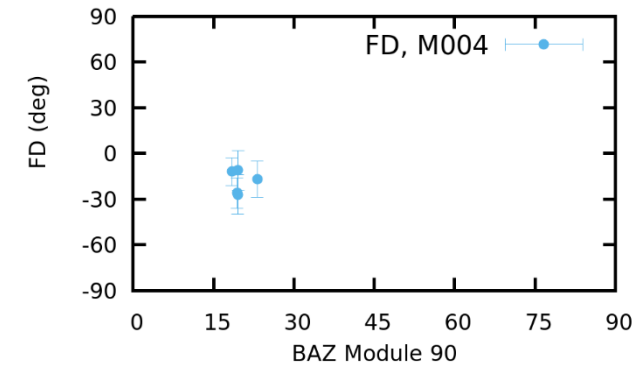

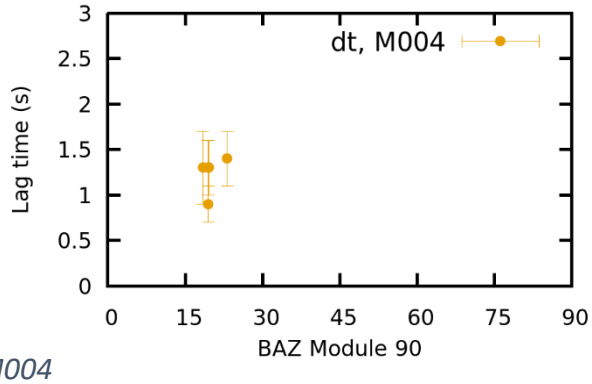

M004

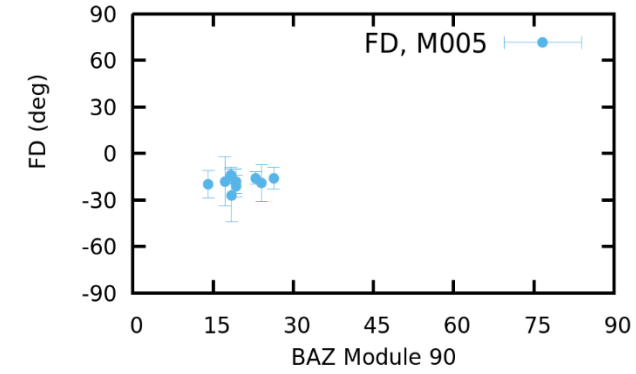

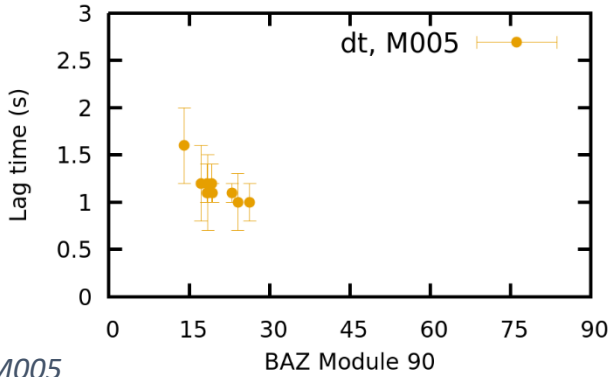

M005

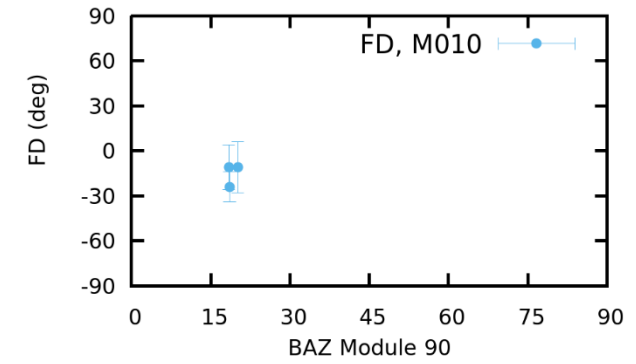

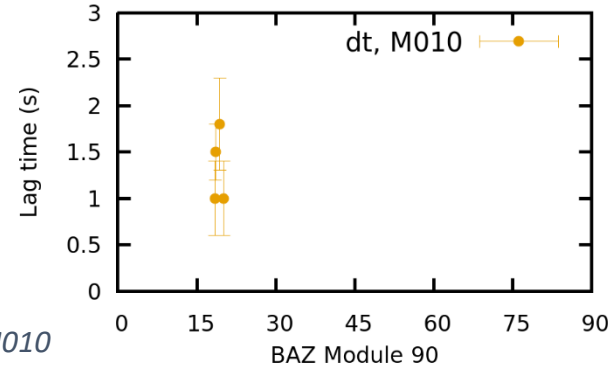

M010

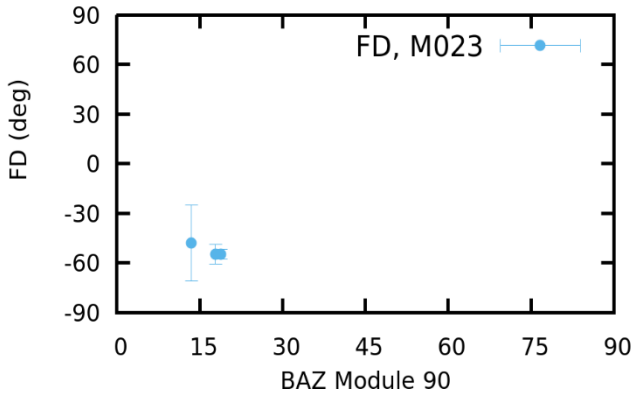

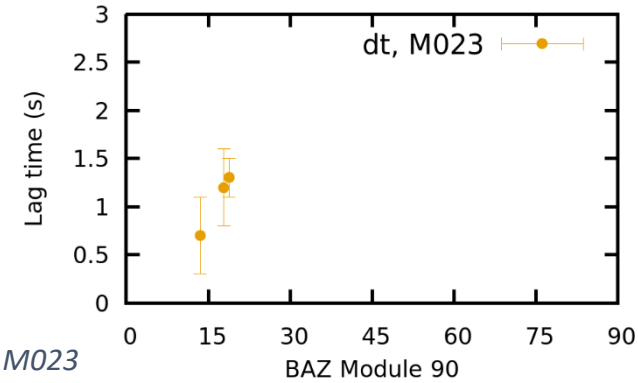

M023

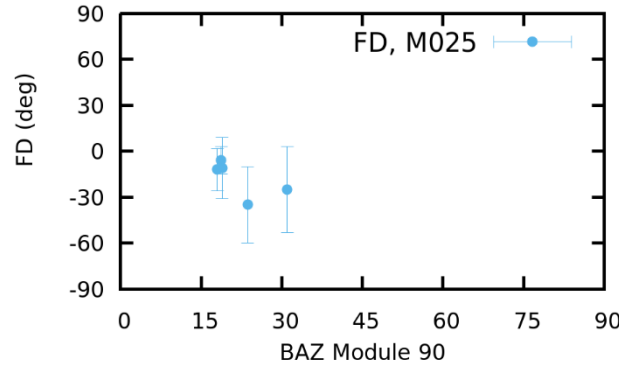

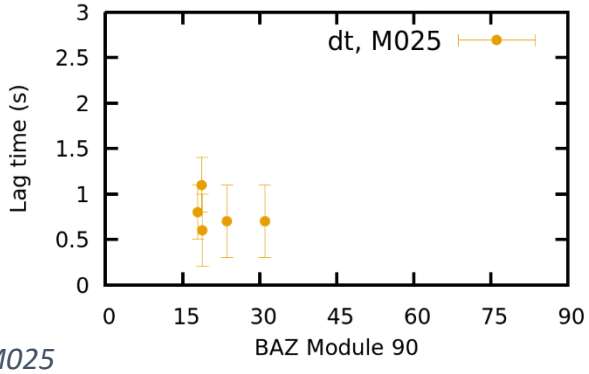

M025

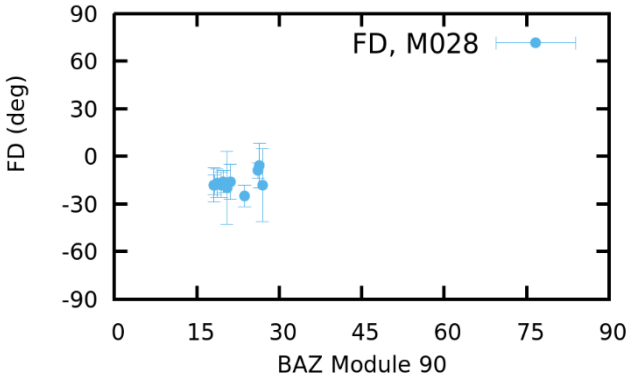

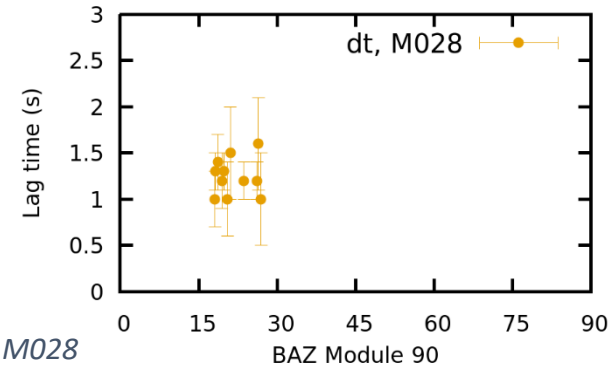

M028

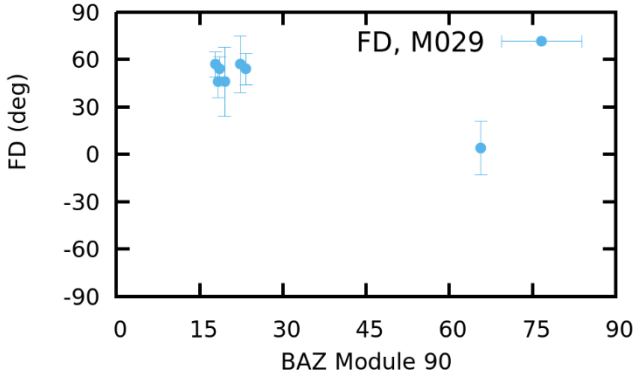

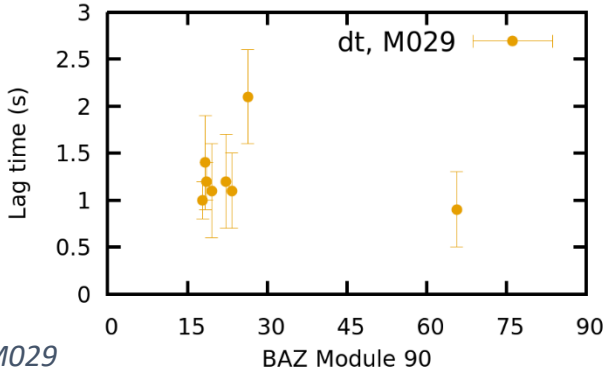

M029

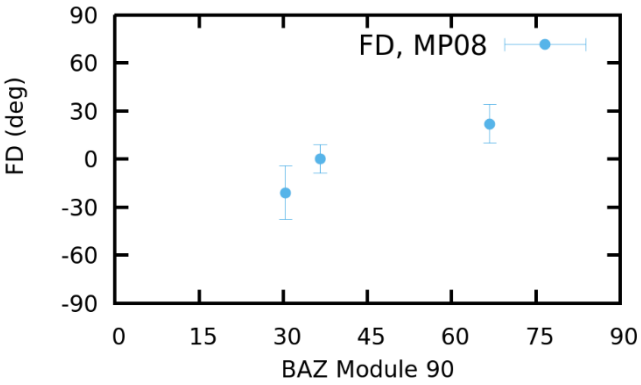

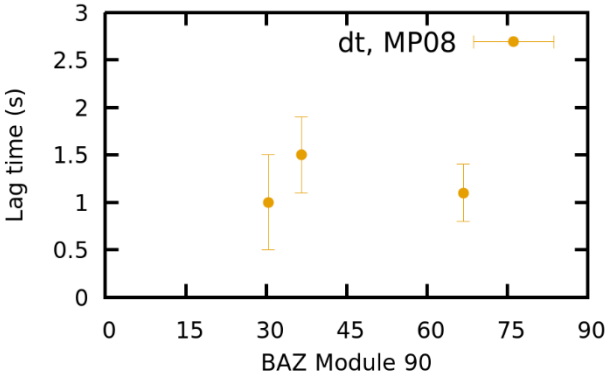

MP08

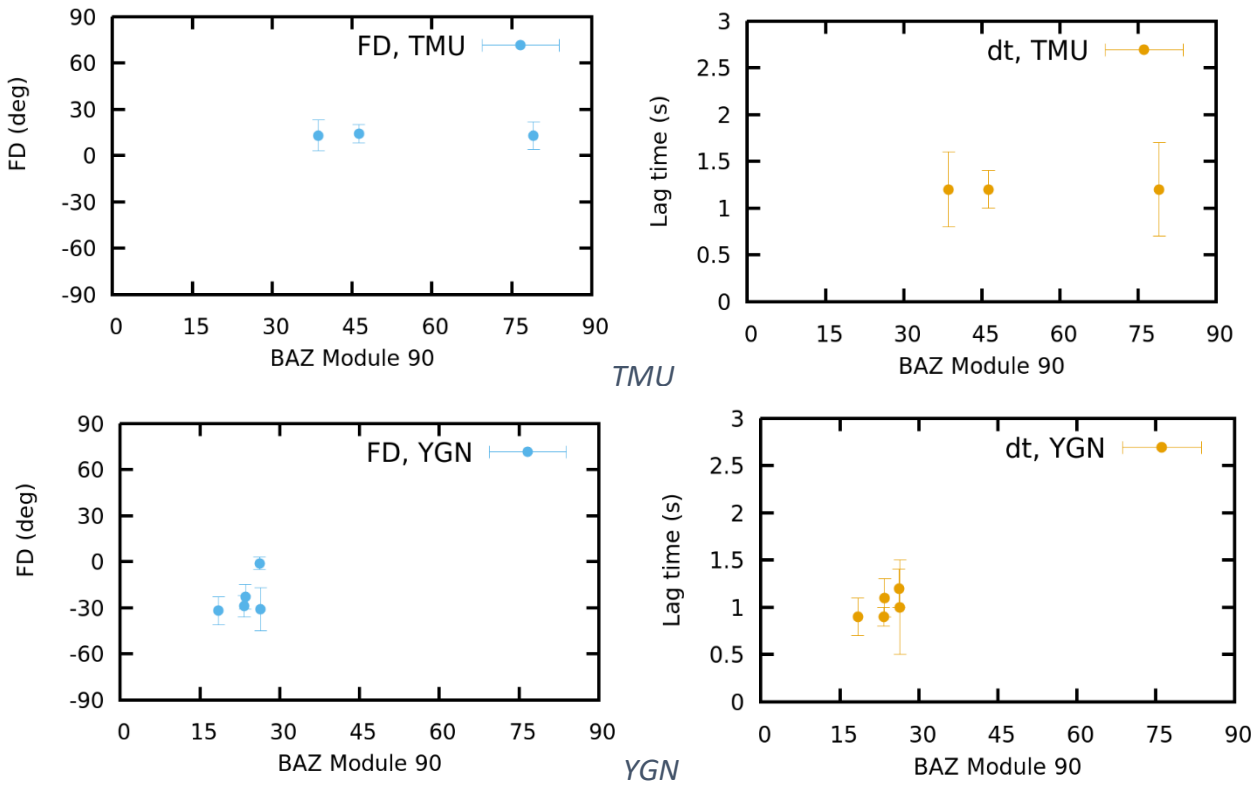
FD, TMU
FD (deg)
BAZ Module 90
dt, TMU
Lag time (s)
BAZ Module 90
TMU
FD, YGN
FD (deg)
BAZ Module 90
dt, YGN
Lag time (s)
BAZ Module 90
YGN